

PARAMETRIC STUDY AND DESIGN OF VIVALDI ANTENNAS AND
ARRAYS

A THESIS SUBMITTED TO
THE GRADUATE SCHOOL OF NATURAL AND APPLIED SCIENCES
OF
MIDDLE EAST TECHNICAL UNIVERSITY

BY

YAKUP ERDOĞAN

IN PARTIAL FULFILLMENT OF THE REQUIREMENTS
FOR
THE DEGREE OF MASTER OF SCIENCE
IN
ELECTRICAL AND ELECTRONICS ENGINEERING

MARCH 2009

Approval of the thesis:

PARAMETRIC STUDY AND DESIGN OF VIVALDI ANTENNAS AND ARRAYS

submitted by **YAKUP ERDOĞAN** in partial fulfillment of the requirements for the degree of **Master of Science in Electrical and Electronics Engineering Department, Middle East Technical University** by,

Prof. Dr. Canan Özgen _____
Dean, Graduate School of **Natural and Applied Sciences**

Prof. Dr. İsmet ERKMEN _____
Head of Department, **Electrical and Electronics Engineering**

Prof. Dr. Gülbin Dural _____
Supervisor, **Electrical and Electronics Engineering Dept., METU**

Examining Committee Members :

Prof. Dr. Altunkan Hızal _____
Electrical and Electronics Engineering Dept., METU

Prof. Dr. Gülbin Dural _____
Electrical and Electronics Engineering Dept., METU

Assoc. Prof. Dr. Sencer Koç _____
Electrical and Electronics Engineering Dept., METU

Assoc. Prof. Dr. Şimşek Demir _____
Electrical and Electronics Engineering Dept., METU

M.Sc. Erhan Halavut _____
ASELSAN

Date: 19.03.2009

I hereby declare that all information in this document has been obtained and presented in accordance with academic rules and ethical conduct. I also declare that, as required by these rules and conduct, I have fully cited and referenced all material and results that are not original to this work.

Name, Last name : Yakup ERDOĞAN

Signature :

ABSTRACT

PARAMETRIC STUDY AND DESIGN OF VIVALDI ANTENNAS AND ARRAYS

Erdoğan, Yakup

M.S., Department of Electrical and Electronics Engineering

Supervisor: Prof. Dr. Gülbin Dural

March 2009, 149 pages

In this thesis, parametric study and design of Vivaldi antennas and arrays are studied. The parameters of single element antennas and arrays are investigated regarding their effects on the design. The return loss responses and radiation patterns are considered in the parametric study. The results of simulations realized using Ansoft HFSS[®], a high frequency electromagnetic field simulation program, are shown and discussed.

Two different Vivaldi antennas operating in 8.5-10.5 GHz frequency band with return loss responses better than 15 dB are designed based on the results of parametric study. Stripline to slotline transition is used in the feeding section of both antennas. In the same manner, two different 8-element uniform linear arrays operating in 8.5-10.5 GHz with half power beam widths smaller than 12° and side lobe levels smaller than 13 dB are designed. Binomial and Dolph-Chebyshev feeding techniques are also investigated in order to improve half power beamwidths and side lobe levels of the designed arrays.

The designed single element Vivaldi antennas and a linear array of Vivaldi antennas are fabricated. The return loss response and radiation patterns of the fabricated antennas and the array are measured and compared with the simulation results.

Keywords: Vivaldi Antennas, Stripline to Slotline Transition, Linear Arrays, Parametric Study

ÖZ

VİVALDİ ANTEN VE ANTEN DİZİLERİNİN PARAMETRİK İNCELENMESİ VE TASARIMI

ERDOĞAN, Yakup

Yüksek Lisans, Elektrik ve Elektronik Mühendisliği Bölümü

Tez Yöneticisi: Prof. Dr. Gülbin DURAL

Mart 2009, 149 sayfa

Bu tez çalışmasında, Vivaldi anten ve anten dizilerinin parametrik incelenmesi ve tasarımı çalışılmıştır. Tek anten ve anten dizilerinin parametreleri tasarım üzerindeki etkilerine göre incelenmiştir. Parametrik çalışmada geriye dönüş kayıpları ve ışıma diagramları dikkate alınmıştır. Yüksek frekanslı elektromanyetik alan simülasyon programı Ansoft HFSS[®] kullanılarak gerçekleştirilen simülasyon sonuçları gösterilmiş ve tartışılmıştır.

Parametrik çalışmanın sonuçları baz alınarak 8.5-10.5 GHz frekans bandında 15 dB'den daha yüksek geriye dönüş kaybına sahip iki farklı Vivaldi anten tasarlanmıştır. Her iki antenin besleme bölümünde şerit kılavuzdan yarı hatta geçiş kullanılmıştır. Aynı biçimde, 8.5-10.5 GHz frekans bandında 12°'den düşük yarı güç hüzme genişliği ve 13 dB'den düşük yan lop seviyesine sahip 8 elemanlı iki farklı düzgün doğrusal anten dizileri tasarlanmıştır. Anten dizilerinin yarı güç hüzme

genişliklerini ve yan loup seviyelerini iyileştirmek için Binomial ve Dolph-Chebyshev besleme teknikleri de incelenmiştir.

Tasarlanan her iki Vivaldi anten ve Vivaldi anten elemanlarından oluşan doğrusal bir anten dizisi üretilmiştir. Üretilen antenlerin ve anten dizisinin geriye dönüş kayıpları ve ışınma diyagramları ölçülmüş ve simülasyon sonuçlarıyla karşılaştırılmıştır.

Anahtar Kelimeler: Vivaldi Antenler, Şerit Kılavuzdan Yarık Hatta Geçiş, Doğrusal Anten Dizileri, Parametrik İnceleme

To my endless love Selcen

ACKNOWLEDGMENTS

I would like to thank Prof. Dr. Gülbin Dural for her valuable supervision and support throughout the development and improvement of this thesis.

I am grateful to Erhan Halavut and Ali Günay Yıldız for their valuable comments throughout the development of this thesis. I am also grateful to Hakan Paruldar, İsmail Bozkurt and Hüsnü Erdösemeci for their great support. I would also like to thank Aselsan Electronics Industries Inc. for the resources and facilities that I used throughout the thesis.

I am grateful to Serdar Tuğcu, Emre Şahin and Mutlu Ertürk for their support and patience. Thanks a lot to all my friends for their great encouragement and their valuable help to accomplish this work.

Lastly, I would like to thank my parents, my lovely brother Ali and extended family for bringing up and trusting in me, and Selcen Oğuz, for giving me the strength and courage to finish this work.

TABLE OF CONTENTS

ABSTRACT	iv
ÖZ	vi
ACKNOWLEDGMENTS	ix
TABLE OF CONTENTS	x
LIST OF TABLES	xiii
LIST OF FIGURES	xiv
LIST OF ABBREVIATIONS	ii
CHAPTERS	
1. INTRODUCTION	1
1.1 A Brief Review of Previous Works	2
1.2 Objectives of the Thesis	3
1.3 Outline of the Thesis	4
2. VIVALDI ANTENNAS AND ARRAYS.....	6
2.1 Tapered Slot Antennas (TSA).....	6
2.2 The Principle of Operation.....	7
2.3 The Feeding Techniques	8
2.3.1 Directly Coupled Transitions	8
2.3.1.1 Coaxial to Slotline Transition	8
2.3.2 Electromagnetically Coupled Transitions	9
2.3.2.1 Microstrip to Slotline Transition	9
2.3.2.2 Stripline to Slotline Transition	11
2.3.2.3 Antipodal Slotline	12
2.3.2.4 Balanced Antipodal Slotline	13
2.4 Arrays	14
2.4.1 Basic Concepts	14
2.4.1.1 Array Pattern	14
2.4.1.2 Mutual Coupling	15
2.4.1.3 Array Directivity	15

2.4.2	Array Configurations	16
2.4.2.1	Geometrical Arrangement.....	16
2.4.2.2	Feeding Characteristics	18
2.4.3	Array Simulation.....	19
2.4.3.1	Method of Moments (MoM) Solution.....	19
2.4.3.2	Finite Difference Time Domain (FDTD) Solution	19
2.4.3.3	Conjugate Gradient Fast Fourier Transform(CG-FFT) Solution...	20
2.4.3.4	Linked Boundary Conditions Solution	20
3.	PARAMETRIC STUDY AND DESIGN OF VIVALDI ANTENNAS.....	22
3.1	Design Insight	22
3.2	Stripline Model	27
3.2.1	Substrate Material	28
3.2.2	Substrate Thickness.....	29
3.2.3	Stripline Width.....	30
3.3	Stripline and Slotline Model	31
3.3.1	Stripline Stub Length	32
3.3.2	Slotline Stub Length.....	34
3.3.3	Slotline Width	35
3.3.4	Antenna Length.....	37
3.3.5	Antenna Width	39
3.3.6	Backwall Offset.....	41
3.4	Antenna Model.....	43
3.4.1	Uniform Slotline Length	44
3.4.2	Taper	46
3.4.3	Mouth Opening	49
3.4.4	Edge Offset.....	51
3.5	Final Design of Single Element Vivaldi Antenna.....	53
4.	PARAMETRIC STUDY AND DESIGN OF VIVALDI ARRAYS	60
4.1	Uniform Linear Array Design.....	61
4.2	Array Parameters.....	64
4.2.1	Array Spacing.....	64
4.2.2	Number of Elements	65
4.2.3	Uniform Slot Width	66

4.2.4	Taper Length	68
4.2.5	Taper Rate	69
4.3	Array Feeding.....	70
4.3.1	Binomial Array.....	71
4.3.2	Dolph-Chebyshev Array	73
4.4	Final Design of Vivaldi Array.....	76
4.5	An Improved Array Design.....	83
5.	FABRICATION AND MEASUREMENTS	98
5.1	Fabrication.....	98
5.2	Measurement Setup	100
5.2.1	Return Loss Response Measurement	101
5.2.2	Radiation Pattern Measurement	104
5.3	Measurement Results	105
5.3.1	Return Loss Measurement Results.....	105
5.3.2	Pattern Measurement Results.....	110
6.	CONCLUSION	133
6.1	Summary	133
6.2	Future Work	135
	REFERENCES.....	137
	APPENDICES	
A.	SIMULATION METHOD	140
B.	MATLAB FUNCTION	142
C.	DATASHEETS	143
D.	A SELSAN TAPERED ANECHOIC CHAMBER	147

LIST OF TABLES

TABLES

Table 3.1 Change in characteristic impedance of the stripline with stripline width..	30
Table 3.2 Change in characteristic impedance of the stripline with stripline length and slotline stub length	31
Table 3.3 Final design parameters of the single Vivaldi element.....	53
Table 4.1 Final design parameters of Vivaldi array.....	77
Table 4.2 Half-power beamwidth of the final design in 8.5-10.5 GHz frequency band	82
Table 4.3 Side lobe and grating lobe levels of the final design in 8.5-10.5 GHz frequency band	82
Table 4.4 Half-power beamwidth of Dolph-Chebyshev array with $R = 20$ dB in 8.5-10.5 GHz frequency band	97
Table 4.5 Side lobe and grating lobe levels of Dolph-Chebyshev array with $R = 20$ dB in 8.5-10.5 GHz frequency band	97
Table 5.1 Measured half-power beamwidth of the array in 2-18 GHz frequency band	131
Table 5.2 Side lobe and grating lobe levels of the array in 2-18 GHz frequency band	132

LIST OF FIGURES

FIGURES

Figure 2.1 Types of TSA; (a) exponentially tapered (Vivaldi), (b) linearly tapered (LTSA) and (c) constant width slot antenna (CWSA).....	7
Figure 2.2 Coaxial to slotline transition.....	9
Figure 2.3 Microstrip to slotline transition.....	10
Figure 2.4 Six-port microstrip to slotline transition.....	11
Figure 2.5 Radial quarter-wavelength stubs.....	12
Figure 2.6 Antipodal slotline transition [18].....	13
Figure 2.7 Balanced antipodal slotline transition.....	14
Figure 2.8 Linear array configuration.....	16
Figure 2.9 Planar array configuration.....	17
Figure 2.10 Dual-polarized array configuration [12].....	18
Figure 3.1 Designed Vivaldi antenna model and the parameters.....	24
Figure 3.2 Stripline model.....	27
Figure 3.3 Stripline model with 80Ω - 50Ω transition.....	28
Figure 3.4 Cascaded identical transitions.....	32
Figure 3.5 Return loss response with three different stripline stub length.....	33
Figure 3.6 Reverse gain with three different stripline stub lengths.....	33
Figure 3.7 Return loss response with three different slotline stub lengths.....	34
Figure 3.8 Reverse gain with three different slotline stub lengths.....	35
Figure 3.9 Return loss response with three different slotline widths.....	36
Figure 3.10 Reverse gain with three different slotline widths.....	37
Figure 3.11 Return loss response with three different antenna lengths.....	38
Figure 3.12 Reverse gain with three different antenna lengths.....	39
Figure 3.13 Return loss response with three different antenna widths.....	40
Figure 3.14 Reverse gain with three different antenna widths.....	40
Figure 3.15 Return loss response with three different backwall offset.....	41

Figure 3.16 Reverse gain with three different backwall offset	42
Figure 3.17 Return loss response and reverse gain of the design with zero backwall offset.....	43
Figure 3.18 Complete antenna model in HFSS®	44
Figure 3.19 Return loss response with three different uniform slotline lengths	45
Figure 3.20 H-plane radiation pattern with three different uniform slotline lengths (f = 9.5 GHz).....	45
Figure 3.21 Return loss response with three different taper lengths.....	46
Figure 3.22 H-plane radiation pattern with three different taper lengths (f = 9.5 GHz)	47
Figure 3.23 Return loss response with three different taper rates.....	48
Figure 3.24 H-plane radiation pattern with three different taper rates (f = 9.5 GHz)	48
Figure 3.25 Return loss response with three different mouth openings.....	50
Figure 3.26 H-plane radiation pattern with three different mouth openings (f = 9.5 GHz).....	50
Figure 3.27 Return loss response with three different edge offsets	52
Figure 3.28 H-plane radiation pattern with three different edge offsets (f = 9.5 GHz)	52
Figure 3.29 Return loss response of the final design	54
Figure 3.30 Reverse gain of the final design.....	54
Figure 3.31 H-plane co-polarization radiation pattern of final design (8.5 GHz).....	55
Figure 3.32 H-plane co-polarization and cross-polarization patterns of the final design (8.5 GHz)	55
Figure 3.33 H-plane total radiation pattern of final design (9.5 GHz).....	56
Figure 3.34 H-plane co-polarization and cross-polarization patterns of the final design (9.5 GHz)	56
Figure 3.35 H-plane total radiation pattern of final design (10.5 GHz).....	57
Figure 3.36 H-plane co-polarization and cross-polarization patterns of the final design (10.5 GHz)	57
Figure 3.37 E-plane pattern of the final design (8.5 GHz).....	58
Figure 3.38 E-plane pattern of the final design (9.5 GHz).....	58
Figure 3.39 E-plane pattern of the final design (10.5 GHz).....	59
Figure 4.1 Linear array of 8 elements	63

Figure 4.2 H-plane array pattern for three different element spacing values ($f = 9.5$ GHz).....	65
Figure 4.3 H-plane array pattern for three different element numbers ($f = 9.5$ GHz).....	66
Figure 4.4 H-plane array pattern for three different element slot width values ($f = 9.5$ GHz).....	67
Figure 4.5 H-plane array pattern for three different taper length values ($f = 9.5$ GHz)	68
Figure 4.6 H-plane array pattern for three different taper rates ($f = 9.5$ GHz)	70
Figure 4.7 H-plane patterns of uniform and binomial arrays ($f = 9.5$ GHz).....	72
Figure 4.8 H-plane patterns of uniform and Chebyshev arrays ($f = 9.5$ GHz)	76
Figure 4.9 H-plane co-polarization pattern of the final design (8.5 GHz).....	78
Figure 4.10 H-plane co-polarization and cross-polarization radiation patterns of the final design	78
Figure 4.11 H-plane co-polarization pattern of the final design (9.5 GHz).....	79
Figure 4.12 H-plane co-polarization and cross-polarization radiation patterns of the final design	79
Figure 4.13 H-plane co-polarization radiation pattern of the final design (10.5 GHz)	80
Figure 4.14 H-plane co-polarization and cross-polarization radiation patterns of the final design	80
Figure 4.15 E-plane pattern of the final design (8.5 GHz).....	81
Figure 4.16 E-plane pattern of the final design (9.5 GHz).....	81
Figure 4.17 E-plane pattern of the final design (10.5 GHz).....	82
Figure 4.18 Return loss response of the second antenna model	84
Figure 4.19 H-plane radiation patterns of first and second antenna designs ($f = 9.5$ GHz).....	84
Figure 4.20 H-plane total radiation pattern of the second antenna (8.5 GHz).....	85
Figure 4.21 H-plane co-polarization and cross-polarization radiation patterns of the second antenna (8.5 GHz).....	85
Figure 4.22 H-plane total radiation pattern of the second antenna (9.5 GHz).....	86
Figure 4.23 H-plane co-polarization and cross-polarization radiation patterns of the second antenna (9.5 GHz).....	86
Figure 4.24 H-plane total radiation pattern of the second antenna (10.5 GHz).....	87

Figure 4.25 H-plane co-polarization and cross-polarization radiation patterns of the second antenna (10.5 GHz)	87
Figure 4.26 E-plane pattern of the second antenna (8.5 GHz).....	88
Figure 4.27 E-plane pattern of the second antenna (9.5 GHz).....	88
Figure 4.28 E-plane pattern of the second antenna (10.5 GHz).....	89
Figure 4.29 H-plane patterns of arrays with the first and second antennas ($f = 9.5$ GHz).....	90
Figure 4.30 H-plane radiation patterns of Dolph-Chebyshev and uniform arrays (SLL = 17 dB)	91
Figure 4.31 H-plane radiation patterns of Dolph-Chebyshev and uniform arrays (SLL = 20 dB).....	91
Figure 4.32 H-plane co-polarization radiation pattern of the second array (8.5 GHz)	92
Figure 4.33 H-plane co-polarization and cross-polarization radiation patterns of the second array	93
Figure 4.34 H-plane co-polarization radiation pattern of the second array (9.5 GHz)	93
Figure 4.35 H-plane co-polarization and cross-polarization radiation patterns of the second array	94
Figure 4.36 H-plane co-polarization radiation pattern of the second array (10.5 GHz)	94
Figure 4.37 H-plane co-polarization and cross-polarization radiation patterns of the second array (10.5 GHz)	95
Figure 4.38 E-plane pattern of the second array (8.5 GHz).....	95
Figure 4.39 E-plane pattern of the second array (9.5 GHz).....	96
Figure 4.40 E-plane pattern of the second array (10.5 GHz).....	96
Figure 5.1 Fabricated Vivaldi antennas	99
Figure 5.2 Fabricated Vivaldi array with its backplane	100
Figure 5.3 Return loss measurement setup for the single antenna.....	101
Figure 5.4 Return loss measurement setup for the array.....	102
Figure 5.5 Array structure with power dividers	102
Figure 5.6 Measured insertion loss of 4-way power divider.....	103

Figure 5.7 Measured and simulated return loss responses of Antenna-1 (8.5-10.5 GHz).....	105
Figure 5.8 Measured and simulated return loss responses of Antenna-1 (2-18 GHz).....	106
Figure 5.9 Measured and simulated return loss responses of Antenna-2 (8.5-10.5 GHz).....	106
Figure 5.10 Measured return loss response of Antenna-2 (2-18 GHz).....	107
Figure 5.11 Measured return loss response of the array (8.5-10.5 GHz).....	108
Figure 5.12 Measured return loss response of the array (2-18 GHz).....	108
Figure 5.13 Measured mutual coupling of the array elements (referenced to 1 st element).....	109
Figure 5.14 Measured mutual coupling of the array elements (referenced to 5 th element).....	110
Figure 5.15 Measured and simulated H-plane co-polarization patterns of Antenna-1 (2 GHz).....	111
Figure 5.16 Measured and simulated H-plane co-polarization patterns of Antenna-1 (6 GHz).....	111
Figure 5.17 Measured and simulated H-plane co-polarization patterns of Antenna-1 (8.5 GHz).....	112
Figure 5.18 Measured and simulated H-plane co-polarization patterns of Antenna-1 (9.5 GHz).....	112
Figure 5.19 Measured and simulated H-plane co-polarization patterns of Antenna-1 (10.5 GHz).....	113
Figure 5.20 Measured and simulated H-plane co-polarization patterns of Antenna-1 (15 GHz).....	113
Figure 5.21 Measured and simulated H-plane co-polarization patterns of Antenna-1 (18 GHz).....	114
Figure 5.22 Measured and simulated H-plane cross-polarization patterns of Antenna-1.....	114
Figure 5.23 Measured and simulated H-plane cross-polarization patterns of Antenna-1.....	115
Figure 5.24 Measured and simulated H-plane cross-polarization patterns of Antenna-1.....	115

Figure 5.25 Measured and simulated E-plane patterns of Antenna-1 (8.5 GHz).....	116
Figure 5.26 Measured and simulated E-plane patterns of Antenna-1 (9.5 GHz).....	116
Figure 5.27 Measured and simulated E-plane patterns of Antenna-1 (10.5 GHz)...	117
Figure 5.28 Measured and simulated H-plane co-polarization patterns of Antenna-2 (2 GHz).....	118
Figure 5.29 Measured and simulated H-plane co-polarization patterns of Antenna-2 (6 GHz).....	118
Figure 5.30 Measured and simulated H-plane co-polarization patterns of Antenna-2 (8.5 GHz).....	119
Figure 5.31 Measured and simulated H-plane co-polarization patterns of Antenna-2 (9.5 GHz).....	119
Figure 5.32 Measured and simulated H-plane co-polarization patterns of Antenna-2 (10.5 GHz).....	120
Figure 5.33 Measured and simulated H-plane co-polarization patterns of Antenna-2 (15 GHz).....	120
Figure 5.34 Measured and simulated H-plane co-polarization patterns of Antenna-2 (18 GHz).....	121
Figure 5.35 Measured and simulated H-plane cross-polarization patterns of Antenna- 2.....	121
Figure 5.36 Measured and simulated H-plane cross-polarization patterns of Antenna- 2.....	122
Figure 5.37 Measured and simulated H-plane cross-polarization patterns of Antenna- 2.....	122
Figure 5.38 Measured and simulated E-plane patterns of Antenna-2 (8.5 GHz).....	123
Figure 5.39 Measured and simulated E-plane patterns of Antenna-2 (9.5 GHz).....	123
Figure 5.40 Measured and simulated E-plane patterns of Antenna-2 (10.5 GHz)...	124
Figure 5.41 Measured and simulated H-plane co-polarization patterns of the array (2 GHz).....	125
Figure 5.42 Measured and simulated H-plane co-polarization patterns of the array (6 GHz).....	125
Figure 5.43 Measured and simulated H-plane co-polarization patterns of the array (8.5 GHz).....	126

Figure 5.44 Measured and simulated H-plane co-polarization patterns of the array (9.5 GHz).....	126
Figure 5.45 Measured and simulated H-plane co-polarization patterns of the array (10.5 GHz).....	127
Figure 5.46 Measured and simulated H-plane co-polarization patterns of the array (15 GHz).....	127
Figure 5.47 Measured and simulated H-plane co-polarization patterns of the array (18 GHz).....	128
Figure 5.48 Measured and simulated H-plane cross-polarization patterns of the array (8.5 GHz).....	128
Figure 5.49 Measured and simulated H-plane cross-polarization patterns of the array (9.5 GHz).....	129
Figure 5.50 Measured and simulated H-plane cross-polarization patterns of the array	129
Figure 5.51 Measured and simulated E-plane patterns of the array (8.5 GHz)	130
Figure 5.52 Measured and simulated E-plane patterns of the array (9.5 GHz)	130
Figure 5.53 Measured and simulated E-plane patterns of the array (10.5 GHz)	131
Figure A.1 Complete antenna model in HFSS.....	140
Figure A.2 The wave-port structure	141
Figure C.1 Rogers RT/Duroid 5880 high frequency laminate datasheet.....	143
Figure C.2 Rogers RT/Duroid 5880 high frequency laminate datasheet.....	144
Figure C.3 Narda 4326B-4 power divider datasheet.....	145
Figure C.4 Narda 4326B-4 power divider datasheet.....	146
Figure D.1 Top view of the tapered anechoic chamber in ASELSAN Inc.	148
Figure D.2 Antenna measurement setup in the anechoic chamber	149

LIST OF ABBREVIATIONS

- CG : Conjugate Gradient
- CWSA : Constant Width Slot Antenna
- FDTD : Finite Difference Time Domain
- FEM : Finite Element Method
- FFT : Fast Fourier Transform
- LTSA : Linearly Tapered Slot Antenna
- MoM : Method of Moments
- PEC : Perfect Electric Conductor
- PMC : Perfect Magnetic Conductor
- TSA : Tapered Slot Antenna
- UWB : Ultra Wide Band
- VSWR : Voltage Standing Wave Ratio

CHAPTER 1

INTRODUCTION

Rapid developing technology of satellite, wireless communication, remote sensing and radar has led to the ultra wide band (UWB) electronic systems. Any radio technology using signals with a spectrum occupying a bandwidth either greater than 20% of the centre frequency or a bandwidth greater than 500MHz is defined as UWB technology [1]. UWB technology requires antennas with broad bandwidth and minimum distortion of received and radiated pulses. Moreover, UWB airborne applications have strict requirements on the size of antenna arrays to be used due to the limited space.

The tapered slot antennas (TSA) are the best candidates for use in UWB technology. These antennas offer a wide bandwidth, significant gain and symmetric patterns in both co-polarization and cross-polarization. TSAs are efficient and light weight. In addition, TSAs are appreciably simple in geometry making them more advantageous. The most commonly used class of TSA in UWB technology is Vivaldi antenna. Vivaldi antenna, first introduced by Gibson [2] in 1979, has an exponentially tapered slotline. As a member of the class of TSA, Vivaldi antenna provides broad bandwidth, low cross polarization and directive propagation at microwave frequencies. Vivaldi antennas are low cost, easy to fabricate and fairly insensitive to dimensional tolerances in fabrication process due to printed circuit technology used for the construction of these antennas. Moreover, Vivaldi arrays are small size and low weight enabling compact arrays. It shall be also noted that the beamwidth and directivity of a Vivaldi antenna might be considerably improved varying the design parameters.

This thesis deals with small size Vivaldi antennas and arrays. The parameters affecting antenna and array designs are studied comprehensively. The designs of

Vivaldi antenna and array with the requirements given in following chapters are realized as well, based on this parametric study.

1.1 A Brief Review of Previous Works

Lewis et al. [3] introduced tapered slot antenna as a broadband stripline array element capable of multioctave bandwidths in his study in 1974. Following TSA, Vivaldi antenna, an exponentially tapered slot antenna, was originated by Gibson [2] in 1979. Gibson stated that Vivaldi antenna had significant gain and linear polarization in a frequency range from below 2 GHz to above 40 GHz. Gibson's Vivaldi antenna with an asymmetric one sided microstrip to slotline transition was constructed on alumina using microwave photolithographic thin film techniques. It served fairly well as an 8-40 GHz video receiver module.

Yngvesson et al. [4] compared three different TSAs, linearly tapered slot antenna (LTSA), constant width slot antenna (CWSA) and Gibson's exponentially tapered slot antenna, Vivaldi antenna. Yngvesson found that Vivaldi antenna had the smallest side lobe levels followed by CWSA and LTSA whereas it had the widest beamwidth and CWSA had the narrowest one. He also investigated the effect of dielectric substrate thickness and the length of Vivaldi antenna on the beamwidth.

E. Gazit [5] proposed two important changes to the traditional Vivaldi design. He used a low dielectric substrate (cuclad, $\epsilon=2.45$) instead of alumina and an antipodal slotline transition. The antipodal slotline transition was constructed by tapering the microstrip line through parallel strip to an asymmetric double sided slot line. This type of transition offered relatively wider bandwidth which was restricted by the microstrip to slotline transition of the traditional design. However, antipodal slotline transition had the problem of high cross polarization.

Langley et al. [6] improved the antipodal transition of E. Gazit with a new and balanced structure in order to improve the cross polarization characteristics. This type of structure, known as balanced antipodal transition, consists of three layers of tapered slots fed directly by a stripline. E-field distribution of the antipodal transition

is balanced with the addition of the mentioned layer. The tapered slots on both sides of the antenna serve as ground planes. The balanced antipodal transition offered a 18:1 bandwidth with fairly well cross polarization characteristics. Then, Langley et al. [7] also constructed a wide bandwidth phased array using this balanced antipodal Vivaldi antenna. He achieved good cross polarization levels as well as wideband wide angle scanning.

The cross polarization of the antipodal Vivaldi antenna was also improved using different techniques. Kim et al. [8] placed the antipodal antenna and its mirror image alternately in the Cross-polarization. The cancellation of cross polarization fields was aimed in this study and more than 20 dB reduction of cross polarization level at broadside was obtained.

Schuppert [9] came up with circular stubs applied to microstrip to slotline transitions in order to offer an easier fabrication whereas Sloan et al. [10] used radial stubs instead of circular ones and improved the bandwidth of these kind of transitions. Schaubert [11] used both circular and radial stubs in order to design a stripline-fed, metal fins placed on both sides of the element, Vivaldi antenna. He stated in his study that the bandwidth of the antenna was improved with these nonuniform stubs and also noted that radial stub was more advantageous regarding the overlapping between circular stripline and slotline stubs. It was also shown in this study that the stripline feeding increased the antenna bandwidth compared with the microstrip feeding.

1.2 Objectives of the Thesis

Vivaldi antennas and arrays are used in a broad range of applications as stated earlier. However, physical structure of these antennas has not been yet understood well and very few studies [11], [12], [13], [14] exist dealing with parametric aspects of Vivaldi antennas or arrays and these papers are not comprehensive enough. Experimental studies are much time consuming and analysis methods with simple structures do not give exact results for this type of antennas. Thus, in this work, it is aimed to investigate Vivaldi antenna design parameters regarding their effects on

antenna impedance, return loss response, and reverse gain characteristics and array parameters regarding their effects on radiation pattern. Ansoft HFSS[®], a high frequency electromagnetic field simulation program utilizing full-wave finite element method (FEM) is used for simulations.

Another objective of this thesis is to design and construct Vivaldi antenna and array operating in 8.5-10.5 GHz frequency band based on the parametric study. A half-power beamwidth smaller than 12° and side lobe levels smaller than 13 dB in H-plane are the requirements of the array design. Two different Vivaldi antennas operating in 8.5-10.5 GHz frequency band with stripline to slotline transition are designed. Using these two Vivaldi antennas mentioned, 8-element linear arrays are also designed. The arrays are fed uniformly as well as using binomial and Dolph-Chebyshev feeding techniques improving the side lobe level and half-power beamwidth characteristics. Finally, both Vivaldi antennas and array are fabricated and the return loss responses and radiation patterns of these single elements are measured.

1.3 Outline of the Thesis

This thesis is organized in six chapters as follows:

Chapter 2 starts with an introduction to the class of TSA. The principle of operation for Vivaldi antenna is described followed by the explanation and comparison of feeding techniques commonly used for this type of antennas. Antenna arrays are investigated in terms of basic array concepts, commonly used configurations and simulation techniques at the end of this chapter.

In Chapter 3, Vivaldi antenna parameters are investigated in three different models: stripline model, stripline&slotline model and antenna model. The effects of these parameters on antenna impedance, return loss response and reverse gain curves are evaluated using Ansoft HFSS[®]. Vivaldi antenna, operating in 8.5-10.5 GHz frequency band, designed regarding this parametric study and its simulation results are also given.

Chapter 4 starts with an 8-element uniform linear array design using Vivaldi antenna mentioned in Chapter 3. Parametric study of Vivaldi arrays is given next regarding the effects on half-power beamwidth, gain and side lobe level of the array. Binomial and Dolph-Chebyshev feeding techniques are also discussed in order to improve radiation pattern of designed array. Based on the parametric study of arrays, a second Vivaldi antenna and array are designed. Radiation pattern of this second array with uniform, binomial and Dolph-Chebyshev feeding simulated using Ansoft HFSS[®] are given at the end of this chapter.

Fabrication process and measurement results of both Vivaldi antennas and the improved array are given in Chapter 5 as well as the description of measurement setup. Measurement results, return loss response and radiation pattern of the antennas and the array are discussed and compared with simulation results.

Finally, both parametric study and design of Vivaldi antennas and arrays are summarized. Moreover, recommendations to extend parametric study and improve array performance are discussed in Chapter 6.

CHAPTER 2

VIVALDI ANTENNAS AND ARRAYS

The Vivaldi antenna is a member of class of aperiodic continuously scaled traveling wave antenna structures. It is first originated by Gibson [2] in 1979. Vivaldi antenna gives significant advantages of efficiency, high gain, wide bandwidth and simple geometry.

The Vivaldi antenna, having an exponentially tapered slot profile, is a type of tapered slot antenna (TSA). TSA is discussed below with its typical characteristics and different types before discussing the Vivaldi antenna and its principle of operation in detail.

2.1 Tapered Slot Antennas (TSA)

The distinctive feature of TSA is a slotline widening with distance from the feed forming the radiating section of the antenna. The profile of radiating section or taper specifies the different types of TSA. The best known types of TSA which are linearly tapered slot antenna (LTSA), constant width slot antenna (CWSA) and exponentially tapered slot antenna (Vivaldi) are shown in Figure 2.1 below.

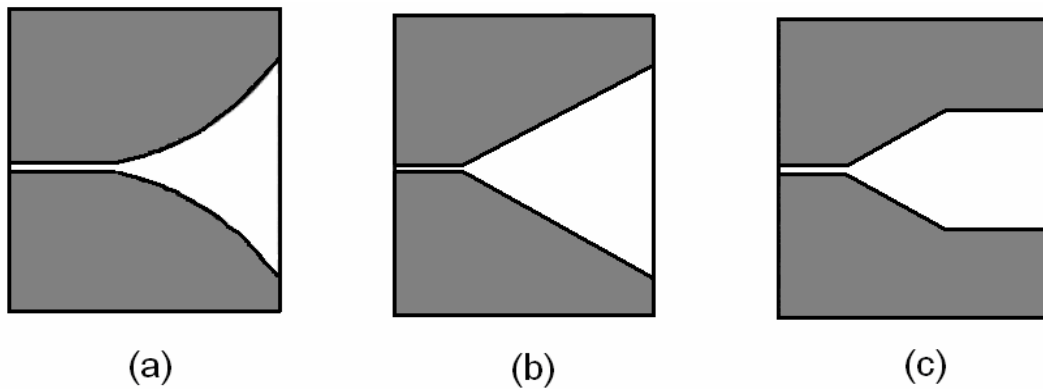


Figure 2.1 Types of TSA; (a) exponentially tapered (Vivaldi), (b) linearly tapered (LTSA) and (c) constant width slot antenna (CWSA)

TSA's are efficient and geometrically simple with significant gain and wide bandwidth and appreciably light weight as mentioned before. Moreover, this kind of antennas produce symmetrical radiation patterns with high directivity and low side lobe levels.

2.2 The Principle of Operation

The Vivaldi antenna belongs to the surface wave class of traveling wave antennas (the other traveling wave antenna type is the leaky wave antenna). In order to describe principle of operation, the surface wave antennas can be divided into two sections: propagating section and radiating section.

The slot width (separation between the conductors) is smaller than one-half free space wavelength ($\lambda_0/2$) and the waves traveling down the curved path along the antenna are tightly bound to the conductors in the propagating section. The bond becomes progressively weaker and the energy gets radiated away from the antenna coupling to the air in the radiating section where the slot width is increasing beyond the one-half wavelength [2].

The waves are traveling along the antenna surface until the limiting case of phase velocity is equal to the free space velocity of light ($c=3 \times 10^8$). The limiting case intends the antenna with air as dielectric. That is to say, radiation from low dielectric

substrates is considerably high and crucial for the antenna operation. The choice of dielectric as the antenna substrate material will be detailed in the next chapter.

2.3 The Feeding Techniques

The Vivaldi antenna, as a member of class of TSA, is most effective with a slotline feeding. Thus, a transition shall be designed to couple signals to the slotline of Vivaldi from the transmitter or receiver circuitry. The transition shall be low loss over a wide frequency range so as not to limit operating bandwidth. It shall also be compact and easy to fabricate.

The feeding techniques may be divided into two types mainly as directly coupled transitions and electromagnetically coupled transitions.

2.3.1 Directly Coupled Transitions

A wire or a solder connection can act as the direct current path providing the electrical contact for this type of transition. The best known directly coupled transition type is coaxial line to slotline transition.

2.3.1.1 Coaxial to Slotline Transition

In this type of transition, the signals are coupled to the slotline from the actual antenna feed through a coaxial line. An open circuited slot and a coaxial line placed perpendicular to it form the transition. The electrical connection of the coaxial cable to the ground plane is provided by the outer conductor on one side of the slot while the inner conductor of the cable is placed over the slot forming a semicircular shape [15]. Figure 2.2 shows coaxial to slotline feed structure.

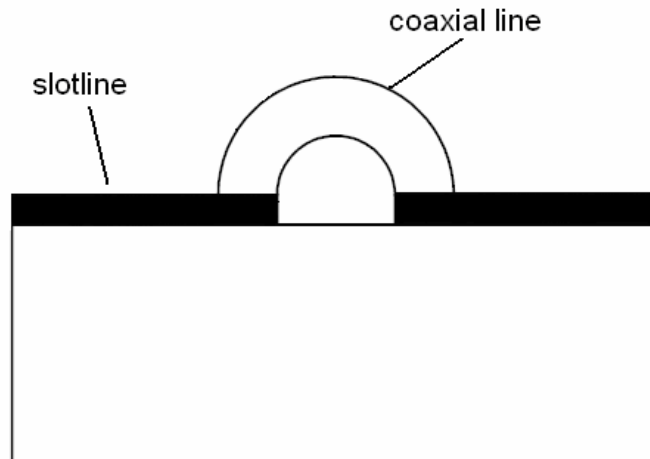


Figure 2.2 Coaxial to slotline transition

The characteristic impedance of the slotline is too high to get an adequate matching characteristic with the slotline etched on single side of the substrate. A better matching, thereby a wider bandwidth, is obtained etching the slotline on both sides of the substrate. However, coaxial feeding is still unfavorable to implement successfully due to etching difficulties.

2.3.2 Electromagnetically Coupled Transitions

The coupling of signals to the slotline is through the electromagnetic fields in this type of transition. Microstrip to slotline, stripline to slotline, antipodal slotline and balanced antipodal slotline are the best known types of electromagnetically coupled transitions.

2.3.2.1 Microstrip to Slotline Transition

The basic microstrip to slotline transition is constructed with microstrip and slotline crossing each other at a right angle. The microstrip is etched on one side of the substrate and the slotline on the other side of the substrate. The microstrip crosses the slotline and extends one quarter of a wavelength further from the slotline in the same way as the slotline extending one quarter wavelength further from the microstrip. The quarter wavelength microstrip stub is open circuited but appears as a short

circuit at the crossing with slotline. The slotline stub is bonded to the ground plane and short circuited but obviously it appears as an open circuit at the crossing. This mechanism makes electromagnetic coupling between the microstrip and the slotline possible. Figure 2.3 shows the basic microstrip to slotline transition structure.

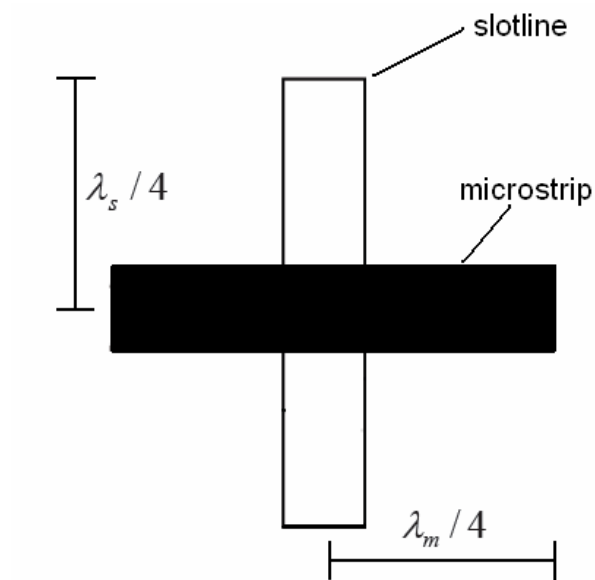


Figure 2.3 Microstrip to slotline transition

This kind of transition reduces the operating bandwidth considerably. Six-port microstrip to slotline transition was proposed by Scieck and Kohler [16] to overcome this problem. However, the transitions of these six ports are too difficult to implement. The structure is shown in Figure 2.4 below.

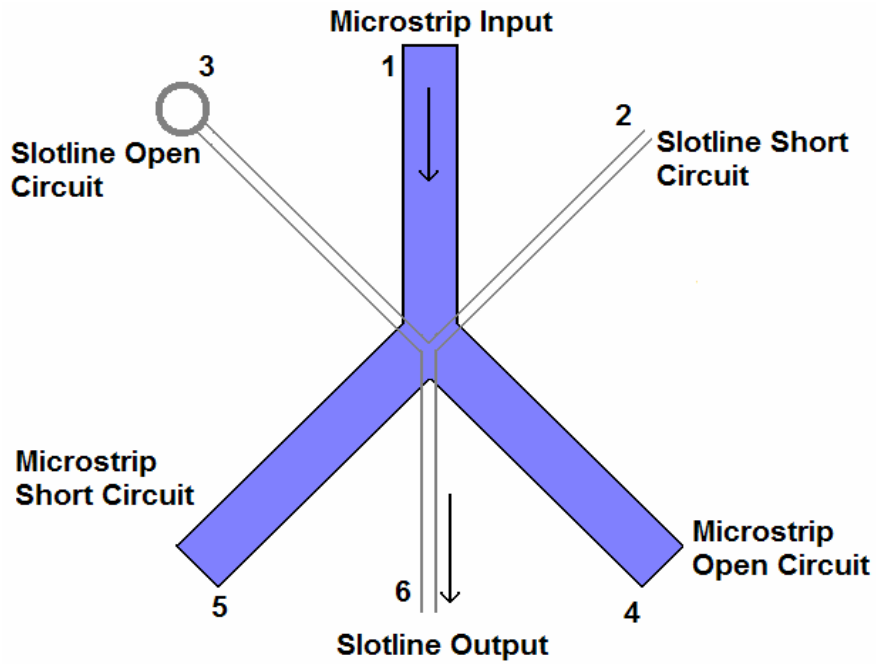


Figure 2.4 Six-port microstrip to slotline transition

2.3.2.2 Stripline to Slotline Transition

The stripline to slotline transition consists of slots etched on both sides of the substrate and a stripline feeding the slotlines at the center of the substrate. The quarter wavelength stub mechanism of microstrip to slotline transition is also used for this structure. The most important advantage of stripline over the microstrip is the increased bandwidth.

Non-uniform stubs may be used for both stripline to slotline and microstrip to slotline transitions in order to increase the bandwidth. The first idea was to use circular quarter-wavelength stubs. Then, it was found out that radial stubs would be the best to increase the bandwidth and reduce overlapping between the microstrip/stripline and slotline at the same time. Figure 2.5 shows this latter application; radial quarter-wavelength stubs.

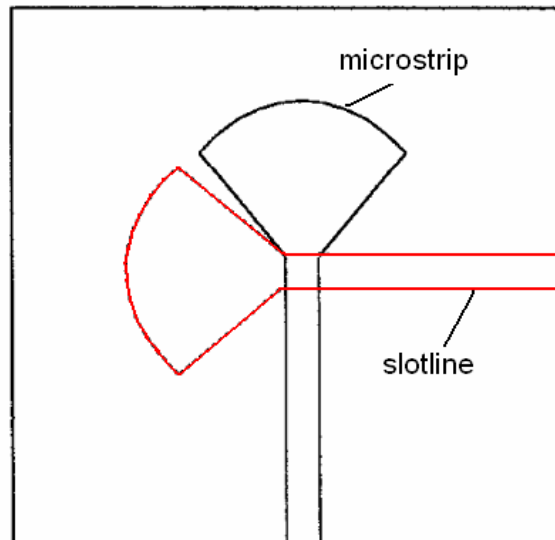


Figure 2.5 Radial quarter-wavelength stubs

2.3.2.3 Antipodal Slotline

Microstrip/stripline to slotline transitions require drilled short holes to connect the conductors on both sides of the substrate; they also limit the bandwidth noticeably due to quarter-wavelength transmission line stubs [5]. Antipodal slotline was first proposed by E. Gazit, overcoming the mentioned disadvantages of the former transitions. Moreover, fed by a microstrip directly, antipodal slotline transition offers a lower impedance compared to that of a slotline. Figure 2.6 gives the antipodal transition.

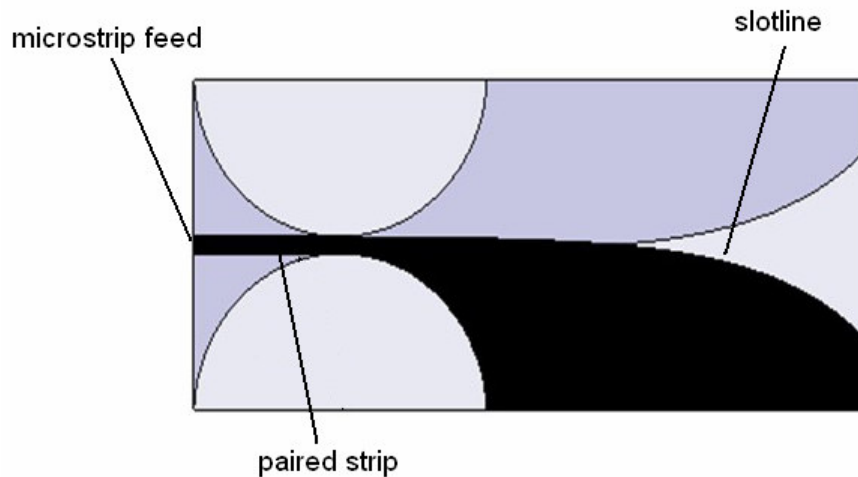


Figure 2.6 Antipodal slotline transition [18]

The input feed of this type of transition is a microstrip as mentioned before. The paired-strip seen in Figure 2.6 is the transition region and the slotline serves as radiating section. The antipodal slotline has a poor cross polarization characteristic despite the improved bandwidth.

2.3.2.4 Balanced Antipodal Slotline

An additional dielectric and metallization layer to the antipodal slotline balance the E-field distribution in the flared-slot, improving the Cross-polarization and forming the so called balanced antipodal slotline. The antenna is fed by a stripline directly in this type of transition. The flared input track on one side of the board and the ground planes on the other side flared out in the opposite direction yield the balanced structure. In Figure 2.7, the balanced antipodal slotline structure is shown.

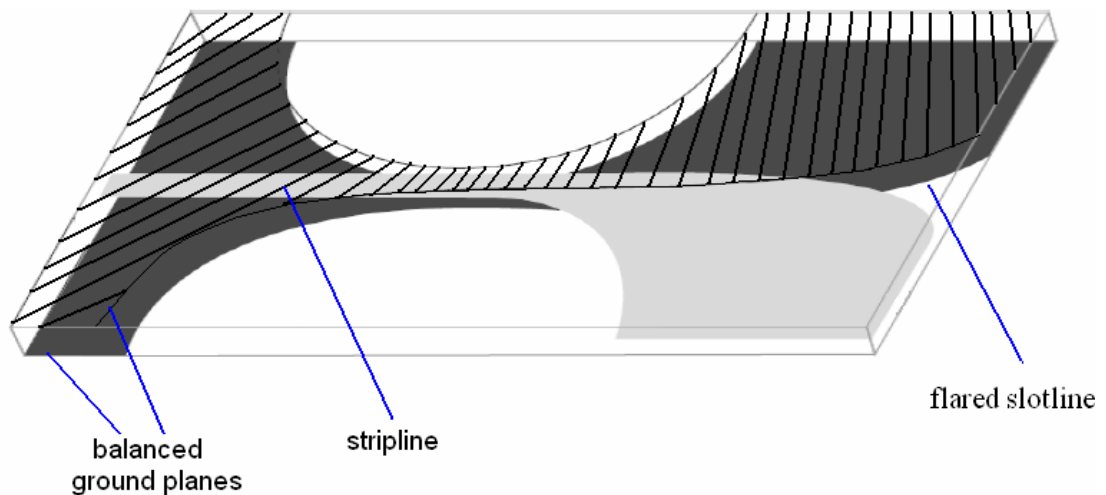


Figure 2.7 Balanced antipodal slotline transition

2.4 Arrays

The single element antenna has low gain throughout the bandwidth. Single element antennas also generate wide radiation patterns. Arrays, assemblies of single elements, are used to get fairly well gain characteristic and directive radiation pattern using rather smaller dimension antennas. The performance of individual elements, the spacing between the elements and their geometrical configuration, amplitude and phase of their excitation determine the radiation pattern of the array.

The basic concepts and configurations of arrays and array simulation methods are described below.

2.4.1 Basic Concepts

2.4.1.1 Array Pattern

The product of the single element pattern and the array factor form the actual array pattern. The array factor does not depend on the actual element pattern of the array and it is found with the elements of the array replaced with the isotropic radiators, the point sources that radiate equally in all directions. The array factor depends on the number of elements used, their spacing, geometrical arrangement, excitation

magnitudes and phases; thus, the isotropic radiators shall pertain to the mentioned setting of the actual element.

Actual array pattern is found using pattern multiplication rule which is given in the following equations [17].

$$F_{tot}(k) = F(k)A(k) \quad (2-1)$$

$$A(k) = a_0 e^{jk d_0} + a_1 e^{jk d_1} + a_2 e^{jk d_2} + \dots \quad (2-2)$$

Where,

F(k) : the single element pattern factor

A(k) : the array factor.

2.4.1.2 Mutual Coupling

The elements placed in an array are not isolated from each other and interact with each other consequently. This interaction changing the input impedance of the elements and disrupting the total radiation pattern of the pattern is known as mutual coupling.

The spacing of the elements, geometrical configuration of the array and the frequency of operation determines the extent of mutual coupling. Mutual coupling is significant in the case of element spacing less than $\lambda/2$ and decreases beyond this value.

2.4.1.3 Array Directivity

Array directivity tells how well the array directs energy toward a particular direction [19]. It is referenced to an array consisting of isotropic radiators directed in z-direction. Array directivity is related to the element spacing and it gets the maximum value when the spacing is $d = \lambda$.

2.4.2 Array Configurations

Array configurations can be classified with the geometrical arrangement and the feeding characteristics of the array elements.

2.4.2.1 Geometrical Arrangement

Array configurations can be divided into three main classes as linear, planar and circular arrays in geometrical arrangement. Linear array is formed placing the elements along a line. Array factor pattern of the linear array is symmetrical about the line of the array. Figure 2.8 shows the linear array structure.

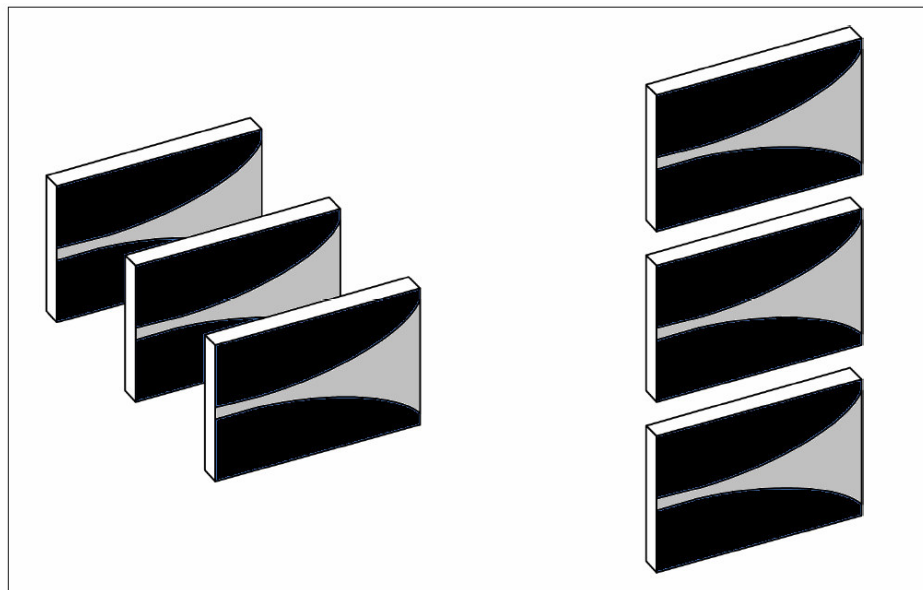


Figure 2.8 Linear array configuration

Arranging the array elements on a flat surface results in planar array as shown in Figure 2.9. Planar array gives the advantage of controlling the radiation pattern and scanning the main beam in the required direction easily. Symmetrical patterns are generated by planar arrays with lower sidelobes compared to those of linear arrays.

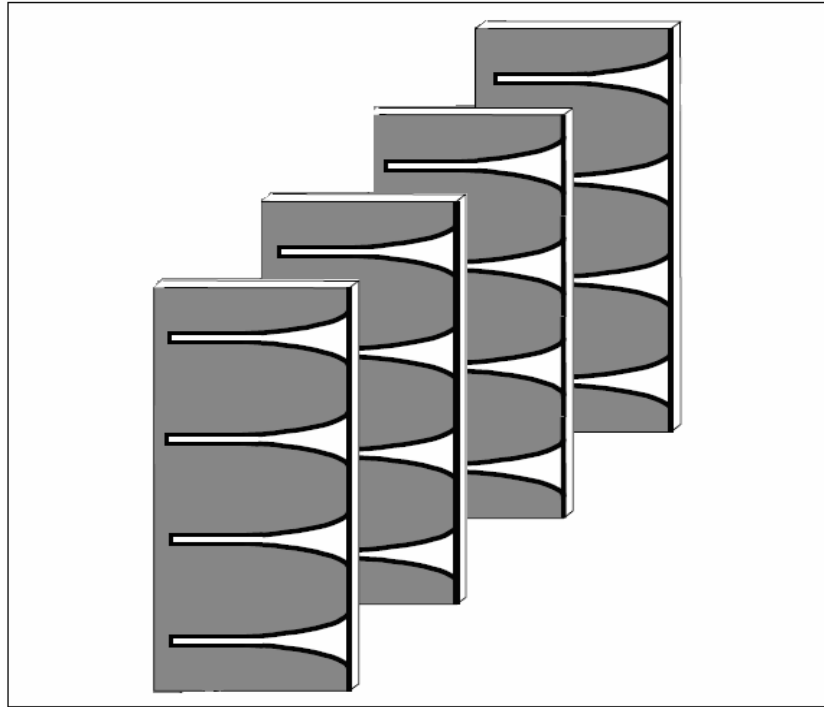


Figure 2.9 Planar array configuration

A special class of uniform planar array configuration to be explained is the dual-polarized arrays. E-plane and H-plane array terms are used to describe the array polarization. Assembling two orthogonal single polarized arrays, dual-polarized array is obtained. This structure gives the advantage of rapid scanning and characterization. Isolation between the individual elements of the array shall be succeeded in order to avoid resonances affecting the array performance. Dual-polarized array configuration is given in Figure 2.10.

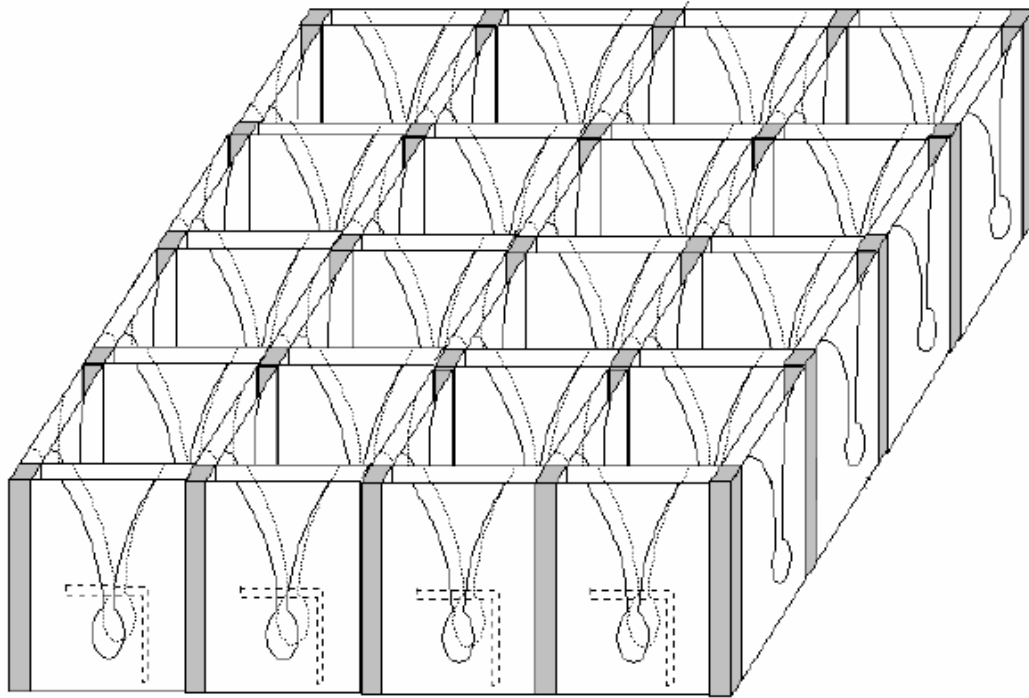


Figure 2.10 Dual-polarized array configuration [12]

In a circular array, the elements of the array are positioned along a circle. The circular array is generally used for specific applications like navigation, radar and sonar.

2.4.2.2 Feeding Characteristics

An array fed with identical amplitude and progressive phase is known as uniform array. Two common types of arrays with nonuniform amplitude distribution of the elements are binomial and Dolph-Chebyshev arrays. The amplitude distributions are determined in accordance with the coefficients of binomial series and Chebyshev coefficients respectively for binomial and Dolph-Chebyshev arrays. Nonuniform or tapered amplitude distribution gives the advantage of controlling the beamwidth and sidelobe level further.

Nonuniform fed characteristics, their advantages and disadvantages over uniform fed will be discussed in Chapter 4.

2.4.3 Array Simulation

The single element and array simulation will be realized using high frequency structure simulator Ansoft HFSS[®]. In this part of the thesis, the simulation and analysis methods used before the strong computational tools are to be studied.

2.4.3.1 Method of Moments (MoM) Solution

This method deals with the surface or volume Green's function applied for the dielectric parts and surface conduction currents defined for the metallic parts. The complete array is analysed decomposing it into triangular or bilinear quadrilateral unit cells and formulating a frequency-domain integral equation.

Large domain MoM provides a time consuming solution with complicated equations compared to small domain MoM. However, it offers much less number of unknowns and a careful optimization reduces solution time considerably [20].

Finding the coefficients of I , J , J_s and M_s through the solution of equations, the required quantities to analyse the array performance can be found. Voltage standing wave ratio (VSWR), impedance, radiation efficiency, losses, near field, far field and radiation patterns are the main parameters to be analysed in order to evaluate array performance.

2.4.3.2 Finite Difference Time Domain (FDTD) Solution

FDTD solution is based on periodic boundary conditions applied for the unit cells of the array. The method includes computation of voltage and current, calculation of impedance and application of Fourier Transform.

FDTD method is constituted assuming an infinite array. Thus, it is more efficient and accurate for considerably large arrays. A four wall structure of two perfect electric conductor (PEC) plates and two perfect magnetic conductor (PMC) plates in parallel

is formed with a single element positioned at the center. PEC walls are parallel to the cross-polarization where PMC walls are parallel to the co-polarization and each wall is at one half of element spacing distance to the element at the center of the structure.

Mutual coupling effects on the radiation pattern of the array cannot be realized with FDTD method due to infinite array approach of the solution. Finite array simulation is much more time consuming and complicated whereas this method explains interaction between the elements of the array clearly [21]. Finite array analysis also deals with array feed network and edge effects.

2.4.3.3 Conjugate Gradient Fast Fourier Transform(CG-FFT) Solution

CG-FFT method intends to reduce the number of unknowns and equations generating the model with conjugate gradient (CG) method and save computation time using fast Fourier transform (FFT). Simple multiplications and short computation times of CG-FFT method enable an efficient analysis of both large arrays and small structures [22].

Different implementations of CG-FFT method are possible in order to get more efficient analysis. Fang et al. [23] proposed that an algorithm converging faster than the conventional implementation could be obtained using biconjugate gradient (BCG) method instead of CG method. A full-wave analysis technique can also be proposed combining CG-FFT method with the full-wave discrete image technique. The full-wave method contains closed-form spatial Green's functions, different from the conventional method with spectral domain Green's functions, resulting in a more accurate and efficient analysis.

2.4.3.4 Linked Boundary Conditions Solution

Linked boundary conditions, also known as periodic boundary conditions are used to simulate a large system performance analysing only small parts apart from the edges.

Linked boundary conditions can be applied to a large array to be analysed using a computational simulation tool so as to save memory and time.

First, a single element model is set up and then the walls of the model are arranged to satisfy linked boundary conditions. The walls on the axis of the array are defined as master and slave boundaries. This model provides a match between each point on the slave and master boundaries regarding the E-field. The model is reduced considerably whereas the side effects are ignored in this method. The radiation pattern of the array is to be obtained with the post-processing. Rajaraman [24] stated that fairly well results for large arrays were obtained using linked boundary conditions method in his study.

CHAPTER 3

PARAMETRIC STUDY AND DESIGN OF VIVALDI ANTENNAS

This chapter describes the parametric study of Vivaldi antennas regarding the design of an antenna with the given specifications. The effect of each parameter is investigated performing simulations with Ansoft HFSS[®]. The simulation method is described in Appendix-A. The Vivaldi antenna model is given in Figure 3.1. The following specifications are used as the case study to apply the design methodology discussed in this chapter: 8.5-10.5 GHz frequency bandwidth, return loss better than 10 dB and 50 Ω characteristic impedance in the feeding section.

3.1 Design Insight

It will be convenient to discuss the feeding technique to be used as the first step of the design. Electromagnetically coupled transitions are more advantageous compared with direct coupling due to ease of implementation as discussed in Chapter 2. Microstrip to slotline and antipodal slotline transitions are unbalanced electromagnetically coupled feeding techniques. These kinds of transitions are unable to produce a spatially symmetric structure leading to perfectly linear polarization in the principal planes unlike the balanced transitions [25]. Besides, microstrip to slotline transition limits the wide bandwidth of Vivaldi antenna whereas antipodal slotline transition produces unacceptable cross polarization levels as stated earlier. Stripline to slotline and balanced antipodal transitions show symmetry owing to their balanced structures. Balanced antipodal slotline can operate in a multi-octave bandwidth with good cross polarization levels. However, the beamwidth of this type of transition increases with increasing frequency which is unacceptable when the beamwidth requirement of the design is too strict as in this study [7]. Thus, stripline

to slotline transition will be the most convenient choice with its beamwidth characteristic and fairly enough bandwidth performance. The stripline to slotline transition bandwidth is improved using nonlinear stubs, radial or circular stubs, as described before. However, a uniform stub will be used to take the advantage of better radiation characteristics since the bandwidth requirements of the design are not so strict. The parameters and design of stripline to slotline transition will be detailed later in this chapter. The designed antenna model with the design parameters are given in Figure 3.1 below.

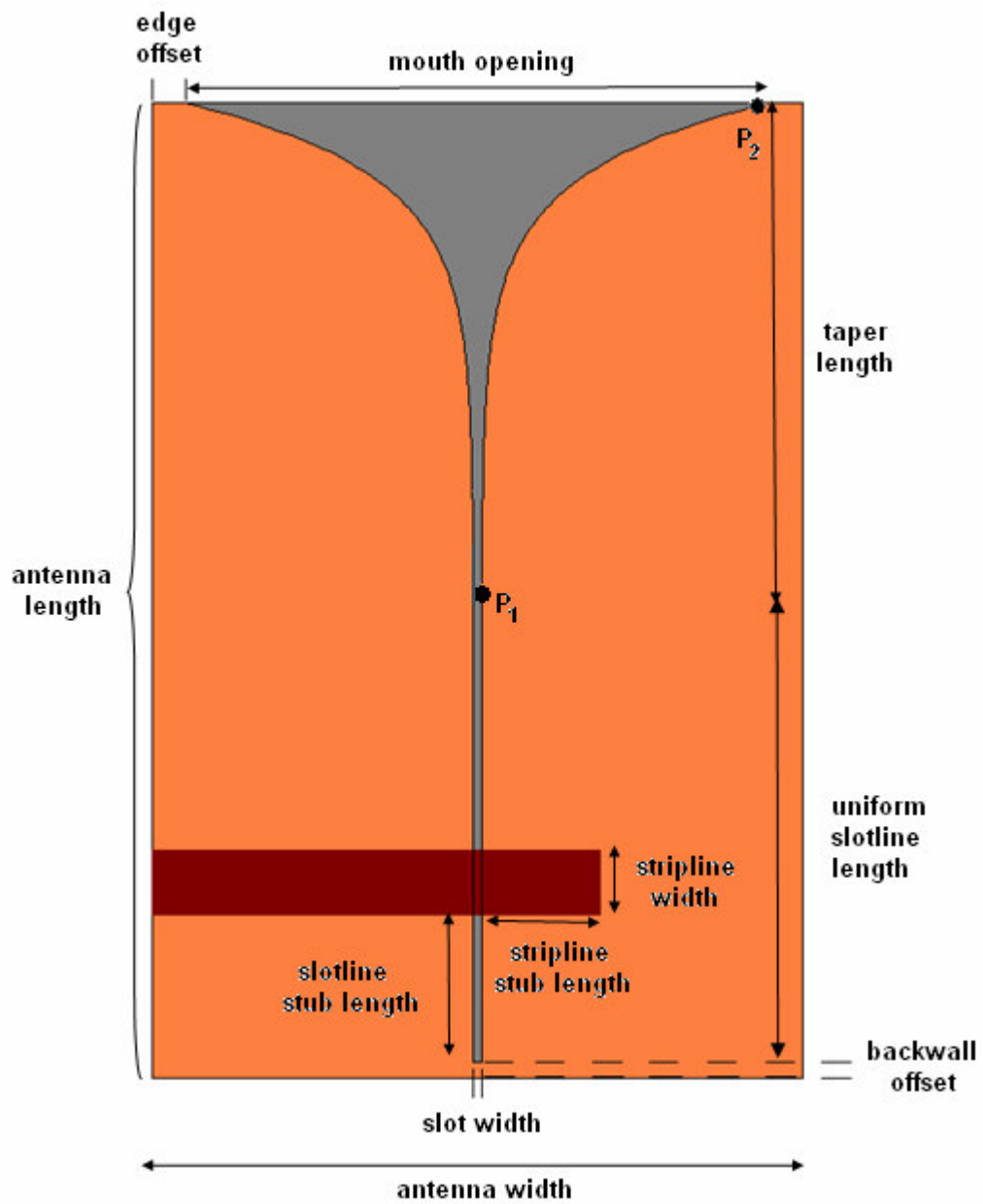


Figure 3.1 Designed Vivaldi antenna model and the parameters

The stripline to slotline transition design starts with the choice of substrate material and thickness. Stripline width is calculated using the stripline characteristic impedance formulas of Equation 3-1 [26] or Equation 3-2 [27].

$$Z_0 = \frac{\eta_0}{2.0\pi\sqrt{\epsilon_r}} \ln \left\{ 1.0 + 0.5 \frac{8.0b}{\pi w'} \left[\frac{8.0b}{\pi w'} + \sqrt{\left(\frac{8.0b}{\pi w'} \right)^2 + 6.27} \right] \right\} \quad (3-1)$$

$$w' = w + \frac{\Delta w}{t} t \quad \frac{\Delta w}{t} = \frac{\ln \left(\frac{5.0b}{t} \right)}{3.2}$$

$$Z_0 = \frac{60}{\sqrt{\epsilon_r}} \ln \left(\frac{4H}{0.67\pi(T + 0.8W)} \right) \Omega \quad (3-2)$$

where,

Z_0 : characteristic impedance of the stripline (Ω)

η_0 : wave impedance of free space (Ω)

ϵ_r : relative permittivity of the dielectric

H : dielectric substrate thickness (mm)

T : stripline thickness (mm)

W : stripline width (mm)

Slotline design completes the design of stripline to slotline transition. Slotline is defined by its wavelength and the characteristic impedance which are calculated for specified substrate material dielectric constant, ϵ_r and thickness, H. The equations for $\epsilon_r = 2.2, 3.0, 6.5, 9.8$ and $0.0015 \leq W/\lambda_0 \leq 1.0$ are given in [17]. The following equations, Equation 3-3 and Equation 3-4 [17], are in accordance with the design specified in this study.

For : $2.22 \leq \epsilon_r \leq 3.8$ and $0.0015 \leq W/\lambda_0 \leq 0.075$

$$\frac{\lambda'}{\lambda_0} = 1.045 - 0.365 \ln \epsilon_r + \frac{6.3 \left(\frac{W}{d} \right) \epsilon_r^{0.945}}{\left(238.64 + \frac{100W}{d} \right)} - \left[0.148 - \frac{8.81(\epsilon_r + 0.95)}{100\epsilon_r} \right] \cdot \ln \left(\frac{d}{\lambda_0} \right) \quad (3-3)$$

$$\begin{aligned}
Z_0 = & 60 + 3.69 \operatorname{strn} \left[\frac{(\epsilon_r - 2.22)\pi}{2} \cdot 36 \right] + 133.5 \ln(10\epsilon_r) \sqrt{\frac{W}{\lambda_0}} \\
& + 2.81 [1 - 0.011\epsilon_r (4.48 + \ln\epsilon_r)] \left(\frac{W}{d}\right) \ln\left(\frac{100d}{\lambda_0}\right) \\
& + 131.1 (1.028 - \ln\epsilon_r) \sqrt{\frac{d}{\lambda_0}} \\
& + \frac{12.48(1 + 0.18 \ln\epsilon_r) \left(\frac{W}{d}\right)}{\sqrt{\epsilon_r - 2.06 + 0.85 \left(\frac{W}{d}\right)^2}}
\end{aligned} \tag{3-4}$$

where,

λ' : slotline wavelength

λ_0 : operating wavelength

W : slotline width

d : dielectric substrate thickness

Z_0 : characteristic impedance of the slotline (Ω)

ϵ_r : relative permittivity of the dielectric

It will also be useful to discuss the theoretical background of the taper design. A tapered slot antenna with the exponential taper results in a Vivaldi antenna design as stated earlier. Taper design is described by opening rate, R, and end points of the taper, $P_1(x_1, y_1)$ and $P_2(x_2, y_2)$ shown in Figure 3.1. The following exponential relation [11] defines the taper section.

$$x = c_1 e^{Ry} + c_2 \tag{3-5}$$

where,

$$c_1 = \frac{x_2 - x_1}{e^{Ry_2} - e^{Ry_1}} \quad c_2 = \frac{x_1 e^{Ry_2} - x_2 e^{Ry_1}}{e^{Ry_2} - e^{Ry_1}}$$

The parametric study and design of single element Vivaldi antenna will be discussed in three different models: stripline model, stripline&slotline model and antenna model. Stripline model includes the choice of the substrate material, substrate

thickness and the stripline width. Stripline stub length, slotline stub length, slotline width, antenna length, antenna width and backwall offset are the parameters to be determined in the stripline&slotline model. Finally, the antenna model is constructed specifying the uniform slotline length, taper length and rate, mouth opening and the edge offset. These models and the effects of each parameter change will be detailed next.

3.2 Stripline Model

First of all, a model is formed to match the characteristic impedance of the stripline to that of the transmission line (feeding the antenna) and the slotline. The substrate material (dielectric constant) and thickness as well as the stripline width determine the characteristic impedance of the structure. Thus, the model consists of the antenna substrate and the stripline only since the whole antenna model will be inessential in order to find the characteristic impedance of the feeding section.

Determining these parameters, the stripline model shown in Figure 3.2 is employed.

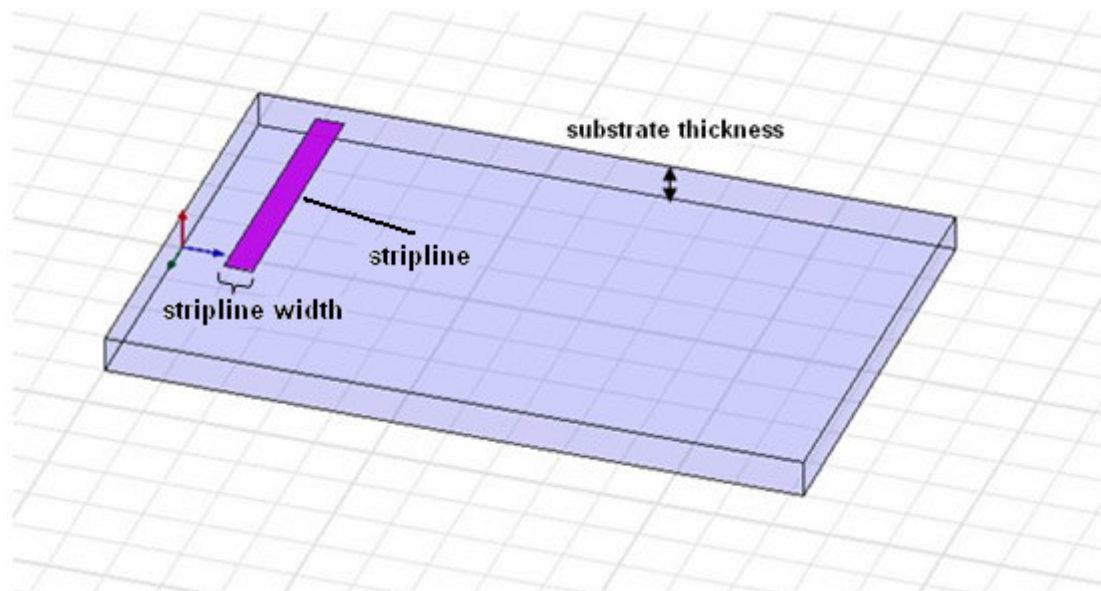


Figure 3.2 Stripline model

Stripline will be designed to have 50Ω characteristic impedance both in the slotline transition and the input of feeding section as stated earlier in this chapter. In fact, Yngvesson [4] showed that the characteristic impedance of the stripline that couples best to the slotline was 80Ω . The stripline width shall be determined so as to satisfy 80Ω characteristic impedance in the slotline transition and 50Ω characteristic impedance in the feeding as seen in Figure 3.3. This method provides a considerable bandwidth increase. However, 50Ω characteristic impedance through the complete stripline will provide the bandwidth requirement of this work as well as an uncomplicated stripline structure.

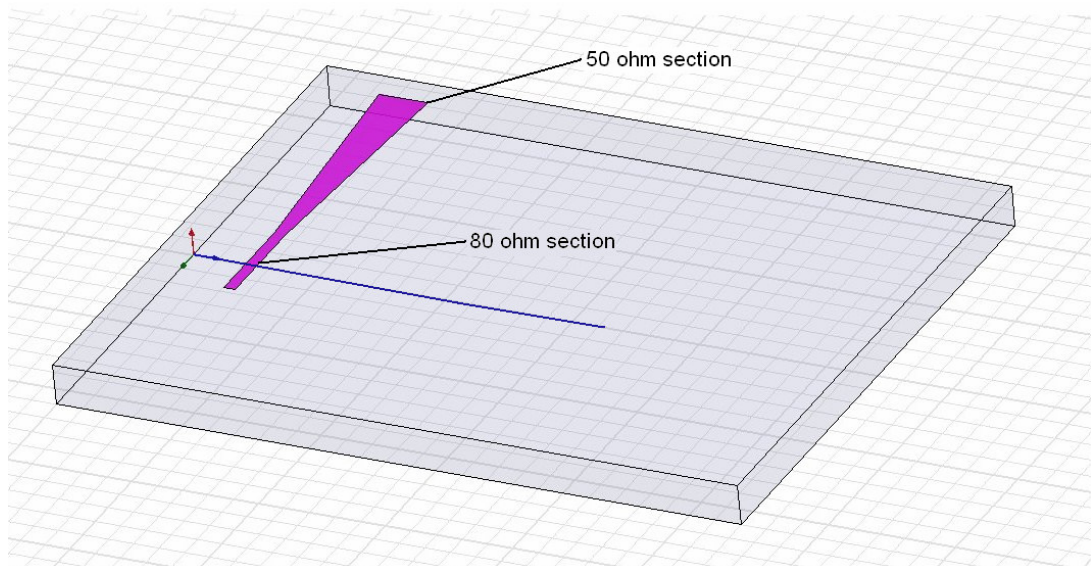


Figure 3.3 Stripline model with 80Ω to 50Ω transition

3.2.1 Substrate Material

Choosing a substrate material of appropriate dielectric constant and tangent loss shall be the first design step. Dielectric constant and the substrate thickness determine the phase velocity of the waves. Propagation of the waves along the antenna lasts until the limiting case of phase velocity is equal to the free space velocity of light, as stated earlier. Thus, the waves will merely radiate in an antenna with air as dielectric. A substrate with sensible dielectric constant will make the waves travel through the

stripline and slotline until the tapered section where the phase velocity approaches free space velocity of light and the radiation comes true. Moreover, the impedance of the antenna with air as dielectric increases with increasing frequency over the bandwidth. A substrate material with dielectric constant greater than that of the air shall be used in order to get constant antenna impedance and realize impedance matching.

Dielectric constant and substrate thickness are the parameters determining the performance and radiation pattern, that is beamwidth, sidelobe level and gain of the antenna. Higher dielectric constant substrates give the advantage of smaller antenna dimensions for same performance. However, a more efficient design and a wider bandwidth is possible with low dielectric constant substrates. Low dielectric constant substrates also lower the scattering along the antenna and consequently spurious fields. Thus, the second parameter, tangent loss, shall also be considered to cope with this trade-off.

For higher frequencies as in the case of this project, the dielectric losses dominating the conductor losses is the loss mechanism to be considered in a stripline design. Dielectric loss is generated by the polarized molecules moving in the substrate and heating the material in the presence of electromagnetic fields.

Among the substrates with dielectric constant in the range of 2.2 to 10.2, Rogers RT/duroid™ 5880 has the minimum tangent loss ($\tan \delta = 0.0009$) and a dielectric constant of $\epsilon_r = 2.2$. Rogers RT/duroid™ 5880 is chosen as the substrate material to be used in this work.

3.2.2 Substrate Thickness

Substrate thickness is restricted to the standard thickness values given by the laminate product. Standard dielectric thickness and tolerance shall be studied before choosing the substrate thickness of the antenna. In this design, two 0.062" (1.570mm) ± 0.002 " thick boards are to be used, i.e. the substrate thickness is 0.124" (3.140mm).

The performance of the antenna is dependent on the substrate thickness also, as stated before. An improvement in the performance is obtained using thicker substrates due to a decrease in the antenna reactance through the whole band. Besides, thicker substrate results in higher antenna gain narrowing the main beam and increasing the sidelobes. However, increasing the substrate thickness generates deeper nulls in the return loss curve. Any change (increase/decrease in substrate thickness) does not affect the bandwidth considerably.

Substrate thickness may be re-evaluated analysing the return loss and the radiation performance with all the antenna design completed, since these parameters affect return loss and radiation pattern as well as the impedance.

3.2.3 Stripline Width

Stripline width is the last parameter to be determined in order to calculate the stripline impedance. Equation 3.1 or 3.2 given above might be used to calculate the characteristic impedance of the stripline. Based on these equations, the stripline width satisfying 50Ω characteristic impedance with the substrate material and width determined above is found to be $W_{ST} = 2.5$ mm for the stripline thickness of 1 oz. (0.035 mm). Table 3.1 gives the calculated and simulated characteristic impedance of the stripline for various stripline width where 3.14 mm thick Rogers RT/duroid™ 5880 dielectric is used. Simulations are carried out using Ansoft HFSS®.

Table 3.1 Change in characteristic impedance of the stripline with stripline width

W_{ST} (mm)	1,5	2,0	2,5	3,0
Z_0 (Ω) (simulated)	65,605	57,283	50,27	44,107
Z_0 (Ω) (calculated)	69,28	59,06	51,47	45,60

Stripline length, L_{ST} , and the slotline stub length, L_{SS} , are the other parameters of the stripline model. It is more convenient to evaluate these parameters through the stripline&slotline model design section since they do not change the impedance noticeably. The effects of stripline length, L_{ST} , and the slotline stub length, L_{SS} , are shown in Table 3.2.

Table 3.2 Change in characteristic impedance of the stripline with stripline length and slotline stub length

L_{SS}	L_{ST}		
	21		21
2	50,358	2	50,358
4	50,286	4	50,286
6	50,143	6	50,143

3.3 Stripline and Slotline Model

In this part, the feeding section of the antenna is modeled. The model is formed cascading two identical transitions designed. Thus, both return loss ($20\log|S_{11}|$) and reverse gain (insertion loss or $20\log|S_{21}|$) of the antenna might be analysed of the mentioned system. The return loss and reverse gain responses of this model are expected to be fairly close to the complete antenna performance since the stripline model parameters and the parameters to be specified here mainly determines the return loss response and the reverse gain of the design. Figure 3.4 shows the cascaded transitions model.

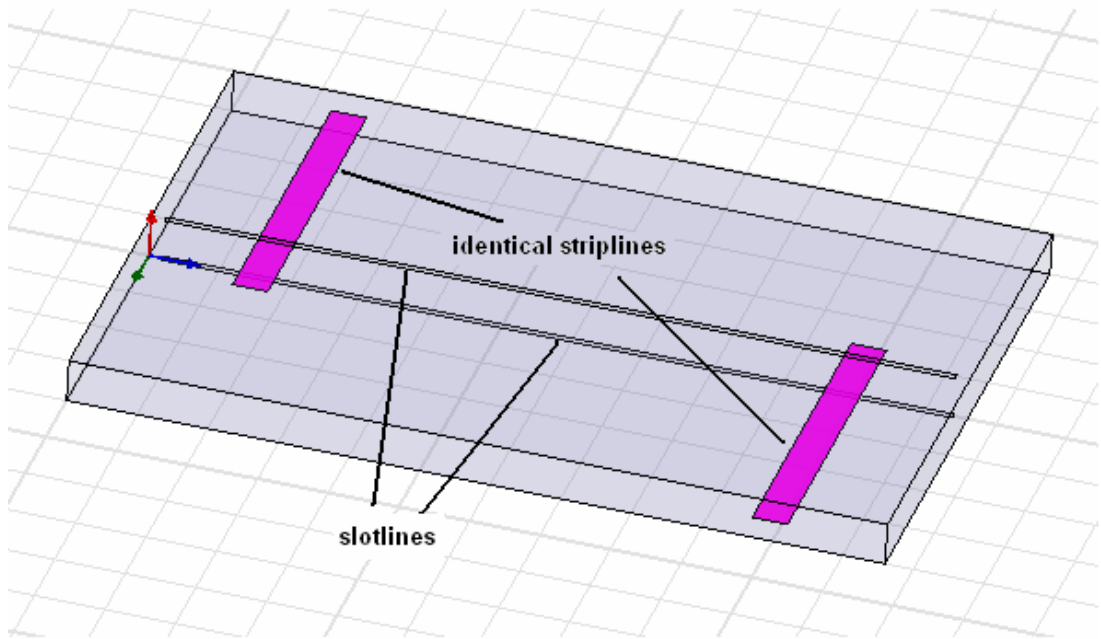


Figure 3.4 Cascaded identical transitions

In addition to the parameters determined in the stripline model section, stripline stub length, slotline stub length, slot width, antenna length, antenna width and backwall offset are to be determined for this model. This model offers a practical way to realize the effect of these parameters on the antenna performance without modeling the whole antenna design.

3.3.1 Stripline Stub Length

The striplines are extended along a finite length and terminated after the stripline to slotline transition. A short circuit is achieved soldering or using an open circuited quarter wavelength stub usually in order to reflect incident waves back to the transition. The stripline length providing the best reflection performance through the whole band shall be found where an open circuited stub is to be used as in this work. An acceptable return loss response is achieved using an open circuited stripline stub of length $L_{SS} = 4$ mm. The simulated return loss and reverse gain responses for the design with $L_{SS} = 7$ mm and $L_{SS} = 1$ mm as well as $L_{SS} = 4$ mm are given in Figure 3.5 and Figure 3.6, it well agrees with the design specifications given in this chapter.

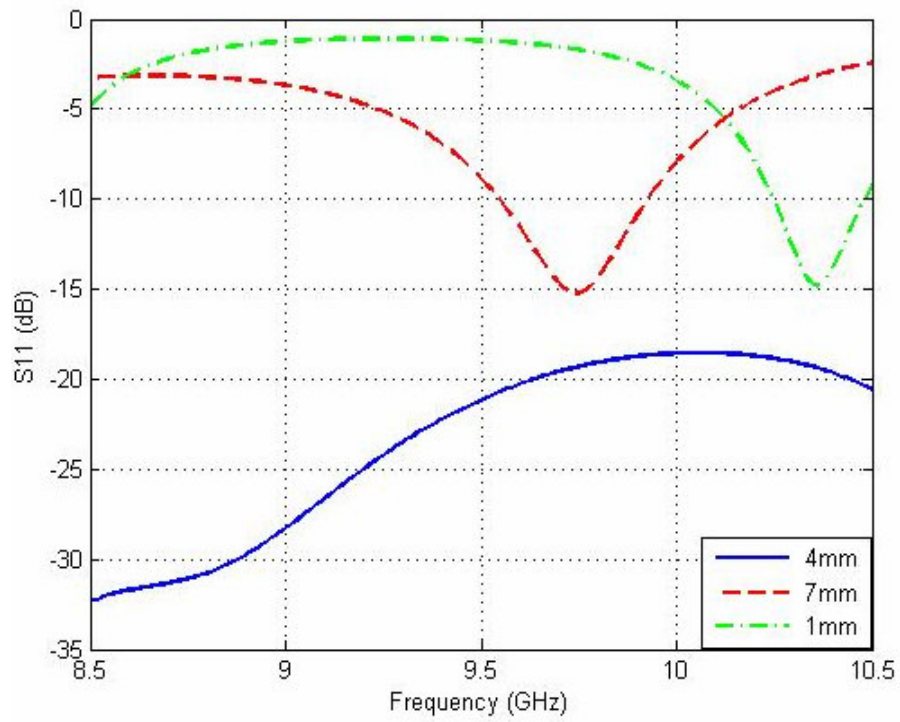


Figure 3.5 Return loss response with three different stripline stub length

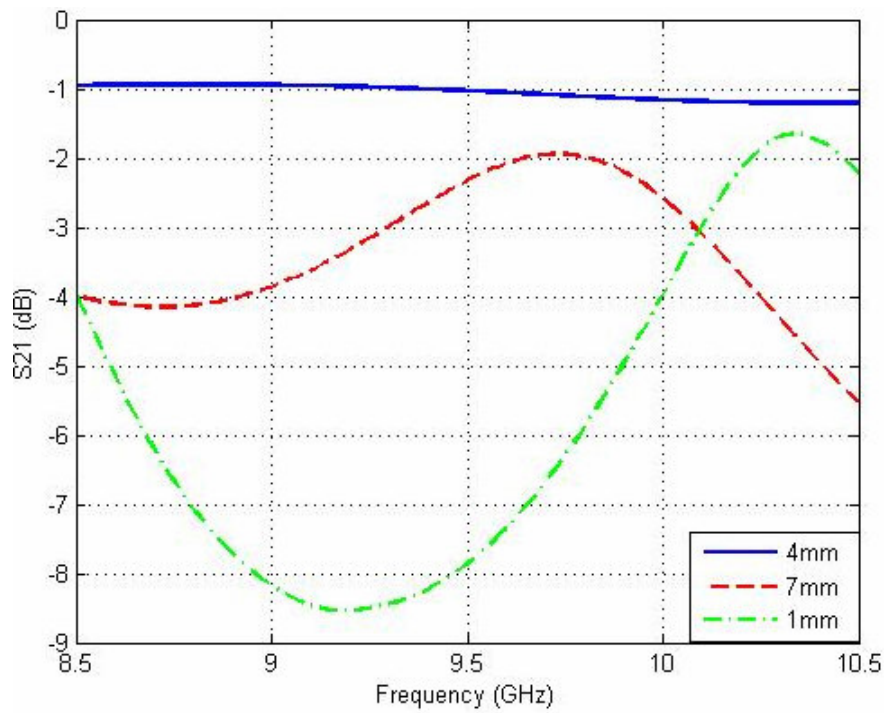


Figure 3.6 Reverse gain with three different stripline stub lengths

In this work, non-uniform stubs (radial or circular) widening the bandwidth are not used because of the relaxed bandwidth requirement.

3.3.2 Slotline Stub Length

The slotline stub length is another important parameter of the transition. This parameter determines the length of slot stub which shall be open circuited by the means of a short circuited quarter wavelength stub in order to improve field coupling as stated before. The slotline stub length providing the best field coupling through the whole band shall be found as in the case of stripline design. The return loss with slotline stub length of 4 mm is seen to generate acceptable return loss response. The simulated return loss and reverse gain responses for the antenna model with the slotline stub lengths of $L_{SS} = 4$ mm, 6 mm and 2 mm are given in Figure 3.7 and Figure 3.8.

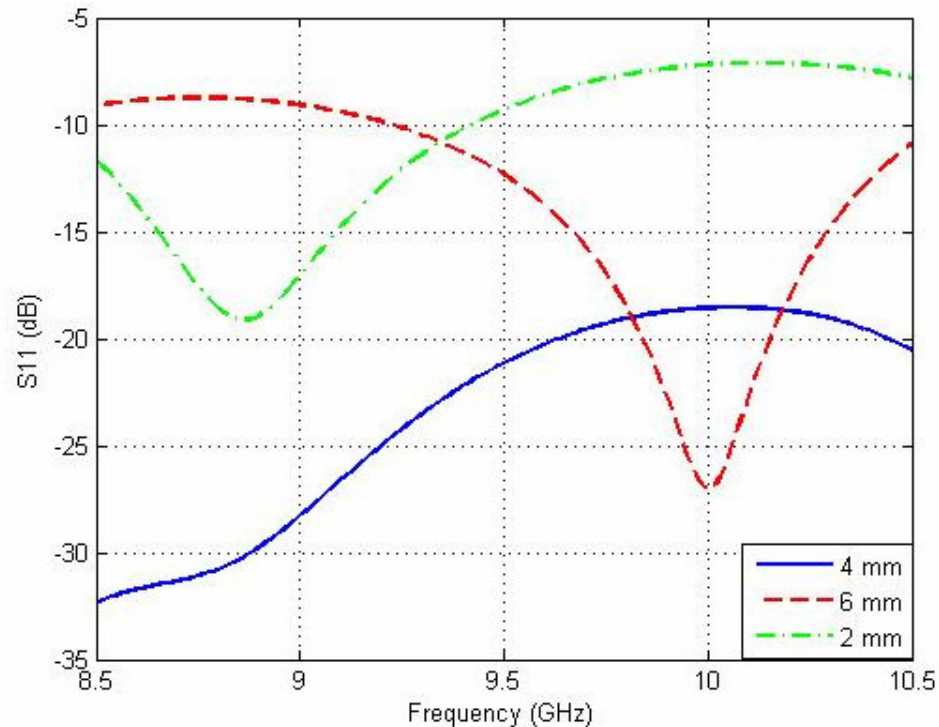


Figure 3.7 Return loss response with three different slotline stub lengths

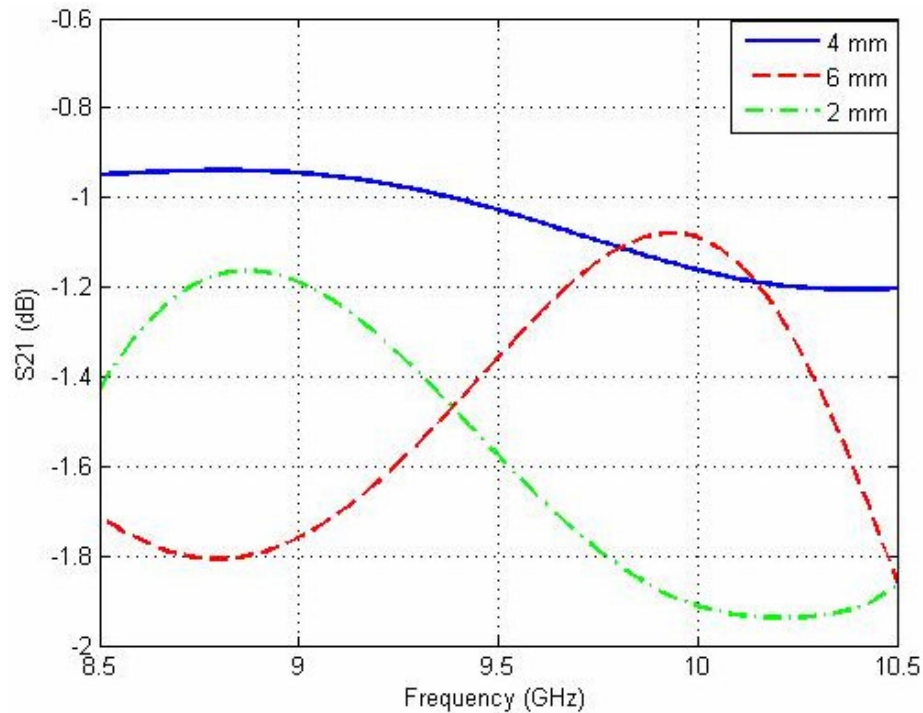


Figure 3.8 Reverse gain with three different slotline stub lengths

As seen in the return loss and reverse gain responses of the stripline to slotline model, a slotline stub length of $L_{SS} = 4$ mm results in the best performance.

3.3.3 Slotline Width

Slotline width, also known as throat width, is the separation between the slotline conductors before the tapered section, that is to say the width of uniform slotline. Throat width, an important parameter to be optimized, is to be determined carefully in order to get the desired return loss.

Stripline to slotline transition determines the operational bandwidth and slotline width is an important parameter of this structure. Any change (increase/decrease) from the optimized value of the slot width degrades return loss response drastically lowering the effectiveness of the stripline to slotline transition.

Schaubert [11] studied broadside bandwidth for various slotline width, stripline width and substrate thickness values. Rogers RT/duroid™ 5880 substrate was used

as in this work. The widest bandwidth was achieved with the slotline width, $W_{SL} = 0.5$ mm and $W_{SL} = 1.0$ mm for which the substrate thickness, $W = 2.88$ mm and stripline width, $W_{ST} = 2.0$ mm were chosen. In this work, the substrate thickness is $W = 3.14$ mm is chosen while the stripline width is $W_{ST} = 2.5$ mm. Thus, the mentioned case suits the design parameters of this work best.

The return loss response for $W_{SL} = 0.5$ mm, $W_{SL} = 1.0$ mm and $W_{SL} = 0.25$ mm were investigated. Figure 3.9 and Figure 3.10 show the simulated return loss and reverse gain of stripline to slotline model for these three different values of slot width.

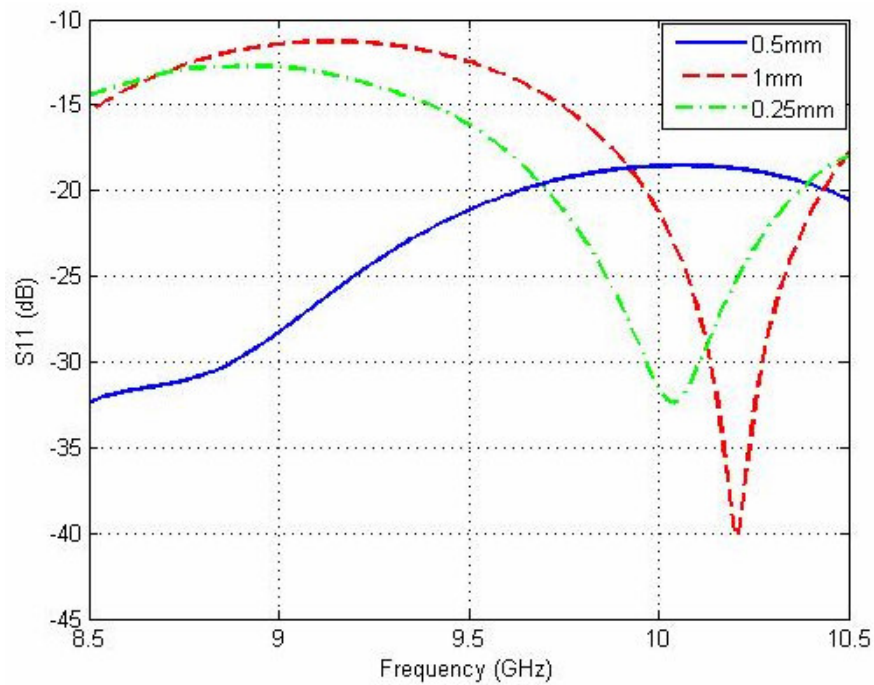


Figure 3.9 Return loss response with three different slotline widths

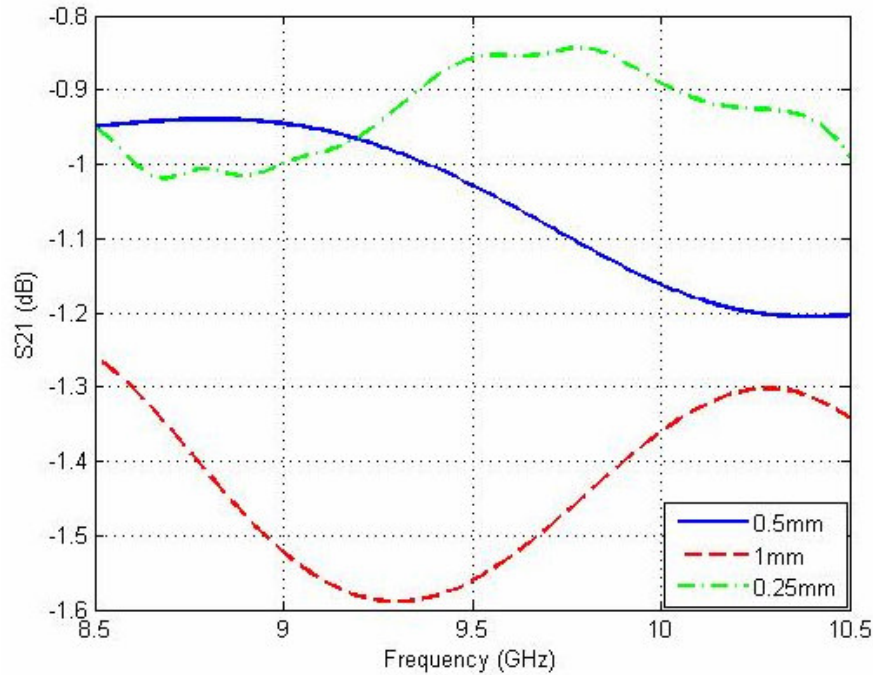


Figure 3.10 Reverse gain with three different slotline widths

Based on these results, slotline width is chosen as $W_{SL} = 0.5$ mm satisfying the design requirements.

3.3.4 Antenna Length

Antenna length should be greater than a free space wavelength at the lowest frequency of operation, 8.5GHz in this case. This requirement guarantees fairly well gain and beamwidth performance.

The lowest frequency of operation, thus the bandwidth, is also dependent on the antenna length; increasing antenna length provides a wider bandwidth. However, when the requirements on the gain and beamwidth are not so strict, an antenna length on the order of the λ_0 will also be enough to get the desired bandwidth.

The wavelength of the minimum operating frequency, 8.5 GHz, is $\lambda_0 = 35,29$ mm. Thus, an antenna length of $L \geq 36$ mm will provide acceptable return loss performance. However, in order to achieve the strict beamwidth requirement of this

work, $L = 61$ mm antenna length was chosen. The return loss response for $L = 36$ mm and $L = 72$ mm was also investigated. The return loss of stripline to slotline model for these three antenna length values is shown in Figure 3.11.

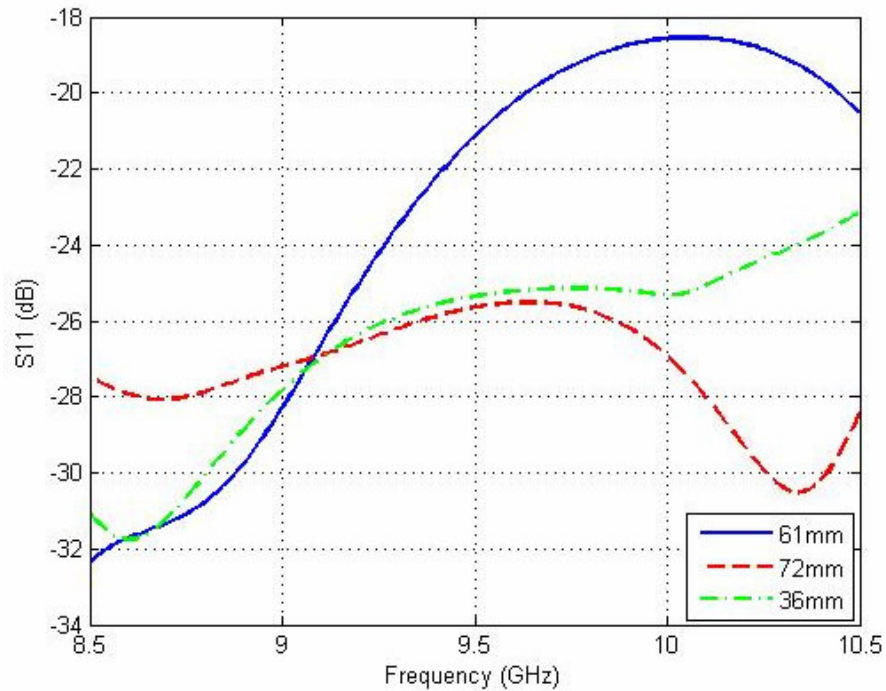


Figure 3.11 Return loss response with three different antenna lengths

As seen in Figure 3.11, the return loss performance with $L = 36$ mm is better than those with $L = 61$ mm and $L = 72$ mm. However, $L = 36$ mm is not a convenient choice considering the beamwidth requirements of the work as stated earlier. The antenna length of $L = 61$ mm seems to be the most convenient choice with satisfactory results and smaller size compared to $L = 72$ mm design. This claim will be reconsidered in the antenna model section. The reverse gain figures of these three designs are shown in Figure 3.12.

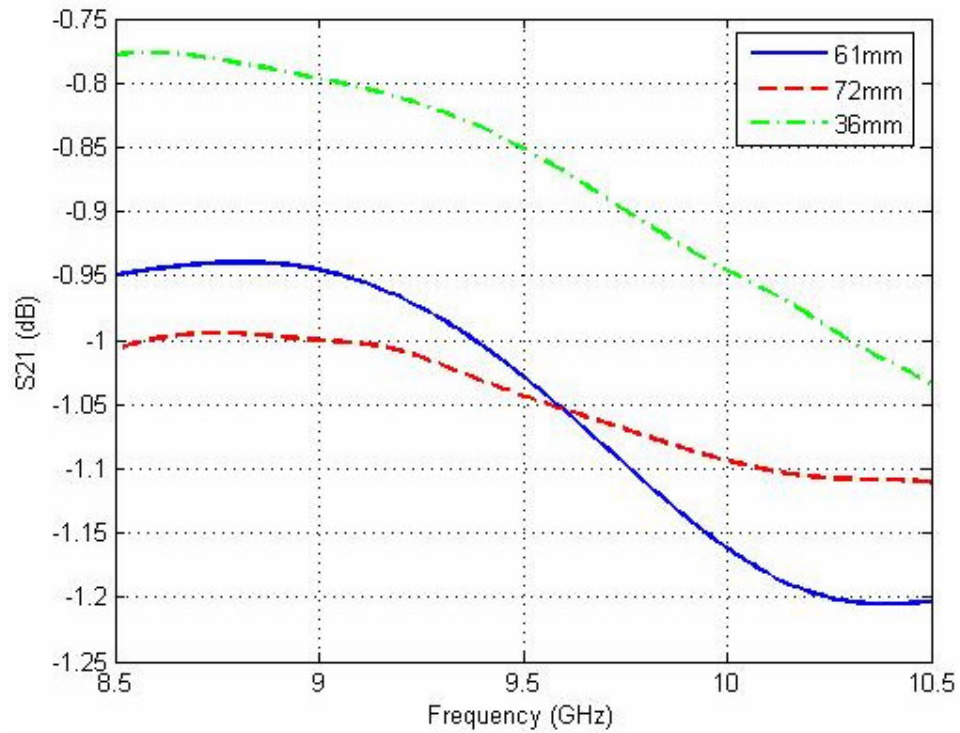


Figure 3.12 Reverse gain with three different antenna lengths

3.3.5 Antenna Width

Antenna width shall be greater than one-half wavelength at the lowest frequency of operation, $\lambda_0/2$, so as to accomplish the desired radiation performance. Decreasing antenna width below this value decreases the lowest frequency of operation, thus the antenna bandwidth considerably.

The wavelength of the minimum operating frequency is $\lambda_0 = 35,29$ mm as calculated before. Thus, an antenna of width $W \geq 18$ mm will provide acceptable radiation performance. The simulated return loss and reverse gain responses for the antenna width values $W = 20$ mm, $W = 40$ mm and $W = 60$ mm were investigated and given in Figure 3.13 and Figure 3.14.

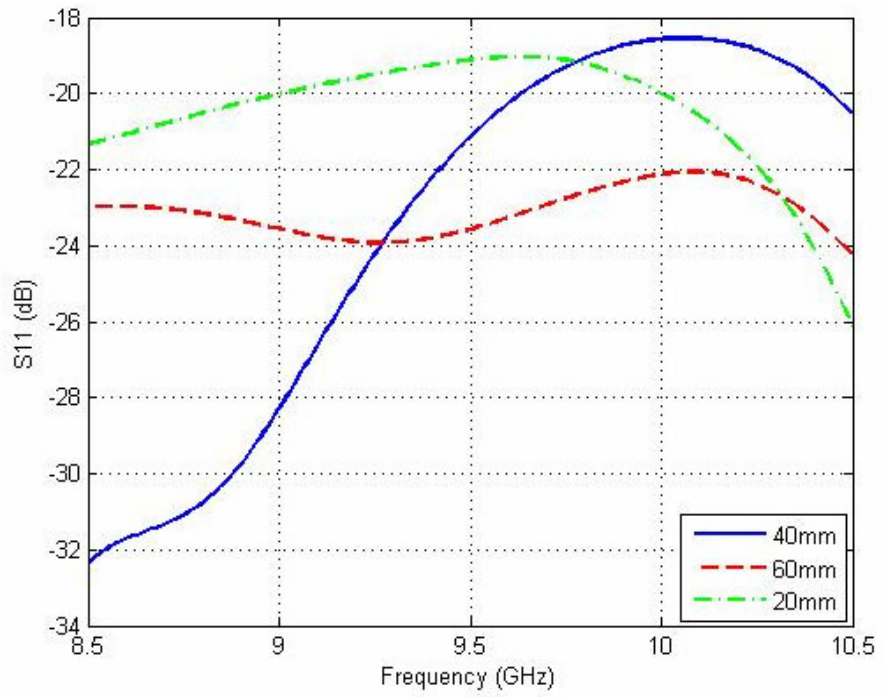


Figure 3.13 Return loss response with three different antenna widths

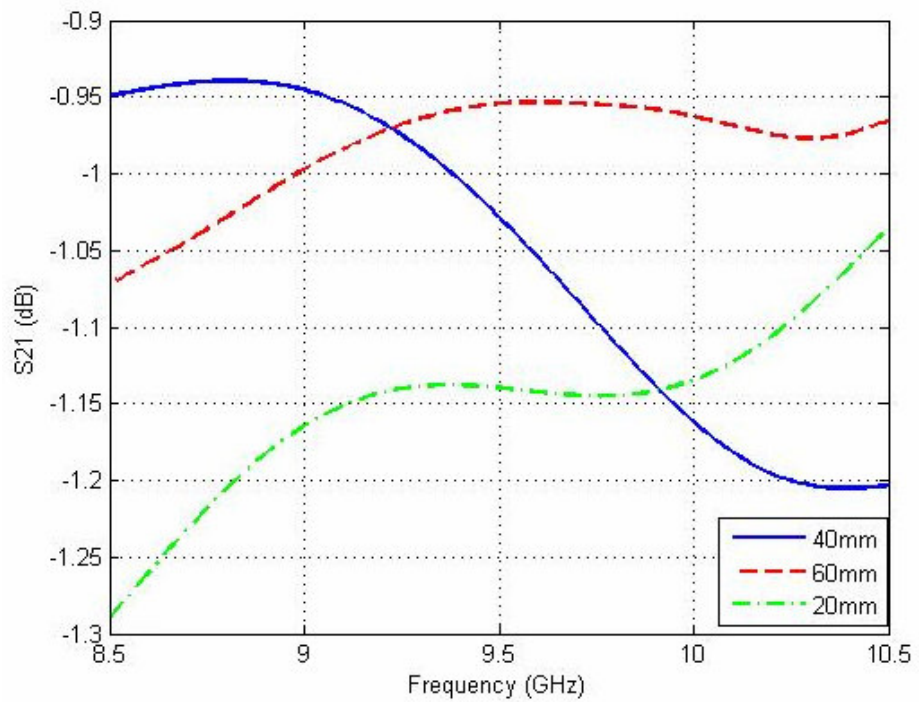


Figure 3.14 Reverse gain with three different antenna widths

The performance of the antenna is found to be satisfactory with an antenna width of $W = 40\text{mm}$.

3.3.6 Backwall Offset

Backwall offset is the extra metallization planted at the beginning of the slotline to prevent the currents in this section coming across an abrupt end. Backwall offset is a parameter to be optimized which means any change (increase/decrease) from the optimum value ends up with deterioration in return loss response of the antenna.

Backwall offset was chosen as 1 mm based on the studies of Schaubert [11]. The simulated return loss and reverse gain response of the antenna with backwall offset values of $d = 1\text{ mm}$, $d = 2\text{ mm}$ and $d = 0.5\text{ mm}$ is given in Figure 3.15 and Figure 3.16 below.

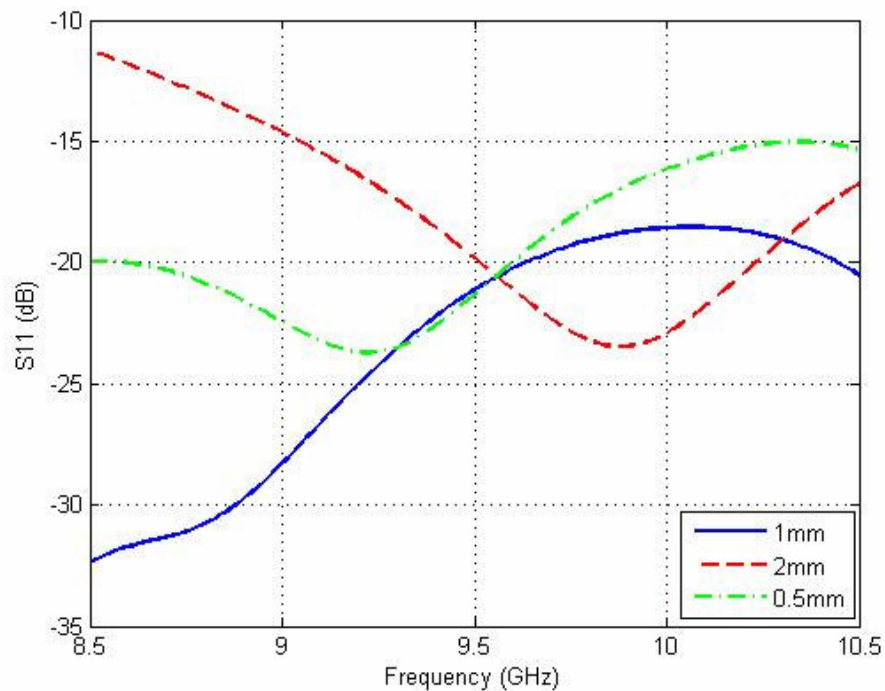


Figure 3.15 Return loss response with three different backwall offset

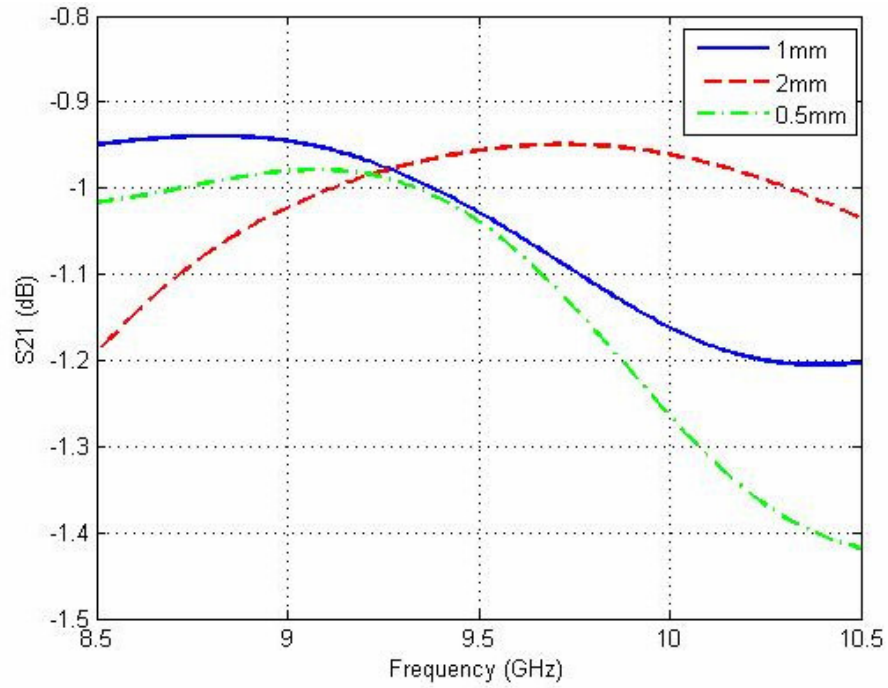


Figure 3.16 Reverse gain with three different backwall offset

Backwall offset does not exist in all Vivaldi antenna designs. However, its absence results in an unacceptable antenna performance whenever a circular or radial slot stub is not used. The backwall offset is removed and the antenna performance is investigated. Figure 3.17 below shows the simulated return loss and reverse gain of the model with the backwall offset removed.

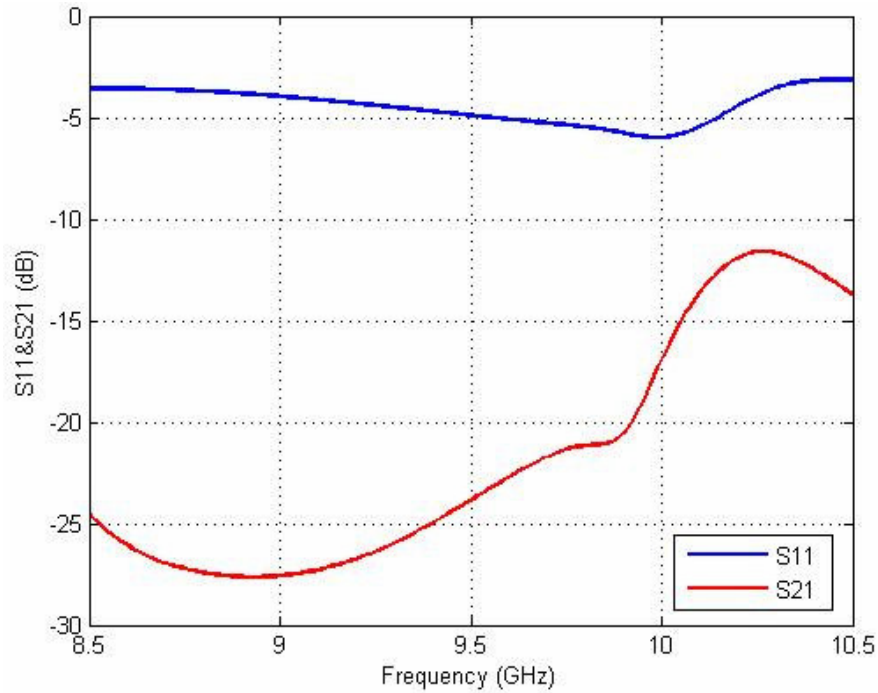


Figure 3.17 Return loss response and reverse gain of the design with zero backwall offset

3.4 Antenna Model

In this section, the complete antenna model is formed determining the uniform slotline length, tapered slotline length, taper rate, mouth opening and edge offset parameters. The complete antenna model with the air box, defined earlier, is given in Figure 3.18.

The parameters to be determined in this section are evaluated regarding the effects of each parameter change in the actual return loss response and the H-plane radiation pattern (at $f = 9.5$ GHz, center frequency) simulating the antenna model using Ansoft HFSS[®]. The antenna length parameter of stripline&slotline model section is reconsidered here using the results of taper length parameter study.

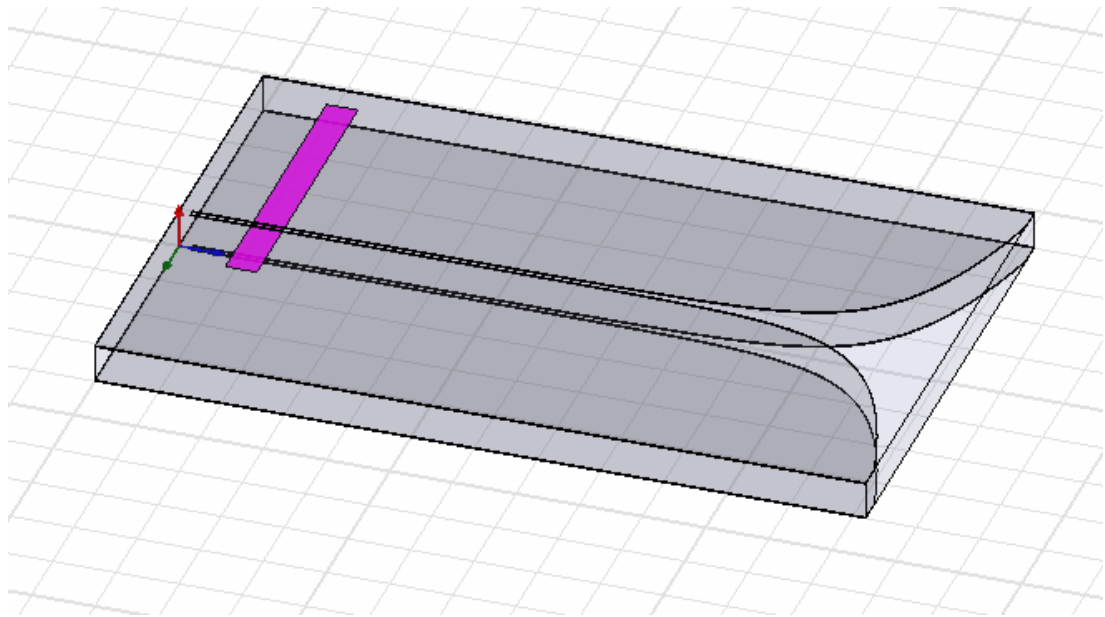


Figure 3.18 Complete antenna model in HFSS®

3.4.1 Uniform Slotline Length

As mentioned in the feeding section, slotline extends a quarter-wave beyond the transition point with the stripline. Thus, a quarter-wavelength stub is achieved expecting to obtain desired transition performance.

An increase further from quarter wavelength results in degradation of return loss response as expected. In the same way, a decrease beyond quarter wavelength degrades radiation performance widening the main pattern and increasing 3-dB beamwidth. Return loss response and the radiation pattern of the antennas with uniform slotline lengths of $S = 8$ mm, $S = 11$ mm and $S = 5$ mm are given in Figure 3.19 and Figure 3.20.

Uniform slotline length of $S = 5$ mm generates deeper nulls both in return loss and radiation pattern of the antenna as seen in Figure 3.19 and Figure 3.20. Uniform slotline lengths of $S = 11$ mm results in a fairly close response to that of $S = 8$ mm case. Antenna with uniform slotline length of $S = 8$ mm has a 3-dB beamwidth of 48° better than that of the antenna with $S = 11$ mm which is 50° . Thus, $S = 8$ mm is the most convenient choice for uniform slotline length of the design.

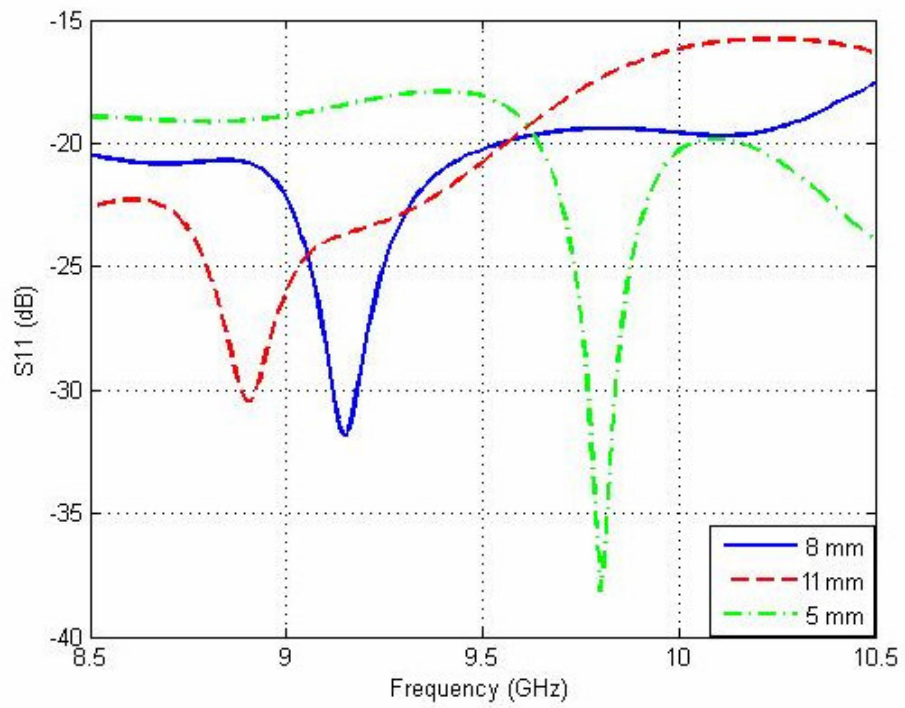


Figure 3.19 Return loss response with three different uniform slotline lengths

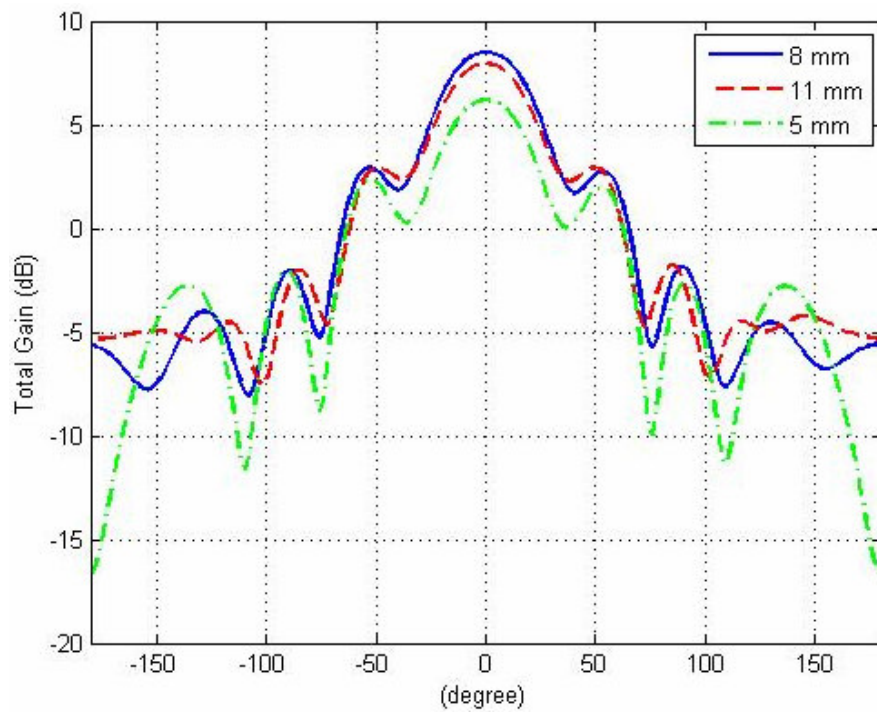


Figure 3.20 H-plane radiation pattern with three different uniform slotline lengths ($f = 9.5$ GHz)

3.4.2 Taper

The taper design includes choosing the tapered slotline length and the taper rate (or flare angle). In fact, the sum of backwall offset length, uniform slotline length and tapered slotline length gives the antenna length. That is to say, determining antenna length, backwall offset length and the uniform slotline length also determines the tapered slotline length. It shall be in the order of a wavelength at the smallest operating frequency in order to get the desired gain and beamwidth performance. The bandwidth is also increasing with an increase in the taper length.

The taper length is chosen as 52 mm regarding the antenna length of $L = 61$ mm of the stripline&slotline model. The return loss responses and radiation patterns of the antenna models with the taper length of $L_T = 52$ mm, $L_T = 63$ mm and $L_T = 41$ mm are given in the Figure 3.21 and Figure 3.22, respectively.

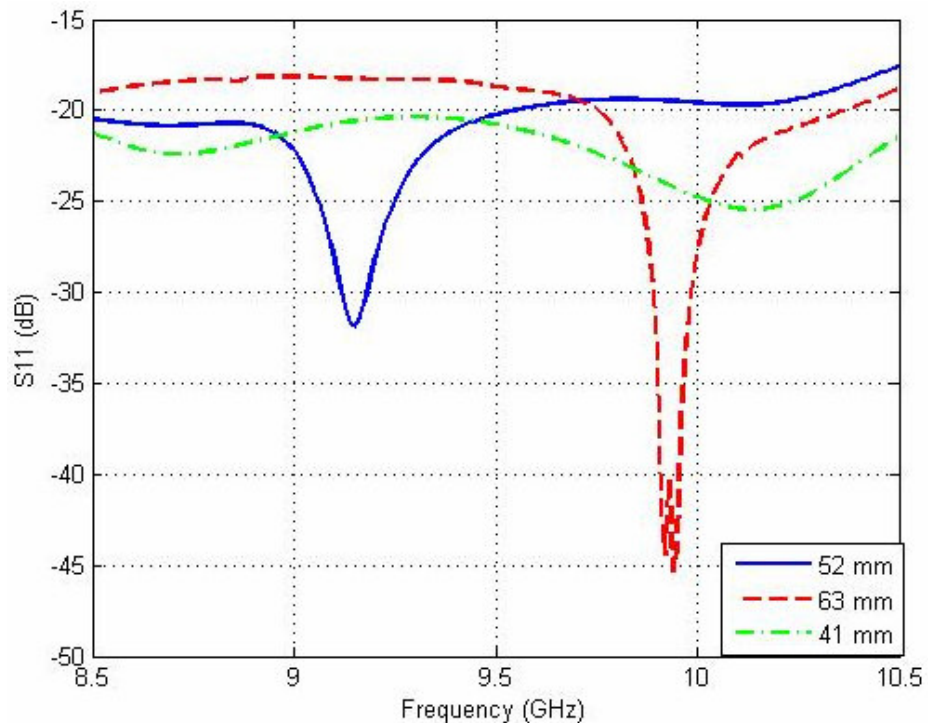


Figure 3.21 Return loss response with three different taper lengths

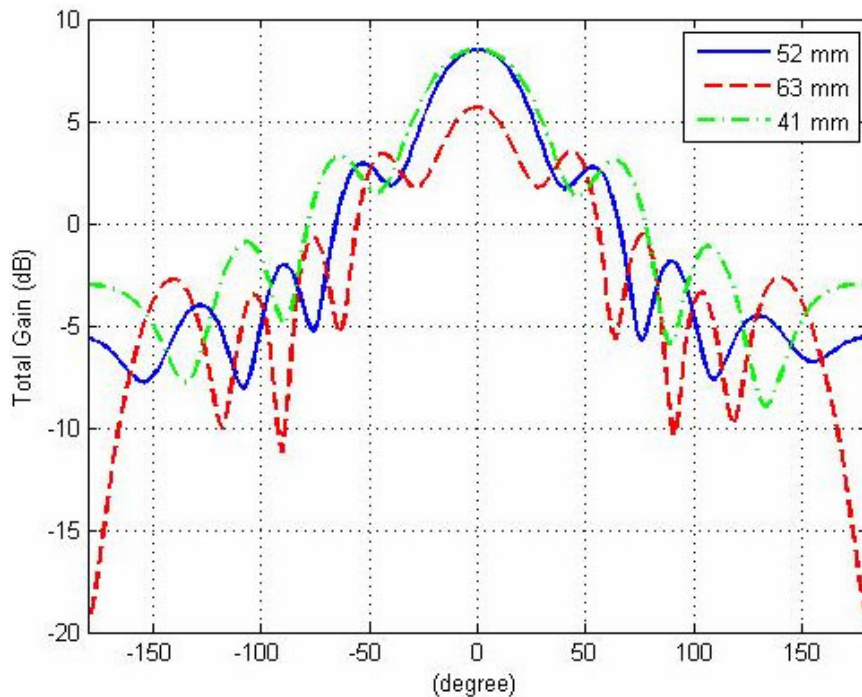


Figure 3.22 H-plane radiation pattern with three different taper lengths ($f = 9.5$ GHz)

In this case, the taper length of $L_T = 63$ mm generates deeper nulls in the return loss response and radiation pattern as well as higher sidelobe levels. $L_T = 41$ mm results in a 3-dB beamwidth of 56° which is fairly higher compared to $L_T = 52$ and $L_T = 63$ case. The taper length of $L_T = 52$ mm, thus the antenna length of $L = 61$ mm, seems to be the most convenient choice regarding these results. However, the taper length will be evaluated again considering its effect on the array radiation pattern.

The taper rate also has a significant effect on the return loss of the antenna. Decreasing the taper rate improves mid-band response effectively while the low-band performance is deteriorated. Thus, the lowest frequency of operation is increased and bandwidth is decreased in expense of improving mid-band return loss. Besides, beamwidth is also dependent on the taper opening rate. Beamwidth is getting narrower and sidelobe power levels are rising with increasing taper rate. Figure 3.23 and Figure 3.24 below give the return loss response and radiation pattern for the taper rates of $R = 0.23$, $R = 0.20$ and $R = 0.26$.

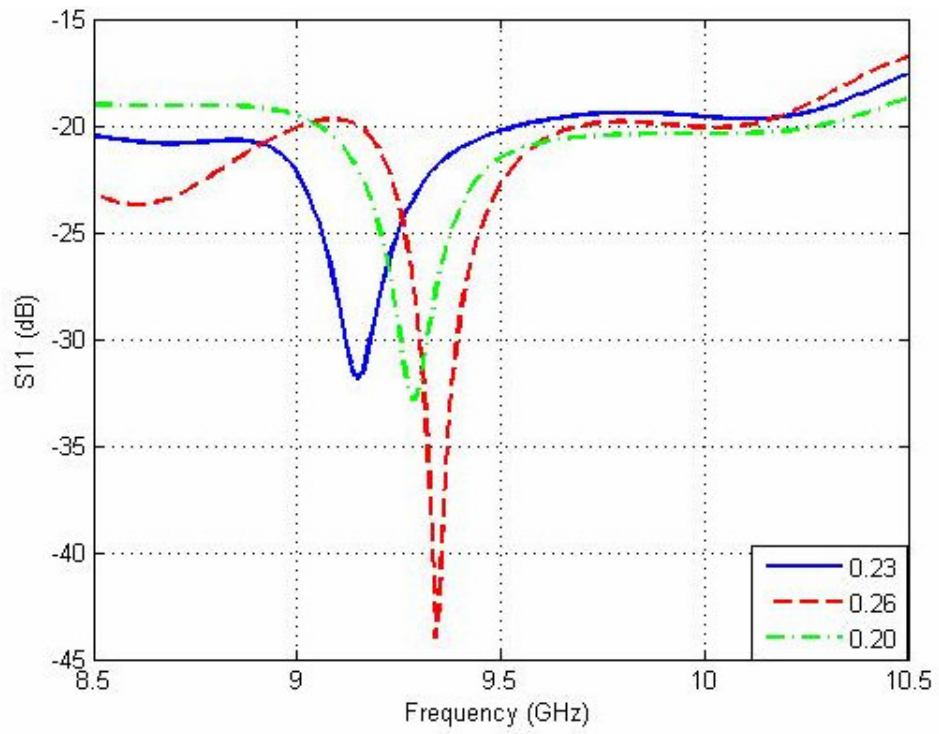


Figure 3.23 Return loss response with three different taper rates

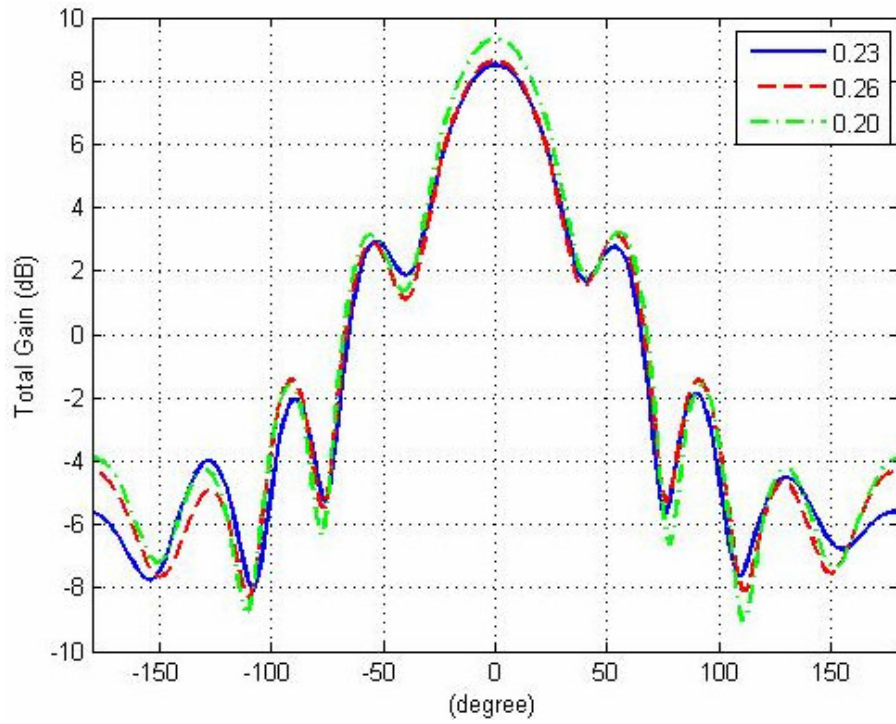


Figure 3.24 H-plane radiation pattern with three different taper rates ($f = 9.5$ GHz)

Taper rates of $R = 0.23$ and $R = 0.20$ gives comparable results as seen in Figure 3.23 and Figure 3.24. The design with a taper rate of $R = 0.23$ has a 3-dB beamwidth of 48° which is 2° better than that of $R = 0.20$ case. The taper rate of $R = 0.26$ has nearly the same radiation pattern with $R = 0.23$ case.

The antennas with taper rates of $R = 0.23$ and $R = 0.26$ have fairly the same characteristics considering the single element performance. The taper rate was chosen to be $R = 0.23$ but, it shall be studied again considering array radiation patterns as in the case of taper length.

3.4.3 Mouth Opening

Mouth opening, or aperture size, is the maximum width of the tapered slotline section. Antenna width comprises of mouth opening and edge offset which will be described later. The radiation of the waves propagating through the slotline increases with increasing slot width further from the half-wavelength of the operating frequency, $\lambda_0/2$, as explained earlier. Thus, the mouth opening shall be on the order of one-half wavelength, at least, in order to improve radiation efficiency through the antenna.

Bandwidth of the antenna is increasing with increasing mouth opening. However, 3-dB beamwidth increases too much when the mouth opening is increased too much. Mouth opening is chosen as 36 mm, one wavelength of the smallest operating frequency. The return loss response and radiation patterns for this value and the effect of increase/decrease ($D = 32$ mm/ $D = 40$ mm) in mouth opening are given in Figure 3.25 and Figure 3.26.

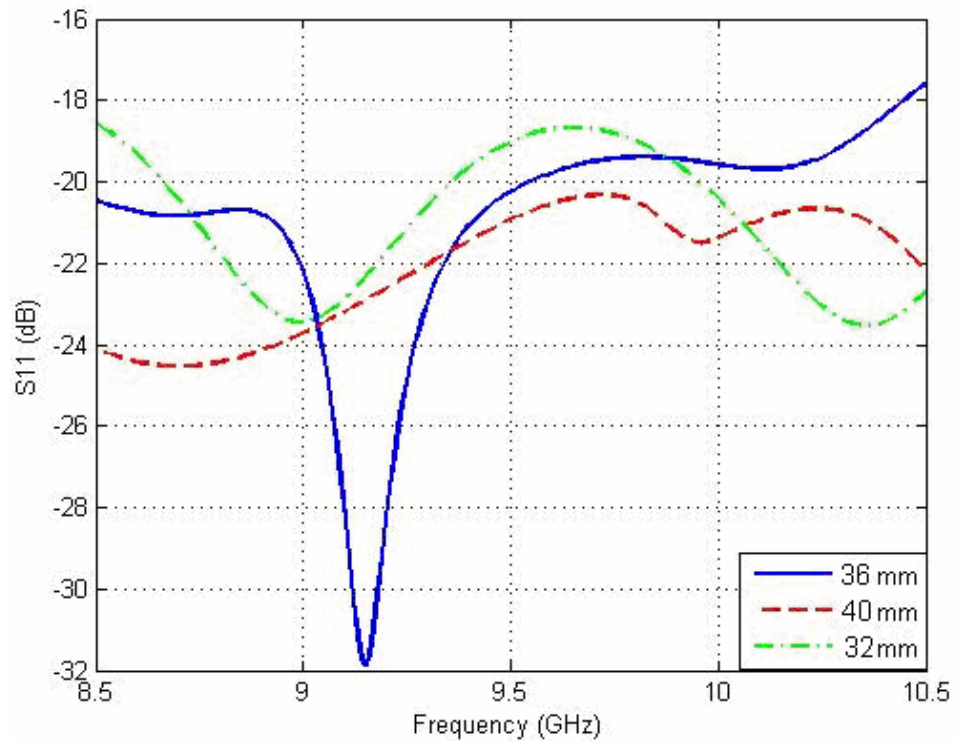


Figure 3.25 Return loss response with three different mouth openings

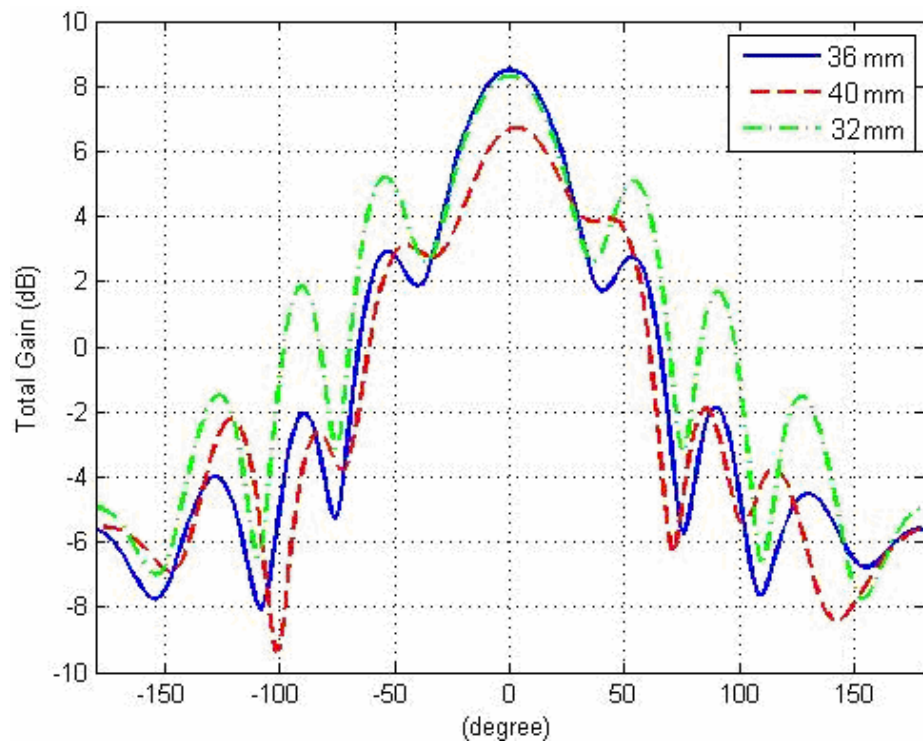


Figure 3.26 H-plane radiation pattern with three different mouth openings ($f = 9.5$ GHz)

The sidelobe levels increased for both increased and decreased mouth opening as seen in Figure 3.26. It shall also be noted that 3-dB beamwidth increased too much (72°) with increasing mouth opening as foreseen. The design with mouth opening of $D = 36$ mm is the most convenient one.

3.4.4 Edge Offset

Edge offset is the extra metallization at the end of tapered slotline. It prevents edge currents to come across a sharp end. The sum of edge offset and mouth opening length gives the total antenna width as stated earlier.

Edge offset is a parameter to be optimized just like the backwall offset. Increasing edge offset beyond this value would not improve return loss response noticeably; besides, the increase could result in deep nulls. Decreasing edge offset below the optimized value would deteriorate the radiation pattern. An edge offset of 2 mm results in better return loss response and radiation pattern as seen in Figure 3.27 and Figure 3.28, respectively. The antenna performance with increased and decreased edge offset values (3 mm and 1 mm respectively) is also shown.

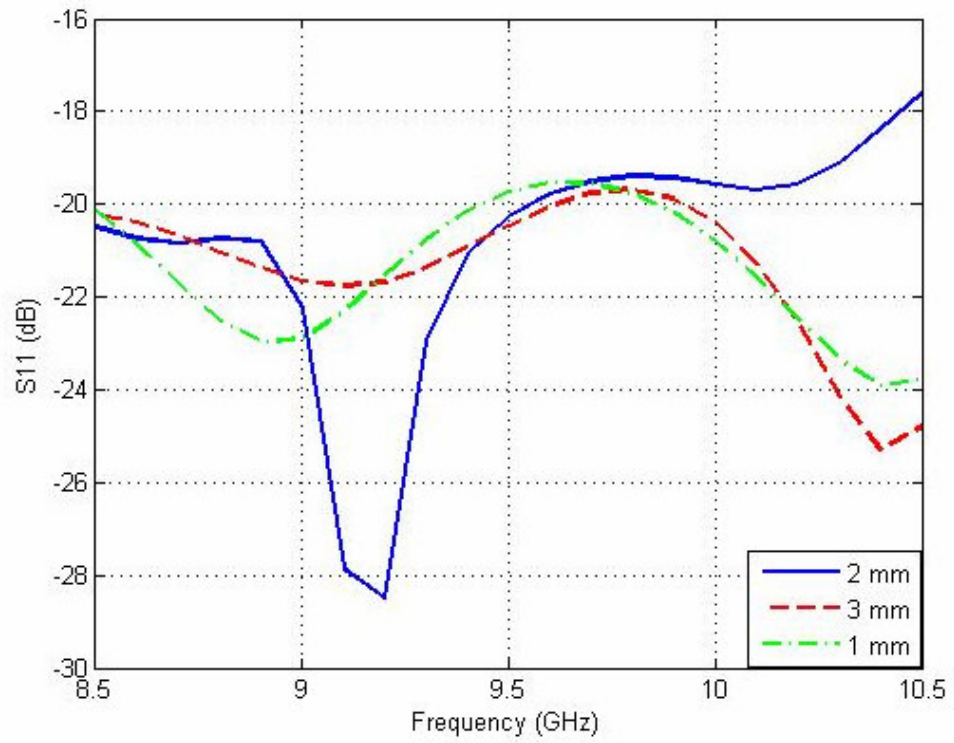


Figure 3.27 Return loss response with three different edge offsets

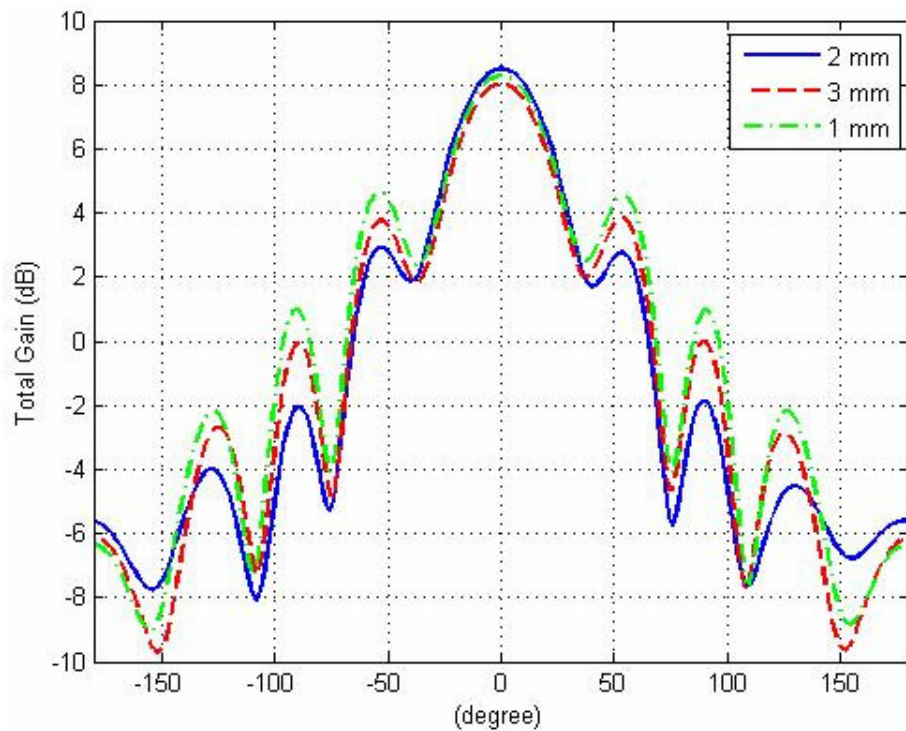


Figure 3.28 H-plane radiation pattern with three different edge offsets ($f = 9.5$ GHz)

The increased and decreased mouth opening values generated comparable return loss responses with the optimized value. However, the sidelobe levels increased with both increase and decrease in mouth opening.

3.5 Final Design of Single Element Vivaldi Antenna

The Vivaldi antenna parameters determined using the results of the stripline model, stripline&slotline model and antenna model are given in Table 3.3 below followed by the results of this final design in Figure 3.29 through Figure 3.36.

Table 3.3 Final design parameters of the single Vivaldi element (see Figure 3.1)

Design Parameter	Value
Substrate Material	Rogers RT Duroid™ 5880
Substrate Thickness	3.14 mm
Stripline Width	2.5 mm
Stripline Length	24 mm
Stripline Distance to the Slotline Starting	4 mm
Slotline Width	0.5 mm
Antenna Length	61 mm
Antenna Width	40 mm
Backwall Offset	1 mm
Slotline Stub Length	4 mm
Taper Length	52 mm
Taper Rate	0.23
Mouth Opening	18 mm
Edge Offset	2 mm

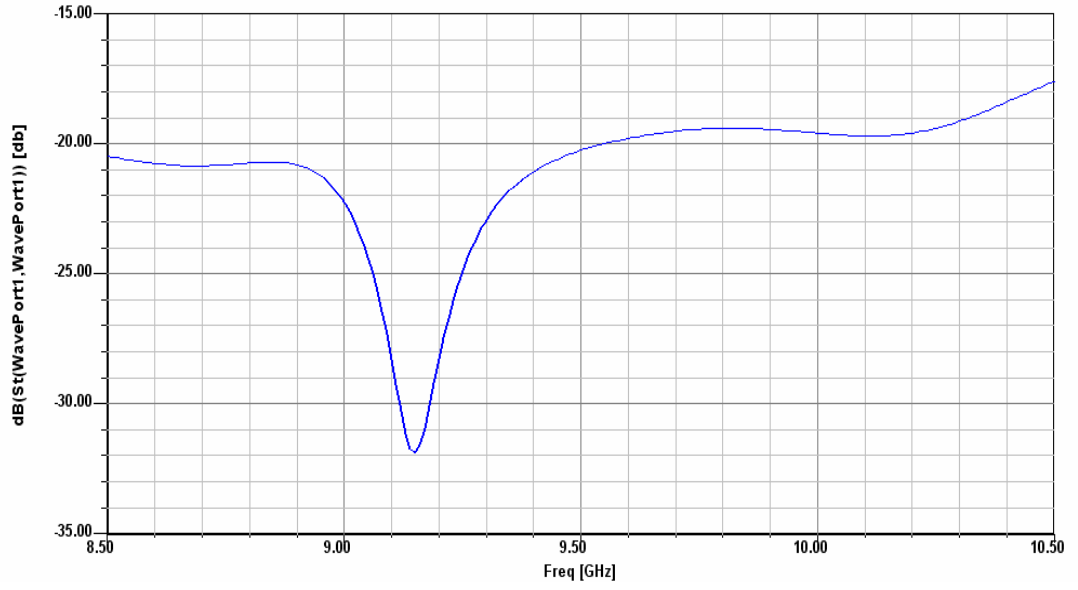


Figure 3.29 Return loss response of the final design

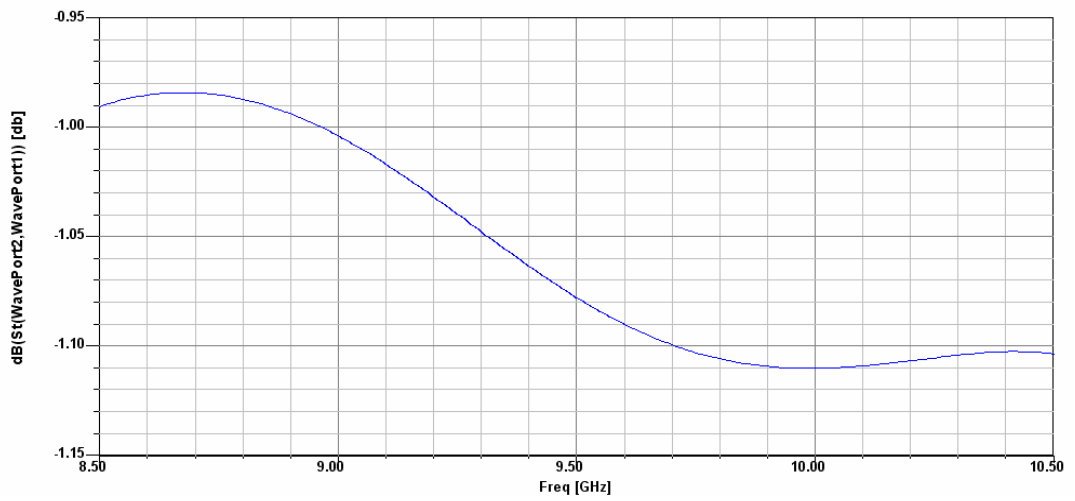


Figure 3.30 Reverse gain of the final design

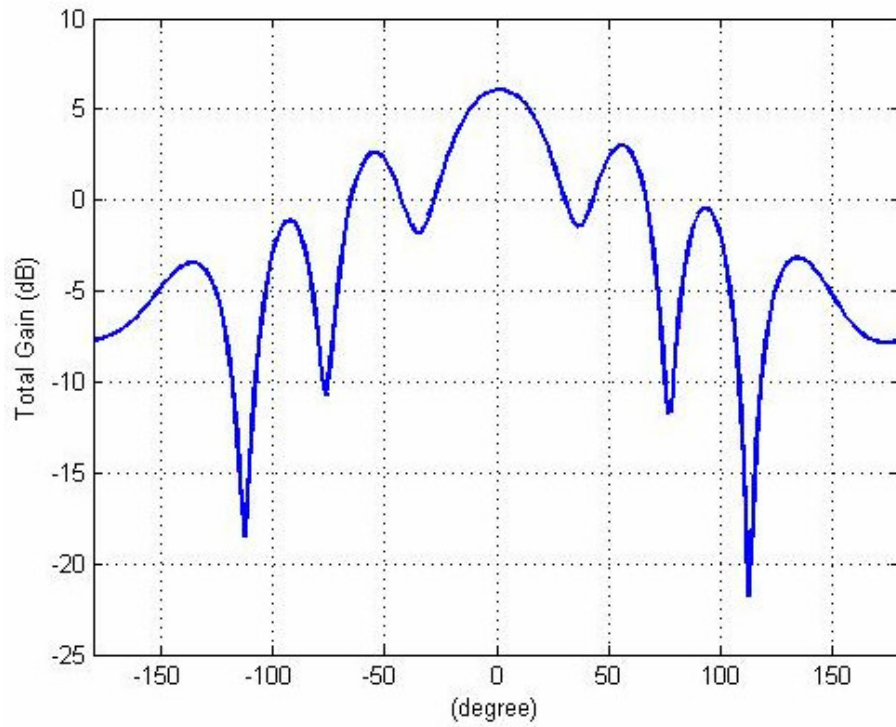


Figure 3.31 H-plane co-polarization radiation pattern of final design (8.5 GHz)

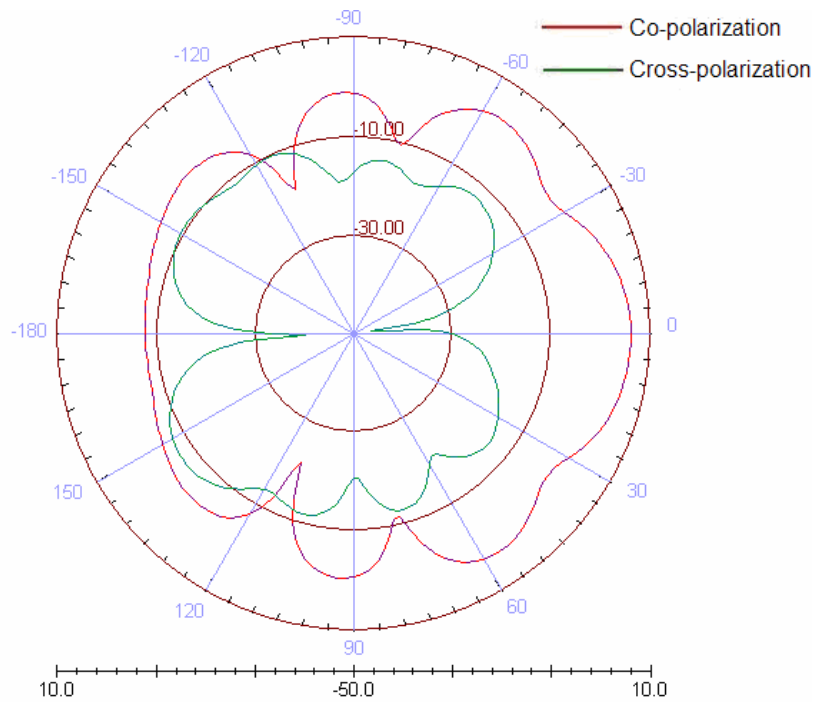


Figure 3.32 H-plane co-polarization and cross-polarization patterns of the final design (8.5 GHz)

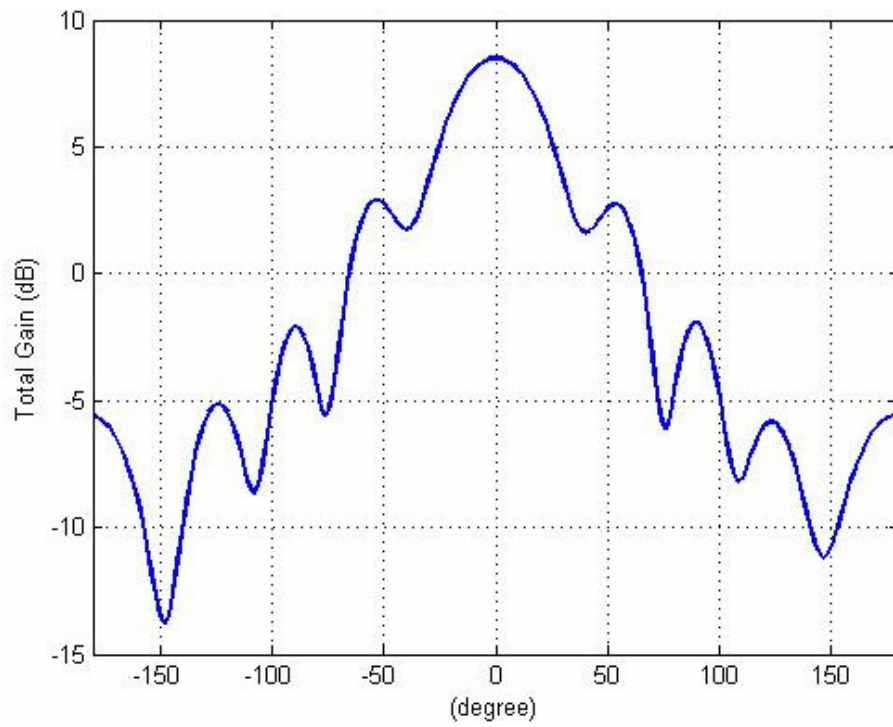


Figure 3.33 H-plane total radiation pattern of final design (9.5 GHz)

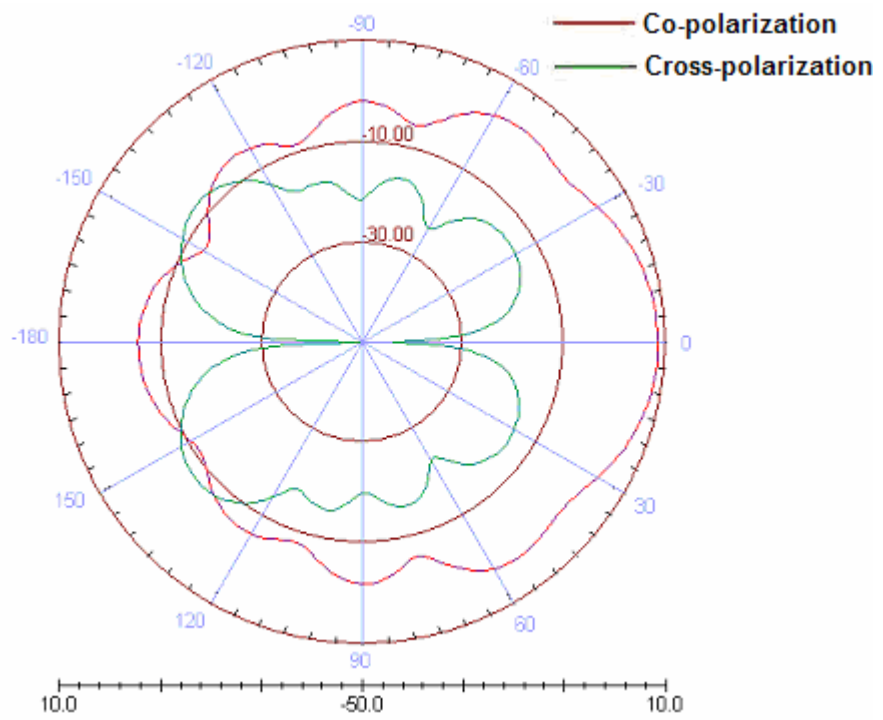


Figure 3.34 H-plane co-polarization and cross-polarization patterns of the final design (9.5 GHz)

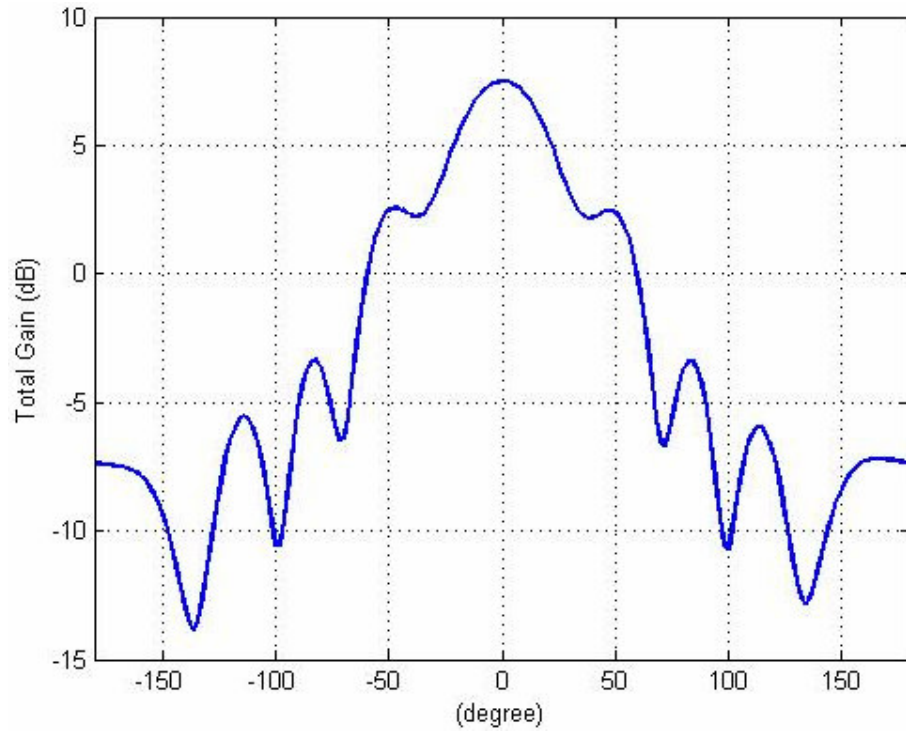


Figure 3.35 H-plane total radiation pattern of final design (10.5 GHz)

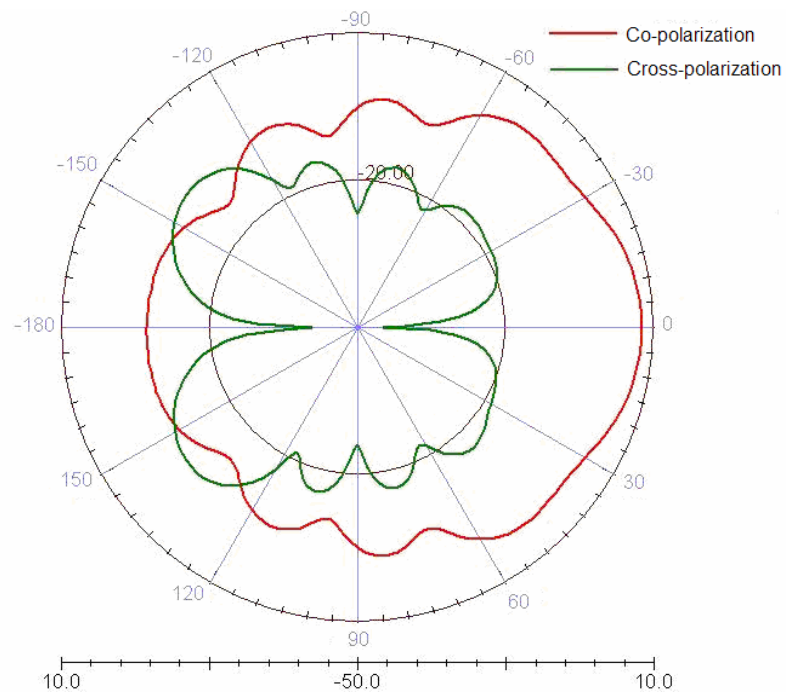


Figure 3.36 H-plane co-polarization and cross-polarization patterns of the final design (10.5 GHz)

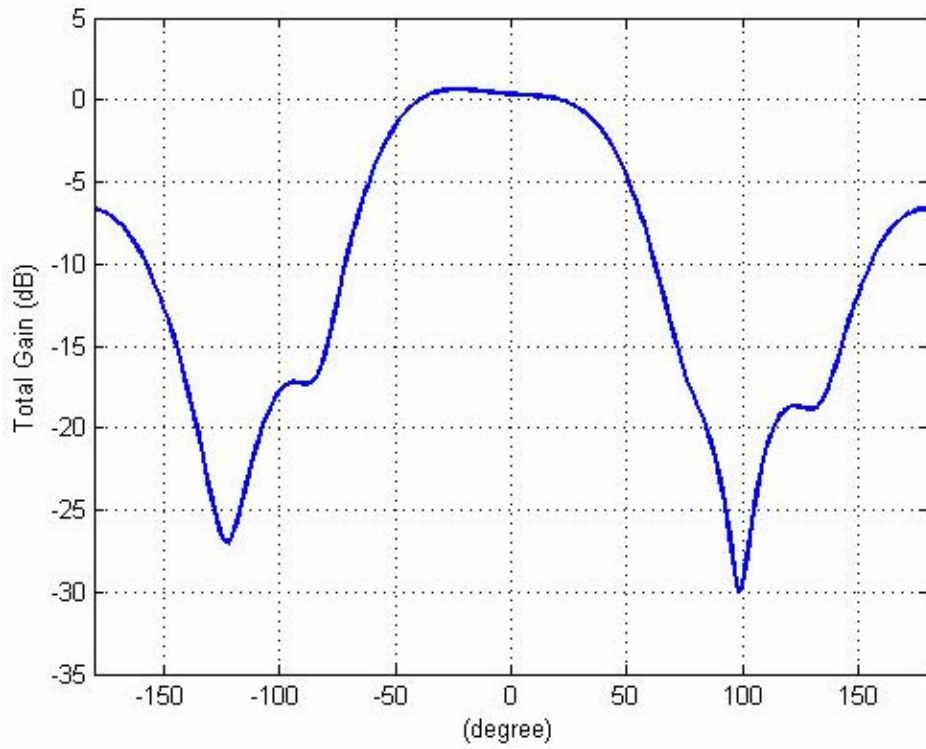


Figure 3.37 E-plane pattern of the final design (8.5 GHz)

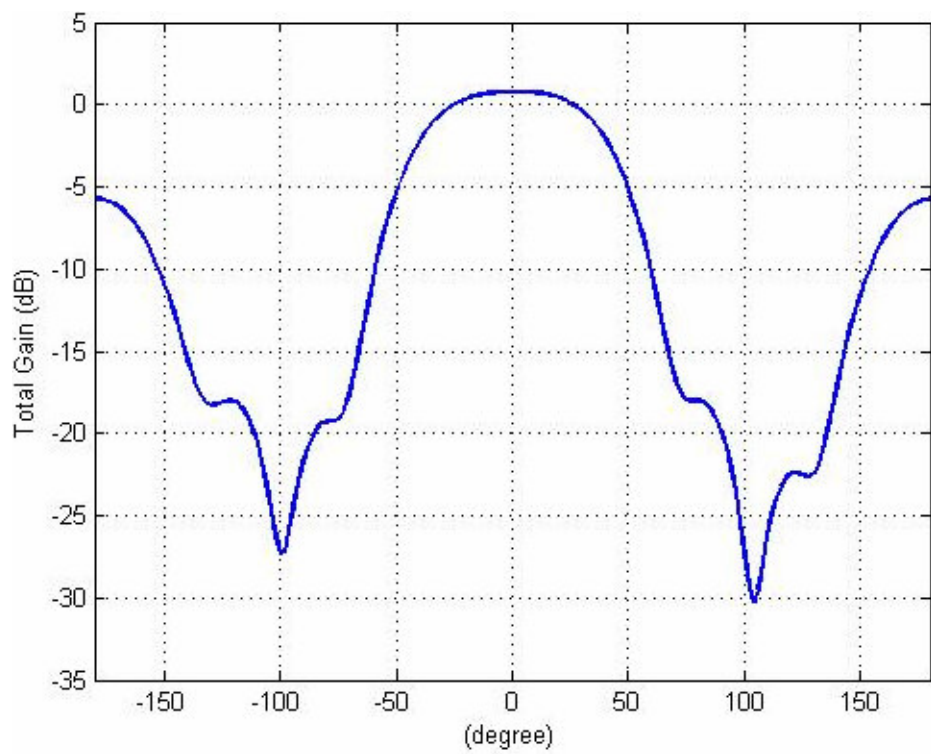


Figure 3.38 E-plane pattern of the final design (9.5 GHz)

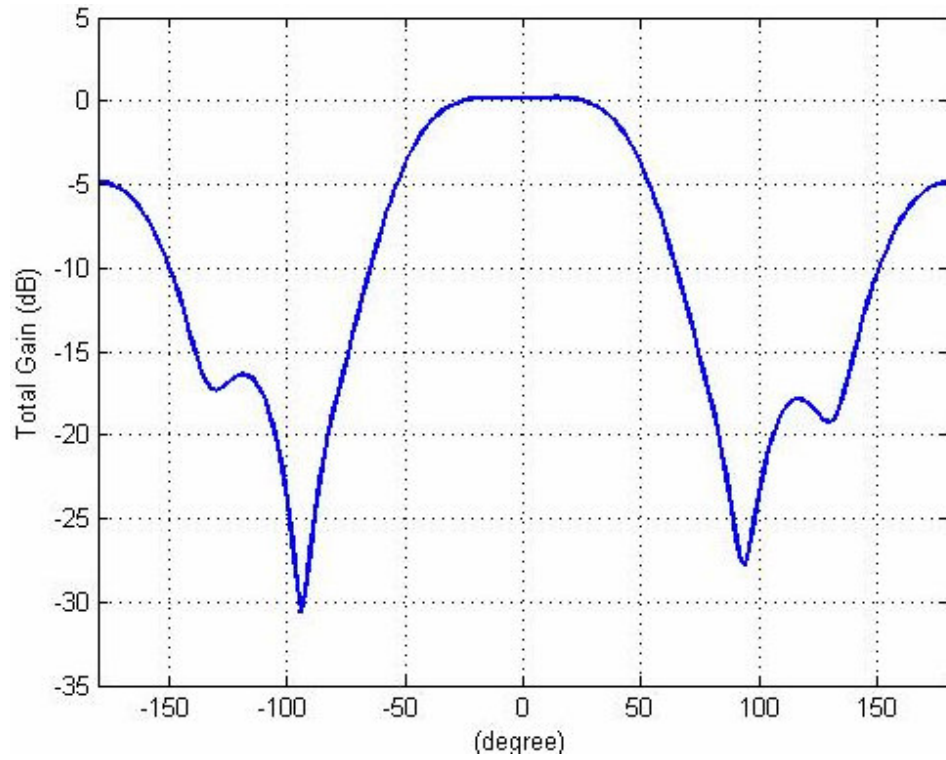


Figure 3.39 E-plane pattern of the final design (10.5 GHz)

Figure 3.29 through Figure 3.39 are the simulated results of the designed Vivaldi antenna. The measurement results of the fabricated antenna designed in this chapter will be given in Chapter 5.

CHAPTER 4

PARAMETRIC STUDY AND DESIGN OF VIVALDI ARRAYS

In this chapter, parametric study of Vivaldi arrays regarding the radiation pattern, half-power beamwidth and side lobe levels is studied. Array design, for which the model is given in Figure 4.1, is used as the case study to apply the design methodology discussed in this chapter with the following specifications: half power beamwidth smaller than 12° in H-plane and side lobe levels smaller than 13 dB. It shall be noted that a fairly directive array is to be designed.

Arrays are used to get fairly well gain characteristics and directive radiation patterns as stated earlier. The total electric field radiated from an N-element array can be found using the following Equation 4-1 [30].

$$E(r) = \frac{\sum_{i=1}^N C_i e^{j\alpha_i} f(\theta, \varphi) e^{-jk_0 r + jk_0 a_r r_i}}{4\pi r} \quad (4-1)$$

where,

C_i : relative amplitude of the i^{th} element

α_i : phase of the i^{th} element

r_i : the position of the the i^{th} element

$f(\theta, \varphi)$: electric field radiation pattern of the elementary antenna

$k_0 a_r r_i$: propagation-phase delay of the distant field

The array factor, $F(\theta, \varphi)$, obtained independent of the single element in the array is expressed by Equation 4-2 [30].

$$F(\theta, \varphi) = \sum_{i=1}^N C_i e^{j\alpha_i + jk_0 a_r r_i} \quad (4-2)$$

The array factor depends on the excitations, phases and locations of the single elements as seen in the equation. The array radiation pattern and thus the directivity, $D(\theta, \varphi)$, is observed to be proportional to $16\pi^2 r^2 |E|^2$ giving an important relation[30].

$$\begin{aligned} D(\theta, \varphi) &\propto |f(\theta, \varphi)|^2 \left| \sum_{i=1}^N C_i e^{j\alpha_i + jk_0 a_r r_i} \right| \\ &= |f(\theta, \varphi)|^2 |F(\theta, \varphi)|^2 \end{aligned} \quad (4-3)$$

The pattern multiplication rule, which states that the product of the single element pattern function and the array pattern function gives the total radiation pattern of the array, is expressed by the above Equation 4-3. It can be concluded that the vector addition of the radiation fields from the single elements gives the total array field. This expression assumes that all the single elements in the array have identical radiation patterns. Mutual coupling effect disturbs this assumption, but it can be neglected if the array spacing is chosen accordingly.

In this study, a uniform linear array configuration is designed at first. This chapter starts with the linear array design and the simulation results of the mentioned structure. Then, the parameters affecting the array performance are studied. The single element antenna parameters affecting the array performance are reconsidered and the geometrical parameters determining the array pattern are investigated. At the end of the chapter, the performance of the linear array fed with the signals of different amplitudes is presented.

4.1 Uniform Linear Array Design

The single element Vivaldi antennas designed through Chapter 3 are assembled along a straight line in z-axis and fed with identical magnitude and progressive phase, forming uniform linear array configuration. A symmetric pattern in θ is

expected theoretically. The array factor of the structure with N-elements will be as in the following Equation 4-4 [29].

$$AF = \sum_{n=1}^N e^{j(n-1)\psi} = e^{j\left[\frac{N-1}{2}\right]\psi} \left[\frac{\sin\left(\frac{N}{2}\psi\right)}{\sin\left(\frac{1}{2}\psi\right)} \right] \quad (4-4)$$

where,

$\psi = kdcos\theta + \beta$ (progressive phase)

The gain of the uniform linear array will be as in the Equation 4-5 [17].

$$g(\varphi) = |A(\psi)|^2 = \left| \frac{\sin\left(\frac{N}{2}\psi\right)}{N\sin\left(\frac{1}{2}\psi\right)} \right|^2 = \left| \frac{\sin\left(\left(\frac{Nkd}{2}\right)\cos\varphi\right)}{N\sin\left(\left(\frac{kd}{2}\right)\cos\varphi\right)} \right|^2 \quad (4-5)$$

Detailed information on the theoretical background of uniform linear arrays can be found in [17] and [29].

The uniform linear array structure described above is formed and the parameters effecting the radiation pattern are investigated. Figure 4.1 shows the mentioned array model formed.

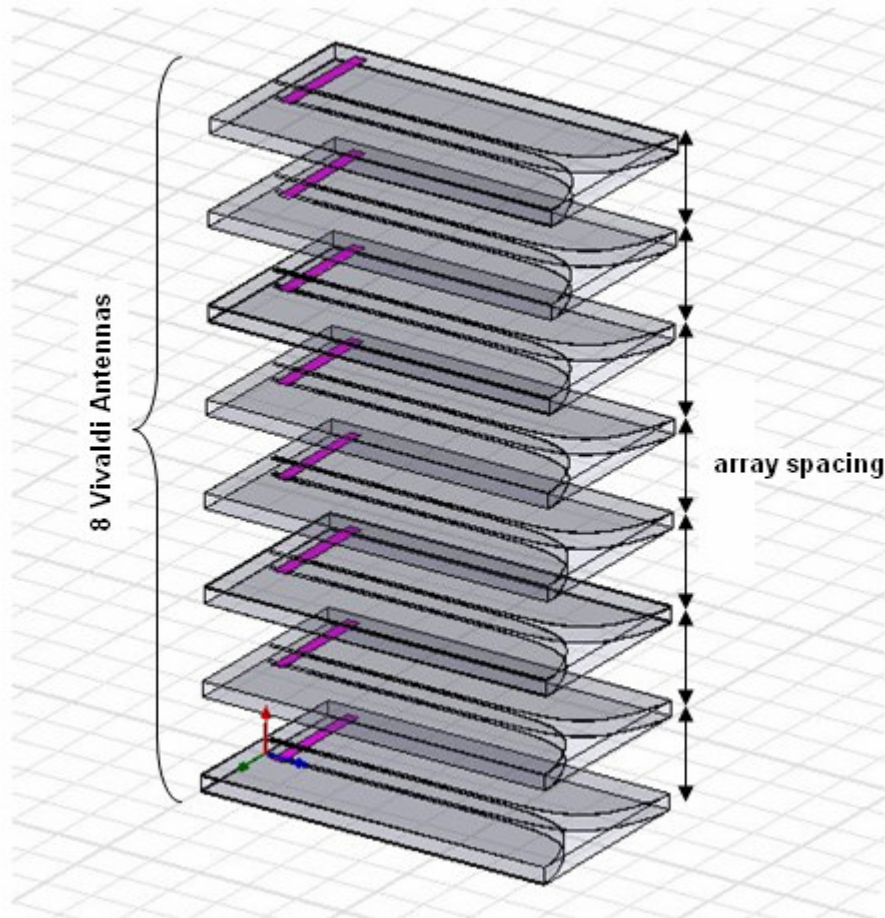


Figure 4.1 Linear array of 8 elements

Designing the single element antenna and choosing the array structure, the element spacing, d , and the number of elements, N , shall be determined next. Besides the mutual coupling effect between the individual antennas, explained earlier, grating lobes should be also considered in this step.

Grating lobes can be defined as the main beam lobes or maxima in other directions than the desired one. In order to avoid grating lobes completely, array spacing should be smaller than one-half wavelength of the maximum operating frequency, $d \leq \lambda/2$.

However, the grating lobes can still be avoided for a spacing up to $d = \lambda$ for narrow beamwidth arrays. The element spacing is chosen as $d = 18 \text{ mm} \approx \lambda/2$.

The number of elements may be chosen considering the sidelobe levels of the radiation pattern. For the uniform arrays with the number of elements $N \geq 6$ and spacing $d \geq \lambda/2$, the sidelobe level reaches the limiting value of 13dB [17]. Thus, the number of elements is chosen as $N = 8$ considering this claim as well as space and cost considerations.

4.2 Array Parameters

The parameters determining the radiation characteristics of the array are considered in this part of the work. The parametric study of array spacing and number of elements are studied as well as uniform slot width, antenna length and taper rate of the single antenna. The simulations are realized at 9.5 GHz in co-polarization H-plane.

4.2.1 Array Spacing

Array spacing affects mutual coupling between the elements, grating lobes, sidelobe levels and resonances of the radiation pattern. It shall be less than one wavelength so as to avoid grating lobes completely as stated before. However, smaller spacing will increase mutual coupling between the individual elements. It should also be noted that larger array spacing will generate resonance in the array pattern in return.

The simulated radiation pattern, sidelobe levels and 3-dB beamwidth of the array with spacing $d = 18$ mm, $d = 12$ mm and $d = 24$ mm are shown in Figure 4.2.

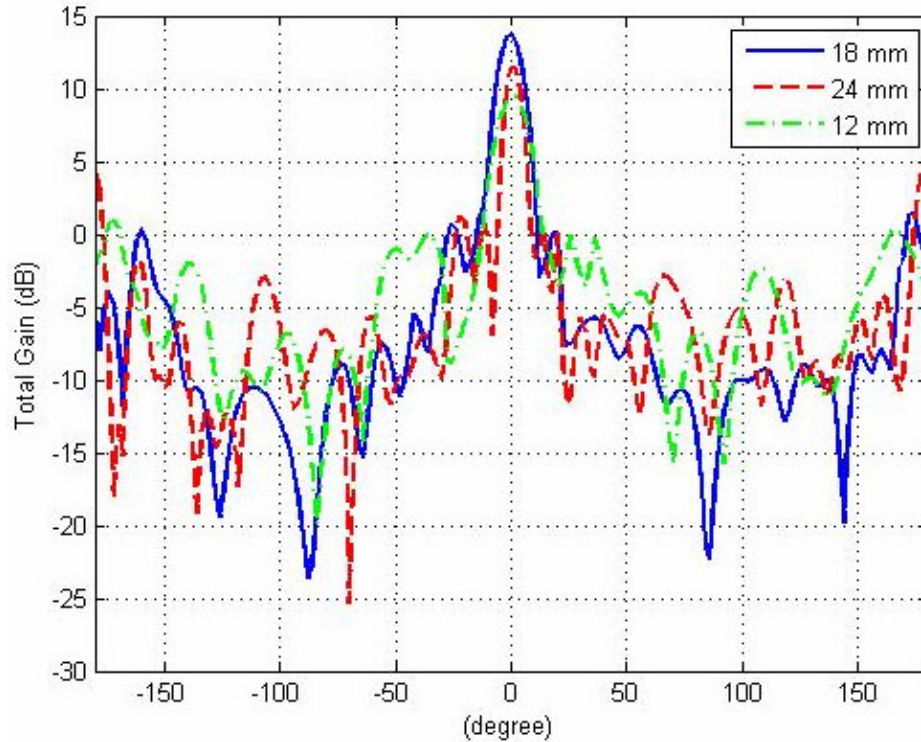


Figure 4.2 H-plane array pattern for three different element spacing values ($f = 9.5$ GHz)

As seen in Figure 4.2, the half power beamwidth improves with the increasing array spacing. The array design with $d = 24$ mm has a beamwidth of $\Delta\phi_{3dB} = 10^\circ$ whereas the spacing chosen for this project, $d = 18$ mm, results in $\Delta\phi_{3dB} = 12^\circ$ half power beamwidth. Another important observation is that the grating lobes and resonance in the radiation pattern increase noticeably with the increasing array spacing.

4.2.2 Number of Elements

The number of elements, N , mainly determines the array directivity. In fact, both increasing element spacing and number of elements provide a decrease in main lobe and consequently an improvement in array directivity. The increase in element spacing causes grating lobes besides. Thus, the number of elements shall be increased in order to get desired directivity and 3 dB beamwidth. However, it should also be noted that the increase in the number of elements will result in a hard and costly fabrication process besides an increase in the space required to implement the designed array.

An array of 8-element is chosen in this work and the resultant radiation pattern is presented in Figure 4.3 as well as the patterns of arrays with increased and decreased number of elements.

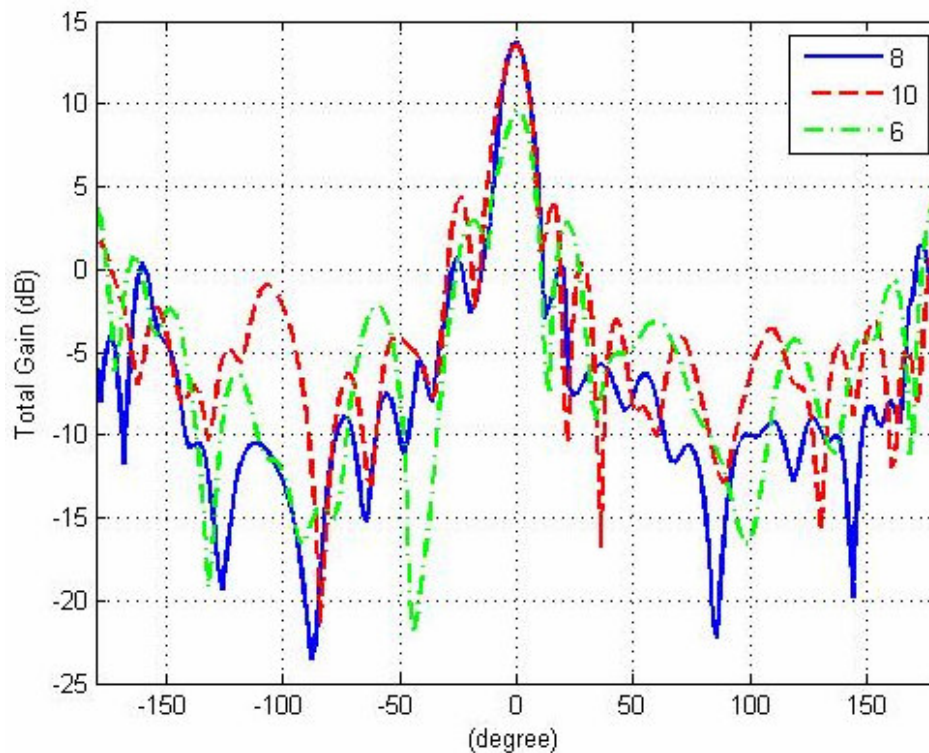


Figure 4.3 H-plane array pattern for three different element numbers ($f = 9.5$ GHz)

It is observed that the 3 dB beamwidth is deteriorated with the decrease in the number of elements. The beamwidth is improved with the increase in the element number and the narrowest result is obtained with 10-element array design. However, side lobe level is increased by about 7 dB compared with the radiation pattern of 8-element array.

4.2.3 Uniform Slot Width

Schaubert [11] showed in his studies that the widest bandwidth would be achieved with the slotline width, $W_{SL} = 0.5$ mm and $W_{SL} = 1.0$ mm for which the substrate

thickness, $W = 2.88$ mm and stripline width, $W_{ST} = 2.0$ mm (fairly similar with this design) as stated in Chapter 3. The return loss response for $W_{SL} = 0.5$ mm was found to be more satisfactory in the single element design. The same array structure is formed using the antennas with $W_{SL} = 1.0$ mm and the resultant radiation pattern is given in Figure 4.4.

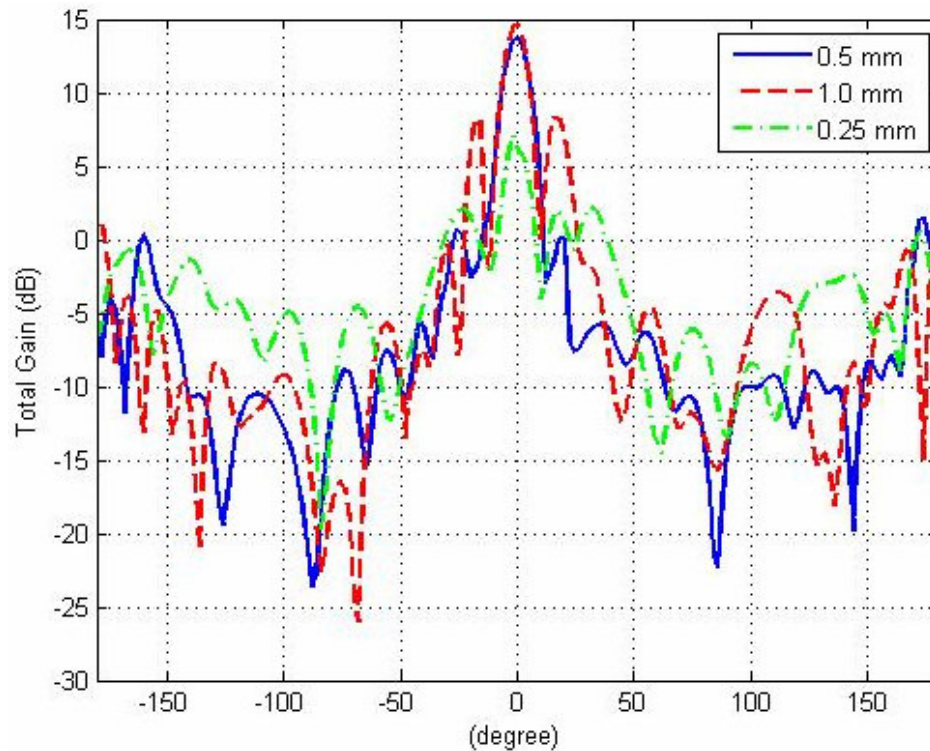


Figure 4.4 H-plane array pattern for three different element slot width values ($f = 9.5$ GHz)

The decrease in the slot width deteriorates the pattern considerably. Comparing the slot width values of $W_{SL} = 0.5$ mm and $W_{SL} = 1.0$ mm, the half power beamwidth is observed to be smaller for the increased slot width, $\Delta\phi_{3dB} = 10^\circ$, whereas $W_{SL} = 0.5$ mm design generated smaller side lobes. The discussion on the slot width will be completed later in this chapter.

4.2.4 Taper Length

The single Vivaldi antennas work best when the taper length and consequently the antenna length is greater than one-wavelength but the arrays with the elements of smaller antenna length have better performance according to general consensus. Schaubert [11] showed that for array sizes up to at least 8×8 elements, longer elements ($L_T > 2\lambda_0$) had weaker resonances, and therefore, would be better candidates than smaller elements for use in small arrays. Figure 4.5 shows the simulated radiation pattern of the arrays with the single elements of taper length $L_T = 52$ mm, $L_T = 63$ mm and $L_T = 41$ mm.

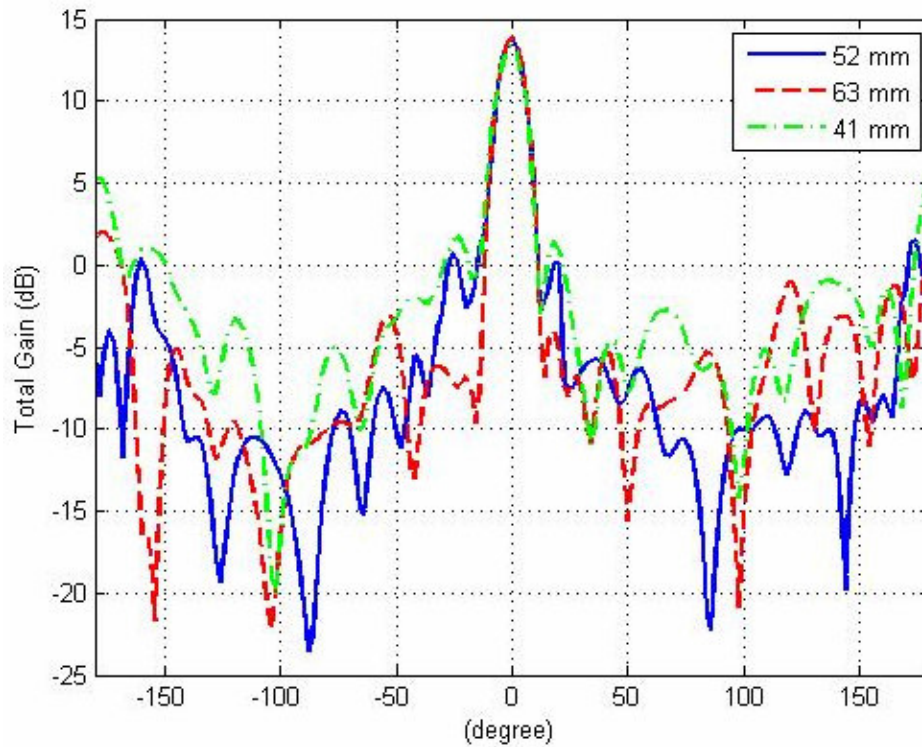


Figure 4.5 H-plane array pattern for three different taper length values ($f = 9.5$ GHz)

The array with the single elements of taper length $L_T = 41$ mm has an unacceptable performance considering the half power beamwidth and side lobe levels. Figure 4.5 shows that the performance is improved with the increasing antenna length. The beamwidth is slightly increased with the taper length of $L_T = 63$ mm compared to the

taper length of $L = 52$ mm. It is also observed that the side lobe levels are lower for $L_T = 63$ mm.

In the single antenna design section, it was observed that the antenna with taper length of $L_T = 52$ mm and $L_T = 63$ mm had comparable return loss and radiation pattern characteristics as well as the array performance simulated in this chapter. These two designs will result in satisfactory performance both, apparently. Thus, the antenna length shall be chosen considering cost or space requirements of the design which makes the design with $L_T = 52$ mm more advantageous.

4.2.5 Taper Rate

The phase velocity of the traveling waves along the antenna and thus the guide wavelength, λ_g , varies with the taper rate of the slotline. This will result in a change in the radiation characteristics and consequently the gain and beamwidth of the array. The taper rates $R = 0.23$ and $R = 0.26$ were found to have nearly same return loss response and radiation pattern considering the single element design. Thus the array radiation pattern for these taper rates and for $R = 0.20$ are investigated and shown in Figure 4.6.

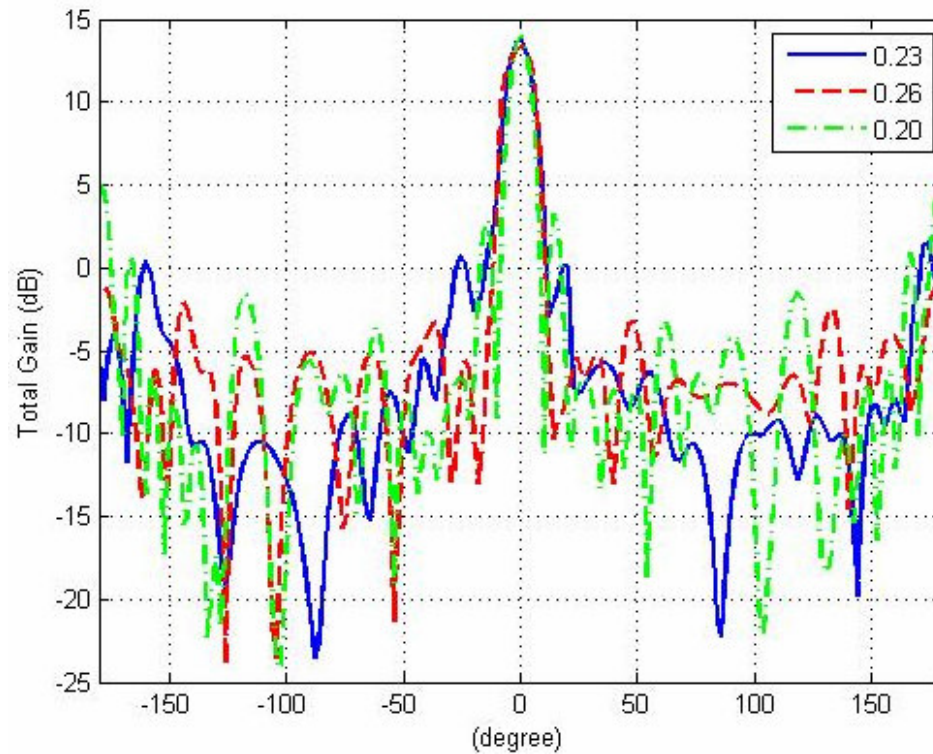


Figure 4.6 H-plane array pattern for three different taper rates ($f = 9.5$ GHz)

As seen in Figure 4.6, an increase or decrease from the chosen taper rate ($R = 0.23$) deteriorates the radiation pattern of the array design considerably, wider beamwidth with increasing rate and increasing side lobe and grating lobe level with decreasing rate. That is to say, the taper rate of $R = 0.23$ is the most convenient choice considering both the array radiation pattern.

4.3 Array Feeding

Nonuniform array feeding gives the advantage of controlling side lobe levels and 3 dB beamwidth of array pattern easily as stated before. Two common types of nonuniform fed, binomial and Dolph-Chebyshev feedings, are investigated in this study to improve the radiation pattern characteristics.

4.3.1 Binomial Array

The array elements are fed in accordance with the binomial expansion coefficients in this type of array. The binomial function $(1+x)^{n-1}$ can be expanded as in the Equation 4-7 [17] to find the coefficients.

$$\frac{(N-1)!}{n!(N-1-n)!} \quad (4-6)$$

where,

N : the total number of array elements

n = 0, 1, ..., N-1

The binomial array factor, $W(\psi)$, for an N-element array is defined as in the following Equation 4-7 [17] in ψ -space.

$$W(\psi) = \left(e^{j\frac{\psi}{2}} + e^{-j\frac{\psi}{2}} \right)^{N-1} = \left[2 \cos\left(\frac{\psi}{2}\right) \right]^{N-1} \quad (4-7)$$

The above function has its peak at $\psi = 0$ and falls until $W(\psi) = 0$ on either sides of the peak. This statement gives the most apparent property of the binomial arrays: a binomial array has no side lobes.

In practice, binomial arrays generate the smallest side lobe levels compared to uniform and Dolph-Chebyshev arrays. These arrays have even no side lobes with the array spacing less than $\lambda/2$. On the contrary, the directivity is lost and the widest half-power beamwidth is produced by the binomial arrays. Closed form expressions for half power beamwidth and directivity can only be derived for array spacing $d = \lambda/2$. The following equations, Equation 4-8 and Equation 4-9 [29] give the directivity and half-power beamwidth of the binomial arrays for $d = \lambda/2$.

$$\Delta\psi_{3-dB} \left(d = \frac{\lambda}{2} \right) = \frac{1.06}{\sqrt{N-1}} \quad (4-8)$$

$$D(\theta, \varphi) \left(d = \frac{\lambda}{2} \right) = \frac{(2N - 2)(2N - 4) \dots 2}{(2N - 3)(2N - 5) \dots 1} \quad (4-9)$$

The wide variations of amplitudes between the array elements, especially for the large number of elements, make the binomial array hard to implement practically. This also results in inefficient antennas.

In our case, an 8-element array, the amplitudes of the elements will be as follows in order to get a binomial array:

$$1 \quad 7 \quad 21 \quad 35 \quad 35 \quad 21 \quad 7 \quad 1$$

Figure 4.7 shows the simulated radiation patterns of uniform fed and binomial array for the design detailed above.

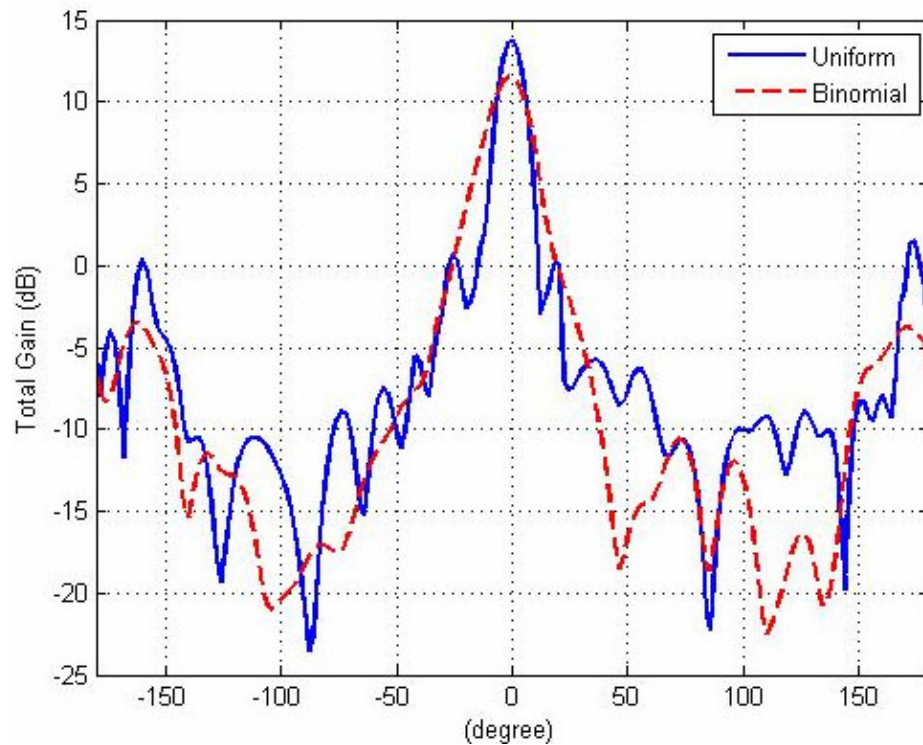


Figure 4.7 H-plane patterns of uniform and binomial arrays (f = 9.5 GHz)

The side lobes near the main lobe are decreased nearly by 10 dB using binomial array design as seen in Figure 4.7. Moreover, the grating lobe levels are decreased by nearly 5 dB compared to the uniform array design. However, the half power beamwidth is increased as predicted. Binomial array has a beamwidth of 18° which is unacceptable regarding the design requirements.

4.3.2 Dolph-Chebyshev Array

In Dolph-Chebyshev type feeding, the excitation amplitudes of array elements are chosen in accordance with Dolph-Chebyshev polynomial coefficients. The Dolph-Chebyshev polynomial $T_m(x)$ and array factor $W(\psi)$ are given in Equation 4-10 and Equation 4-11 [17] respectively.

$$T_m(x) = \cos(m \arccos(x)) \quad (4-10)$$

$$W(\psi) = T_{N-1}(z), \quad z = z_0 \cos(\psi/2) \quad (4-11)$$

where,

z_0 : scaling factor ($z_0 > 1$)

Minimum side lobe level is obtained using binomial arrays followed by Dolph-Chebyshev and uniform arrays, whereas comparing these three feeding techniques the minimum beamwidth is provided by uniform arrays followed by Dolph-Chebyshev and binomial arrays. Thus, Dolph-Chebyshev arrays offer an optimization between side lobe level and 3-dB beamwidth of the array. For a given side lobe level, the most directive pattern and thus the smallest half power beamwidth is obtained with Dolph-Chebyshev array. In the same manner, Dolph-Chebyshev array generates the smallest side lobe level for a given half power beamwidth. The directivity of Dolph-Chebyshev arrays can be found using Equation 4-12 [30].

$$D_0 = \frac{2R_0^2}{1 + (R_0^2 - 1)f \frac{\lambda}{(L + d)}} \quad (4-12)$$

$$f = 1 + 0.636 \left\{ \frac{2}{R_0} \cosh \left[\sqrt{[(\cosh)^{-1} R_0]^2 - \pi^2} \right] \right\}^2$$

where,

R_0 : side lobe level (in dB)

L : single element length (mm)

d : array spacing (mm)

f : beam broadening factor

In the design process, the desired side lobe level, R , and the number of elements, N , shall be specified first. Next step is to calculate the side lobe level in voltage ratio, $R_0(VR)$, and scaling factor, z_0 , which gives the point where Chebyshev polynomial is equal to desired side lobe level, $T_m(z_0) = R_0$, as given in Equations 4-13 and 4-14 [29].

$$R_0(VR) = 10^{R_0/20} \quad (4-13)$$

$$z_0 = \cosh \left[\frac{1}{P} \cosh^{-1}(R_0(VR)) \right] \quad (4-14)$$

where,

$R_0(VR)$: side lobe level in voltage ratio

z_0 : scaling factor

P : order of Chebyshev polynomial

Finally, Equation 4-15 [29] is used to calculate the Chebyshev polynomials and the array elements are fed in accordance with these coefficients.

$$\alpha_n = \begin{cases} \text{for even } 2M \text{ elements} \\ \sum_{q=n}^M (-1)^{M-q} (z_0)^{2q-1} \frac{(q+M-2)!(2M-1)}{(q-n)!(q+n-1)!(M-q)!} \\ \text{for odd } 2M+1 \text{ elements} \\ \sum_{q=n}^{M+1} (-1)^{M-q+1} (z_0)^{2(q-1)} \frac{(q+M-2)!(2M)}{\varepsilon_n (q-n)!(q+n-2)!(M-q+1)!} \end{cases} \quad (4-15)$$

where,

a_n : Chebyshev polynomial coefficients

z_0 : scaling factor

$n = 1, 2, \dots, N$

$$\varepsilon_n = \begin{cases} 2, & n = 1 \\ 1, & n \neq 1 \end{cases}$$

The MATLAB function `dolph.m` [26] given in Appendix-B is used to determine the Chebyshev polynomials in order to construct an 8-element Dolph-Chebyshev array. Using the designed uniform array parameters $N = 8$ and $R = 13$ dB, the following coefficients are obtained.

$$1.0000 \quad 0.6357 \quad 0.7512 \quad 0.8141 \quad 0.8141 \quad 0.7512 \quad 0.6357 \quad 1.0000$$

The simulated radiation patterns of uniform fed and Dolph-Chebyshev array is given in Figure 4.8 below.

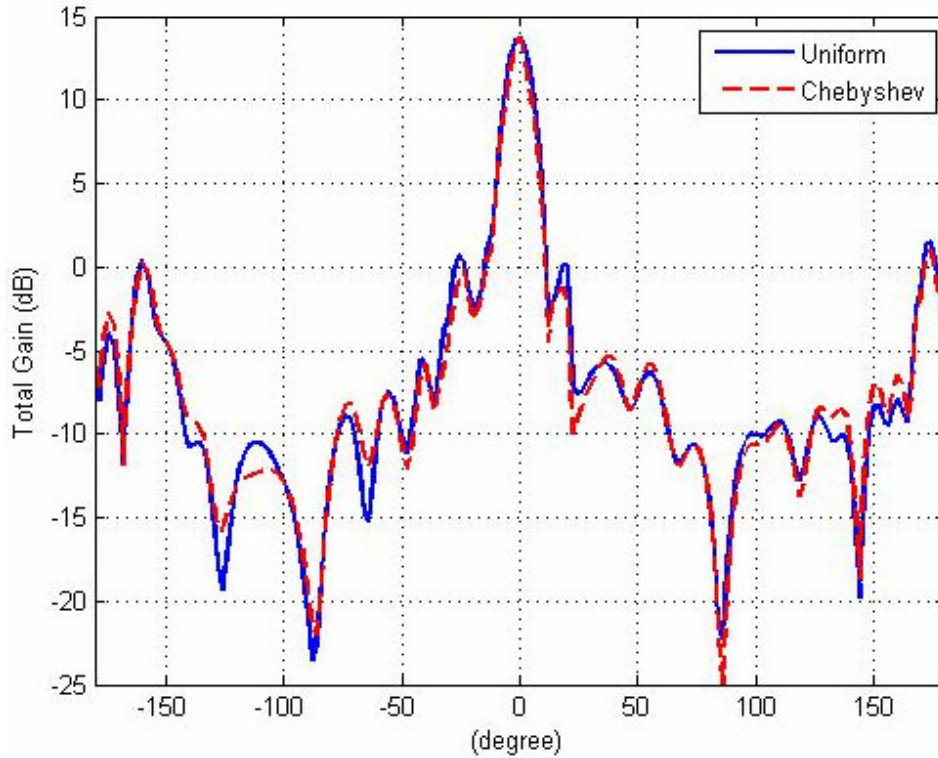


Figure 4.8 H-plane patterns of uniform and Chebyshev arrays ($f = 9.5$ GHz)

The radiation patterns for uniform and Dolph-Chebyshev arrays are nearly same in general since the Dolph-Chebyshev polynomial coefficients are calculated for the side lobe level of $SLL = 13$ dB, as seen in Figure 4.8. Dolph-Chebyshev array has slightly better directivity compared with the uniform array. The half power beamwidth of Dolph Chebyshev array is observed to be improved by 2° , $\Delta\phi_{3dB} = 10^\circ$.

4.4 Final Design of Vivaldi Array

The parameters of the linear Vivaldi array with Dolph-Chebyshev feeding, given in Table 4.1 Final design parameters of Vivaldi array are determined using the results of the parametric study of Vivaldi single element and array. The results of this final design are given below in Figure 4.9 through Figure 4.17.

Table 4.1 Final design parameters of Vivaldi array

Design Parameter	Value
Substrate Material	Rogers RT Duroid™ 5880
Substrate Thickness	3.14 mm
Stripline Width	2.5 mm
Stripline Length	24 mm
Stripline Distance to the Slotline Starting	4 mm
Slotline Width	0.5 mm
Antenna Length	61 mm
Antenna Width	40 mm
Backwall Offset	1 mm
Slotline Stub Length	4 mm
Taper Length	52 mm
Taper Rate	0.23
Mouth Opening	18 mm
Edge Offset	2 mm
Array Spacing	18 mm
Number of Elements	8

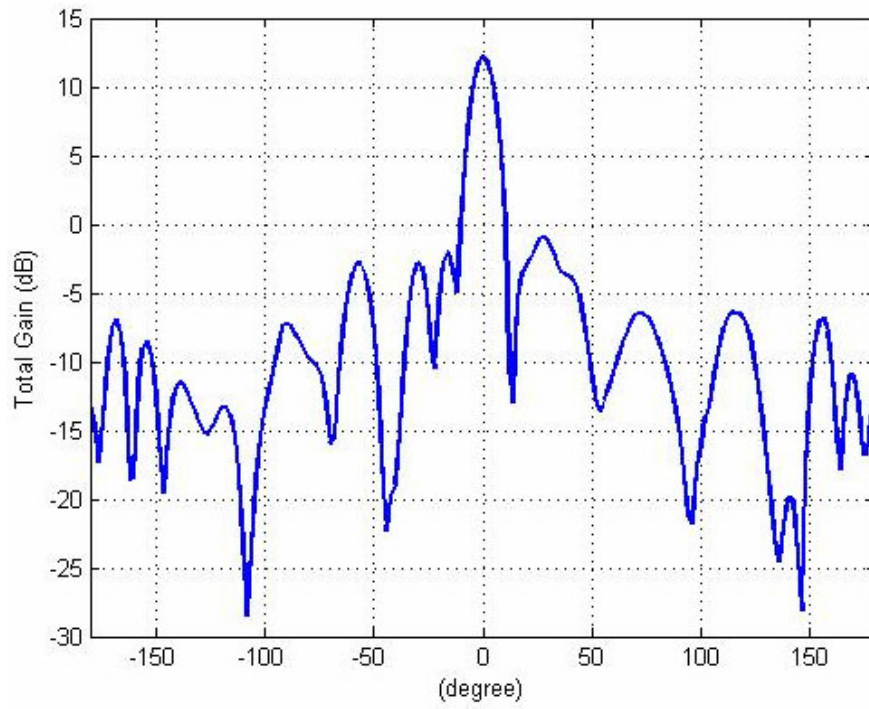


Figure 4.9 H-plane co-polarization pattern of the final design (8.5 GHz)

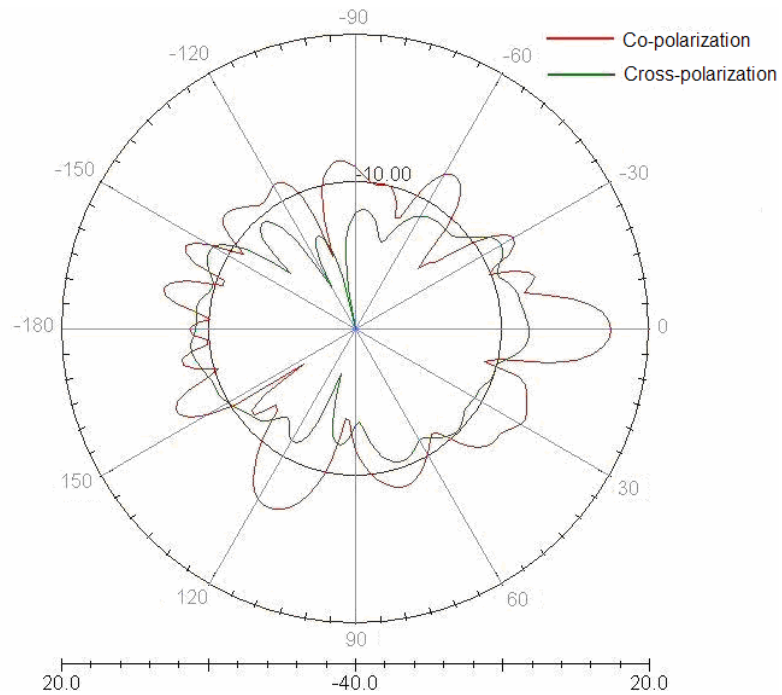


Figure 4.10 H-plane co-polarization and cross-polarization radiation patterns of the final design (8.5 GHz)

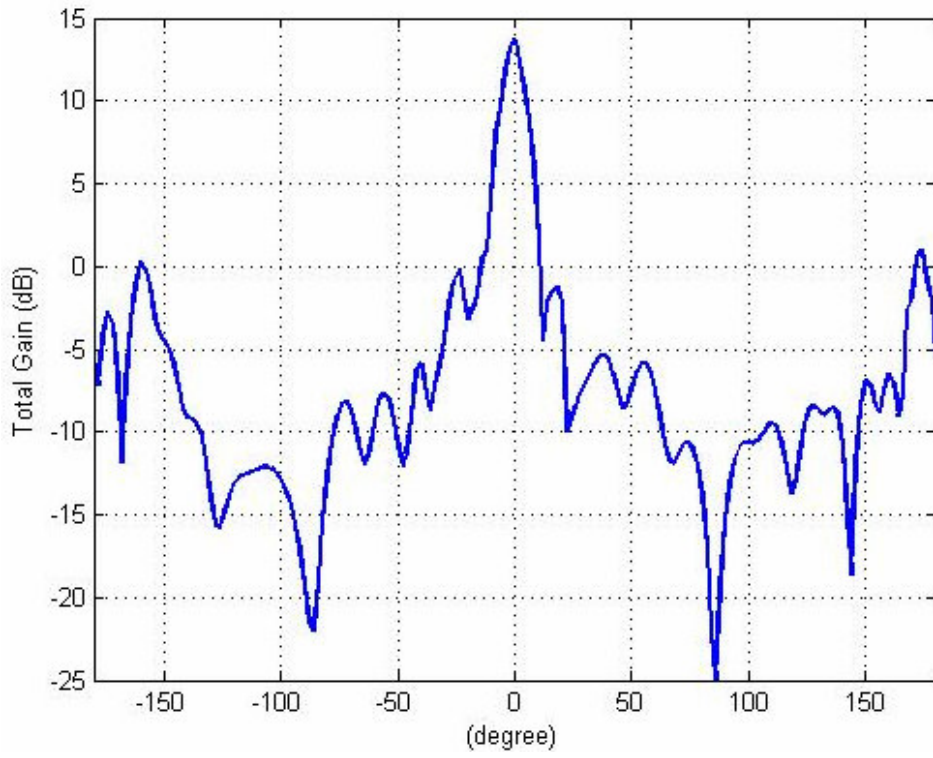


Figure 4.11 H-plane co-polarization pattern of the final design (9.5 GHz)

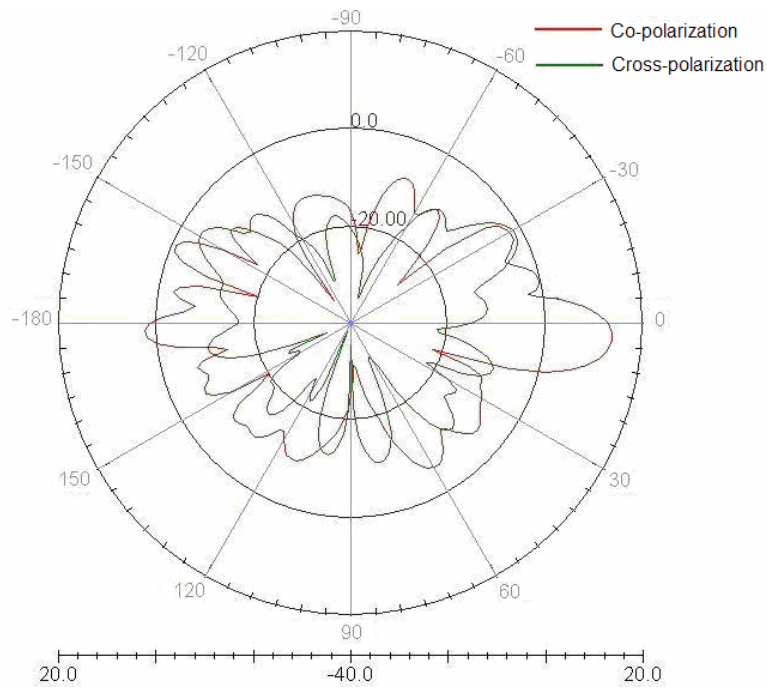


Figure 4.12 H-plane co-polarization and cross-polarization radiation patterns of the final design (9.5 GHz)

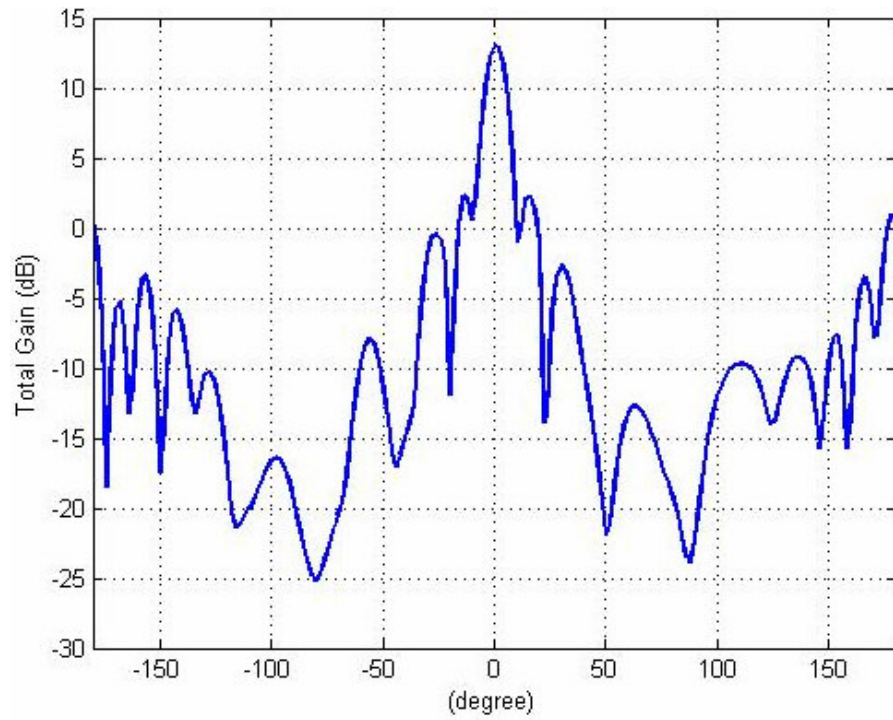


Figure 4.13 H-plane co-polarization radiation pattern of the final design (10.5 GHz)

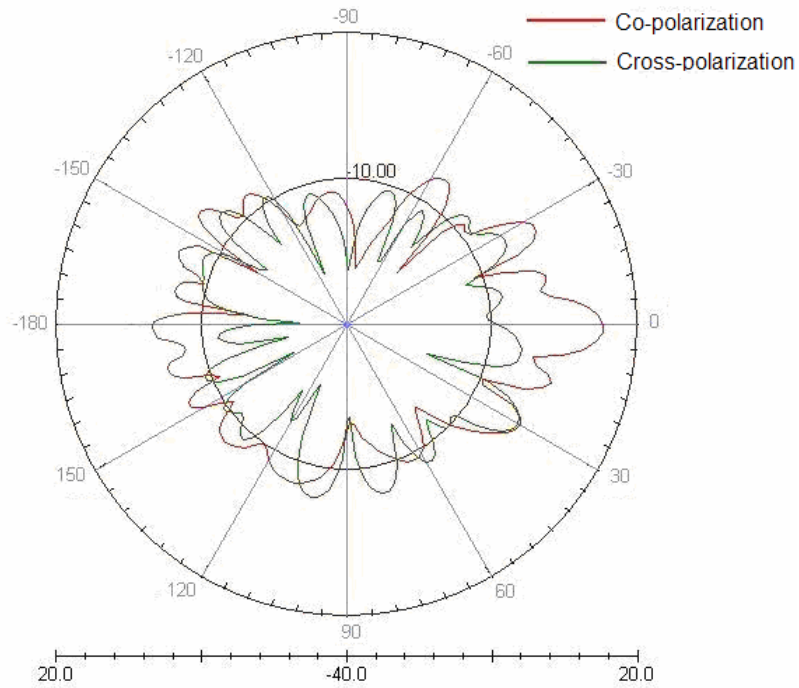


Figure 4.14 H-plane co-polarization and cross-polarization radiation patterns of the final design (10.5 GHz)

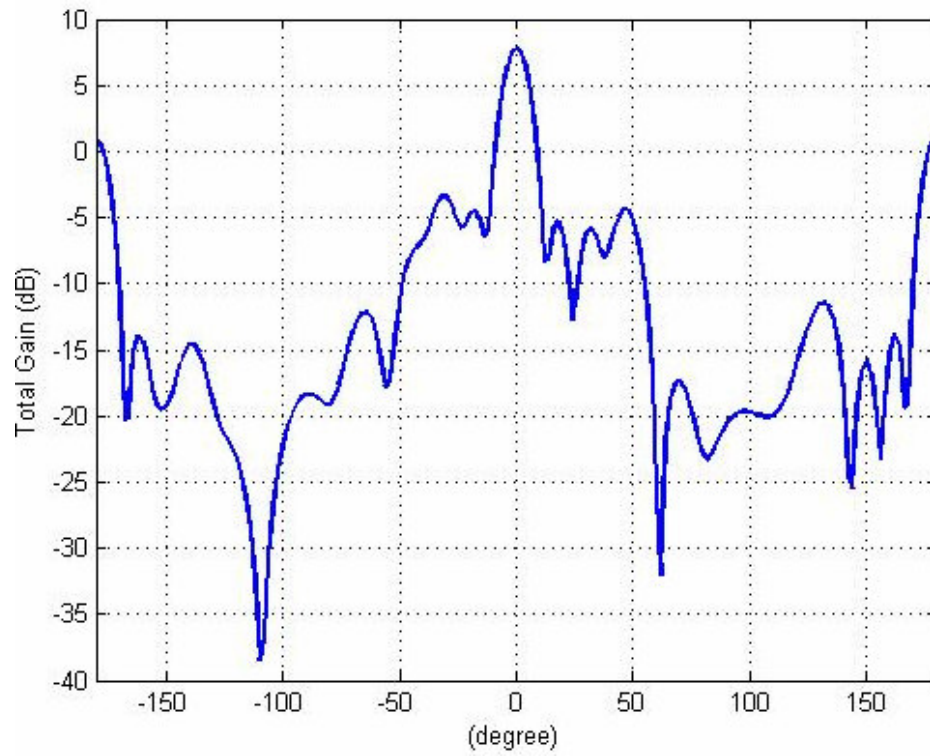


Figure 4.15 E-plane pattern of the final design (8.5 GHz)

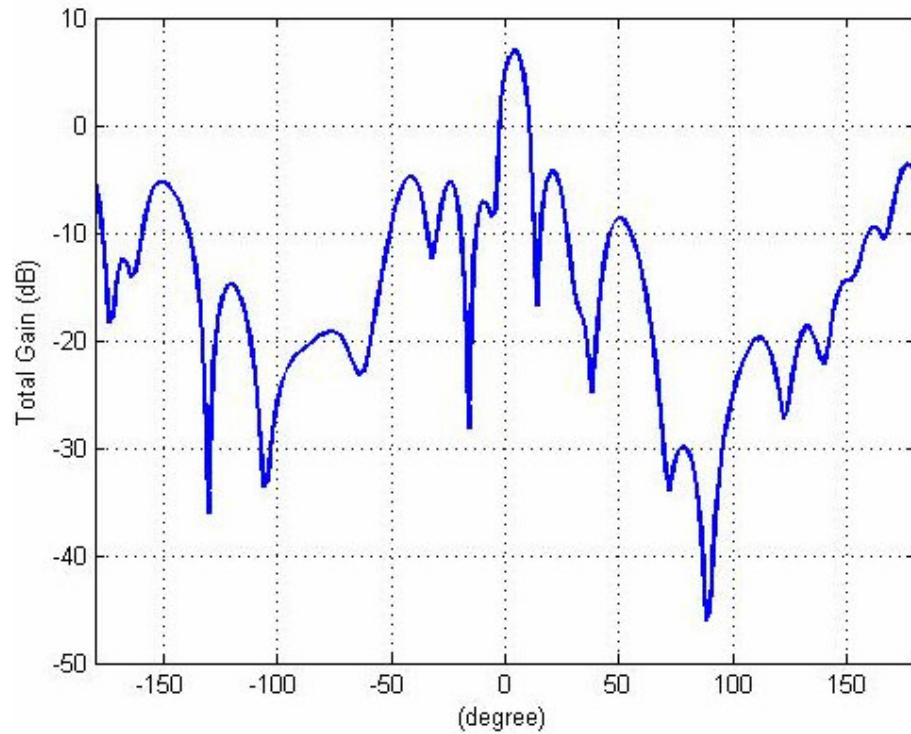


Figure 4.16 E-plane pattern of the final design (9.5 GHz)

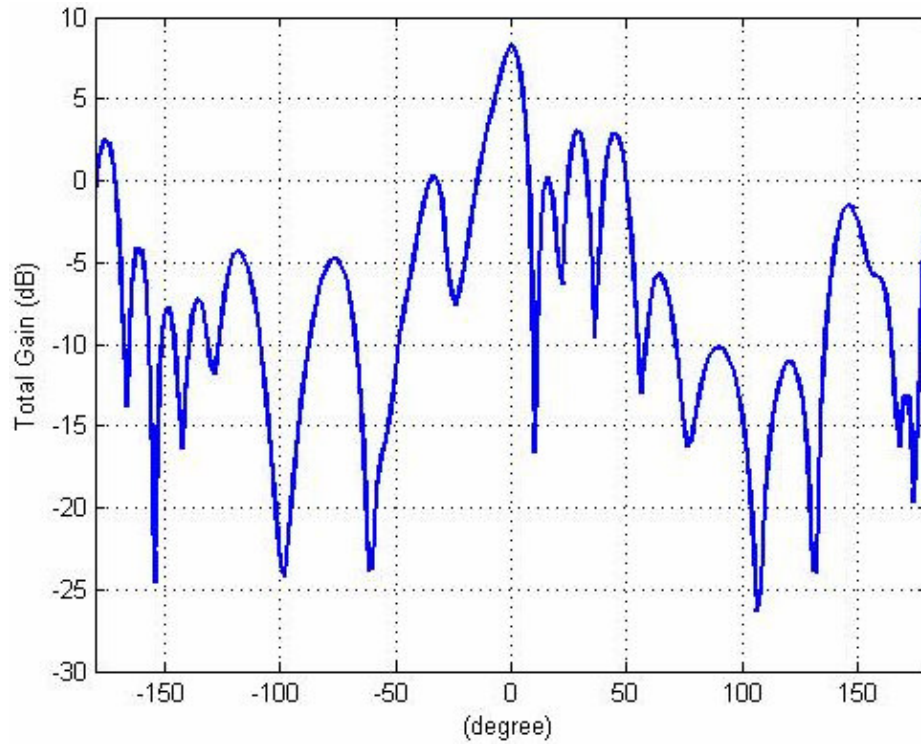


Figure 4.17 E-plane pattern of the final design (10.5 GHz)

Table 4.2 Half-power beamwidth of the final design in 8.5-10.5 GHz frequency band

Frequency of Operation	3-dB Beamwidth
8.5 GHz	11°
9.0 GHz	10°
9.5 GHz	10°
10.0 GHz	9°
10.5 GHz	9°

Table 4.3 Side lobe and grating lobe levels of the final design in 8.5-10.5 GHz frequency band

Frequency of Operation	Side Lobe Level	Grating Lobe Level
8.5 GHz	16 dB	15 dB
9.0 GHz	13 dB	14 dB
9.5 GHz	13 dB	12 dB
10.0 GHz	11 dB	10 dB
10.5 GHz	11 dB	8 dB

4.5 An Improved Array Design

Vivaldi antenna parameters were observed regarding their effects on array radiation pattern as well as single antenna return loss. Based on the results of single element study, another single Vivaldi antenna was designed and its array performance was investigated. The single element and the array performance of the mentioned design were satisfactory. It was also observed in the array design section that an antenna with a comparable single element performance and an improved array pattern could be designed with an increase in slot width and taper length. Thus, the second antenna is designed with a slot width of $W_{SL} = 1.0$ mm and a taper length of $L = 63$ mm. The linear array design of 8-element described above is also constructed with the second antenna.

The single element return loss response and array radiation pattern for the second antenna design are observed. Figure 4.18 and Figure 4.19 below gives the simulated single element return loss response and radiation pattern of the second design compared with the first antenna at 9.5 GHz and the radiation patterns at 8.5 GHz and 10.5 GHz in Figure 4.20 through Figure 4.28.

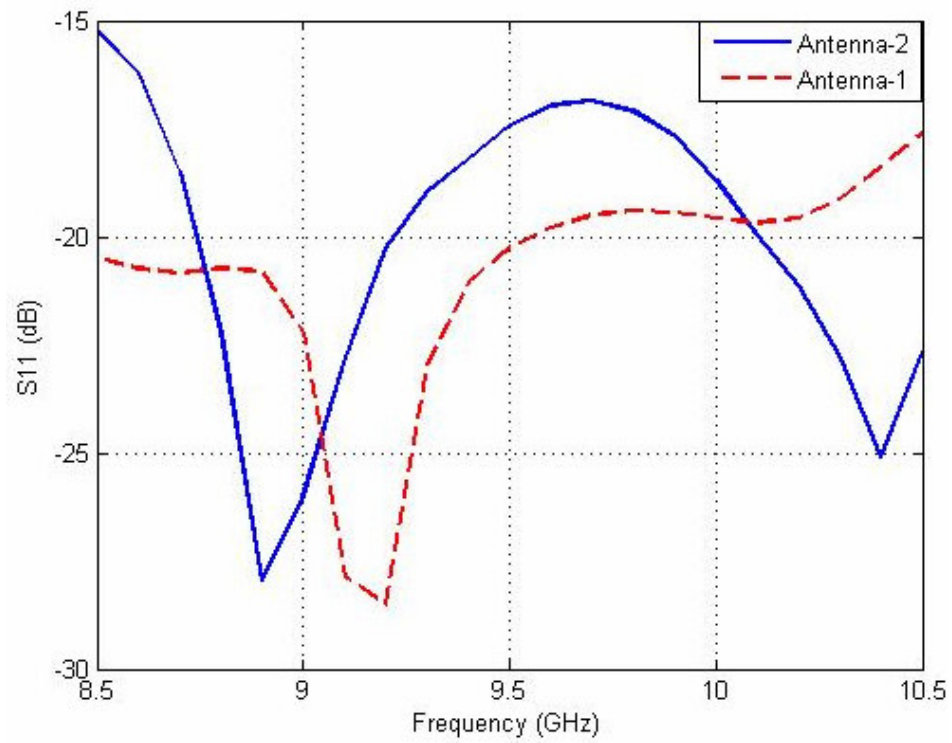


Figure 4.18 Return loss response of the second antenna model

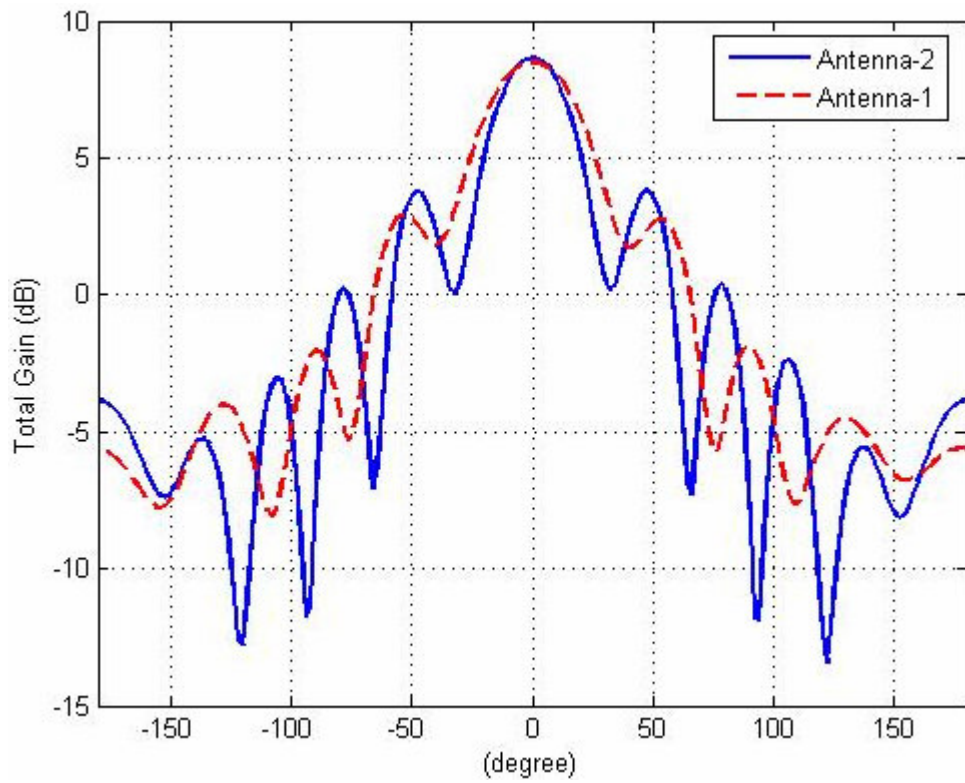


Figure 4.19 H-plane radiation patterns of first and second antenna designs (f = 9.5 GHz)

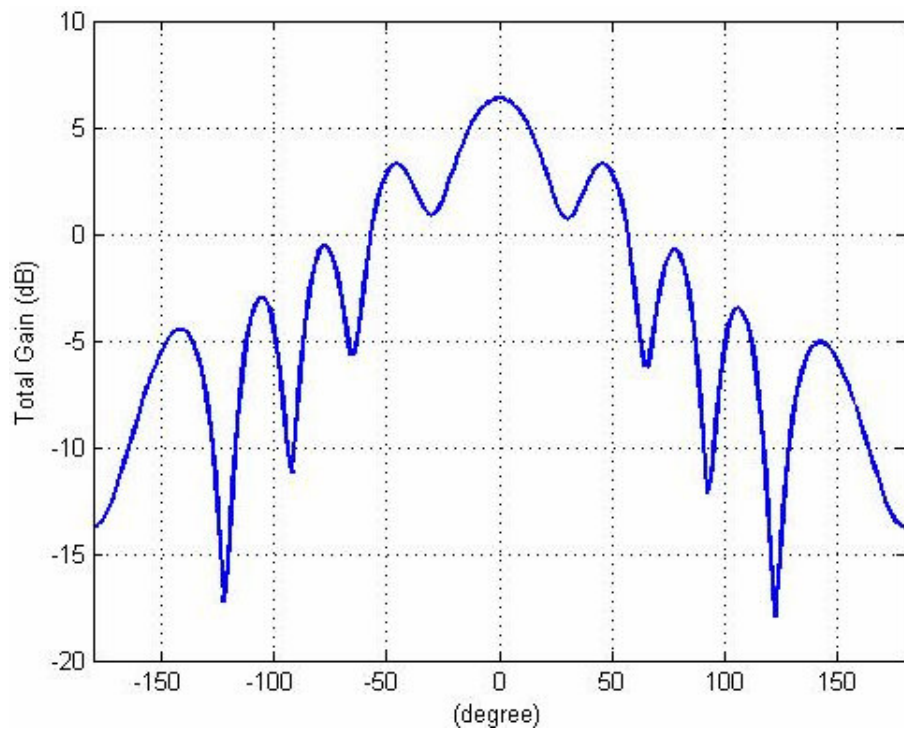


Figure 4.20 H-plane total radiation pattern of the second antenna (8.5 GHz)

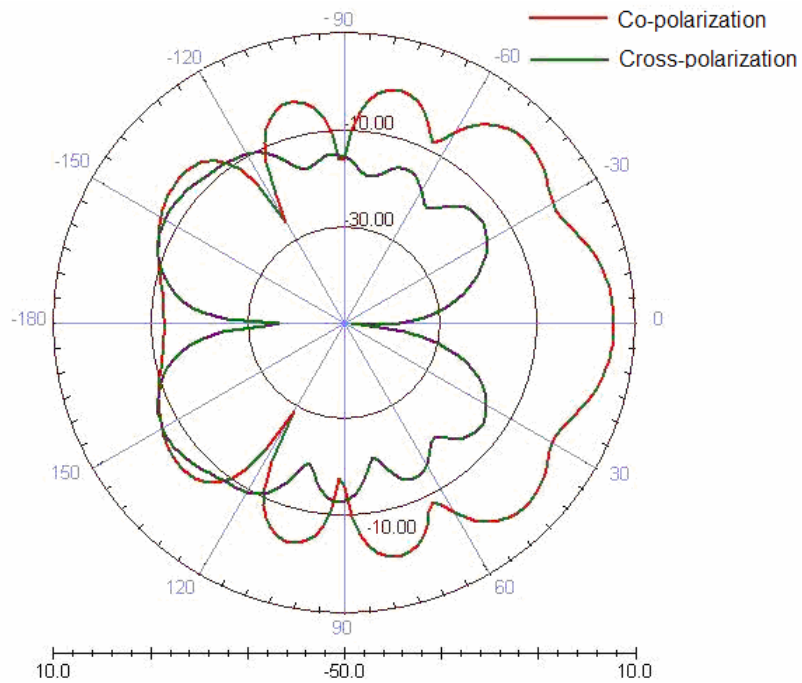


Figure 4.21 H-plane co-polarization and cross-polarization radiation patterns of the second antenna (8.5 GHz)

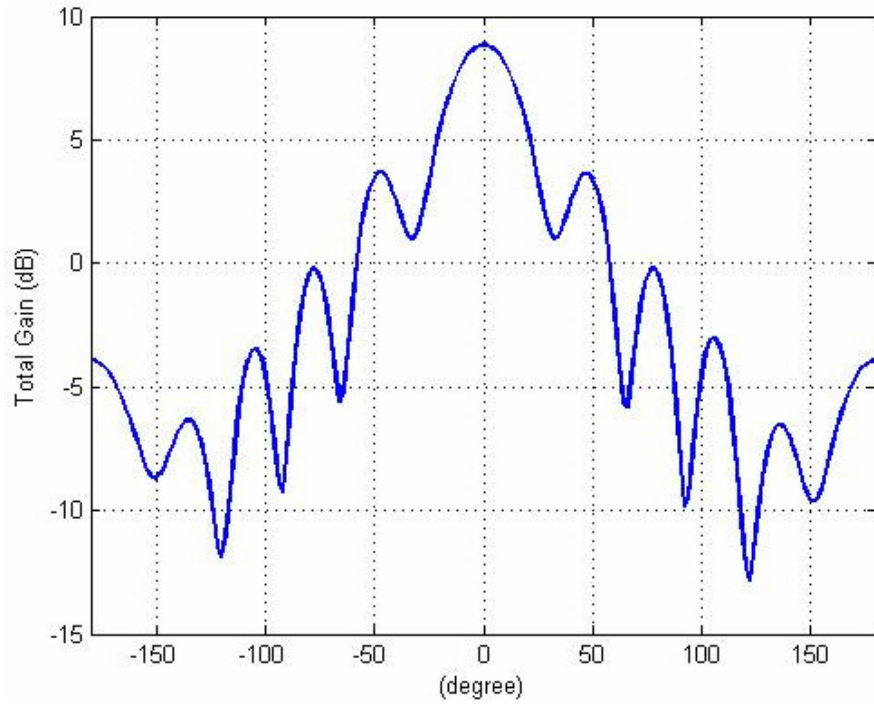


Figure 4.22 H-plane total radiation pattern of the second antenna (9.5 GHz)

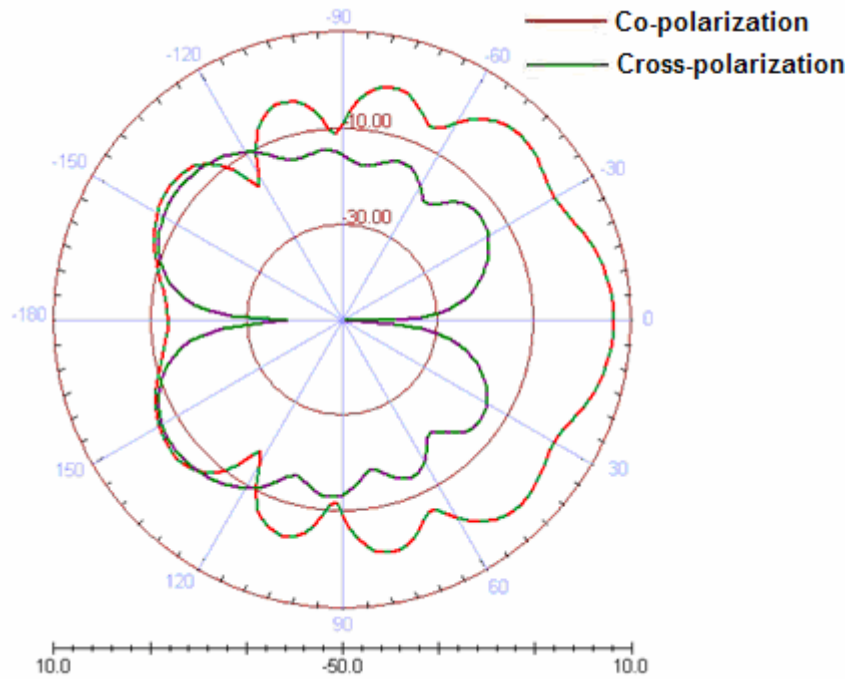


Figure 4.23 H-plane co-polarization and cross-polarization radiation patterns of the second antenna (9.5 GHz)

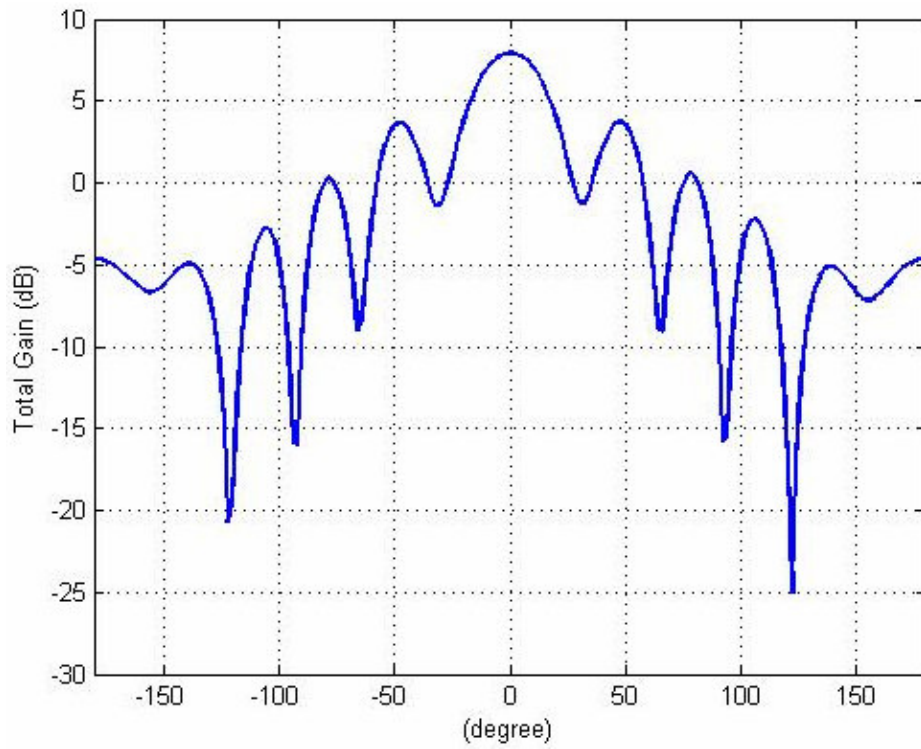


Figure 4.24 H-plane total radiation pattern of the second antenna (10.5 GHz)

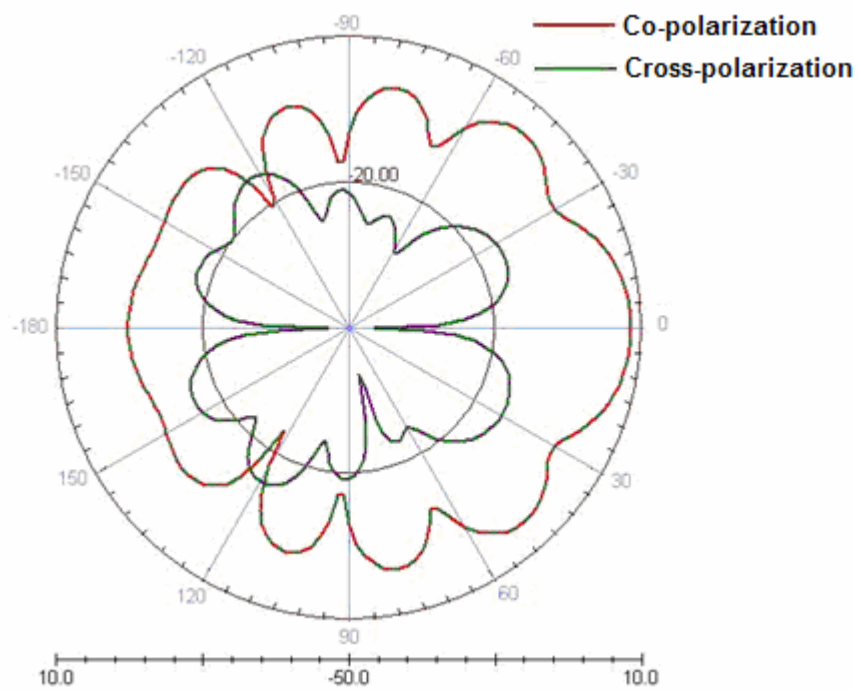


Figure 4.25 H-plane co-polarization and cross-polarization radiation patterns of the second antenna (10.5 GHz)

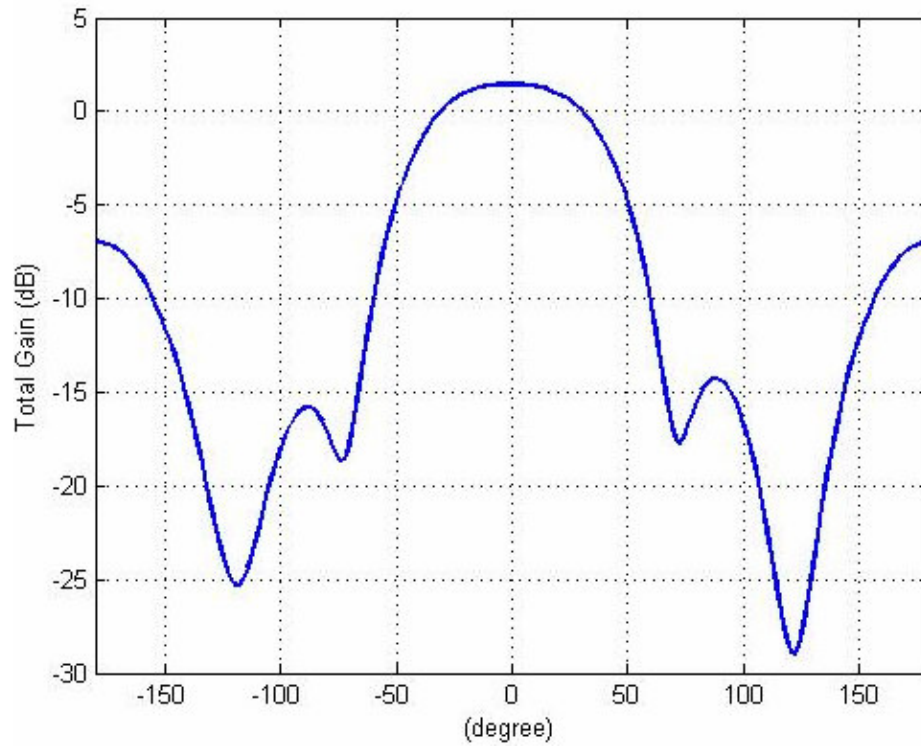


Figure 4.26 E-plane pattern of the second antenna (8.5 GHz)

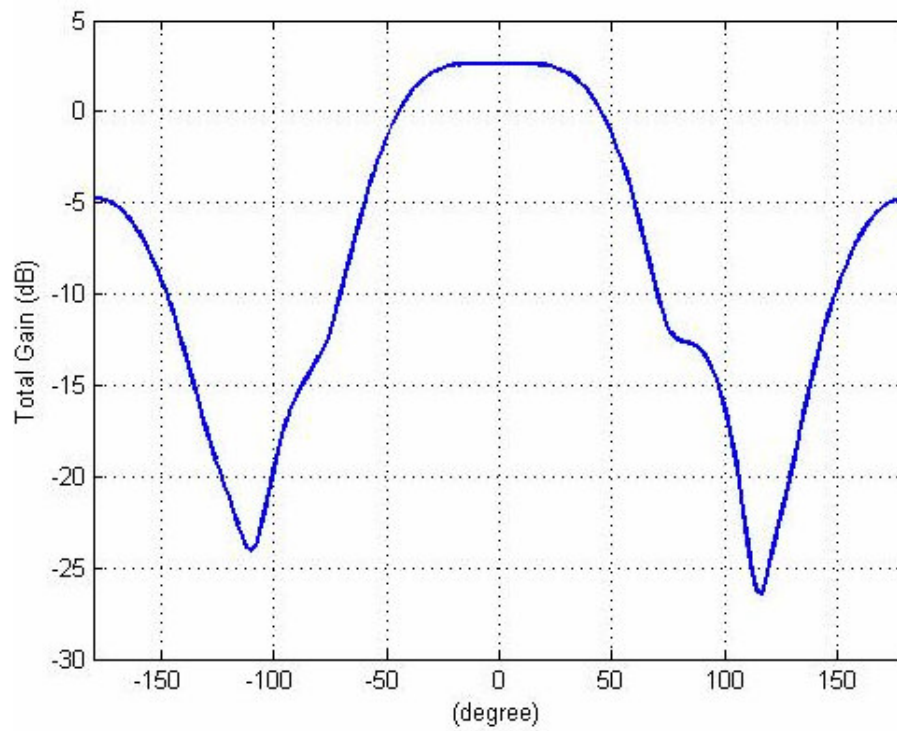


Figure 4.27 E-plane pattern of the second antenna (9.5 GHz)

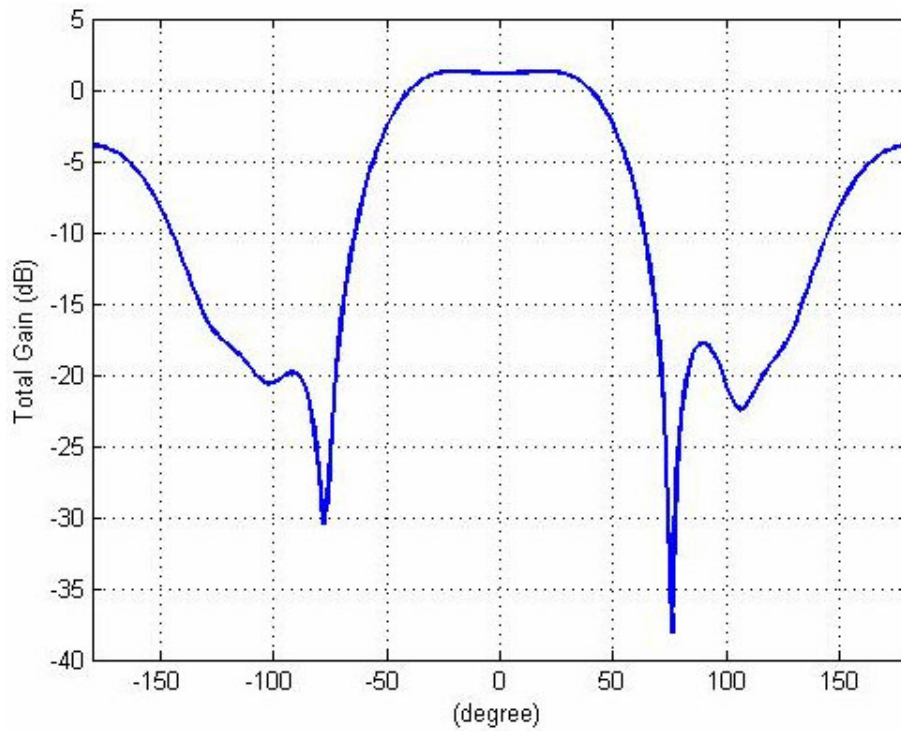


Figure 4.28 E-plane pattern of the second antenna (10.5 GHz)

The return loss response of the first antenna design is better along the frequency band, especially in the lower band, compared to that of the second antenna design. However, the return loss response of the second antenna is still acceptable as seen in Figure 4.18. Besides, the second antenna is more directive with its half-power beamwidth of $\Delta\phi_{3\text{dB}} = 36^\circ$ at 9.5 GHz compared to the first antenna as seen in Figure 4.19.

The radiation pattern of 8-element uniform linear array constructed with the second antenna design is shown in Figure 4.29

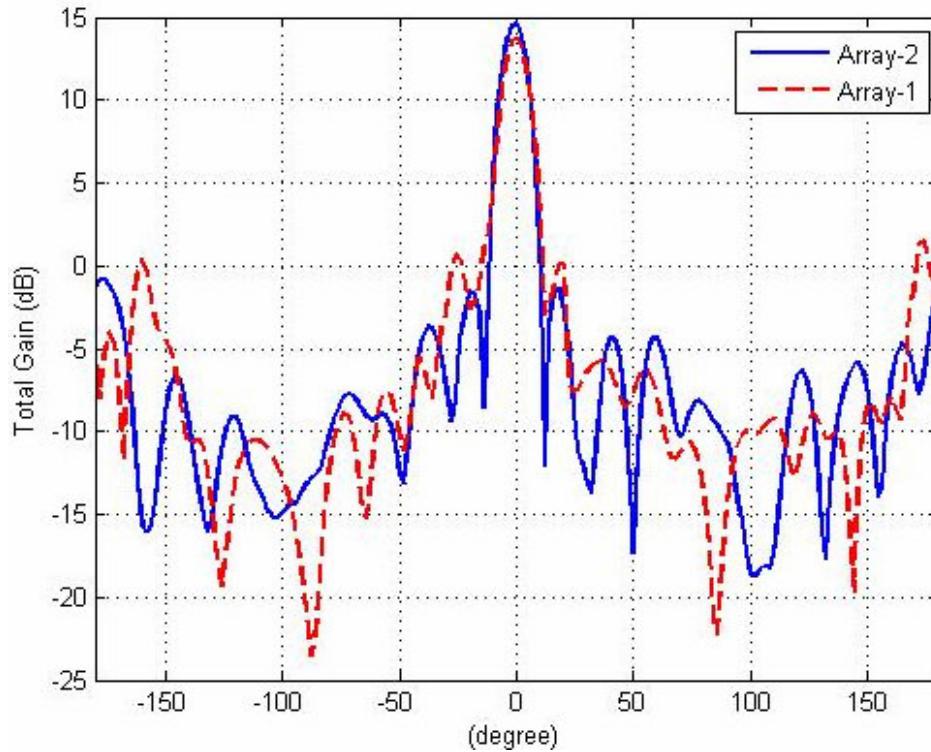


Figure 4.29 H-plane patterns of arrays with the first and second antennas (f = 9.5 GHz)

The array with the second antenna has side lobe levels of $R = 17$ dB, improved by nearly 4 dB compared to that of with the first antenna. The second antenna improved the half power beamwidth also. The beamwidth of the second array is $\Delta\phi_{3dB} = 10^\circ$ where the first array has a beamwidth of $\Delta\phi_{3dB} = 12^\circ$.

Dolph-Chebyshev array is formed in order to improve the half-power beamwidth with the same side lobe level and improve the side lobe level with the same half power beamwidth. The Chebyshev polynomial coefficients for $SLL = 17$ dB and for $SLL = 20$ dB are given below respectively.

1.0000 0.9117 1.1491 1.2833 1.2833 1.1491 0.9117 1.0000

1.0000 1.1386 1.5091 1.7244 1.7244 1.5091 1.1386 1.0000

Dolph-Chebyshev arrays with the second Vivaldi antenna design are given below for the side lobe levels of $SLL = 17$ dB and $SLL = 20$ dB respectively in Figure 4.30 and Figure 4.31.

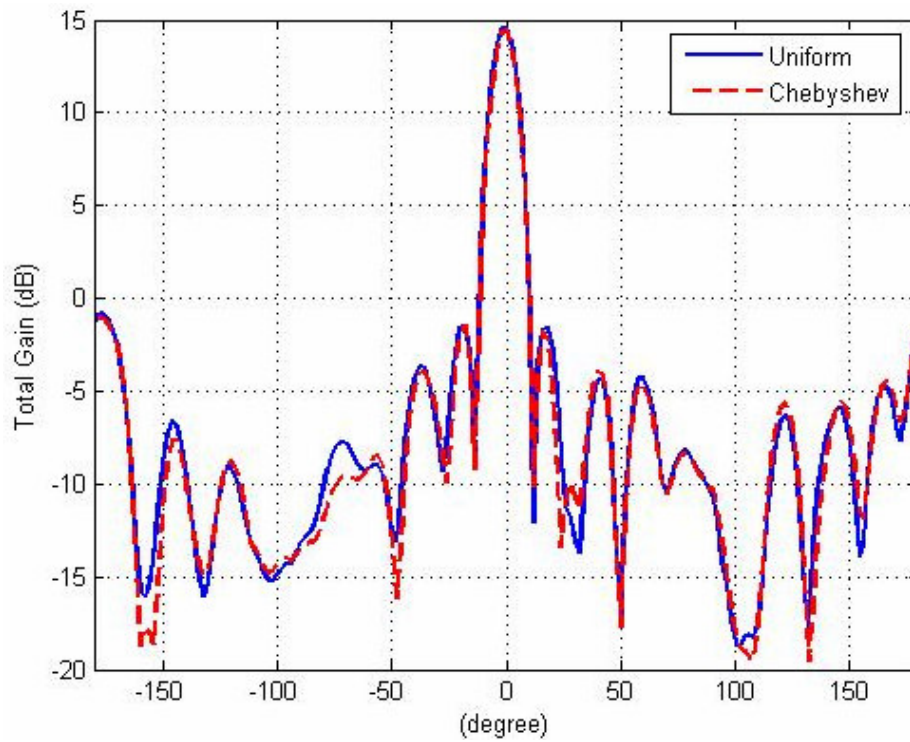


Figure 4.30 H-plane radiation patterns of Dolph-Chebyshev and uniform arrays (SLL = 17 dB) ($f = 9.5$ GHz)

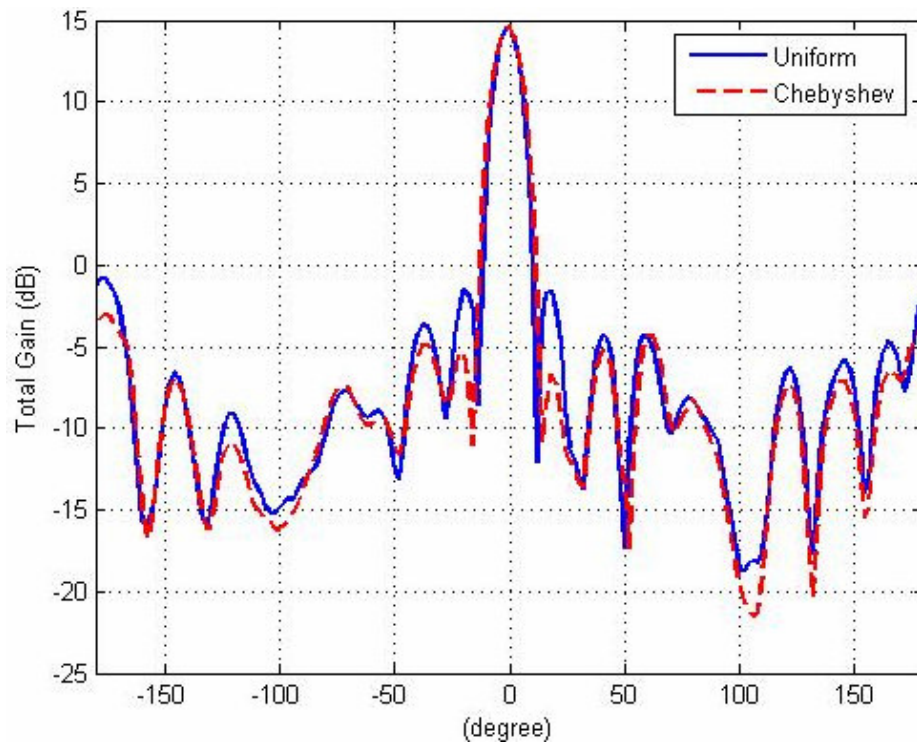


Figure 4.31 H-plane radiation patterns of Dolph-Chebyshev and uniform arrays (SLL = 20 dB) ($f = 9.5$ GHz)

Dolph-Chebyshev array designed for the same side lobe level with the uniform array, that is $SLL = 17$ dB has an improved half-power beamwidth. It has a beamwidth of $\Delta\phi_{3dB} = 8^\circ$ where the uniform has $\Delta\phi_{3dB} = 10^\circ$. Besides, Dolph-Chebyshev array designed for the side lobe level of $SLL = 20$ dB has a deteriorated half power beamwidth, $\Delta\phi_{3dB} = 11^\circ$ which is still acceptable.

The radiation patterns of Dolph-Chebyshev array in 8.5-10.5 GHz frequency band with the side lobe level of 17 dB at 9.5 GHz are given below in Figure 4.32 through Figure 4.40.

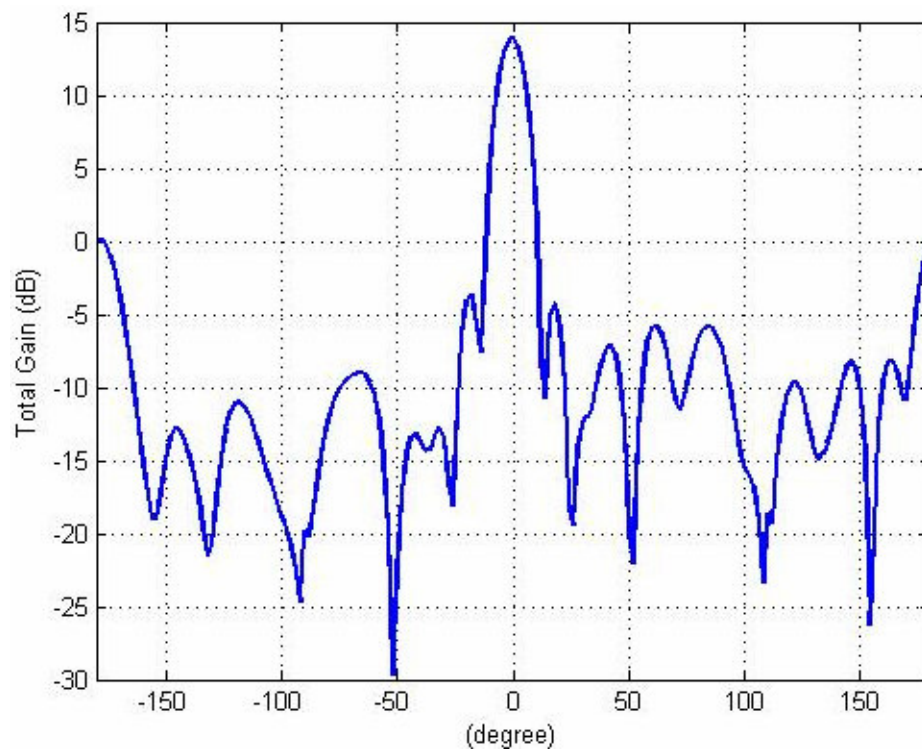


Figure 4.32 H-plane co-polarization radiation pattern of the second array (8.5 GHz)

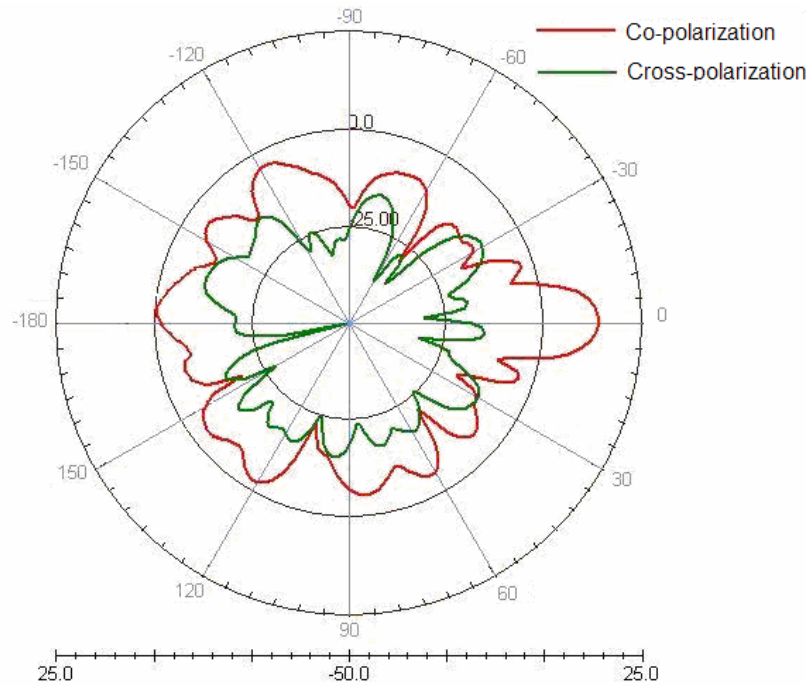


Figure 4.33 H-plane co-polarization and cross-polarization radiation patterns of the second array (8.5 GHz)

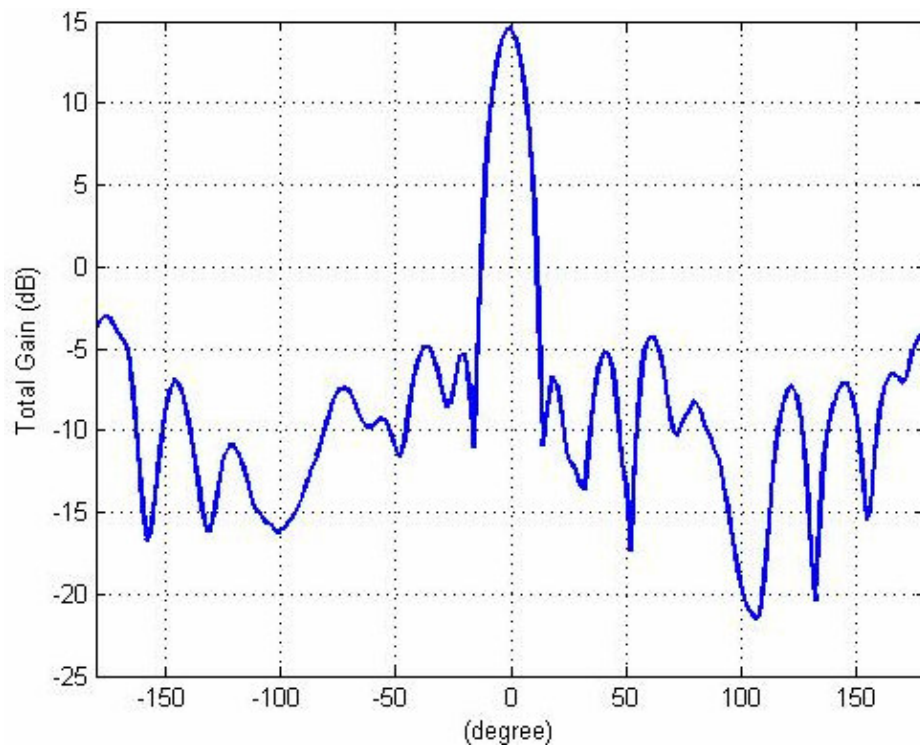


Figure 4.34 H-plane co-polarization radiation pattern of the second array (9.5 GHz)

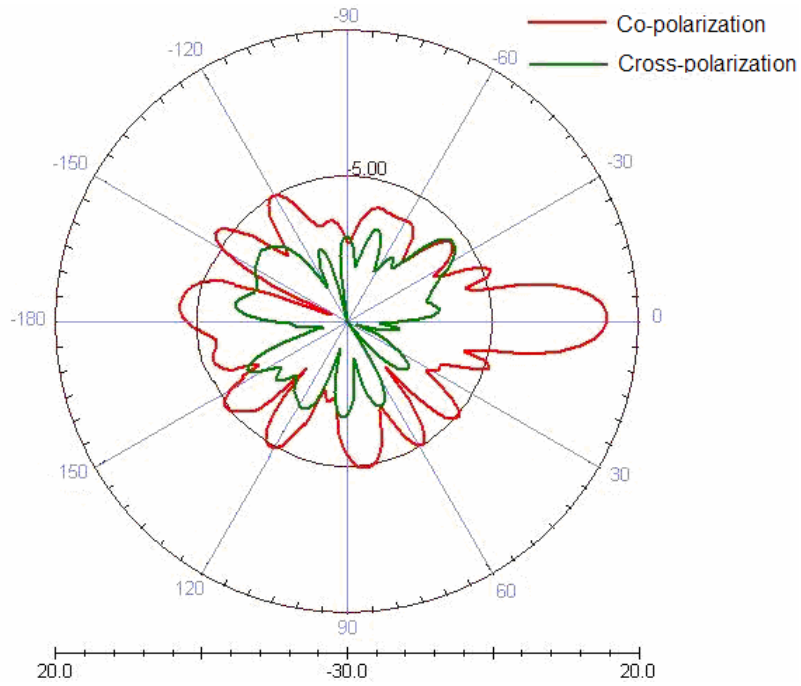


Figure 4.35 H-plane co-polarization and cross-polarization radiation patterns of the second array (9.5 GHz)

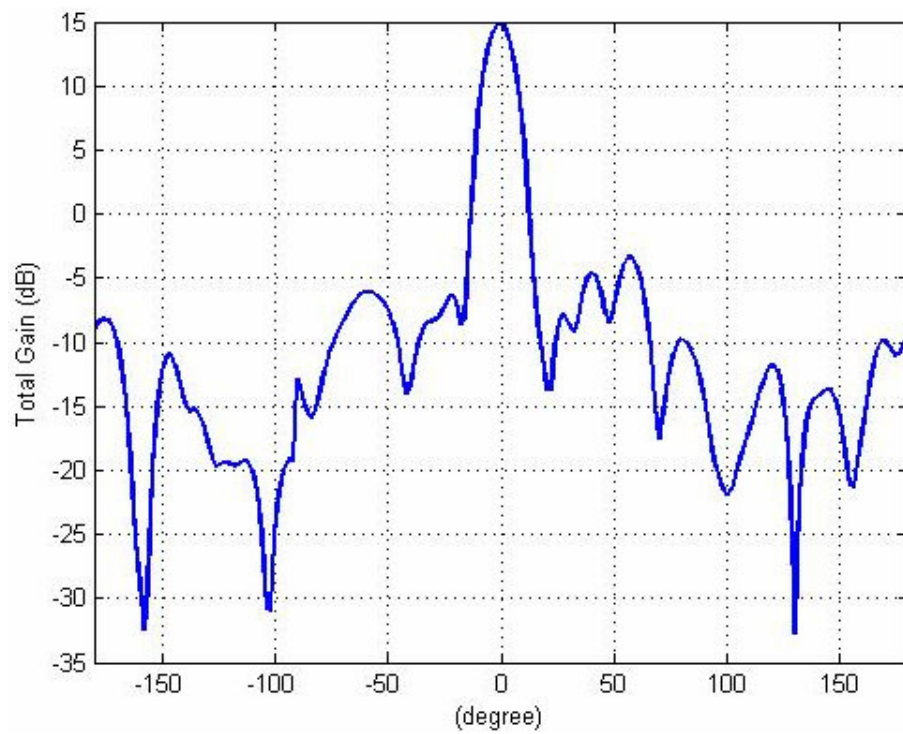


Figure 4.36 H-plane co-polarization radiation pattern of the second array (10.5 GHz)

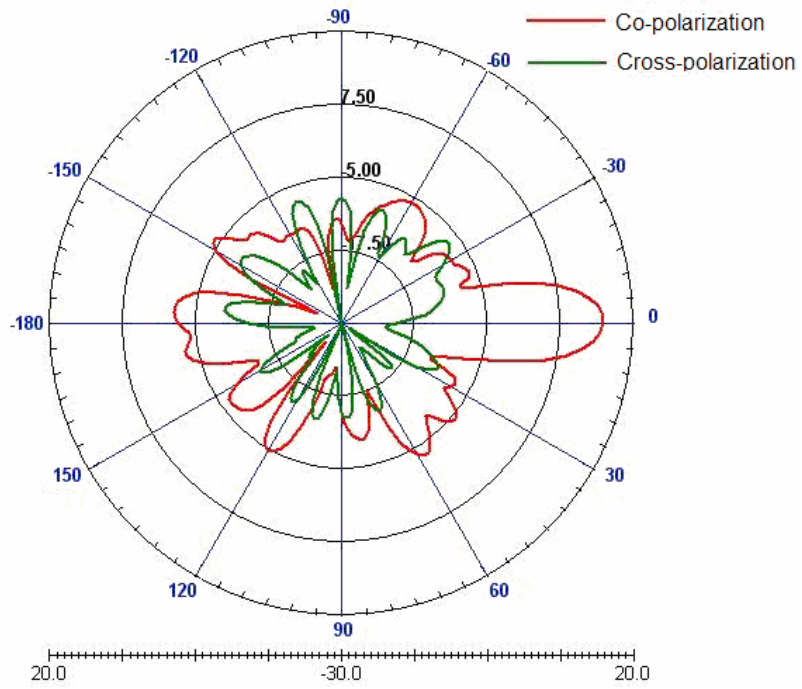


Figure 4.37 H-plane co-polarization and cross-polarization radiation patterns of the second array (10.5 GHz)

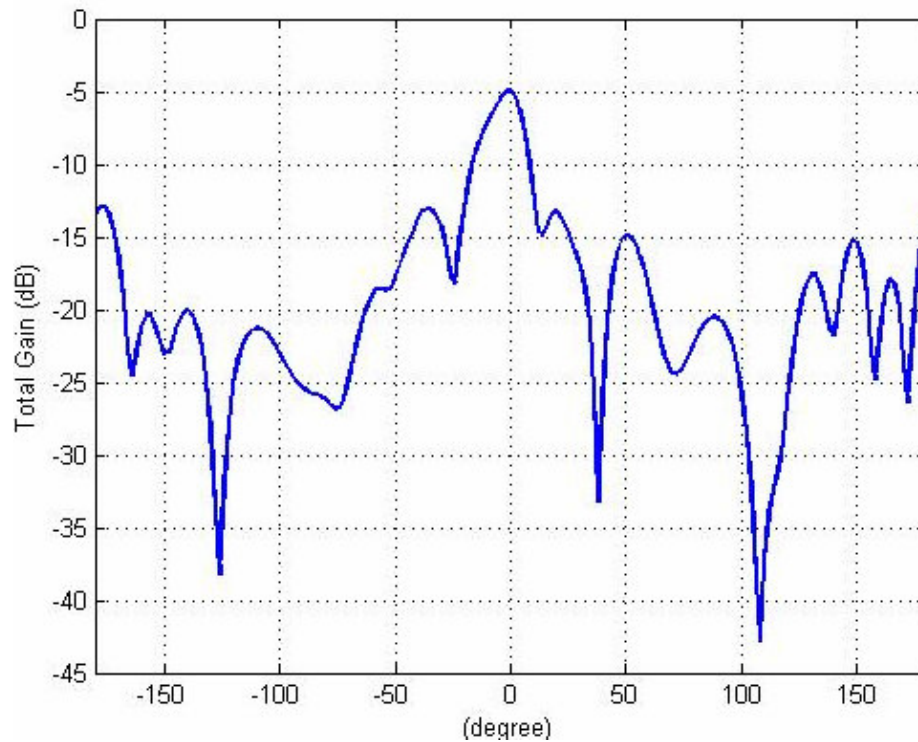


Figure 4.38 E-plane pattern of the second array (8.5 GHz)

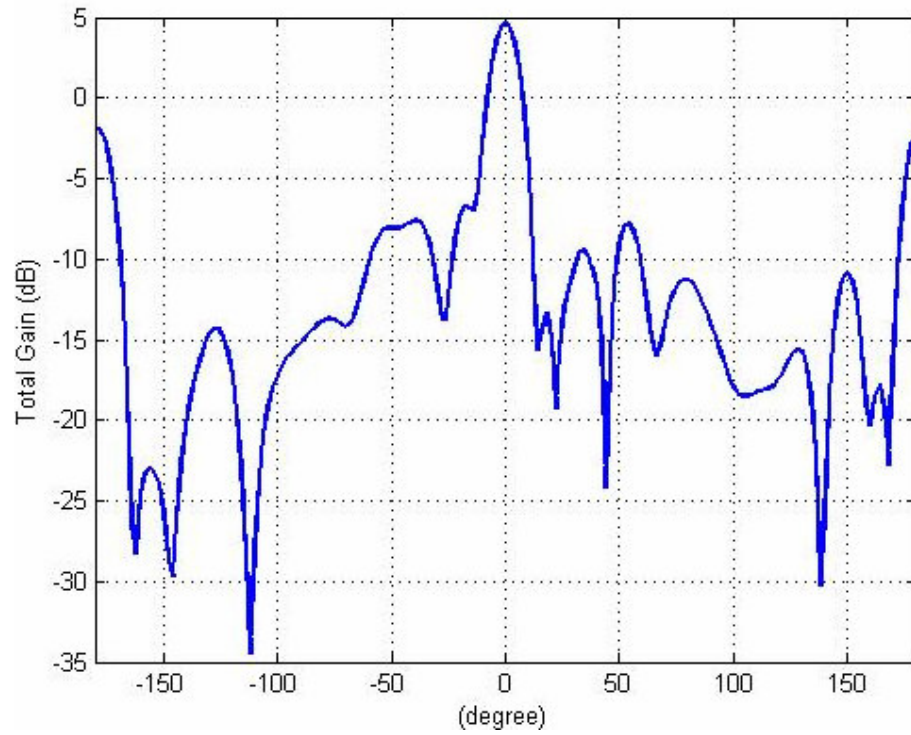


Figure 4.39 E-plane pattern of the second array (9.5 GHz)

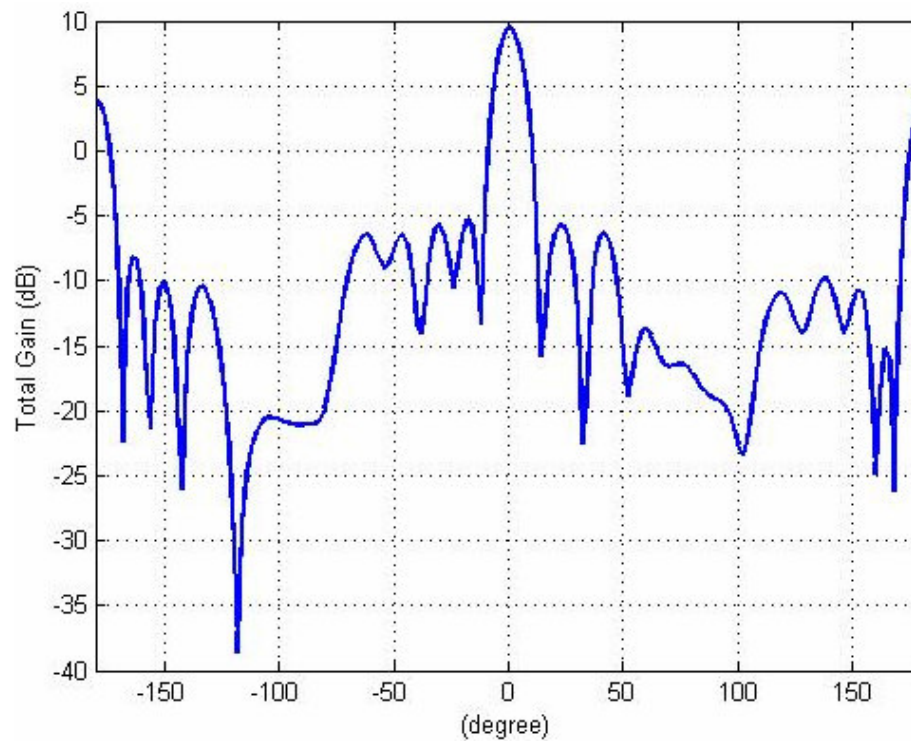


Figure 4.40 E-plane pattern of the second array (10.5 GHz)

Table 4.4 Half-power beamwidth of Dolph-Chebyshev array with R = 20 dB in 8.5-10.5 GHz frequency band

Frequency of Operation	3-dB Beamwidth
8.5 GHz	12°
9.0 GHz	11°
9.5 GHz	11°
10.0 GHz	10°
10.5 GHz	10°

Table 4.5 Side lobe and grating lobe levels of Dolph-Chebyshev array with R = 20 dB in 8.5-10.5 GHz frequency band

Frequency of Operation	Side Lobe Level	Grating Lobe Level
8.5 GHz	17 dB	16 dB
9.0 GHz	17 dB	17 dB
9.5 GHz	18 dB	16 dB
10.0 GHz	20 dB	16 dB
10.5 GHz	18 dB	16 dB

CHAPTER 5

FABRICATION AND MEASUREMENTS

The single element Vivaldi antennas and the array constructed with the second antenna are fabricated in Aselsan Inc. Laboratories. The fabrication process is explained early in this chapter. The fabricated antennas and the array are measured also in Aselsan Inc. and the measurement setup as well as the return losses and radiation patterns are given next. This chapter concludes with the comparison of simulation and measurement results.

5.1 Fabrication

Fabrication of both Vivaldi antennas is realized as three layer structures using printed circuit board technology. Each antenna is constructed on two 62 mils (1.575 mm) Rogers RT/duroid™ 5880 boards for which the detailed information is given in Appendix-C. Each board has the designed tapered slot on one side. Metallic layer on the other side of one of the boards is removed completely whereas the other board has the designed stripline on the other side. The two boards are bonded together forming a triplet structure with tapered slot sections on the top and bottom layers and stripline on the middle layer. Thus, a stripline fed three-layer structure is obtained. A 50 Ω SMA connector, Suhner™ 23 SMA 50-0-2, is used to feed the stripline. The center pin of the connector is soldered to the stripline before bonding the two boards. Bonding is realized using Loctite adhesive substance. If physical strength and lifetime of the antennas are important, the boards shall be bonded using special purpose bonding films at a temperature above 200°C. The final step of the antenna fabrication is to solder the outer pins of the connector to the slotline ground planes in order to realize ground connection of the feeding.

The array constructed with the second antenna and having better radiation pattern characteristics is also fabricated using Aselsan Inc. printed circuit board utilities. 8 single antennas of triplet structure are fabricated and bonded as explained above. The array structure is constructed bonding the single elements to a metallic backplane. The metallic backplane is used to reflect radiations in the opposite direction and improve forward radiation in this way as well as keep the single elements together.

The pictures of single element Vivaldi antennas and the array fabricated are given below in Figure 5.1 and Figure 5.2.



Figure 5.1 Fabricated Vivaldi antennas



Figure 5.2 Fabricated Vivaldi array with its backplane

5.2 Measurement Setup

The return loss responses and radiation patterns of the single element Vivaldi antennas and the array are measured. The reflections from the other objects and the ground plane shall be minimized in both measurements, especially radiation patterns, for more accurate results. Measurement setups for return loss response and radiation pattern are detailed below respectively.

5.2.1 Return Loss Response Measurement

The return loss response is measured to see the matching between an antenna and its feeding. This measurement, also known as S11 measurement, is done using a network analyzer and given in dB. Before the measurement, for which the setup is given in Figure 5.3, the network analyzer is calibrated in the required frequency band connecting open, short and load connectors to the Port-1 of the analyzer. The antenna is connected to the same port next and the return loss response of the antenna is obtained in dB through one port measurement with the calibrated network analyzer.

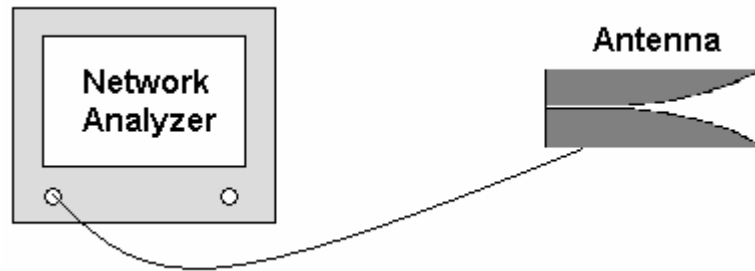


Figure 5.3 Return loss measurement setup for the single antenna

The return loss response of the array is measured in the same way. Power dividers are used between the network analyzer and the array different from the measurement setup of Figure 5.3 to feed all the single elements at the same time. Three identical 4-way power dividers, Narda™ 4326B-4 for which the detailed information is given in Appendix-C, is used in this work. Two ports of the first power divider are terminated with 50Ω loads to prevent reflections. It shall also be noted that the cables connecting the power divider and the array elements are to be identical in length and characteristics to ensure a proper measurement. Minibend™ L-10 cables are used in this work. The pictures of the array with the power dividers and the plot of return loss measurement setup for the array are given below.

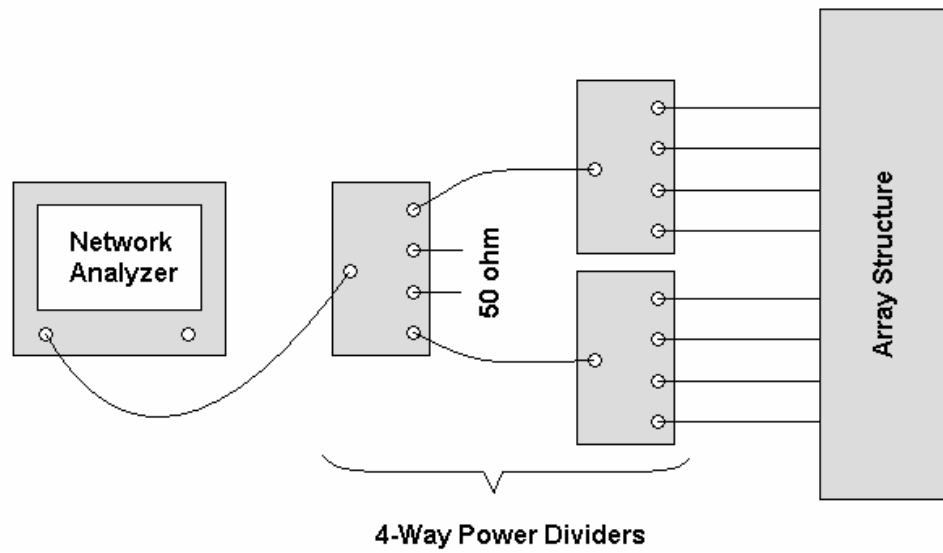


Figure 5.4 Return loss measurement setup for the array

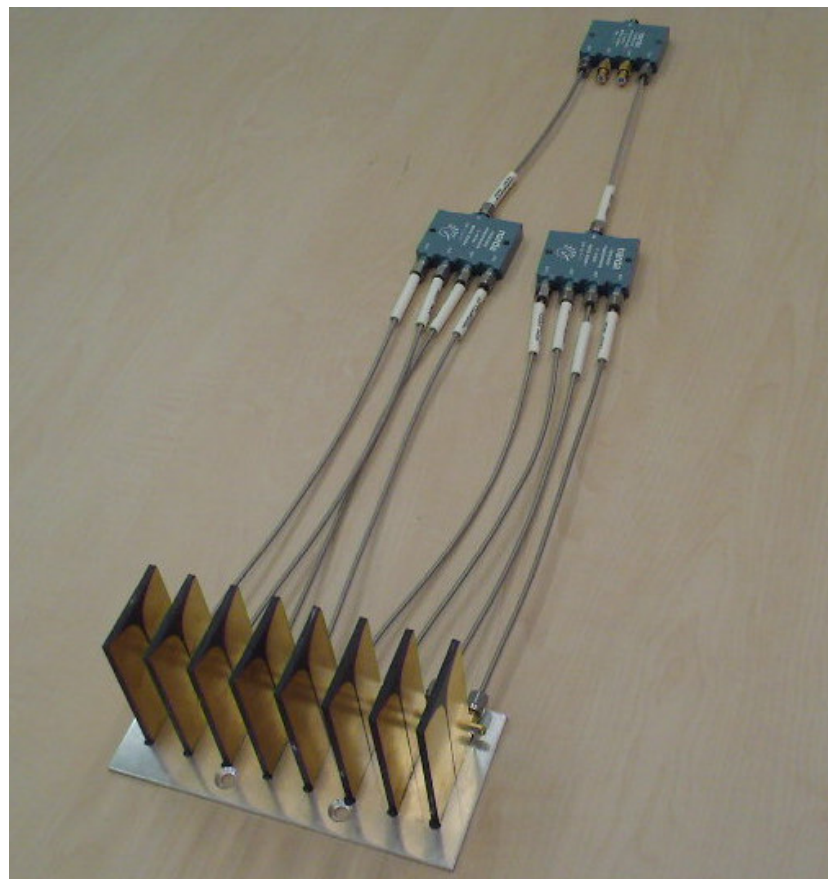


Figure 5.5 Array structure with power dividers

The power divider in the first block and the dividers in the second block cause 6 dB losses resulting in a total of 12 dB loss in each antenna input. However, the total structure with the cables is observed to have 13.4 dB loss at the first array element input. This input is taken as reference and the losses at the array element inputs relative to this reference are measured using network analyzer and drawn below in Figure 5.6. It is observed that the maximum power difference between the ports of the power dividers is 3.3 dB through 2-18 GHz band and about 2 dB in the operating bandwidth of 8.5-10.5 GHz.

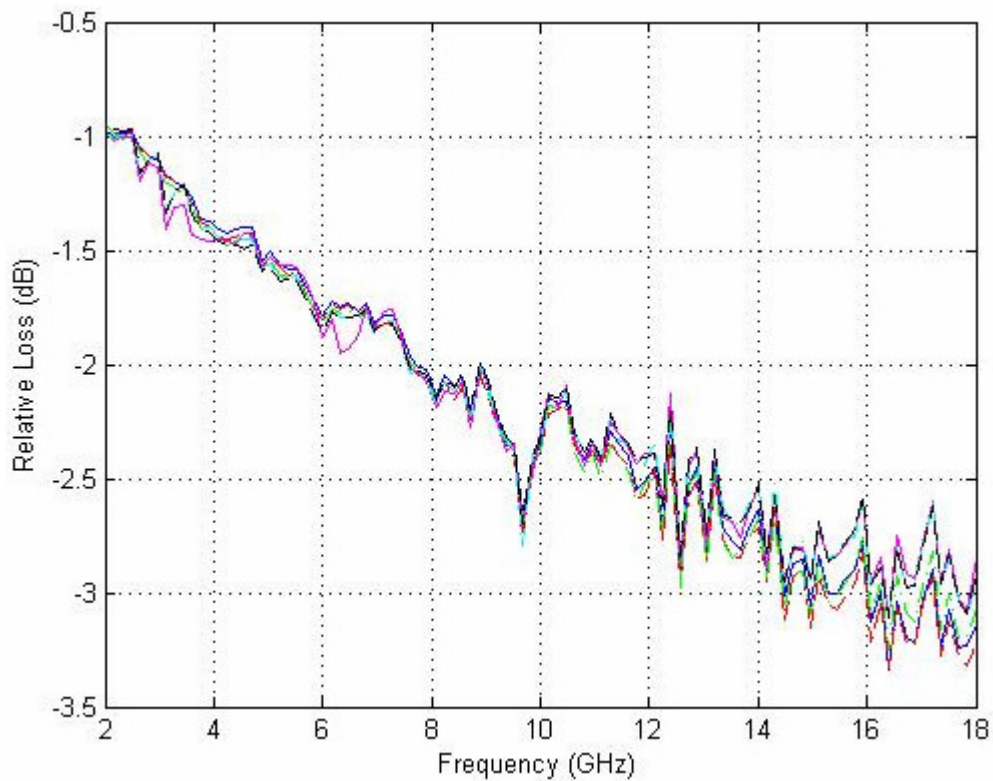


Figure 5.6 Measured insertion loss of 4-way power divider

The return loss response measurements of the single Vivaldi antennas and the array are realized in Aselsan Inc. RF Design Laboratories.

5.2.2 Radiation Pattern Measurement

A graphical representation of the field magnitude at a fixed distance from an antenna as a function of direction is known as antenna pattern [31]. A standard and the antenna to be tested are included in the test setup. The standard antenna is used in transmitting mode and the antenna under test is used in receiving mode usually, as if the reciprocal is also acceptable. Incident wavefront illuminated by the source antenna must be uniform in magnitude and phase over the surface of the antenna under test. Moreover, the source antenna should have a sufficient beamwidth to illuminate the whole antenna under test.

Pattern measurements may be made in an outdoor antenna range or an anechoic chamber. Reflections from the ground and nearby objects in an outdoor range may result in considerable errors, nulls and peaks due to reflections, in pattern measurements. Thus, an anechoic chamber, a reflection free room covered by absorbers, is more advantageous for pattern measurements.

Pattern characteristics are measured in the anechoic chamber of Aselsan Inc., for which the detailed views are given in Appendix-D. The mentioned anechoic chamber is a tapered one in the shape of a pyramidal horn. It tapers from the small source end to a large rectangular test region covered with high quality absorbing material on the side walls, floor and ceiling. An azimuth positioner, Scientific Atlanta 5023 Positioner, holds up the test antenna whereas a polarization positioner, Scientific Atlanta 56060 Polarization Positioner, holds up the standard transmitter antenna in this tapered anechoic chamber [32].

The radiation pattern measurements are done on the plane of polarization and the plane perpendicular to the polarization. The plane of polarization, also known as E-plane, is vertical in case of a vertically polarized Vivaldi antenna. H-plane is the plane perpendicular to the polarization and it is the horizontal plane in case of a vertically polarized Vivaldi antenna.

5.3 Measurement Results

The measurements described above are performed for single Vivaldi antennas and the array fabricated. The measurement results are given below in two parts: return loss measurement results and pattern measurement results.

5.3.1 Return Loss Measurement Results

Return loss response measurement results compared to the simulation results for Vivaldi Antenna-1 and Vivaldi Antenna-2 in 8.5-10.5 GHz and 2-18 GHz frequency bands are given in Figure 5.7 through Figure 5.10. Simulations and measurements in 2-18 GHz band are performed in order to determine the complete operating bandwidth of the antennas.

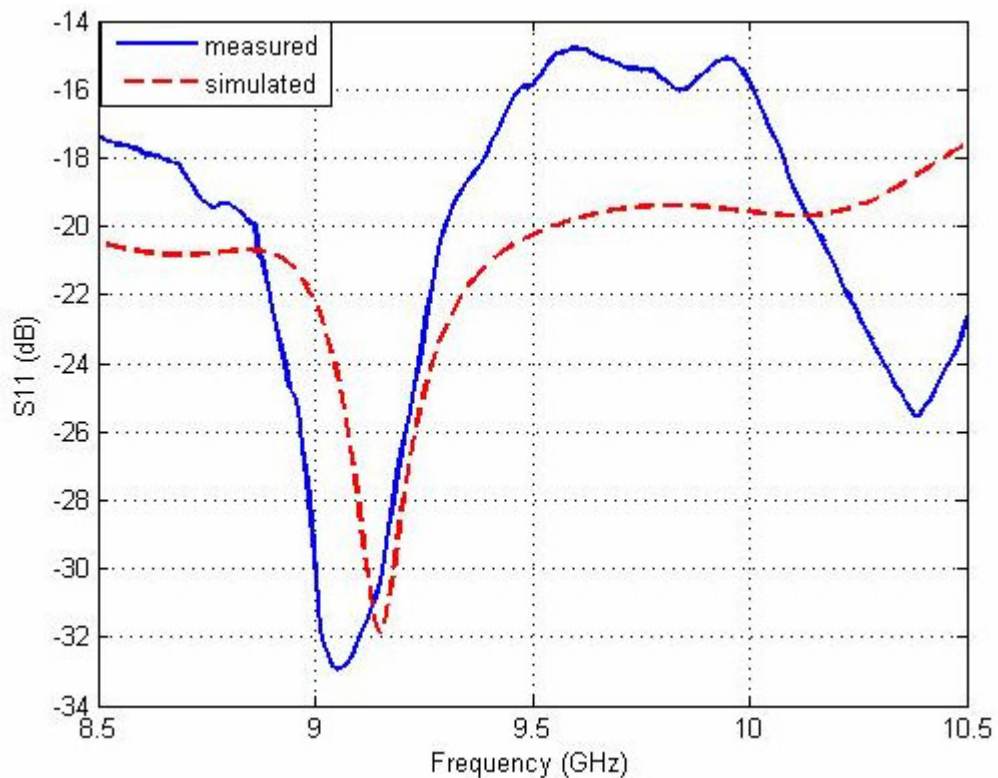


Figure 5.7 Measured and simulated return loss responses of Antenna-1 (8.5-10.5 GHz)

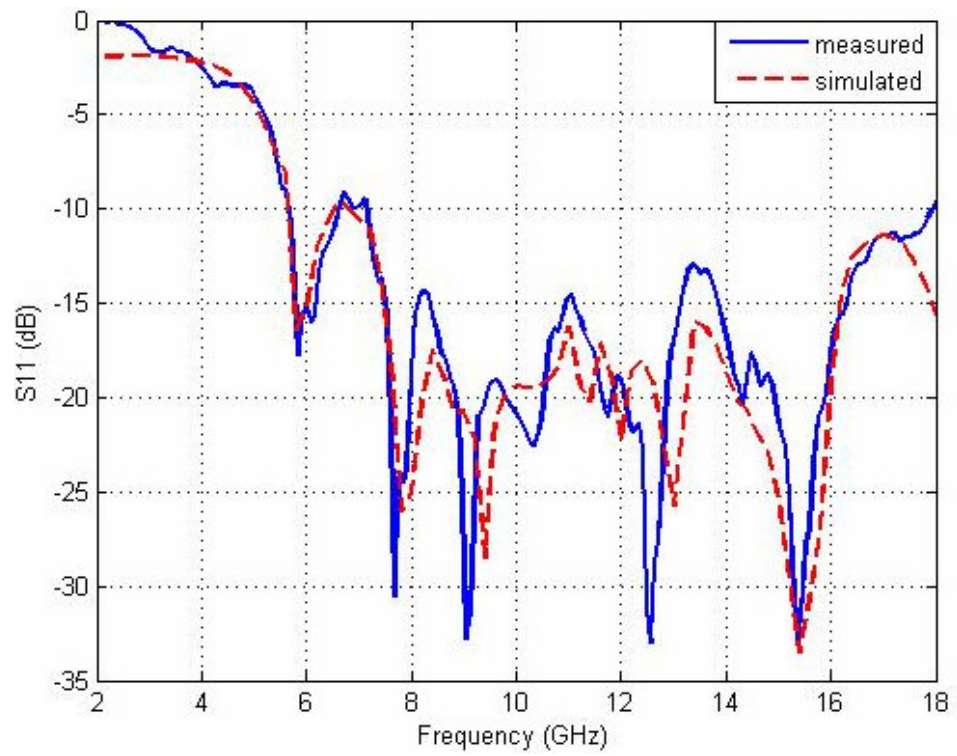


Figure 5.8 Measured and simulated return loss responses of Antenna-1 (2-18 GHz)

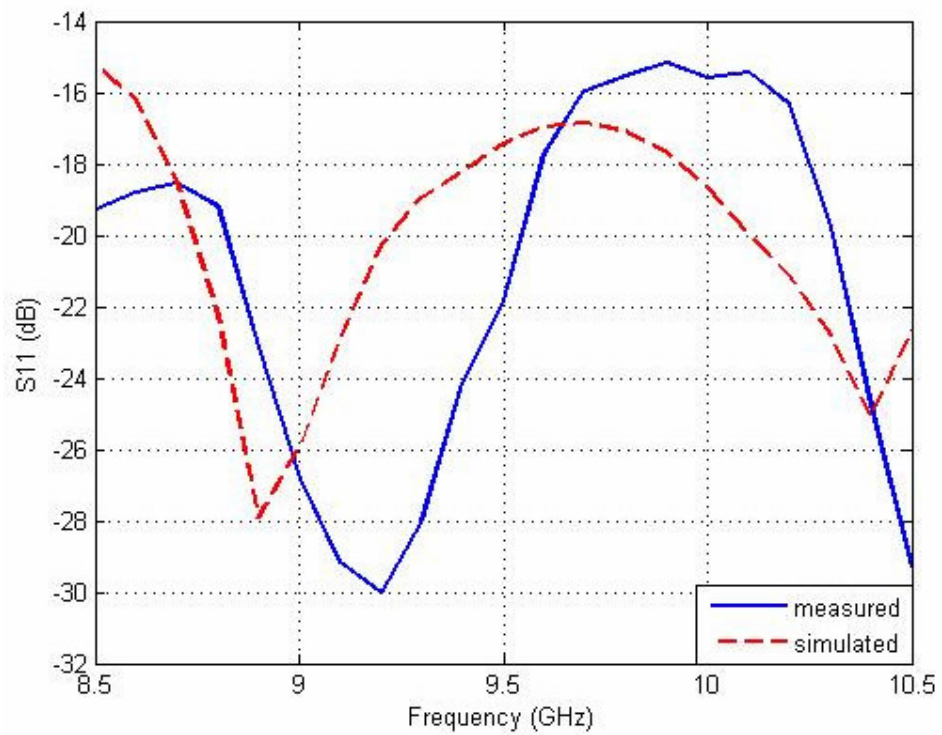


Figure 5.9 Measured and simulated return loss responses of Antenna-2 (8.5-10.5 GHz)

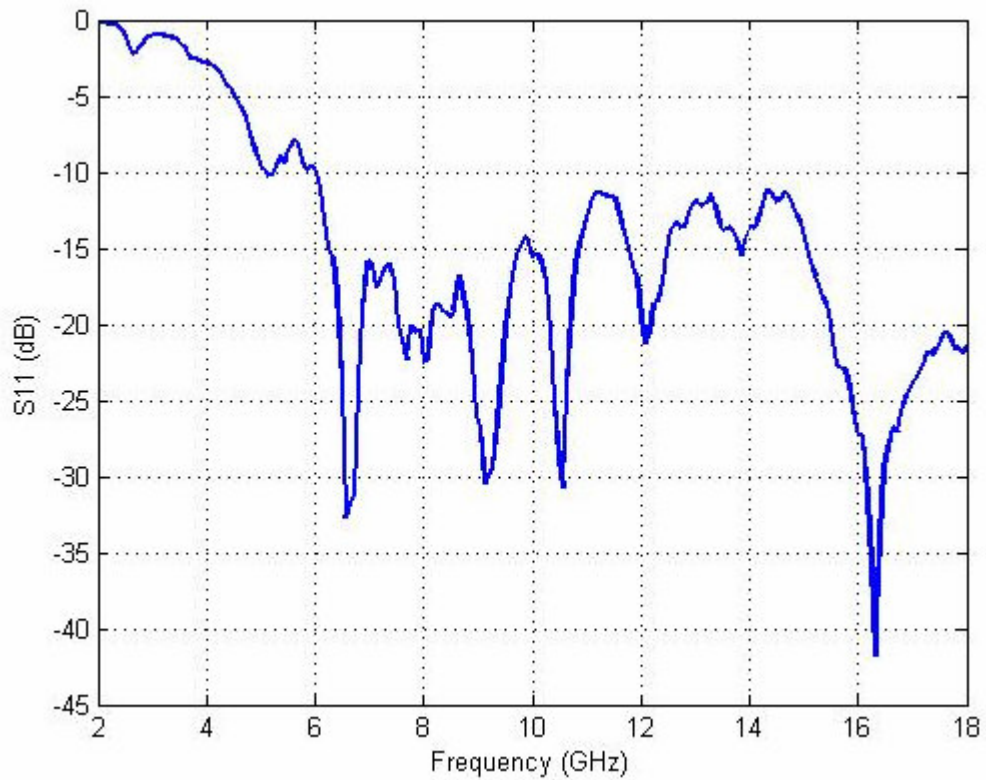


Figure 5.10 Measured return loss response of Antenna-2 (2-18 GHz)

The measurement results of the Antenna-1 are in accordance with the simulation results. The measured responses of the antenna have deeper nulls compared to the simulation results because of the environmental reflections. The return loss response of the Antenna-2 could not be simulated due to convergence problems. Both antennas have return loss responses lower than 10 dB in 6-18 GHz and thus the antennas are expected to operate in this frequency band.

Figure 5.11 and Figure 5.12 below show the measured return loss response of the array in 8.5-10.5 GHz and 2-18 GHz frequency ranges.

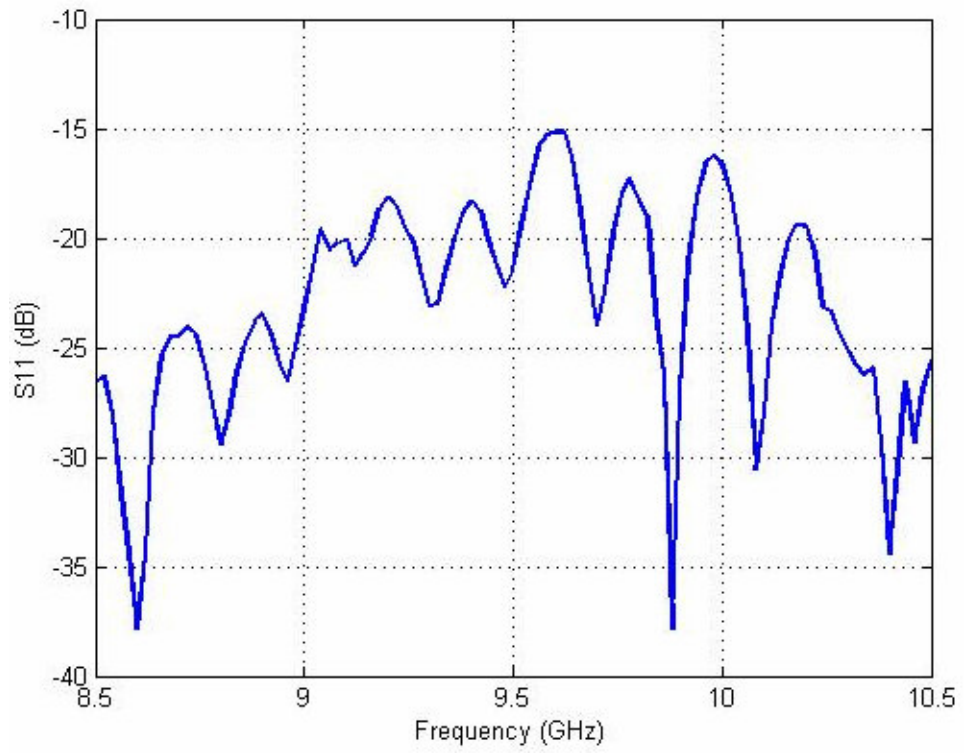


Figure 5.11 Measured return loss response of the array (8.5-10.5 GHz)

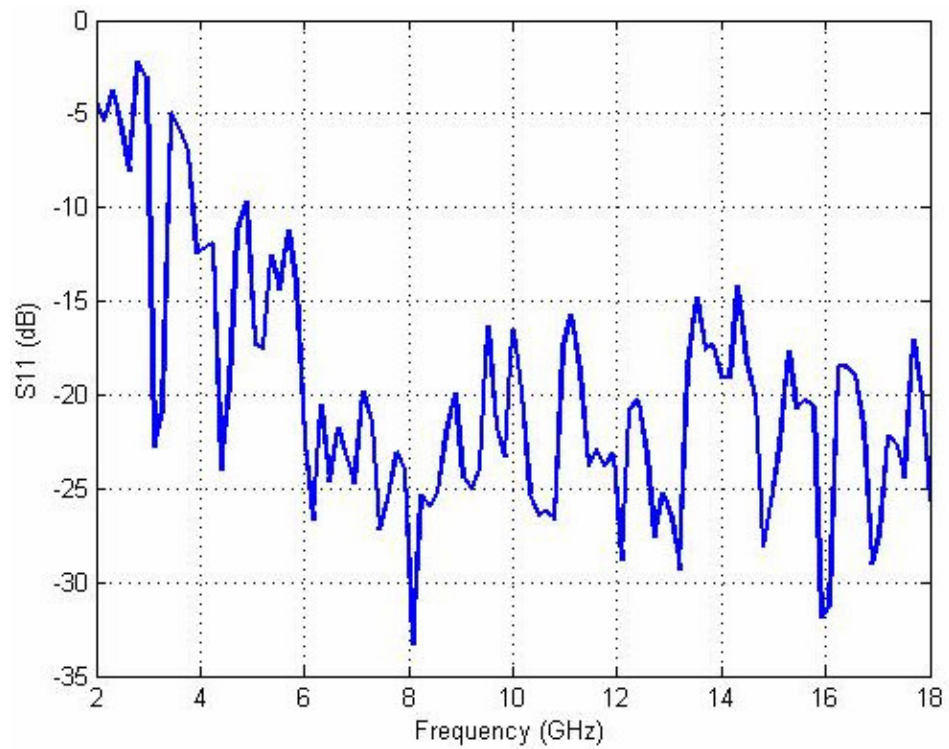


Figure 5.12 Measured return loss response of the array (2-18 GHz)

The array return loss response with the power dividers in 8.5-10.5 GHz bandwidth is observed to be greater than 15 dB which is fairly satisfying. The array has an acceptable return loss response through 4-18 GHz frequency band. The return loss response of the array could not be simulated because of the inadequate convergence for the 8-element structure.

Mutual coupling characteristics of the array are also measured using two-port calibration property of the network analyzer. The coupling throughout the operating frequency range is observed to be smaller than approximately 20 dB. Mutual coupling measurement results of the 1st and 5th elements of the array are given below in Figure 5.13 and Figure 5.14.

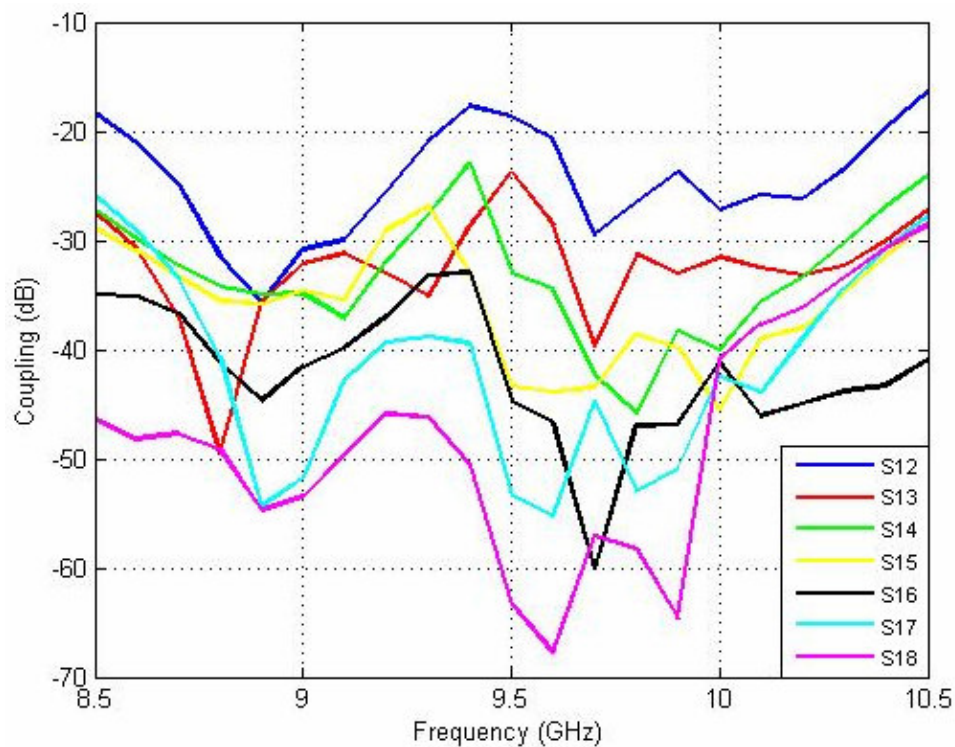


Figure 5.13 Measured mutual coupling of the array elements (referenced to 1st element)

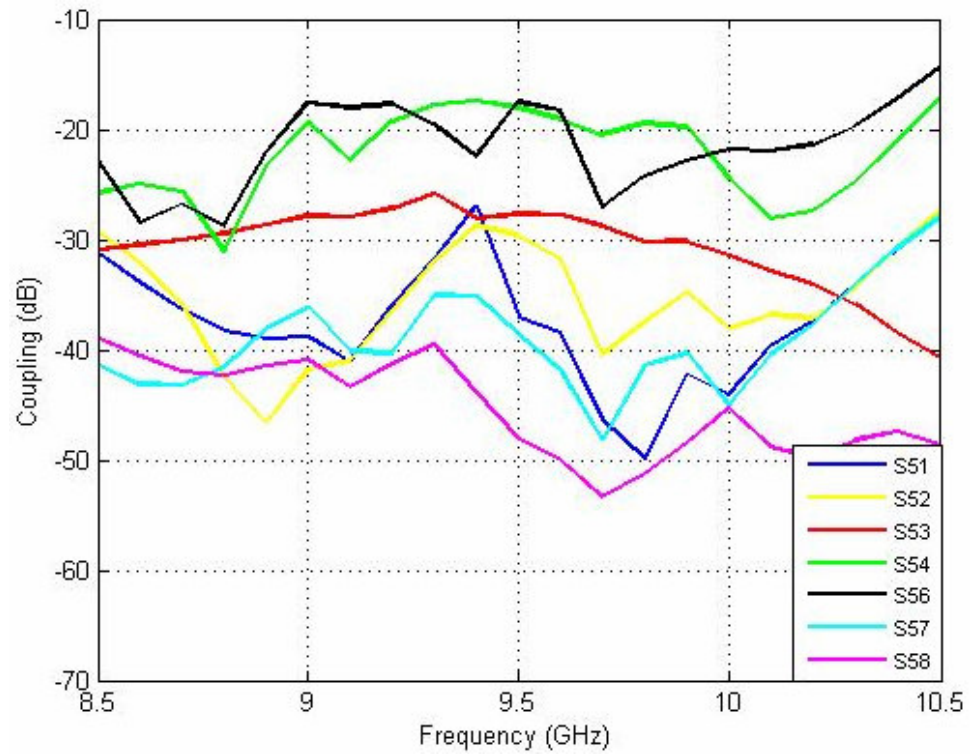


Figure 5.14 Measured mutual coupling of the array elements (referenced to 5th element)

5.3.2 Pattern Measurement Results

Radiation pattern measurements of the antennas and the array in H-plane co-polarization are compared with the simulations in 2 GHz, 6 GHz, 8.5 GHz, 9.5 GHz, 10.5 GHz, 15 GHz and 18 GHz. The comparison of measured and simulated H-plane cross-polarization patterns and E-plane patterns are also plotted in 8.5 GHz, 9.5 GHz and 10.5 GHz. These plots are given below.

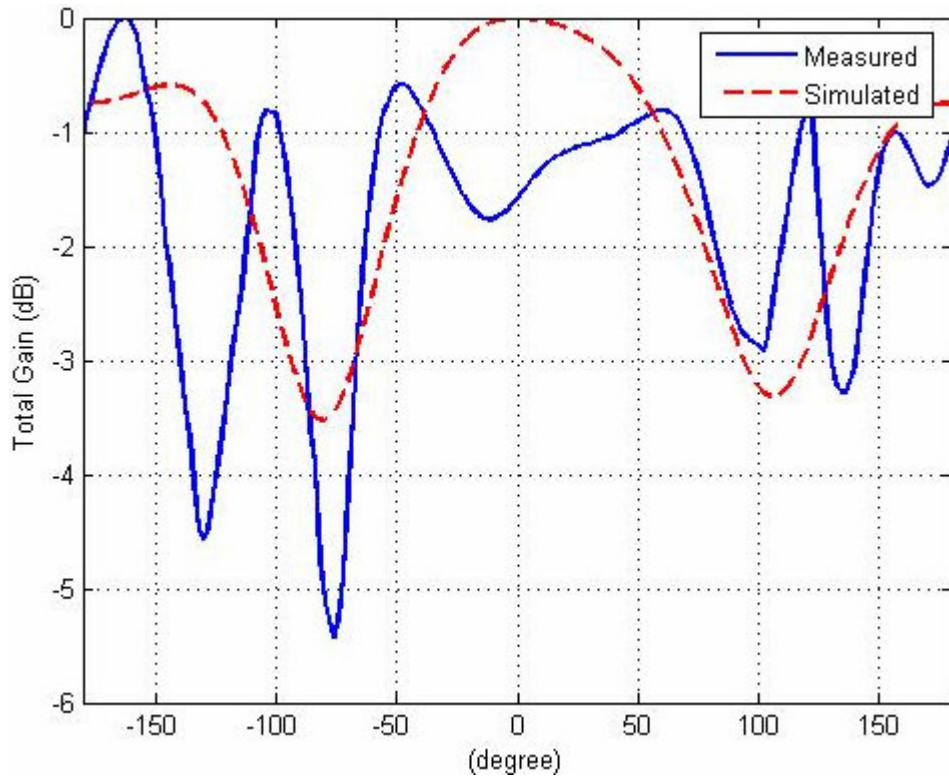


Figure 5.15 Measured and simulated H-plane co-polarization patterns of Antenna-1 (2 GHz)

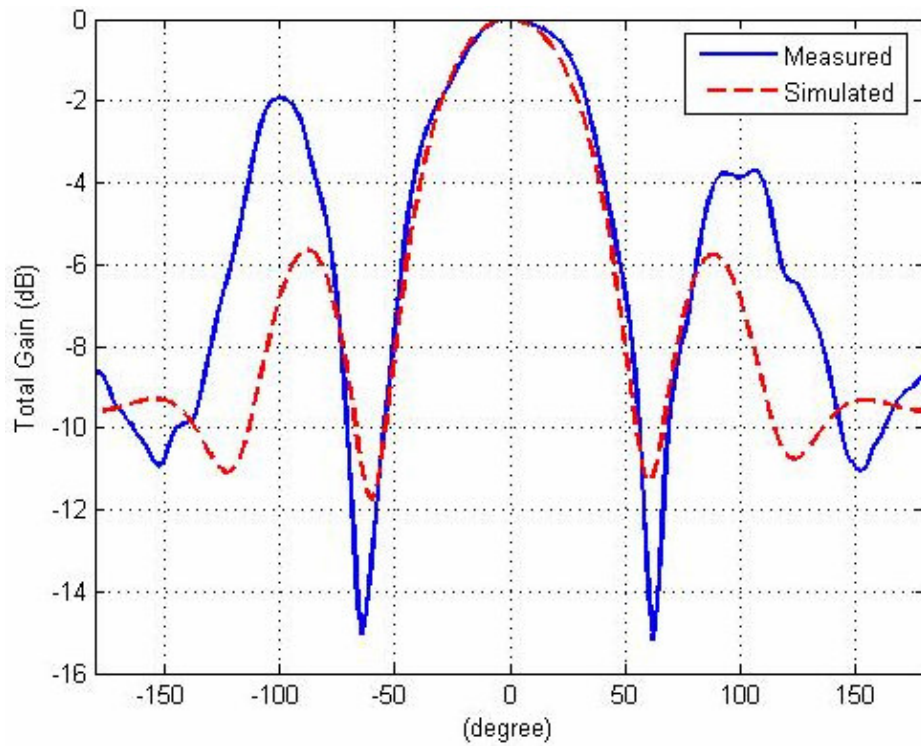


Figure 5.16 Measured and simulated H-plane co-polarization patterns of Antenna-1 (6 GHz)

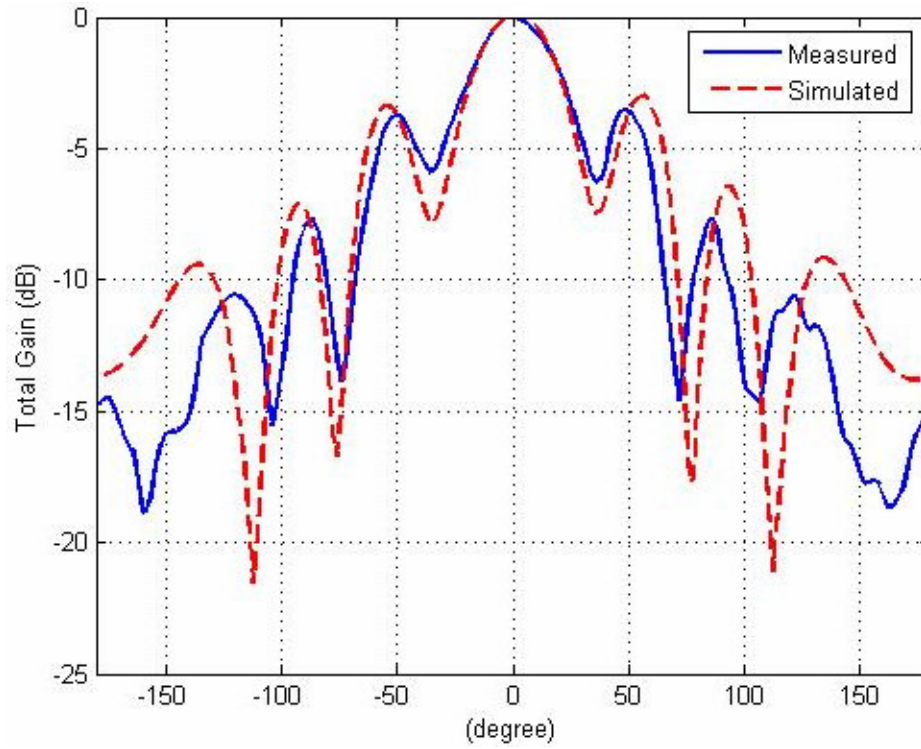


Figure 5.17 Measured and simulated H-plane co-polarization patterns of Antenna-1 (8.5 GHz)

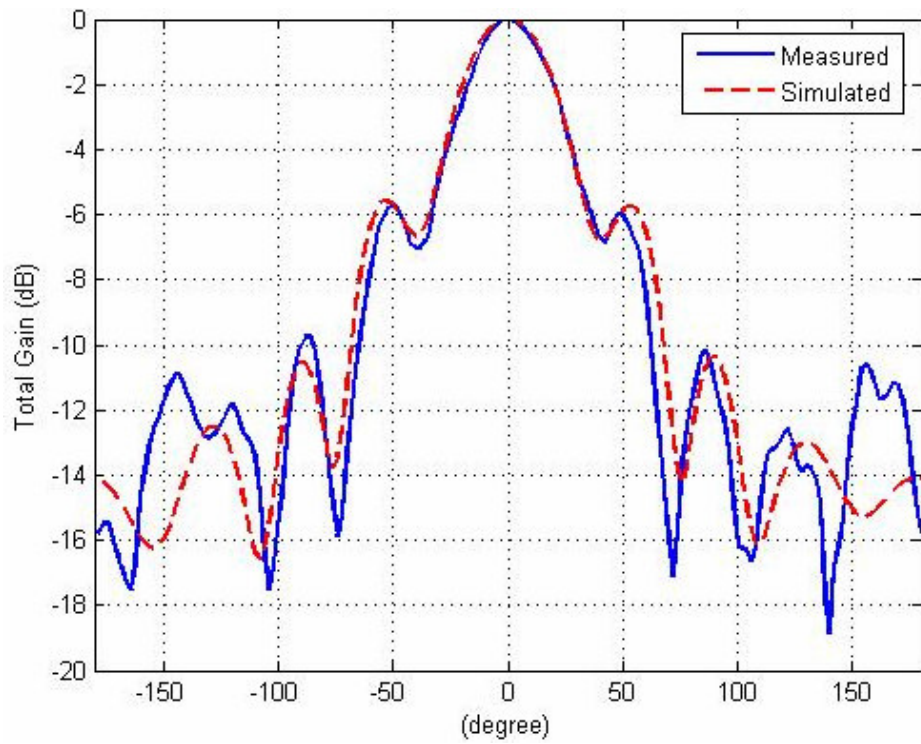


Figure 5.18 Measured and simulated H-plane co-polarization patterns of Antenna-1 (9.5 GHz)

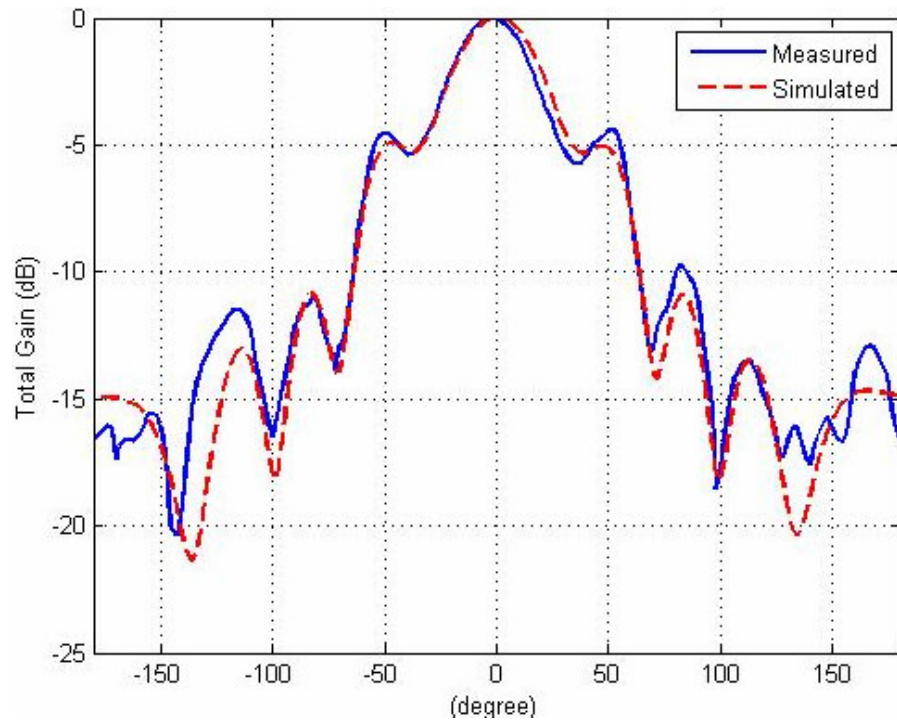


Figure 5.19 Measured and simulated H-plane co-polarization patterns of Antenna-1 (10.5 GHz)

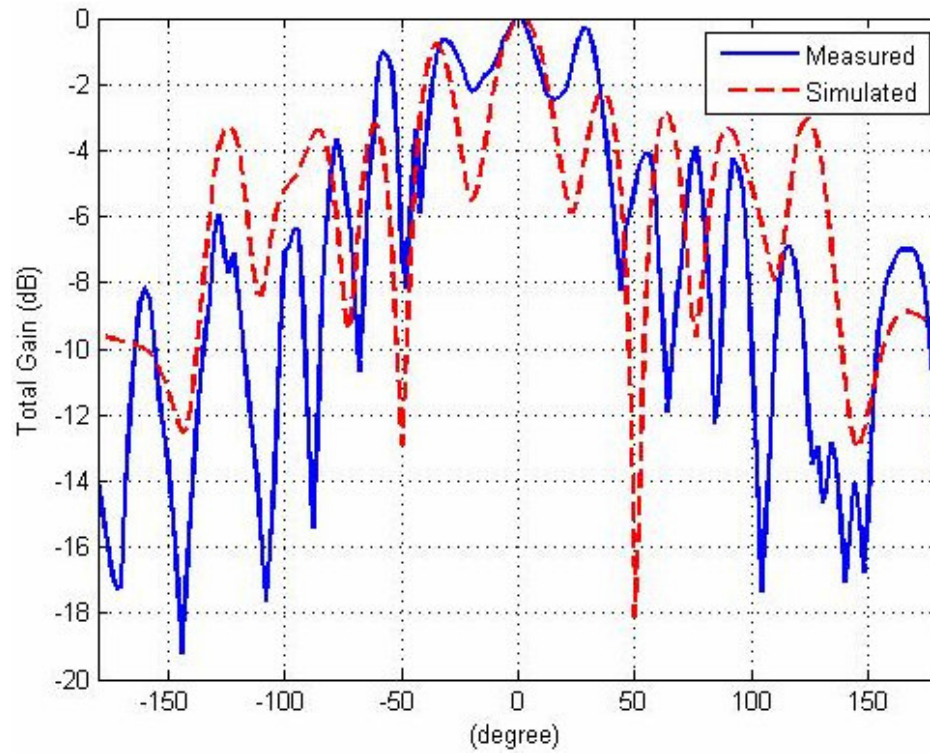


Figure 5.20 Measured and simulated H-plane co-polarization patterns of Antenna-1 (15 GHz)

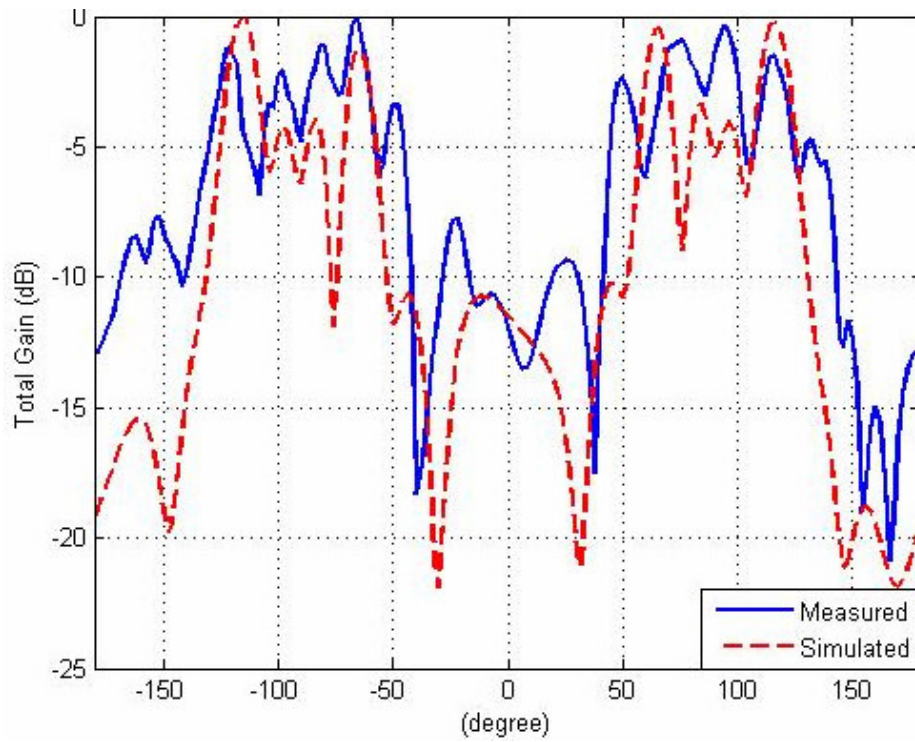


Figure 5.21 Measured and simulated H-plane co-polarization patterns of Antenna-1 (18 GHz)

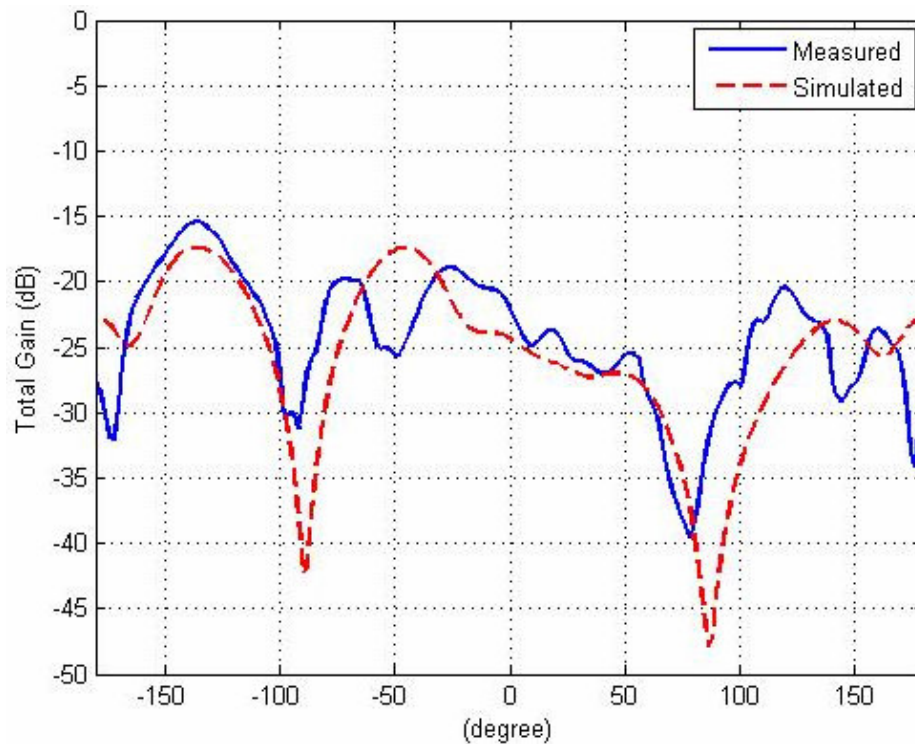


Figure 5.22 Measured and simulated H-plane cross-polarization patterns of Antenna-1 (8.5 GHz)

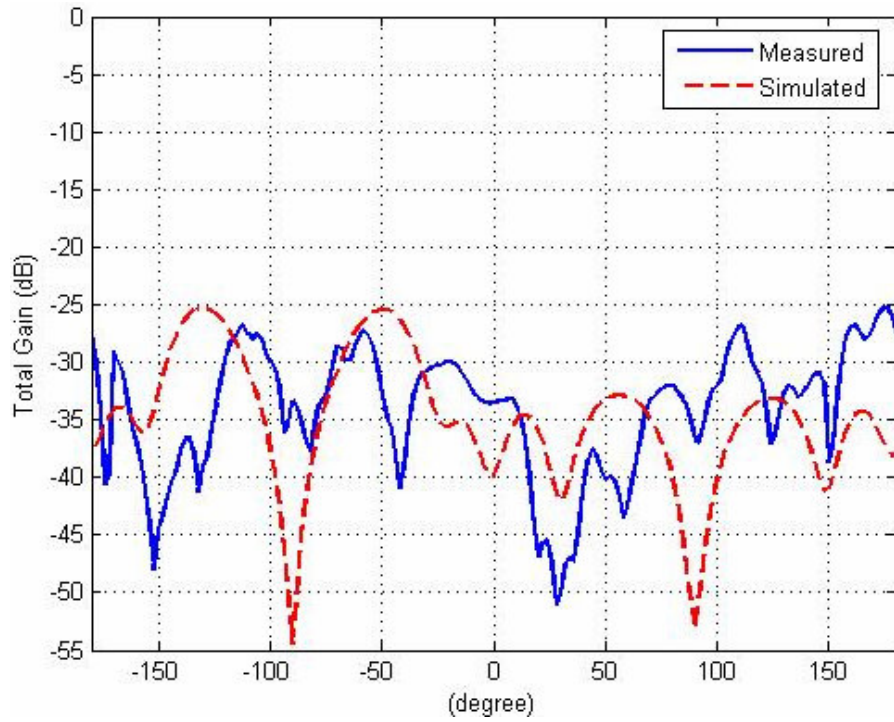


Figure 5.23 Measured and simulated H-plane cross-polarization patterns of Antenna-1 (9.5 GHz)

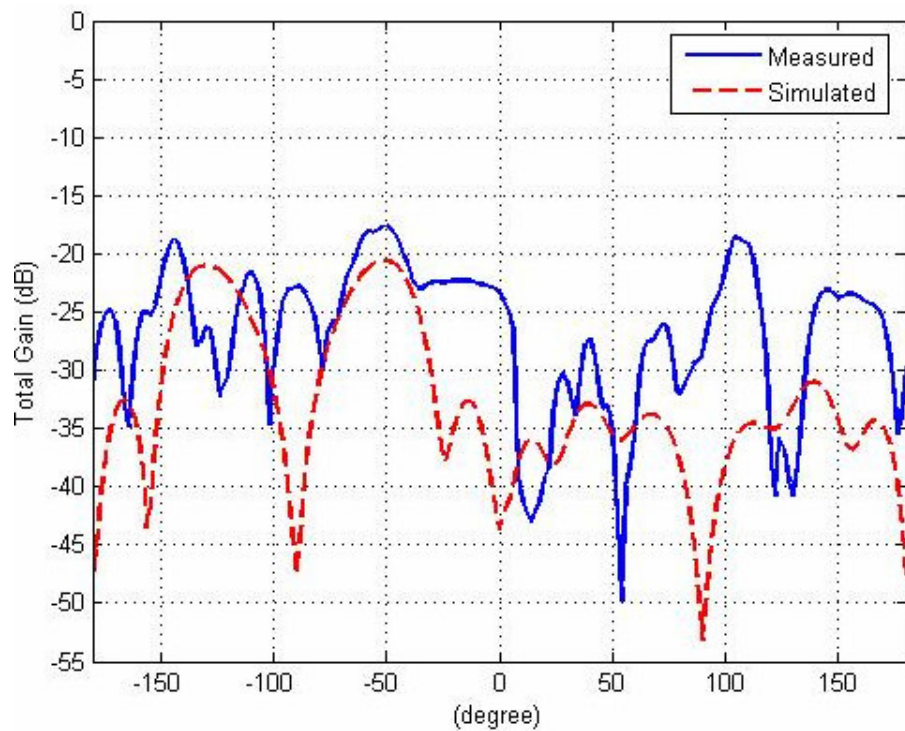


Figure 5.24 Measured and simulated H-plane cross-polarization patterns of Antenna-1 (10.5 GHz)

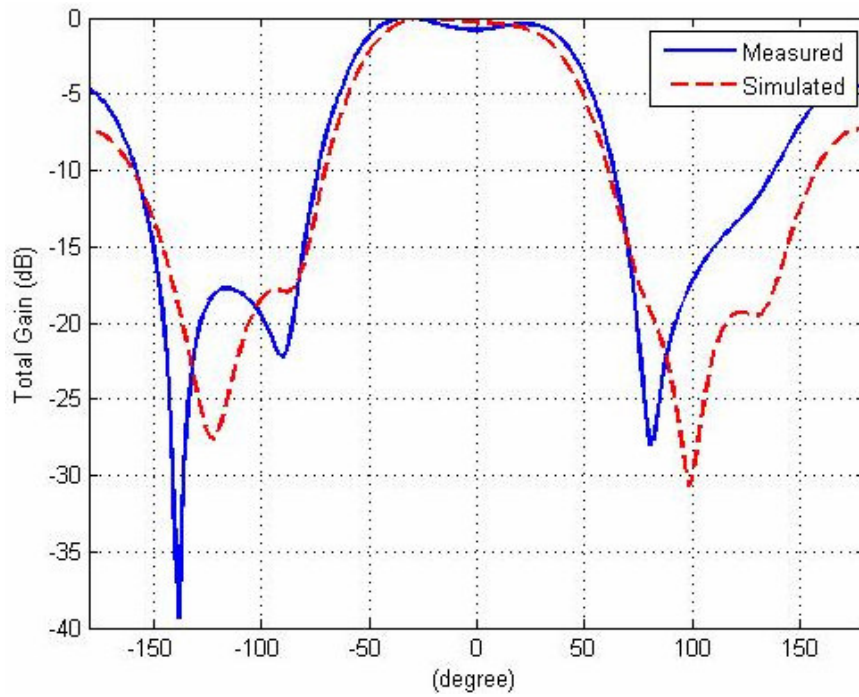


Figure 5.25 Measured and simulated E-plane patterns of Antenna-1 (8.5 GHz)

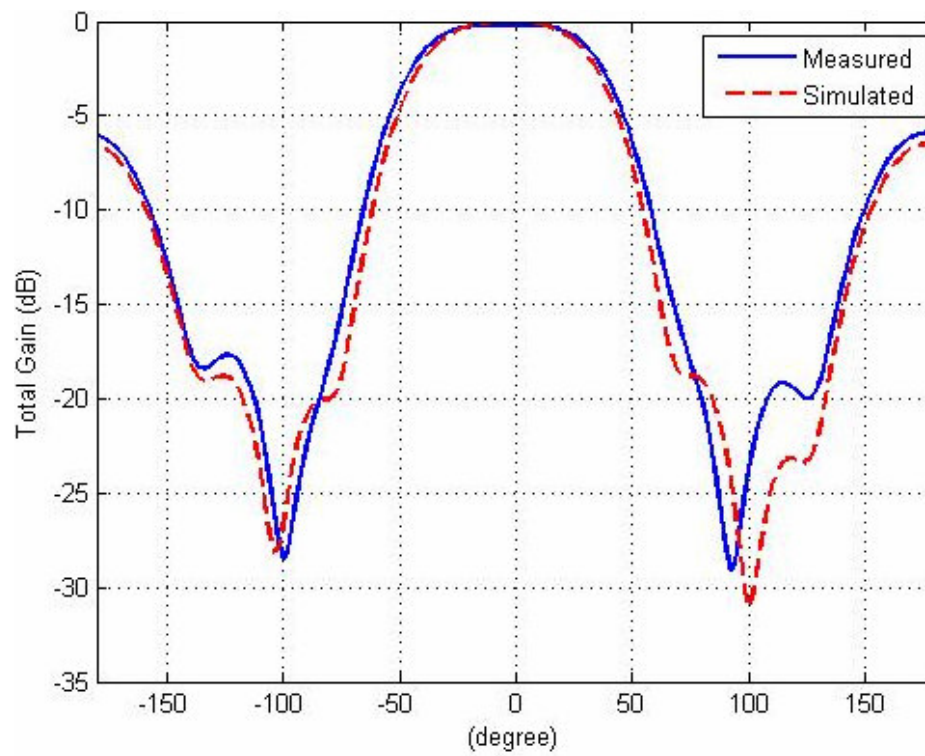


Figure 5.26 Measured and simulated E-plane patterns of Antenna-1 (9.5 GHz)

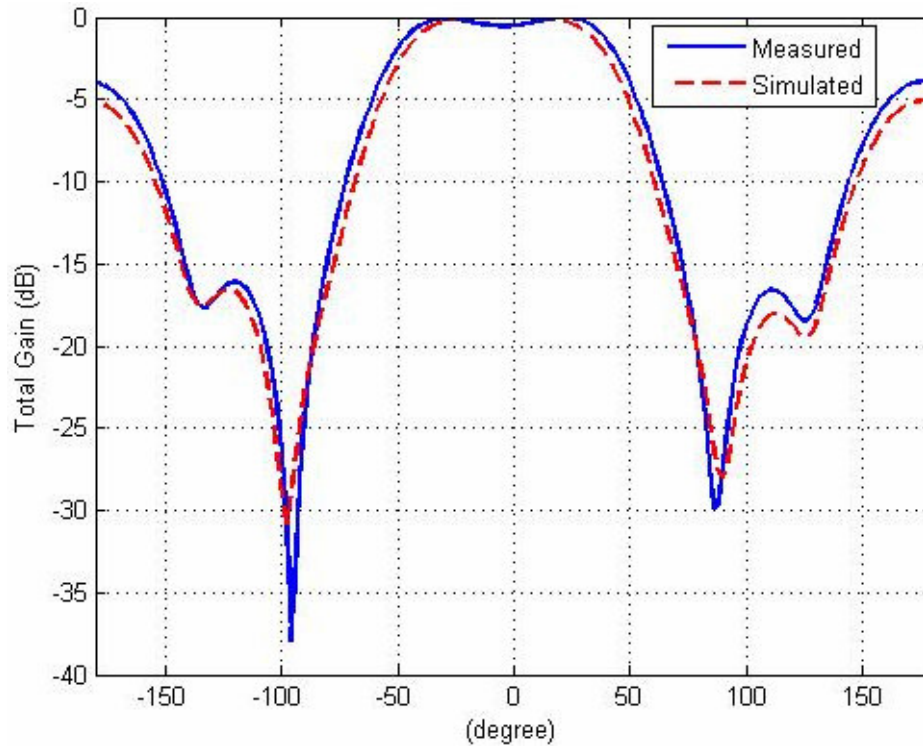


Figure 5.27 Measured and simulated E-plane patterns of Antenna-1 (10.5 GHz)

H-plane co-polarization and cross-polarization patterns of the Antenna-1 are given above in Figure 5.15 through Figure 5.24. Measurement and simulation results are consistent especially below 15 GHz. The reflections caused by the metallic structure in the test setup increase with the increasing frequency. Thus, deeper and more nulls are observed in the radiation patterns at 15 GHz and 18 GHz. Measured and simulated E-plane patterns of the antenna are also compared in Figure 5.25 through Figure 5.27.

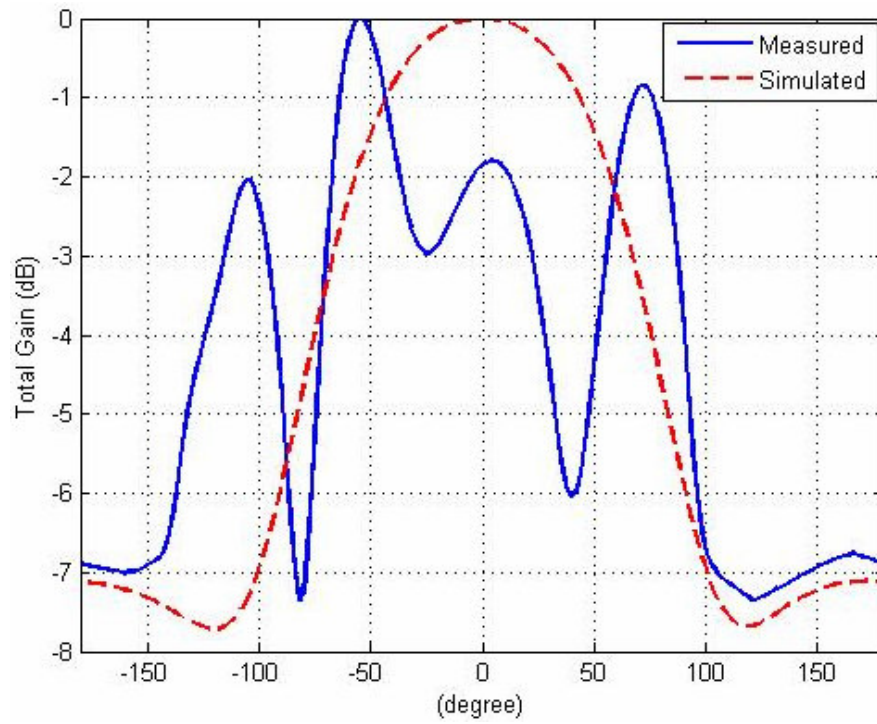


Figure 5.28 Measured and simulated H-plane co-polarization patterns of Antenna-2 (2 GHz)

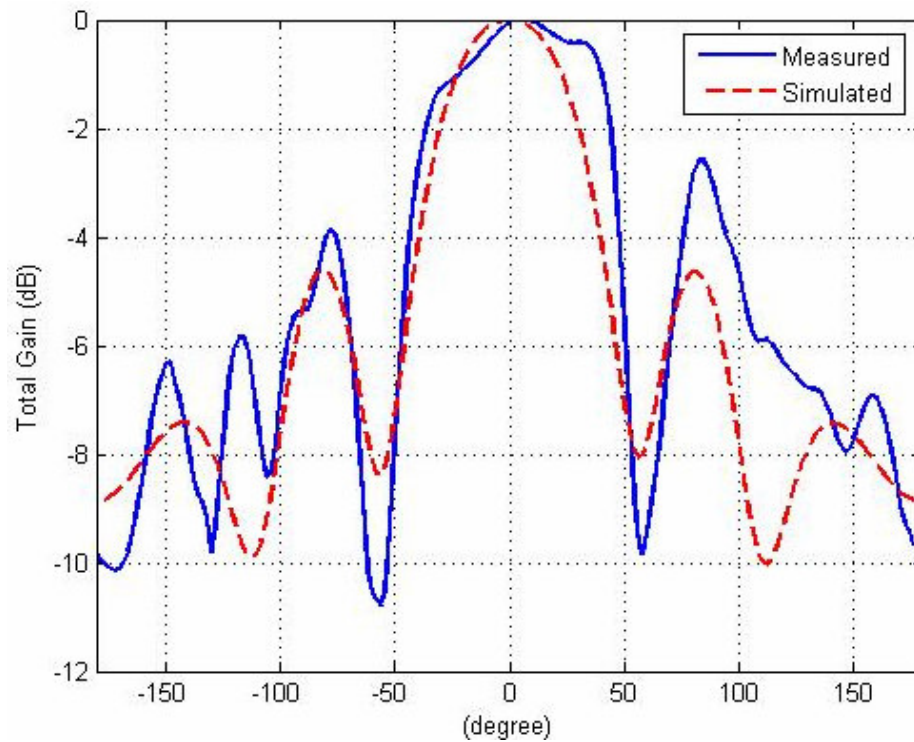


Figure 5.29 Measured and simulated H-plane co-polarization patterns of Antenna-2 (6 GHz)

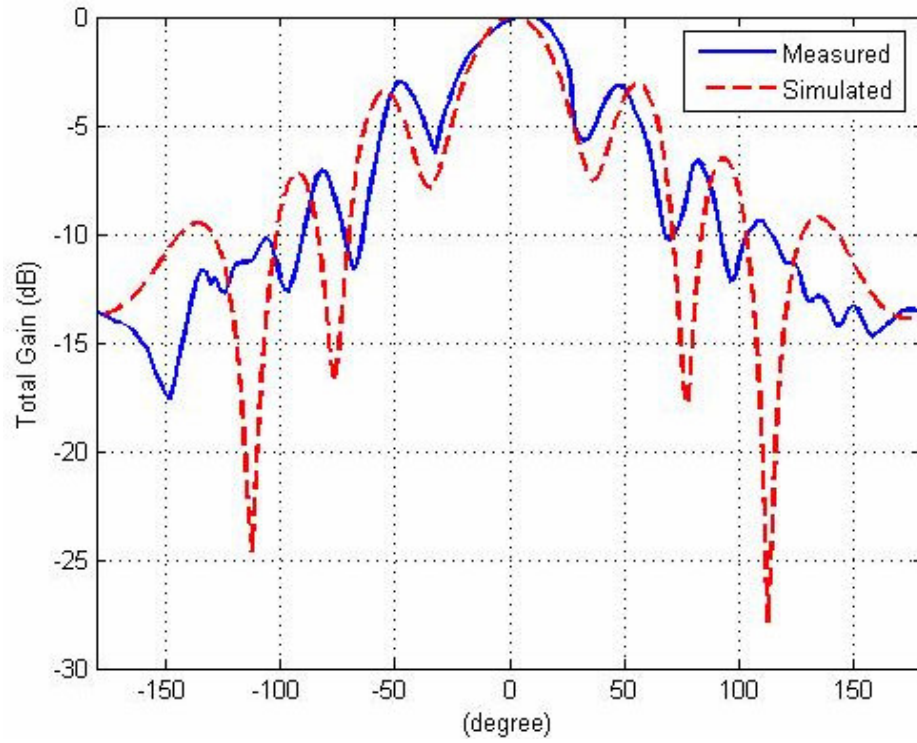


Figure 5.30 Measured and simulated H-plane co-polarization patterns of Antenna-2 (8.5 GHz)

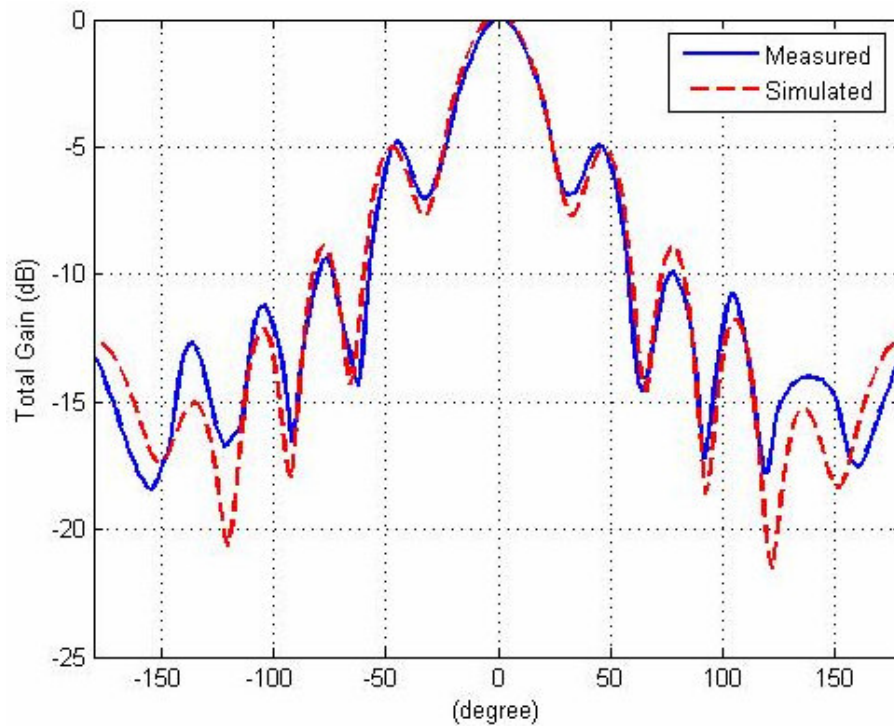


Figure 5.31 Measured and simulated H-plane co-polarization patterns of Antenna-2 (9.5 GHz)

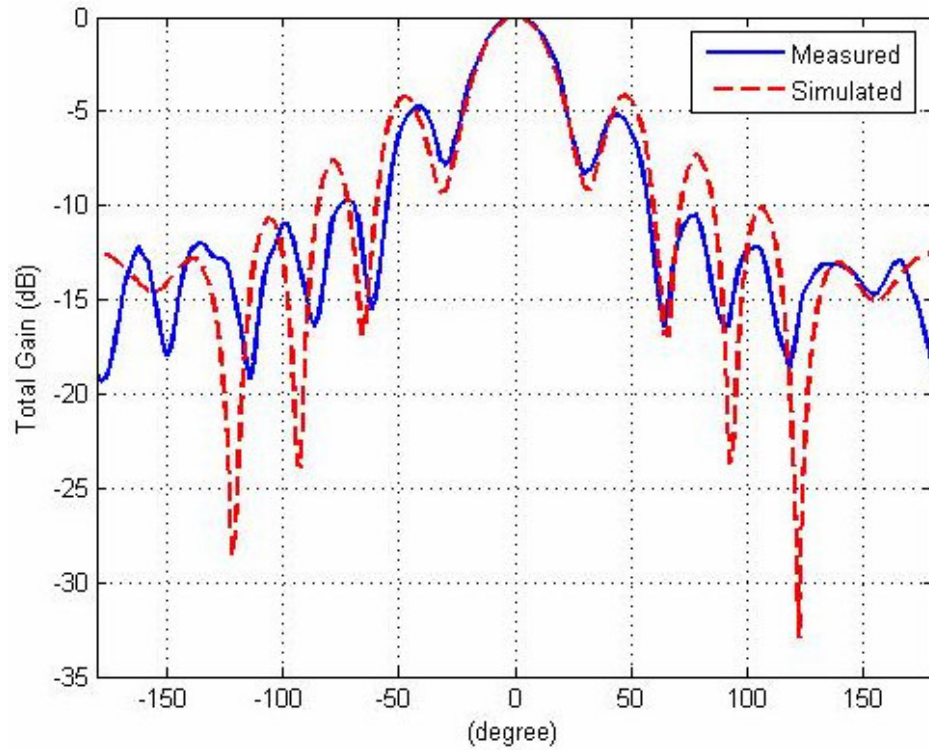


Figure 5.32 Measured and simulated H-plane co-polarization patterns of Antenna-2 (10.5 GHz)

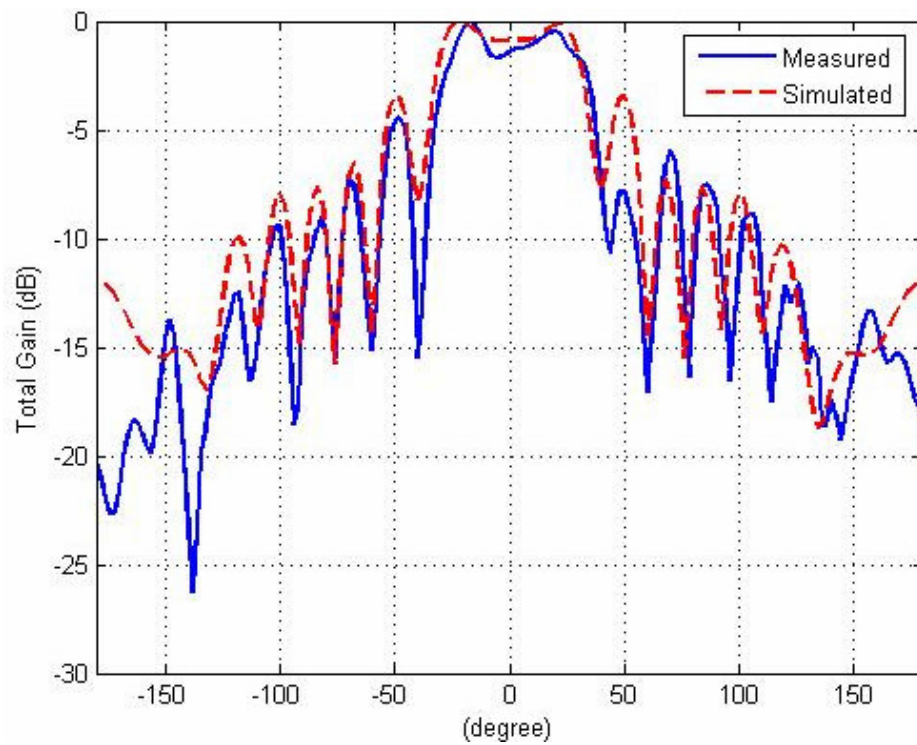


Figure 5.33 Measured and simulated H-plane co-polarization patterns of Antenna-2 (15 GHz)

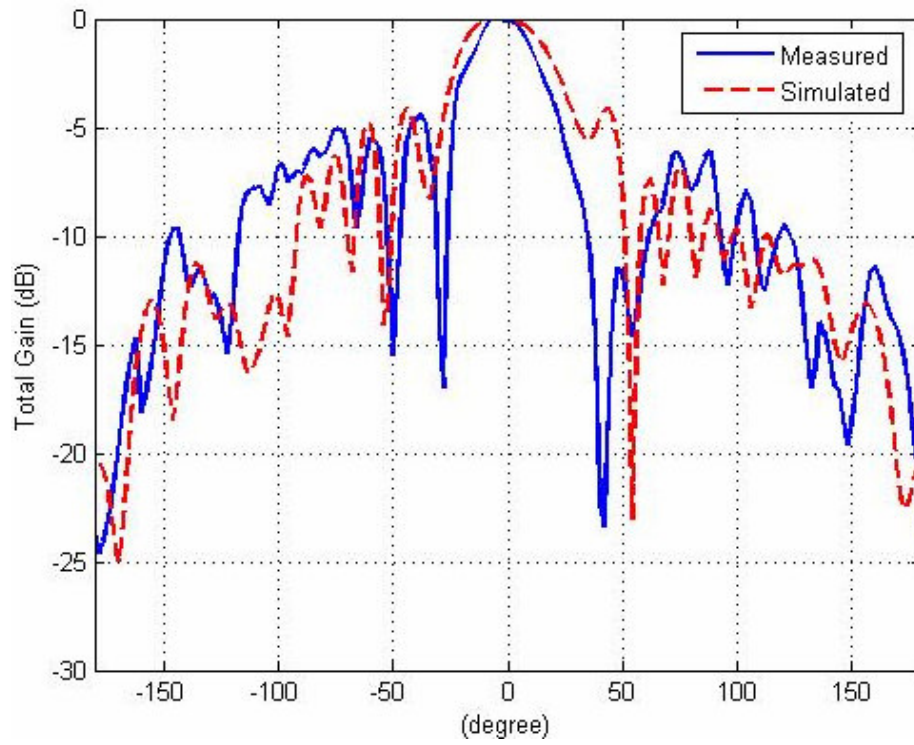


Figure 5.34 Measured and simulated H-plane co-polarization patterns of Antenna-2 (18 GHz)

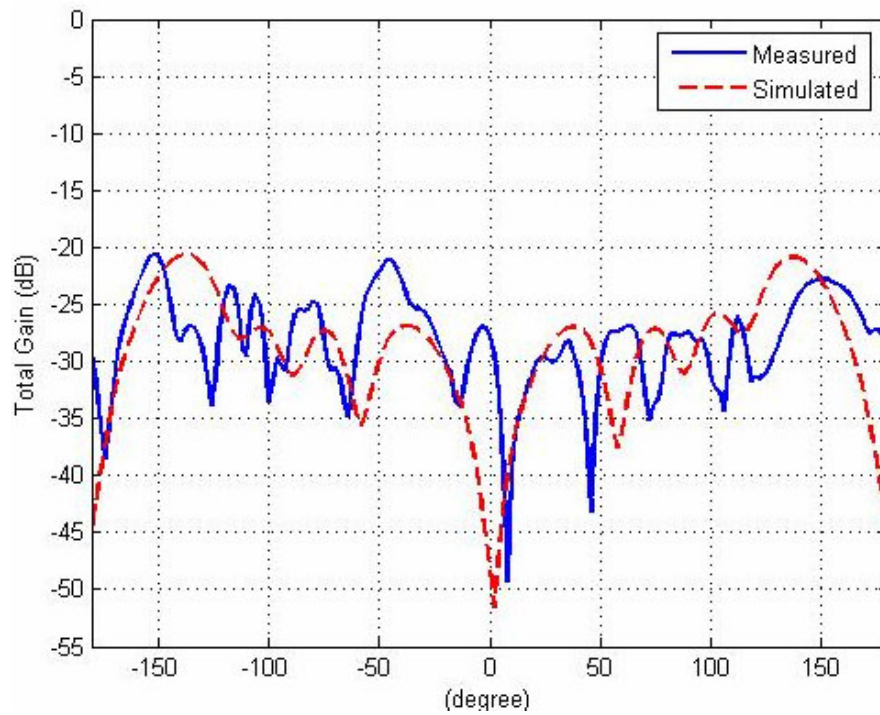


Figure 5.35 Measured and simulated H-plane cross-polarization patterns of Antenna-2 (8.5 GHz)

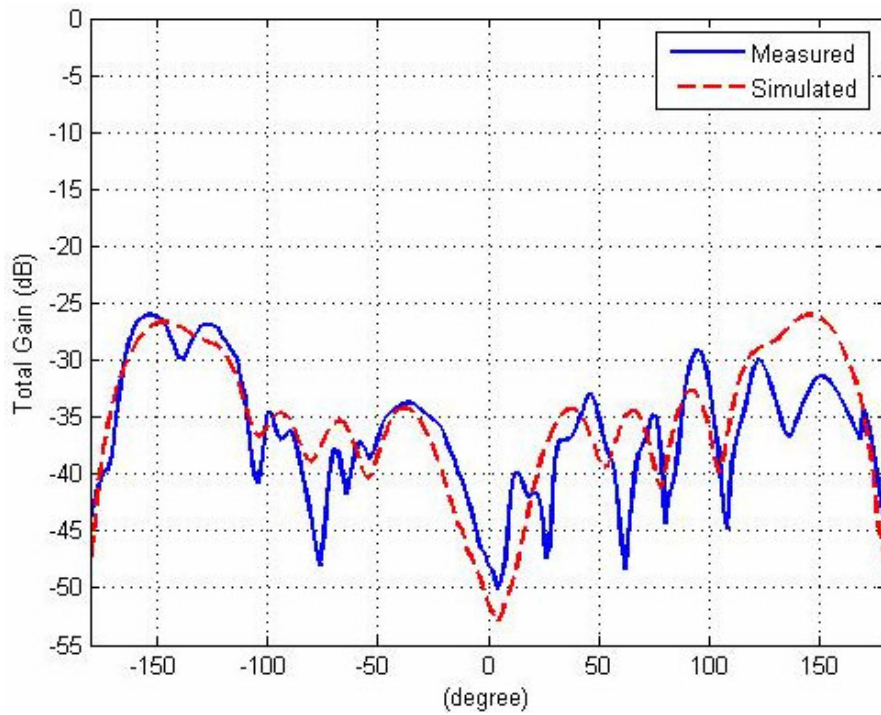


Figure 5.36 Measured and simulated H-plane cross-polarization patterns of Antenna-2 (9.5 GHz)

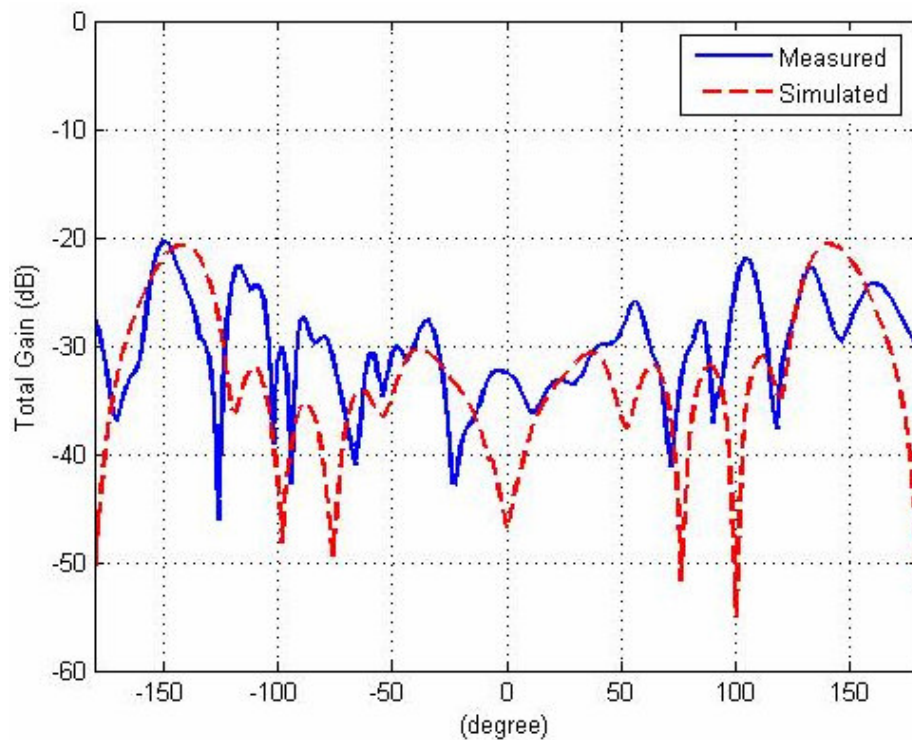


Figure 5.37 Measured and simulated H-plane cross-polarization patterns of Antenna-2 (10.5 GHz)

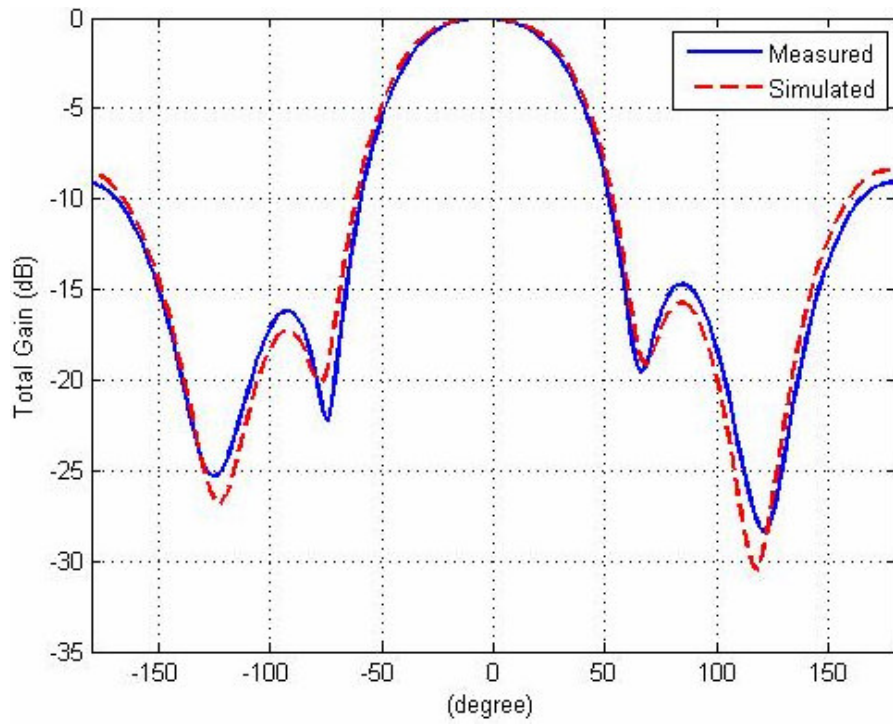


Figure 5.38 Measured and simulated E-plane patterns of Antenna-2 (8.5 GHz)

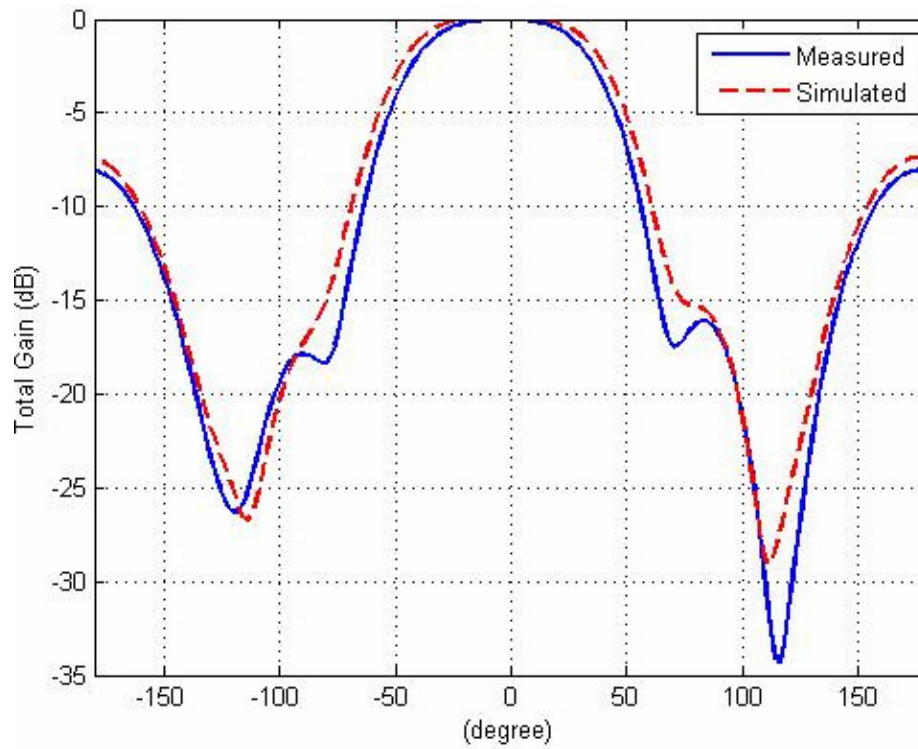


Figure 5.39 Measured and simulated E-plane patterns of Antenna-2 (9.5 GHz)

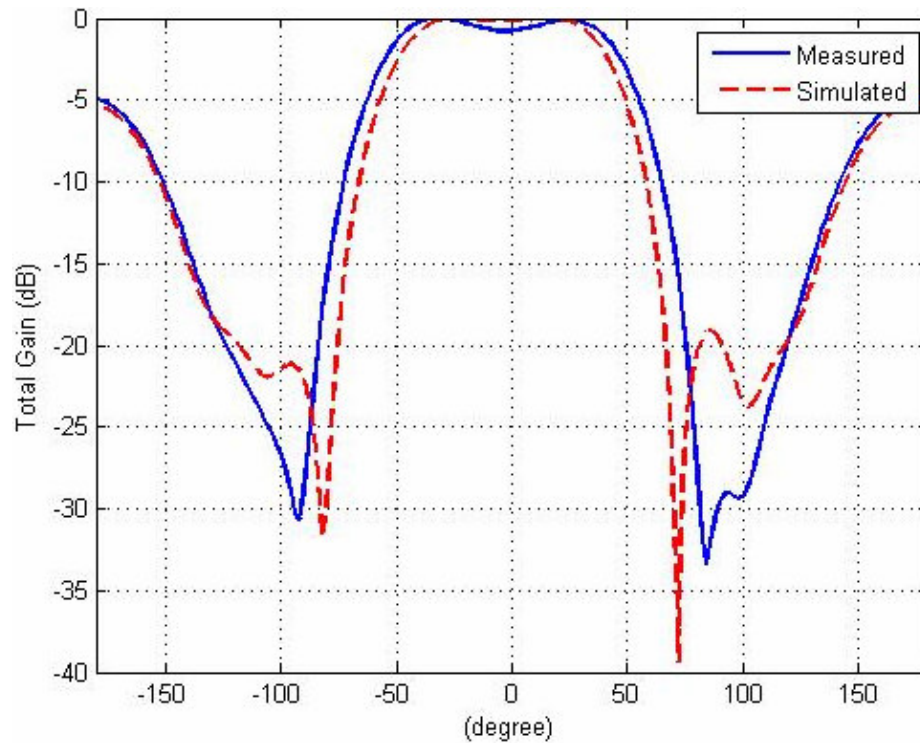


Figure 5.40 Measured and simulated E-plane patterns of Antenna-2 (10.5 GHz)

The plots comparing measured and simulated radiation patterns in co-polarization and cross-polarization are given above in Figure 5.28 through Figure 5.37. The reflections caused by the measurement setup result in deeper nulls in radiation patterns at higher frequencies as in the measurement of Antenna-1. It can be said that the measured and simulated patterns of Antenna-2 are fairly the same. Measured and simulated E-plane patterns of the antenna are also given in Figure 5.38 through Figure 5.40.

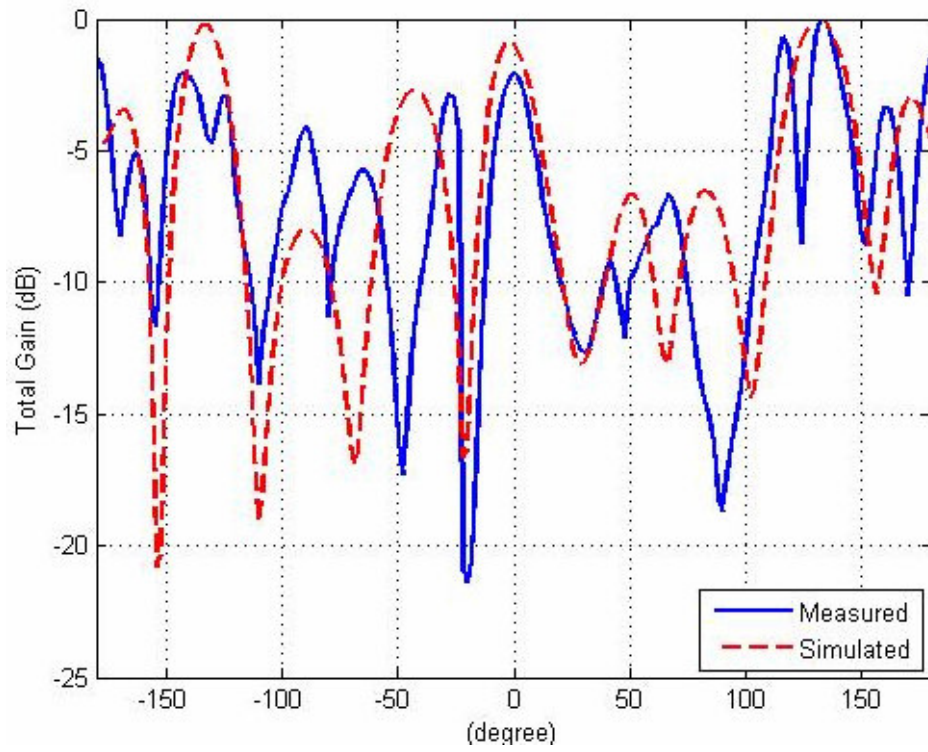


Figure 5.41 Measured and simulated H-plane co-polarization patterns of the array (2 GHz)

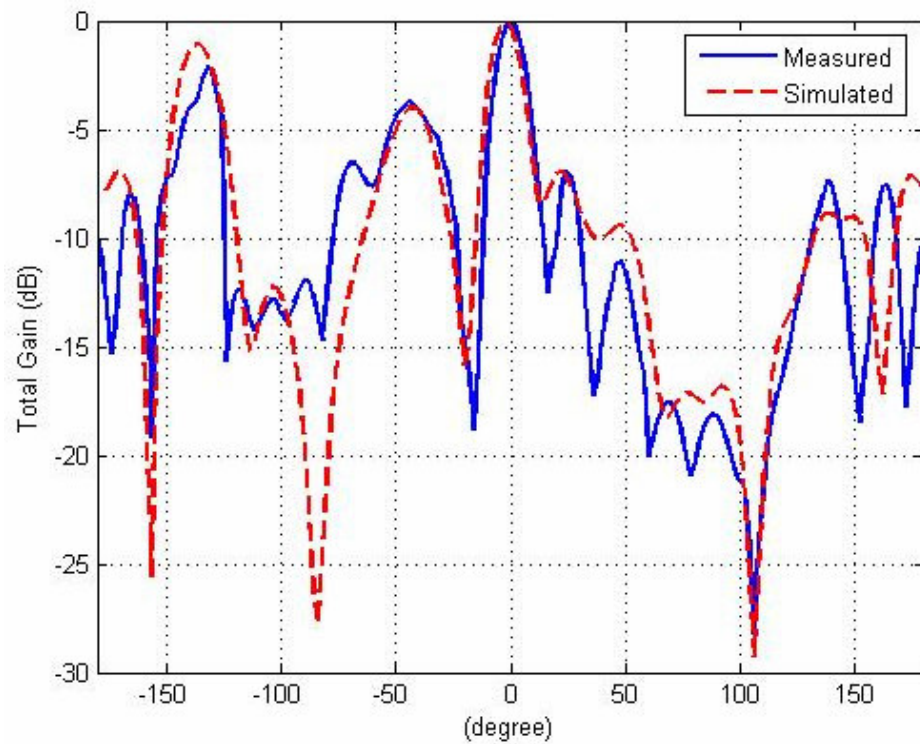


Figure 5.42 Measured and simulated H-plane co-polarization patterns of the array (6 GHz)

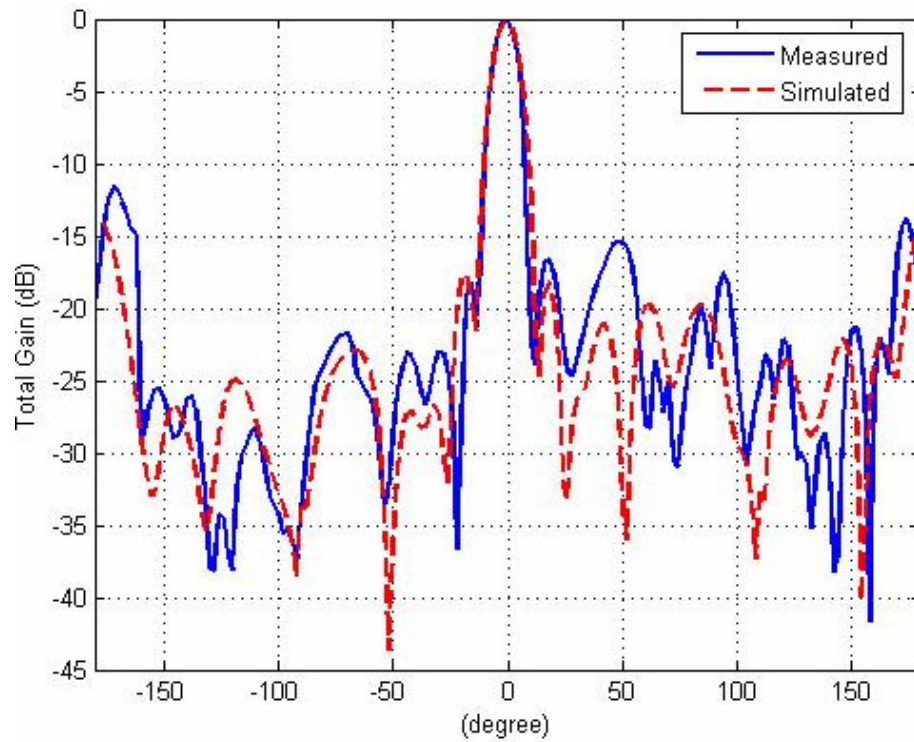


Figure 5.43 Measured and simulated H-plane co-polarization patterns of the array (8.5 GHz)

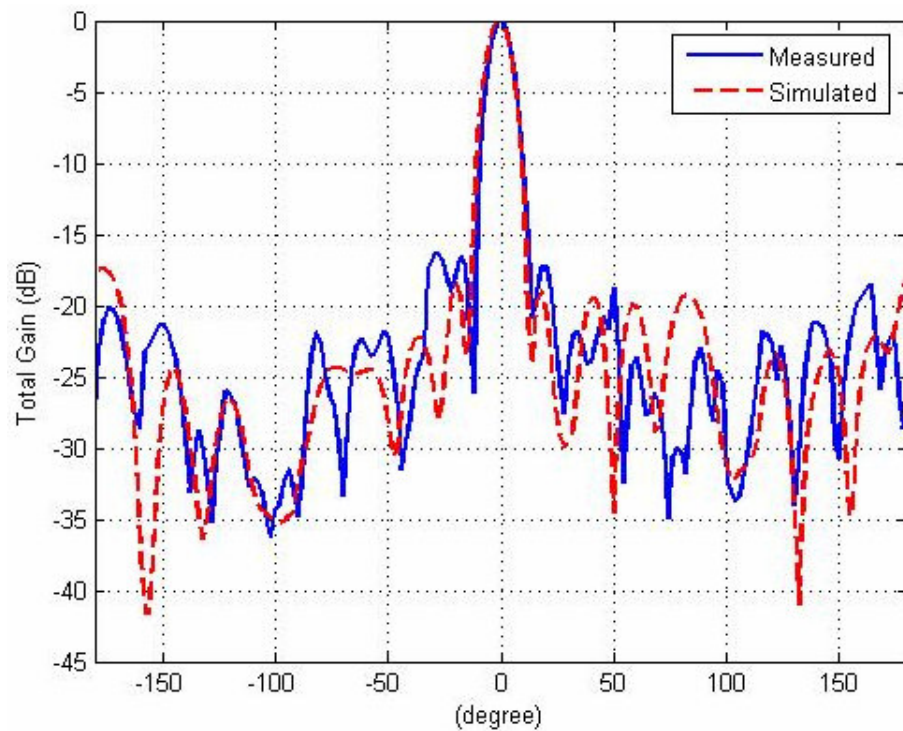


Figure 5.44 Measured and simulated H-plane co-polarization patterns of the array (9.5 GHz)

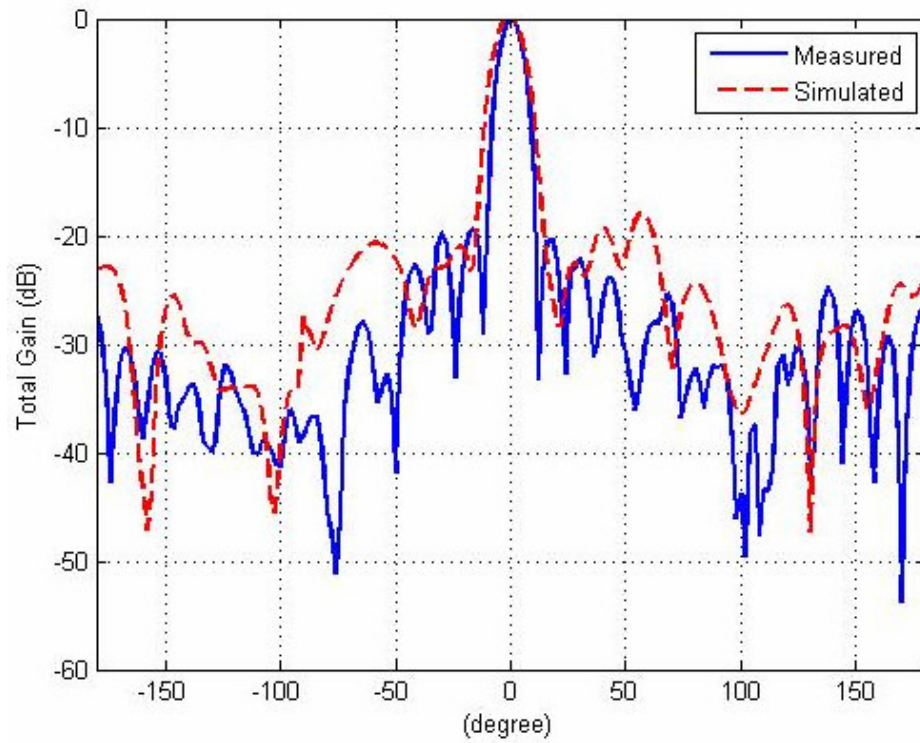


Figure 5.45 Measured and simulated H-plane co-polarization patterns of the array (10.5 GHz)

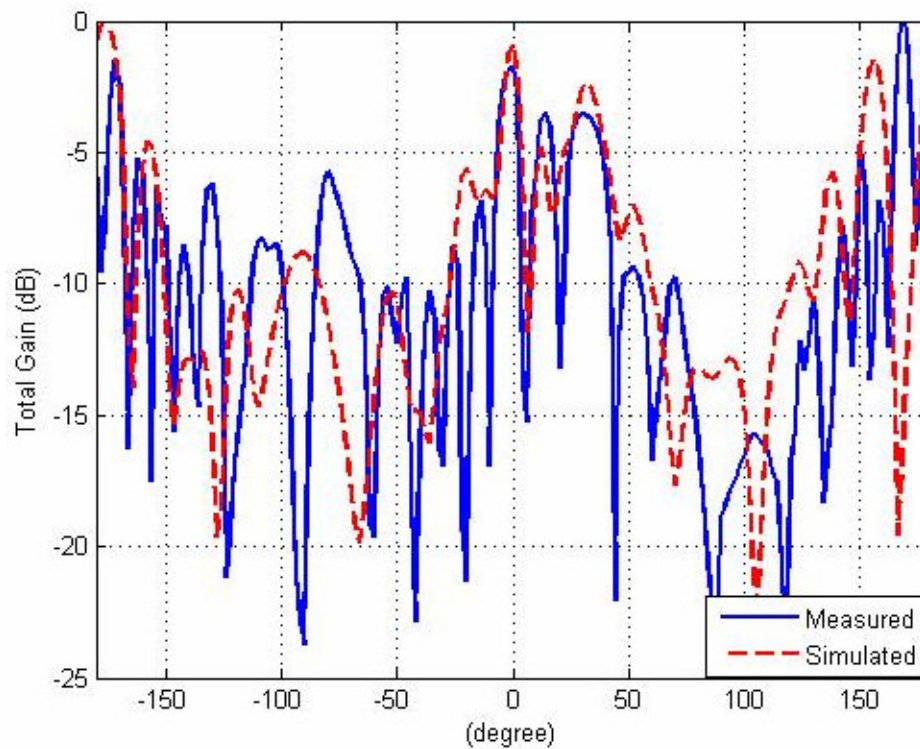


Figure 5.46 Measured and simulated H-plane co-polarization patterns of the array (15 GHz)

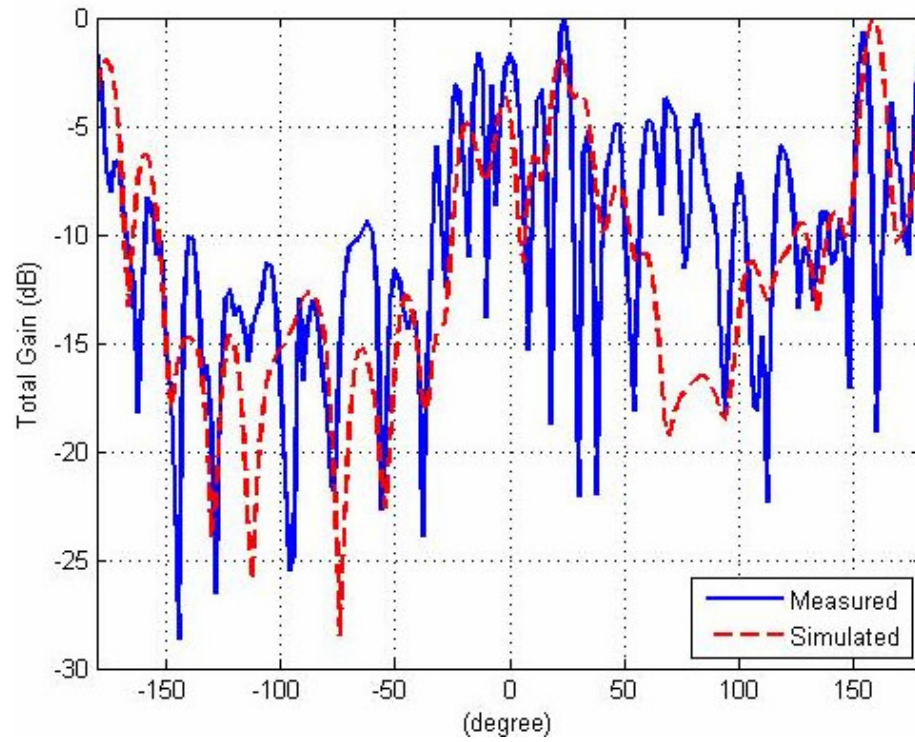


Figure 5.47 Measured and simulated H-plane co-polarization patterns of the array (18 GHz)

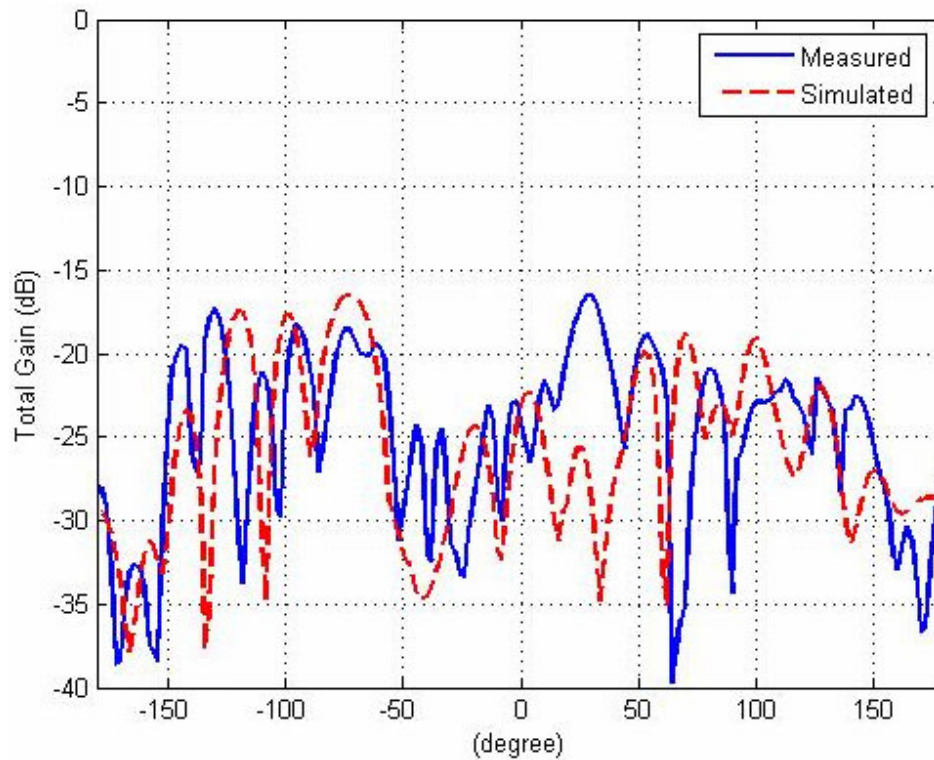


Figure 5.48 Measured and simulated H-plane cross-polarization patterns of the array (8.5 GHz)

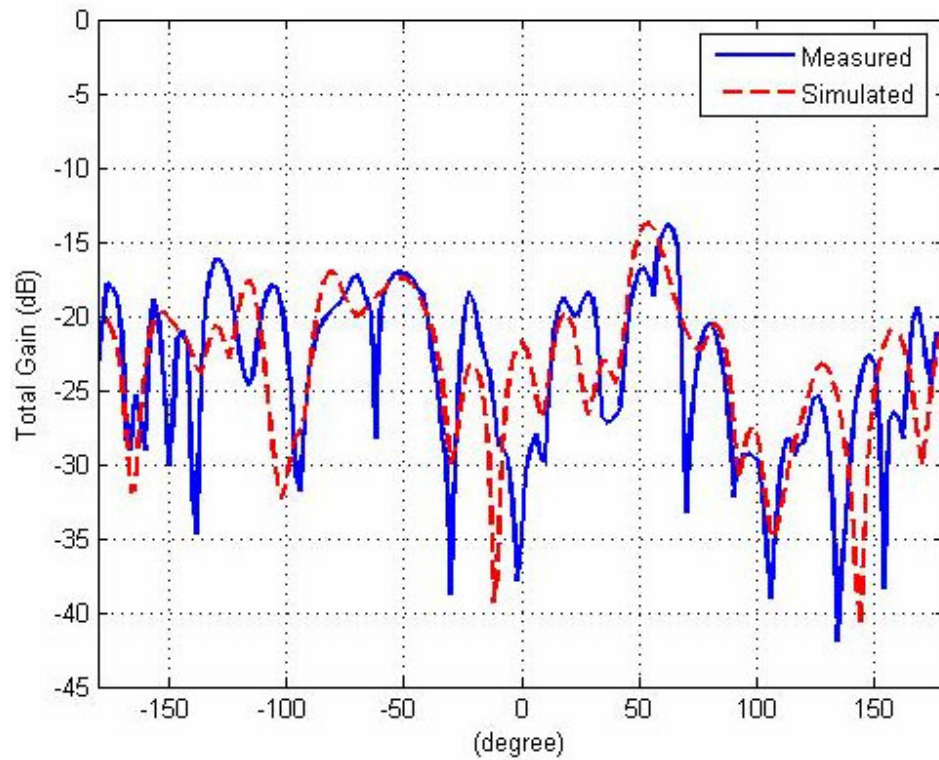


Figure 5.49 Measured and simulated H-plane cross-polarization patterns of the array (9.5 GHz)

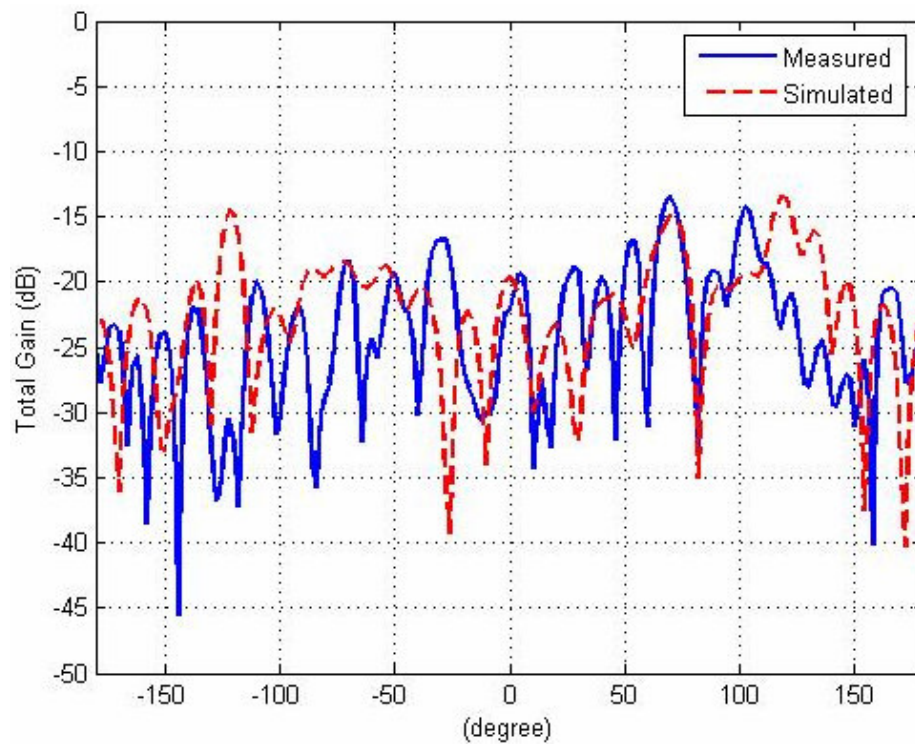


Figure 5.50 Measured and simulated H-plane cross-polarization patterns of the array (10.5 GHz)

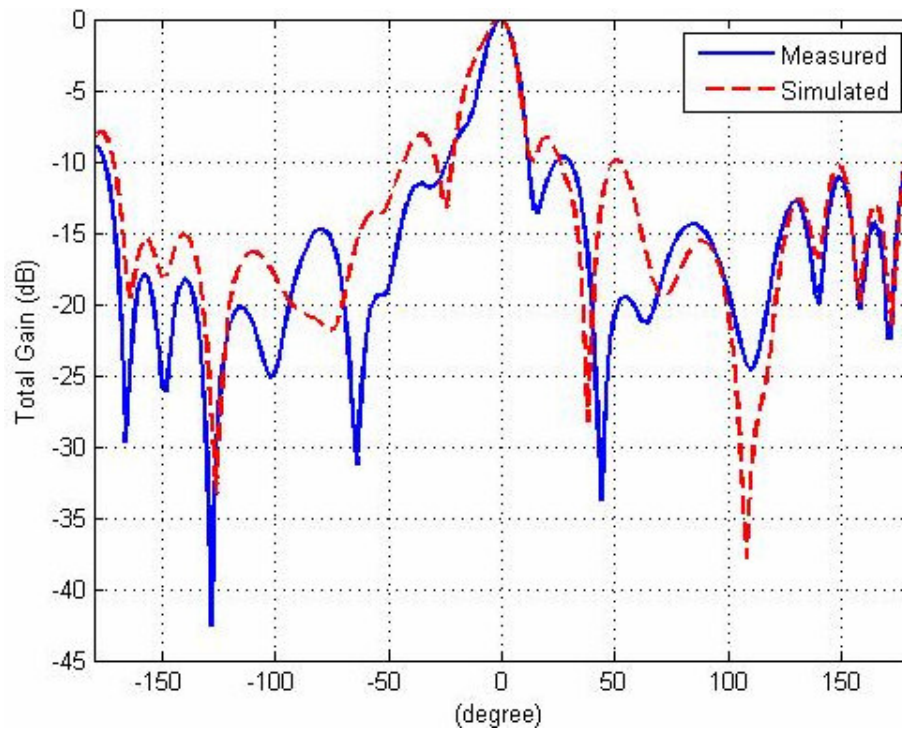


Figure 5.51 Measured and simulated E-plane patterns of the array (8.5 GHz)

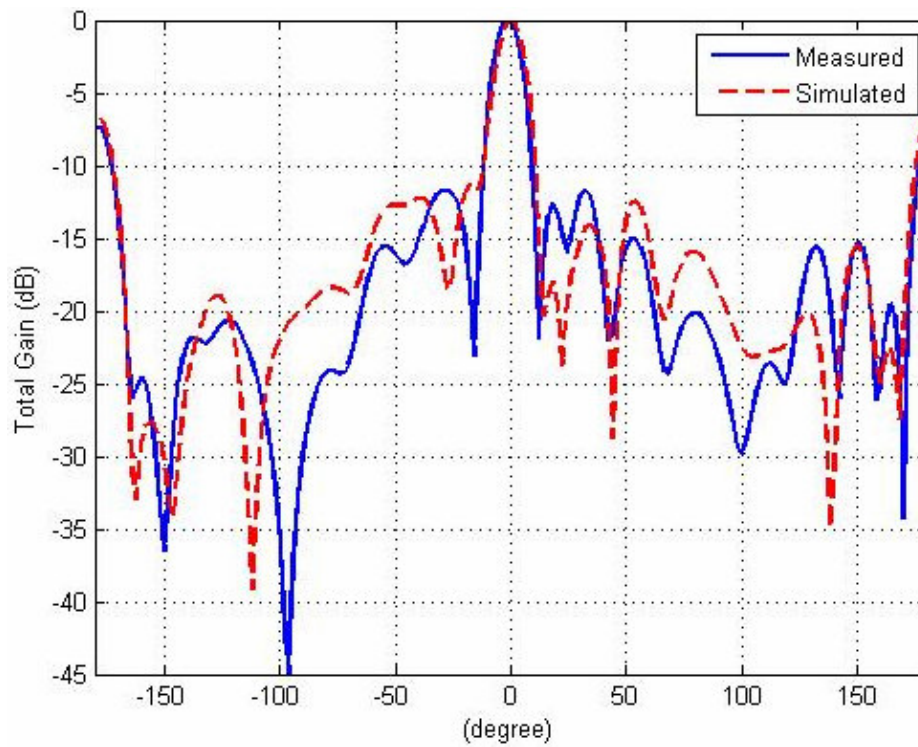


Figure 5.52 Measured and simulated E-plane patterns of the array (9.5 GHz)

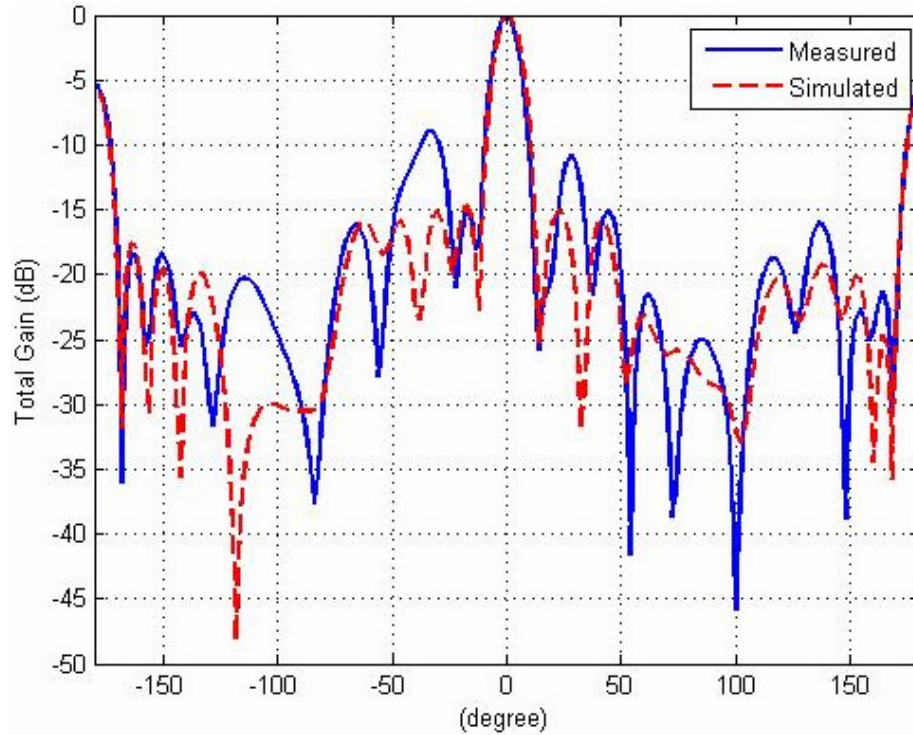


Figure 5.53 Measured and simulated E-plane patterns of the array (10.5 GHz)

Radiation patterns of the array in co-polarization and cross-polarization are shown in Figure 5.41 through Figure 5.50. The measured and simulated radiation patterns are consistent especially in lower frequencies. The nulls observed in radiation patterns at 15 GHz and 18 GHz are due to the reflections both from the test setup and the metallic backplane of the array. Measured and simulated E-plane patterns of the antenna are also compared in Figure 5.51 through Figure 5.53. Measured 3-dB beamwidth, side lobe and grating lobe levels of the array in H-plane are given below.

Table 5.1 Measured half-power beamwidth of the array in 2-18 GHz frequency band

Frequency of Operation	3-dB Beamwidth
2.0 GHz	16°
6.0 GHz	14°
8.5 GHz	11°
9.5 GHz	10°
10.5 GHz	10°
15 GHz	9°
18 GHz	8°

Table 5.2 Side lobe and grating lobe levels of the array in 2-18 GHz frequency band

Frequency of Operation	Side Lobe Level	Grating Lobe Level
2.0 GHz	1 dB	2 dB
6.0 GHz	4 dB	3 dB
8.5 GHz	15 dB	12 dB
9.5 GHz	16 dB	18 dB
10.5 GHz	13 dB	20 dB
15 GHz	2 dB	2 dB
18 GHz	2 dB	1 dB

Table 5.1 and Table 5.2 show that the array provides the design requirements, half power beamwidth less than 12° and side lobe level greater than 13 dB in 8.5-10.5 GHz operating bandwidth. It can be said that the Dolph-Chebyshev feeding discussed in Chapter 4 will result in extra decrease in the side lobe levels considering the consistency between simulated and measured results.

CHAPTER 6

CONCLUSION

6.1 Summary

The Vivaldi antenna, a type of TSA with its exponentially tapered profile, is observed in this thesis. As a member of the class of TSA, Vivaldi antenna provides broad bandwidth, low cross polarization and directive propagation at microwave frequencies. Vivaldi antennas are low cost and easy to fabricate due to printed circuit technology used for the construction of these antennas. Vivaldi arrays are also small size and low weight enabling compact arrays. The beamwidth and directivity of a Vivaldi antenna might be considerably improved varying the design parameters.

Vivaldi antenna design parameters are investigated in this work. The effects of each antenna parameter on antenna impedance return loss response and reverse gain characteristics are simulated and observed. The simulations are realized using Ansoft HFSS[®]. Based on the results of this study, a Vivaldi antenna with the requirements of 8.5-10.5 GHz frequency bandwidth, return loss better than 10 dB and 50 Ω characteristic impedance in the feeding section is designed. Stripline to slotline transition is chosen due to its beamwidth characteristic and fairly enough bandwidth performance. The simulation results reveals that the designed Vivaldi antenna has a return loss response better than 17 dB and reverse gain response smaller than 1.15 dB in the operating bandwidth. The antenna has also side lobe level better than 5 dB and half power beamwidth smaller than 48° in H-plane.

The array parameters are also observed regarding their effects on radiation pattern. An 8-element uniform linear array with the designed single antenna. The array has side lobe level better than 11 dB, grating lobe level better than 8 dB and half power beamwidth smaller than 13° in H-plane observing simulation results.

The designed array is fed using binomial and Dolph-Chebyshev feeding techniques next. Binomial array provides a 10 dB decrease in side lobe level whereas the half power beamwidth is 18° for this type of feeding. The half power beamwidth is observed to be smaller than 11° with side lobe level better than 11 dB for Dolph-Chebyshev feeding technique. The simulated results of the array are not satisfying regarding the design requirements: half power beamwidth smaller than 12° and side lobe level better than 13 dB in H-plane.

The parametric study of arrays has led to another single element Vivaldi antenna design with a longer taper and wider slotline. The simulation results show that the second antenna is more directive with a half power beamwidth of 36° at 9.5 GHz and smaller than 44° through the operating bandwidth.

An improved uniform linear array design is realized using the second Vivaldi antenna designed. The array has a better radiation pattern with side lobe level of 17 dB and half power beamwidth of 10° at 9.5 GHz. Dolph-Chebyshev feeding technique is applied to this array too. Dolph-Chebyshev polynomial coefficients are chosen to get a side lobe level of 17 dB first and this structure provides a half power beamwidth of 8° at 9.5 GHz. Then, the coefficients are chosen with a side lobe level of 20 dB which results in a half power beamwidth of 11° at 9.5 GHz. The latter Dolph-Chebyshev array is found fairly satisfactory regarding the design requirements. The simulation results in the operating bandwidth has revealed that the Dolph-Chebyshev array provides a half power beamwidth smaller than 12° , side lobe level better than 17 dB and grating lobe level better than 16 dB.

The single element Vivaldi antennas and the improved array detailed above are fabricated in Aselsan Inc. using printed circuit board technology. Return loss responses and the radiation patterns of the fabricated antennas and array are measured and compared with the simulation results.

The measured return loss responses of both single element Vivaldi antennas are consistent with the simulation results. These antennas are observed to have return

loss responses better than 15 dB in the operating frequency band. Moreover, the antennas have return loss responses better than 10 dB in 6-18GHz frequency band. The radiation patterns of these antennas are measured in 2-18 GHz frequency band in the anechoic chamber of Aselsan Inc. and observed to be in accordance with the simulation results in the operating bandwidth. However, the measured radiation patterns have deeper nulls at the higher frequencies, greater than 12 GHz, due to the reflections from the metallic structure of the test setup.

The array is fabricated with a metallic backplane and fed using three identical 4-way power dividers. Return loss response of the array is measured in 2-18 GHz frequency band. It is observed to have return loss response better than 15 dB in 8.5-10.5 GHz operating band. The array has an acceptable return loss response, better than 10 dB, in 4-18 GHz frequency range. The return loss response of the array could not be simulated because of the convergence problem in the simulation tool used. The measured radiation pattern of the array is fairly consistent with the simulated patterns especially in the operating bandwidth. There exist deeper nulls at the higher frequencies as in the case of single antenna radiation pattern measurements. The metallic backplane of the array as well as the metallic structure of the test setup cause this generate this discrepancy.

6.2 Future Work

In the future, the followings might be considered in order to extend and improve this work :

- The parametric study of Vivaldi antennas and arrays might be extended observing their effects on antenna and array performance in a broader bandwidth.
- Dolph-Chebyshev feeding technique might be considered and realized when highly directive array designs with acceptable side lobe levels are to be fabricated.

- The backwall offset of the single element antennas might be chosen considering the metallic backplane to be used in order to reflect radiations in the opposite direction and improve forward radiation of the array. This will reduce the reflections observed in the radiation pattern measurements and prevent the discrepancy between measured and simulated results at higher frequencies.
- The microstrip to slotline, antipodal and balanced antipodal transitions as well as the stripline to slotline transitions with nonuniform stubs might be considered in order to observe the effects of parameters on the designs with different antenna feeding techniques.
- A dual-polarized array constructed with the designed Vivaldi array would have a fairly narrow beamwidth as well as the rapid scanning advantage of dual-polarized arrangement. This array might be used for Synthetic Aperture Radar (SAR) applications.

REFERENCES

- [1] Federal Communication Commission, "First Order and Report, Revision of Part 15 of the Commission's Rules Regarding UWB Transmissions Systems," FCC 02-48, April 2002.
- [2] P. J. Gibson, "The Vivaldi Aerial," Proc. 9th European Microwave Conference, Brighton, U.K., Oct. 1979, pp. 101-105.
- [3] L. R. Lewis, M. Fasset, and J. Hunt. "A broadband stripline array," IEEE A P-S Synip., June 1974, p. 335.
- [4] K. S. Yngvesson., T. L. Korzienowski, Y. S. Kim, E. L. Kollberg, J. F. Johansson, "Endfire Tapered Slot Antenna on Dielectric Substrates," IEEE Trans. Antennas & Prop., Vol. AP-33, No. 12, December 1985, pp. 1392- 1400.
- [5] E. Gazit, "Improved design of a Vivaldi antenna," IEEE Proc. H, April 1988, pp. 89-92.
- [6] J. D. S. Langley, P. S. Hall, P. Newham, "Novel ultrawide-bandwidth Vivaldi antenna with low cross polarization," Electronic Letters, Vol. 29, No. 23, November 1993, pp. 2004-2005.
- [7] J. D. S Langley, P. S. Hall and P. Newham, "Balanced Antipodal Vivaldi Antenna for Wide Bandwidth Phased Arrays", IEEE Proc. Antennas and Propagation, Vol. 143, No. 2, April 1996, pp. 97-102.
- [8] S. G. Kim, K. Chang, "A low cross-polarized antipodal Vivaldi antenna array for wide-band operation," in *Proc. IEEE Int. AP-S Symp.*, Monterey, CA, June 2004, pp. 2269–2272.
- [9] B. Schuppert, "Microstrip/Slotline Transitions: Modeling and Experimental Investigation," IEEE Transactions on Microwave Theory and Techniques, Vol. 36, No. 8, August 1988, pp. 1272-1282.
- [10] R. Sloan, M. M. Zinieris, L. E. Davis, "A broadband microstrip to slotline transition," Microwave and Optical Technology Letters, Vol. 18, No. 5, August 1998, pp. 339-342.

- [11] D. H. Schaubert, J. Shin, "A Parameter Study of Stripline-Fed Vivaldi Notch Antenna Arrays," *IEEE Transactions on Antennas and Propagation*, Vol. 47, No. 5, May 1999, pp. 879-886.
- [12] D. H. Schaubert, T. H. Chio, "Parameter Study and Design of Wideband, Widescan Dual-Polarized Tapered Slot Antenna Arrays," *IEEE Transactions on Antennas and Propagation*, Vol. 48, No. 6, June 2000, pp. 879-886.
- [13] A. N. Sharp, R. Kyprianou, "Vivaldi Antennas: Wideband Radar Antennas Simulation and Reality," *IET International Conference on Radar Systems*, October 2007, pp. 1-5.
- [14] S. Wang, X. D. Chen, C. G. Parini, "Analysis of Ultra Wideband Antipodal Vivaldi Antenna Design," *Loughborough Antennas and Propagation Conference*, April 2007, pp. 129-132.
- [15] J. B. Knorr, "Slotline transitions," *IEEE Trans.*, Vol. MTT-22, May 1974, pp. 548-554.
- [16] B. Schiek, J. Kohler, "An Improved Microstrip-to-Microslot Transition," *IEEE Trans. on Microwave Theory and Techniques*, Vol. 24, No. 4, April 1976, pp. 231-233.
- [17] S. J. Orfanidis, *Electromagnetic Waves & Antennas*, ECE Department Rutgers University, June 2004
- [18] Y. Yang, Y. Wang, A. E. Fathy, "Design of Compact Vivaldi Antenna Arrays For UWB See Through Wall Applications," *Progress in Electromagnetics Research*, Pier 82, 2008, pp. 401-418.
- [19] N. Fourikis, *Advanced Array Systems Applications and RF Technologies*, Academic Press, 2000.
- [20] B. M. Notaros, B. D. Popovic, J. P. Weem, R. A. Brown, Z. Popovic, "Efficient Large-Domain MoM Solutions to Electrically Large Practical EM Problems," *IEEE Trans. on Microwave Theory and Techniques*, Vol. 49, No. 1, January 2001, pp. 151-159.
- [21] M. Kragalot, W. Pickles, M. Kluskens "Design of a 5 : 1 Bandwidth Stripline Notch Array from FDTD Analysis," *IEEE Transactions on Antennas and Propagation*, Vol. 48, No. 11, November 2000, pp. 1733-1741.
- [22] T. K. Sarkar, E. Arvas, S. M. Rao, "Application of FFT and the Conjugate Gradient Method for the Solution of Electromagnetic Radiation from Electrically Large and Small Conducting Bodies," *IEEE Transactions on Antennas and Propagation*, Vol. 35, No. 5, May 1987, pp. 607-609.

- [23] C. Fang, F. Ling, J. M. Jin “A Fast Full-Wave Analysis of Scattering and Radiation from Large Finite Arrays of Microstrip Antennas,” IEEE Transactions on Antennas and Propagation, Vol. 46, No. 10, October 1998, pp.1467-1474.
- [24] R. Rajaraman, “Design of a Wideband Vivaldi Antenna Array For The Snow Radar,” Ms. Thesis, University of Kansas, February 1999.
- [25] M. E. Saygmer, “ Design and Realization of a Circular Array of Vivaldi Antennas,” Ms. Thesis, Middle East Technical University, June 1994.
- [26] B. C. Wadell, Transmission Line Design Handbook, Artech House, 1991.
- [27] High Speed Board Layout Guidelines-
http://www.altera.com/literature/hb/stx2/stx2_sii52012.pdf, Altera Corp, May 2007.
- [28] K.C. Gupta, R. Garg and I.J. Bahl, Microstrip Lines and Slotlines, Artech House, 1979.
- [29] C. A. Balanis, Antenna Theory Analysis and Design, 2nd Edition, John Wiley&Sons, 1997.
- [30] R. E. Collin, Antennas and Radiowave Propagation, Mc-Graw Hill, 1985.
- [31] W. L. Stutzman, G. A. Thiele, Antenna Theory and Design, 2nd Edition, John Wiley&Sons, 1998.
- [32] A.G. Yıldız, “Small Size Wideband Vivaldi Antennas For Phased Array Systems,” Ms. Thesis, Middle East Technical University, Dec 2001.

APPENDIX A

SIMULATION METHOD

The simulations in this study are realized using Ansoft HFSS[®], a high frequency electromagnetic field simulation program utilizing full-wave finite element method (FEM). The antenna model is constructed as in Figure A.1 below.

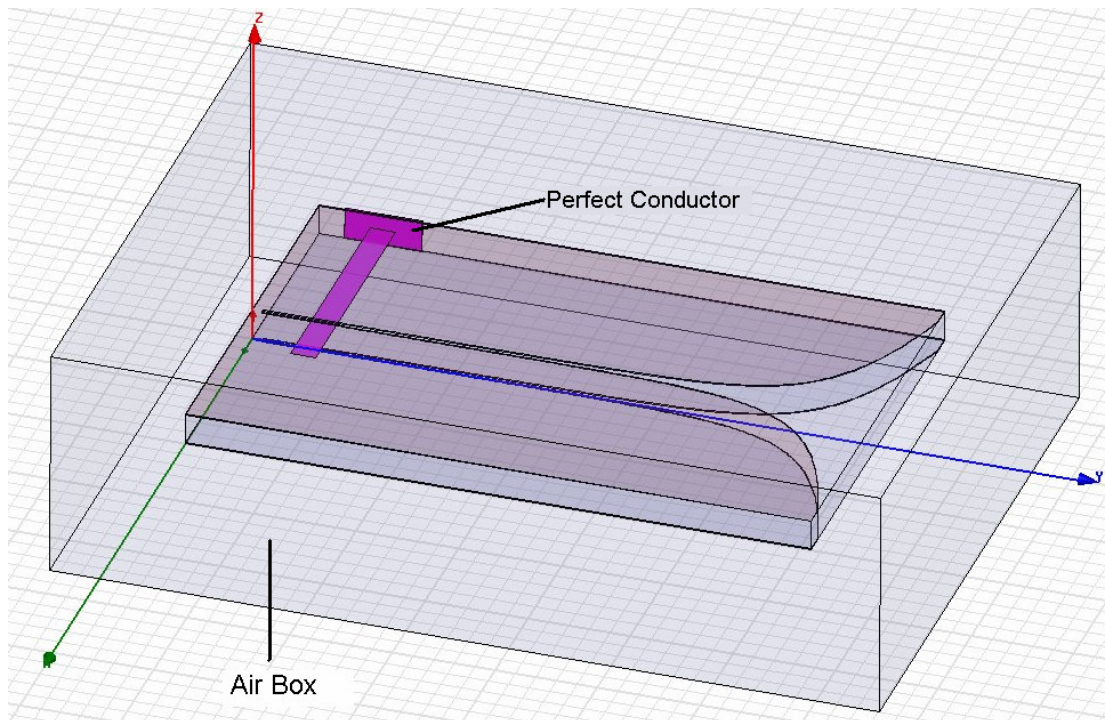


Figure A.1 Complete antenna model in HFSS

The perfect conductor seen in the Figure A.1 above is used to feed the stripline. A wave-port exciting the model is formed on the inner face of the perfect conductor, touching on the stripline. Wave-port excitation is used to indicate the area where the energy enters the system. A port-line is defined to direct the fields from the live

terminal, stripline in this case, to the ground. Figure A.2 below shows the wave-port structure and the port-line.

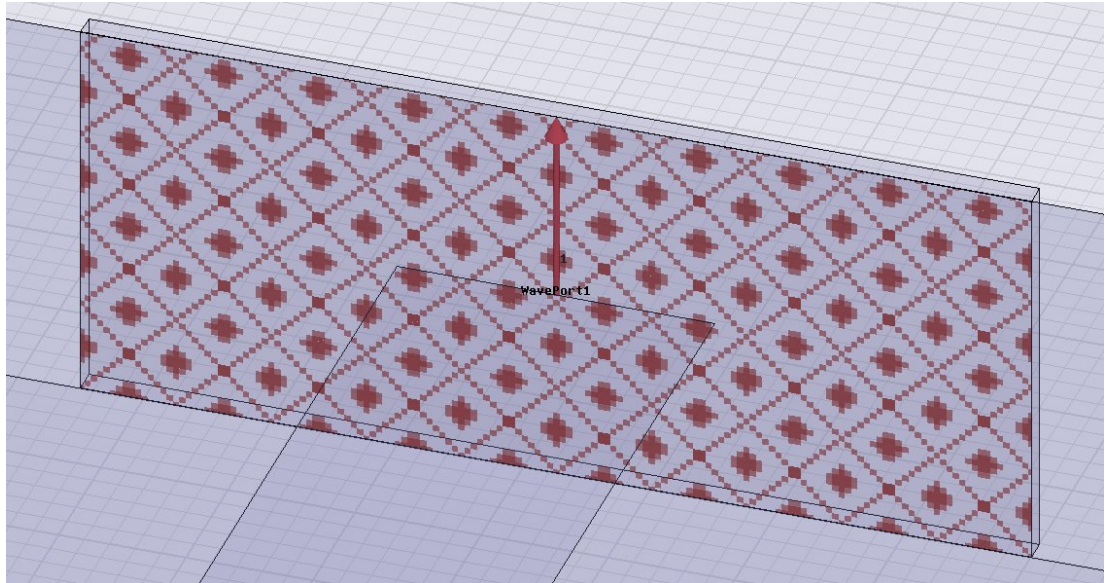


Figure A.2 The wave-port structure

The air box seen in the Figure A.1 is defined to represent open space. Ansoft suggests it to be placed to a quarter wavelength distance from the model. Air box boundaries are defined to be radiation boundary so that the radiation from the structure is absorbed not reflected back.

The last step of the simulation model is to define a solution setup. Solution frequency is chosen as 9.5 GHz. The solution setup is defined including 8.5-10.5 GHz sweep in order to investigate the whole band antenna performance. Radiation patterns as well as return loss and reverse gain curves are obtained running the simulations.

APPENDIX B

MATLAB FUNCTION

The function below is used to determine the coefficients of N^{th} order Dolph-Chebyshev polynomial.

```
N1 = N-1; % number of zeros  
Ra = 10^(R/20); % sidelobe level in absolute units  
x0 = cosh(acosh(Ra)/N1); % scaling factor  
i = 1:N1;  
xi = cos(pi*(i-0.5)/N1); % N1 zeros of Chebyshev polynomial  
psi = 2 * acos(xi/x0); % N1 array pattern zeros in psi-space  
zi = exp(j*psi); % N1 zeros of array polynomial  
a = real(poly(zi)); % zeros-to-polynomial form (N coefficients)
```

APPENDIX C

DATASHEETS



Advanced Circuit Materials

Advanced Circuit Materials Division
100 S. Roosevelt Avenue
Chandler, AZ 85226
Tel: 480-961-1382, Fax: 480-961-4533
www.rogerscorporation.com

Data Sheet
1.5000

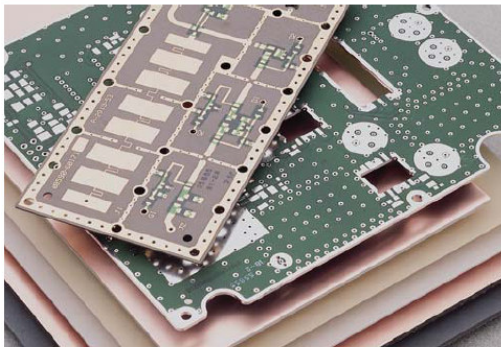
RT/duroid®5870 /5880 High Frequency Laminates

Features:

- Lowest electrical loss for reinforced PTFE material.
- Low moisture absorption.
- Isotropic
- Uniform electrical properties over frequency.
- Excellent chemical resistance.

Some Typical Applications:

- Commercial Airline Telephones
- Microstrip and Stripline Circuits
- Millimeter Wave Applications
- Military Radar Systems
- Missile Guidance Systems
- Point to Point Digital Radio Antennas



RT/duroid® 5870 and 5880 glass microfiber reinforced PTFE composites are designed for exacting stripline and microstrip circuit applications.

Glass reinforcing microfibers are randomly oriented to maximize benefits of fiber reinforcement in the directions most valuable to circuit producers and in the final circuit application.

The dielectric constant of RT/duroid 5870 and 5880 laminates is uniform from panel to panel and is constant over a wide frequency range. Its low dissipation factor extends the usefulness of RT/duroid 5870 and 5880 to Ku-band and above.

RT/duroid 5870 and 5880 laminates are easily cut, sheared and machined to shape. They are resistant to all solvents and reagents, hot or cold, normally used in etching printed circuits or in plating edges and holes.

Normally supplied as a laminate with electrodeposited copper of $\frac{1}{4}$ to 2 ounces/ft.² (8 to 70 μ m) on both sides, RT/duroid 5870 and 5880 composites can also be clad with rolled copper foil for more critical electrical applications. Cladding with aluminum, copper or brass plate may also be specified.

When ordering RT/duroid 5870 and 5880 laminates, it is important to specify dielectric thickness, tolerance, rolled or electrodeposited copper foil, and weight of copper foil required.

Figure C.1 Rogers RT/Duroid 5880 high frequency laminate datasheet

Typical Values

RT/duroid® 5870/5880 Laminates

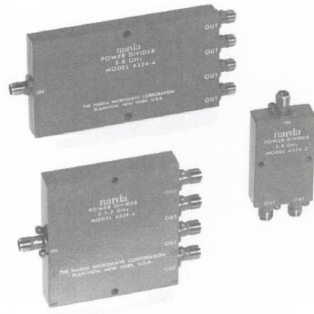
PROPERTY	TYPICAL VALUE				DIRECTION	UNITS	CONDITION	TEST METHOD	
	RT/duroid® 5870		RT/duroid 5880						
Dielectric Constant, ϵ_r	2.33 2.33 ± 0.02 spec.		2.20 2.20 ± 0.02 spec.		Z		C24/23/50 C24/23/50	1 MHz IPC-TM-650, 2.5.5.3 10 GHz IPC-TM-2.5.5.5	
Dissipation Factor, $\tan \delta$	0.0005 0.0012		0.0004 0.0009		Z		C24/23/50 C24/23/50	1 MHz IPC-TM-650, 2.5.5.3 10 GHz IPC-TM-2.5.5.5	
Thermal Coefficient of ϵ_r	-115		-125			ppm/°C	-50 - 150°C	IPC-TM-650, 2.5.5.5	
Volume Resistivity	2×10^7		2×10^7		Z	Mohm cm	C96/35/90	ASTM D257	
Surface Resistivity	2×10^8		3×10^7		Z	Mohm	C96/35/90	ASTM D257	
Tensile Modulus	Test at 23°C	Test at 100°C	Test at 23°C	Test at 100°C		MPa (kpsi)	A	ASTM D638	
	1300 (189)	490 (71)	1070 (156)	450 (65)	X				
ultimate stress	1280 (185)	430 (63)	860 (125)	380 (55)	Y	%	A	ASTM D695	
	50 (7.3)	34 (4.8)	29 (4.2)	20 (2.9)	X				
ultimate strain	42 (6.1)	34 (4.8)	27 (3.9)	18 (2.6)	Y	%	A	ASTM D695	
	9.8	8.7	6.0	7.2	X				
Compressive Modulus	9.8	8.6	4.9	5.8	Y	MPa (kpsi)	A	ASTM D621	
	1210 (176)	680 (99)	710 (103)	500 (73)	X				
ultimate stress	1360 (198)	860 (125)	710 (103)	500 (73)	Y	%	A	ASTM D648	
	803 (120)	520 (76)	940 (136)	670 (97)	Z				
ultimate strain	30 (4.4)	23 (3.4)	27 (3.9)	22 (3.2)	X	J/g/K (cal/g/C)	D24r/1.4 MPa (2 Kpsi)	ASTM D621	
	37 (5.3)	25 (3.7)	29 (5.3)	21 (3.1)	Y				
Deformation Under Load, Test at 150°C	54 (7.8)	37 (5.3)	52 (7.5)	43 (6.3)	Z	mg (%)	1.82 MPa (264 psi)	ASTM D570	
	4.0	4.3	8.5	8.4	X				
Heat Distortion Temperature	>260 (>500)		>260 (>500)		X,Y	°C (°F)		ASTM D648	
Specific Heat	0.96 (0.23)		0.96 (0.23)			W/m/K		ASTM D621	
Moisture Absorption	Thickness 0.31" (0.8mm)	0.9 (0.02)		0.9 (0.02)		mm/m	D24/23	ASTM D3386 (10K/min) (Values given are total change from a base tem- perature of 35°C)	
	0.62" (1.6mm)	13 (0.015)		13 (0.015)					
Thermal Conductivity	0.22		0.20		Z	°C TGA		ASTM D3850	
Thermal Expansion	X	Y	Z	X	Y	Z	mm/m	ASTM D3386 (10K/min) (Values given are total change from a base tem- perature of 35°C)	
	-5.0	-5.5	-11.6	-6.1	-8.7	-18.7			-100°C
	-0.6	-0.9	-4.0	-0.9	-1.8	-6.9			15
	-0.3	-0.4	-2.6	-0.5	-0.9	-4.5			25
	0.7	0.9	7.5	1.1	1.5	8.7			75
	1.8	2.2	22.0	2.3	3.2	28.3			150
3.4	4.0	58.9	3.8	5.5	69.5	250			
Td	500		500			°C TGA		ASTM D3850	
Density	2.2		2.2					ASTM D792	
Copper Peel	20.8 (3.7)		22.8 (4.0)			pli (N/mm)	after solder float	IPC-TM-650 2.4.8	
Flammability	94V-0		94V-0					UL	
Lead-Free Process Compatible	Yes		Yes						

[1] SI unit given first with other frequently used units in parentheses.
 [2] References: Internal TR's 1430, 2224, 2654. Test were at 23°C unless otherwise noted.
 Typical values should not be used for specification limits.

STANDARD THICKNESS:	STANDARD PANEL SIZE:	STANDARD COPPER CLADDING:
0.005" (0.127mm), 0.010" (0.254mm), 0.015" (0.381mm), 0.020" (0.508mm)	18" X 12" (457 X 305mm) 18" X 24" (457 X 610mm) 18" X 36" (457 X 915mm) 18" X 48" (457 X 1,224mm)	¼ oz. (8 µm) electrodeposited copper foil. ½ oz. (17 µm), 1 oz. (35 µm), 2 oz. (70 µm) electrodeposited and rolled copper foil.

The information in this data sheet is intended to assist you in designing with Rogers' circuit material laminates. It is not intended to and does not create any warranties express or implied, including any warranty of merchantability or fitness for a particular purpose or that the results shown on this data sheet will be achieved by a user for a particular purpose. The user should determine the suitability of Rogers' circuit material laminates for each application.
 These commodities, technology and software are exported from the United States in accordance with the Export Administration regulations. Diversion contrary to U.S. law prohibited.
 RT/duroid and DUROID are licensed trademarks of Rogers Corporation.
 © 1989, 1994, 1995, 1999, 2002, 2005, 2006 Rogers Corporation, Printed in U.S.A. All rights reserved.
 Revised 11/06 0696-1106-0.5CC Publication #92-101

Figure C.2 Rogers RT/Duroid 5880 high frequency laminate datasheet



0.5-33 GHz

Multi-Octave 2- and 4-Way Power Dividers

- Broadband Frequency Coverage from 0.5 to 33 GHz
- Excellent Phase and Amplitude Tracking
- Low Input VSWR
- High Isolation Between Output Ports
- Precision SMA or 2.92 mm Connectors

Specifications

FREQUENCY RANGE GHz	MODEL	BAND SEGMENT GHz	VSWR		INSERTION LOSS (max)	ISOLATION dB (min)	AMP BAL dB	PHASE BAL Degrees	AVERAGE* POWER Watts			WEIGHT	
			INPUT	OUTPUT					A	B	C	oz	gr
2-Way Power Dividers													
0.5-2.0	4321B-2	0.5-2.0	1.25	1.15	0.6	22	0.2	2.0	30	20	3	1.1	30
0.5-2.5	4322-2	0.5-2.5	1.35	1.15	0.3	18	0.2	2.0	30	10	1	2.0	55
0.8-2.2	4325-2	0.8-2.2	1.25	1.15	0.6	23	0.2	2.0	30	20	3	1.1	30
2-8	4324-2	2-4	1.35	1.35	0.2	20	0.2	3.0	30	10	1	1.2	35
		4-8	1.35	1.25	0.5	20	0.3	4.0	30	10	1	1.2	35
5-18	4326B-2	5-12.4	1.35	1.30	0.4	19	0.2	3.0	30	10	1	0.7	20
		12.4-18	1.4	1.35	0.5	20	0.3	6.0	30	10	1	0.7	20
2-18	4456-2	2-8	1.3	1.25	0.5	20	0.2	3.0	30	10	1	1.4	38
		8-18	1.4	1.4	1.2	19	0.3	6.0	30	10	1	1.4	38
1.7-26.5	4327C-2	1.7-2	1.5:1	1.5:1	1.1	19	0.3	6.0	30	10	2	1.8	50
		2-18	1.4:1	1.35:1	1.4	21	0.3	6.0	30	10	2	1.8	50
		18-26.5	1.7:1	1.5:1	2.4	16	0.5	10.0	30	10	2	1.8	50
10-33	4328B-2 **	10-18	1.5	1.5	1.5	15	0.5	6.0	30	10	1	0.8	22
		18-33	2.0	2.0	1.5	15	0.5	12.0	30	10	1	0.8	22
4-Way Power Dividers													
0.5-2	4321C-4	0.5-2	1.45	1.30	1.3	20	0.3	4.0	30	10	1	2.9	80
0.5-2.5	4322-4	0.5-2.5	1.45	1.25	0.7	20	0.3	4.0	30	10	1	5.8	165
0.8-2.2	4325-4	0.8-2.2	1.25	1.20	0.9	22	0.3	3.0	30	10	1	2.9	80
2-8	4324-4	2-8	1.45	1.35	0.9	18	0.4	4.0	30	10	1	4.3	120
		5-18	4326B-4	5-6	1.60	1.40	0.5	18	0.3	3.0	30	10	1
5-18	4326B-4	6-18	1.50	1.40	0.9	19	0.5	6.0	30	10	1	2.2	60
		2-18	4456-4	2-8	1.40	1.40	1.0	20	0.4	6.0	30	10	1
2-18	4456-4	8-18	1.50	1.40	1.8	18	0.8	10.0	30	10	1	4.3	120

*Average Power Rating into a load VSWR of (A) 1.2 to 1, (B) 2 to 1 and (C) ∞VSWR

** Custom-order basis. Minimum quantity may apply.

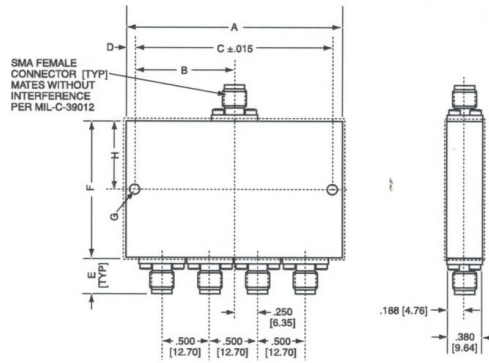
Note: All models use precision SMA Female connectors, except Models 4327C-2 and 4328B-2 which use 2.92 mm Female type.

435 MORELAND ROAD • HAUPPAUGE, NY 11788
 USA TEL: (1) 631 231-1700 • INT'L TEL: (1) 631 231-1390 • FAX (1) 631 231-1711
 E-MAIL: nardaeast@L-3COM.com • www.nardamicrowave.com

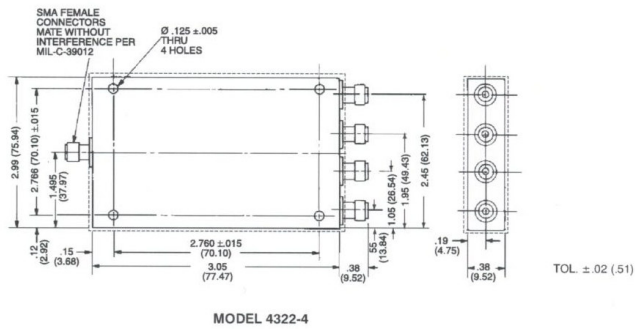


Figure C.3 Narda 4326B-4 power divider datasheet

Outline Drawings - Multi-Octave 4-Way Power Dividers



MODEL	A	B	C	D	E	F	G (Thru 2 Holes)	H
4321C-4	2.343 (59.51)	1.171 (29.74)	2.153 (54.68)	.095 (2.41)	.375 (9.52)	2.11 (53.62)	.104 ^{+0.004} -.002 Dia.	1.055 (26.79)
4324-4	1.940 (49.27)	.970 (24.63)	1.688 (42.87)	.126 (3.20)		3.448 (87.57)	.146 Dia.	1.724 (43.78)
4325-4	2.343 (59.51)	1.171 (29.74)	2.153 (54.68)	.095 (2.41)	406 (10.31)	2.11 (53.62)	.104 ^{+0.004} -.002 Dia.	1.055 (26.79)
4326B-4	1.940 (49.27)	.970 (24.63)	1.688 (42.87)	.126 (3.20)	.375 (9.52)	1.418 (36.01)	.146 Dia.	.709 (18.00)
4456-4						3.448 (87.57)		1.724 (43.78)



MODEL 4322-4

Allow .020 for sealant buildup per surface.

Dimensions in parentheses are in millimeters and for reference only.

435 MORELAND ROAD • HAUPPAUGE, NY 11788
 USA TEL: (1) 631 231-1700 • INT'L TEL: (1) 631 231-1390 • FAX (1) 631 231-1711
 E-MAIL: nardaeast@L-3COM.com • www.nardamicrowave.com

narda
 an |  communications company

145



Figure C.4 Narda 4326B-4 power divider datasheet

APPENDIX D

ASELSAN TAPERED ANECHOIC CHAMBER

The measurements and evaluation of the sinuous antennas are performed in an anechoic chamber, Figure D.1. Anechoic chamber is a reflection free (i.e. the reflectivity levels of the absorbers covering the whole room are very low, about -20 dB) room inside of which is covered by absorbers.

The tapered anechoic chamber is designed in the shape of pyramidal horn that tapers from the small source end to a large rectangular test region, and with high quality absorbing material covering the side walls, floor and ceiling. The tapered anechoic chamber in the R&D department of Aselsan Inc. is used with an azimuth over elevation positioner holding up the antenna under test, a polarization positioner holding up the standard transmitter antenna, an Agilent PNA model vector network analyzer, and HP PII series computers using programs written in HP VEE program at Aselsan and which communicate with the above listed equipment through the aid of HP-IB's. Antenna measurement set up in anechoic chamber is shown in Figure D.2.

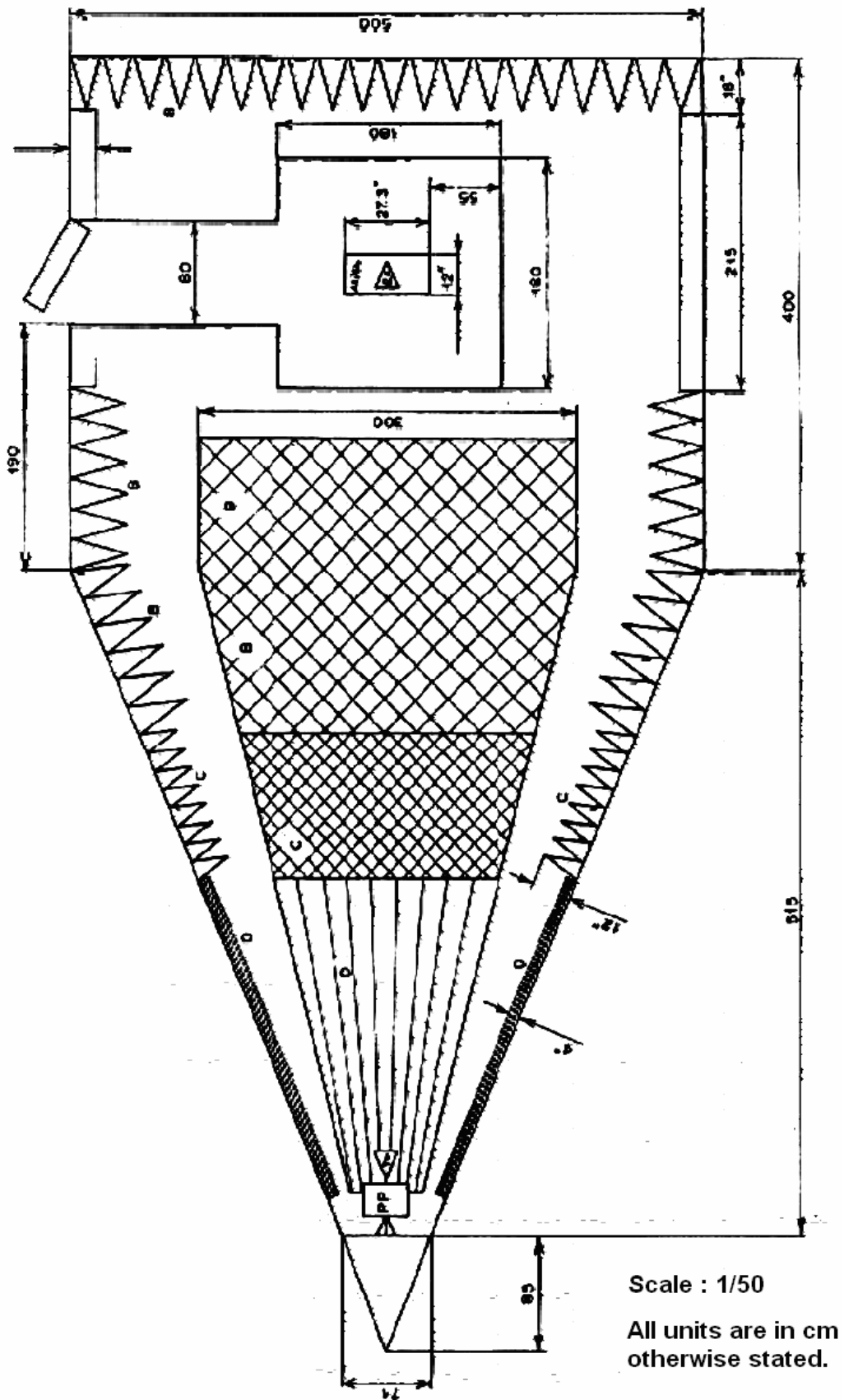


Figure D.1 Top view of the tapered anechoic chamber in ASELSAN Inc.

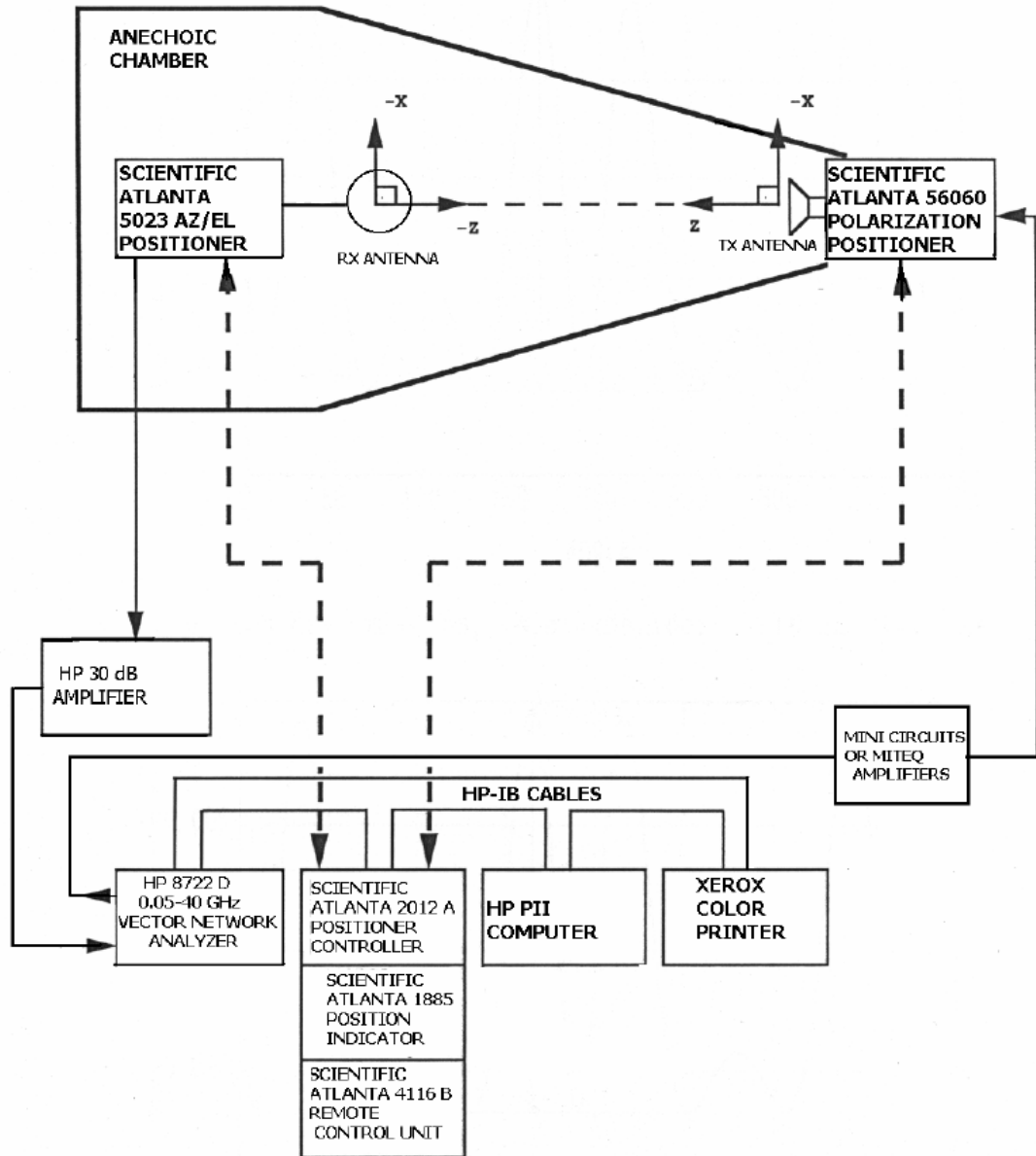


Figure D.2 Antenna measurement setup in the anechoic chamber